Analysis of pore pressure influence on failure mechanisms in structural systems

Emina Hadžalić

Par **Emina HADŽALIĆ**

Analysis of pore pressure influence on failure mechanisms in structural systems

Thèse présentée en cotutelle pour l'obtention du grade de Docteur de l'UTC

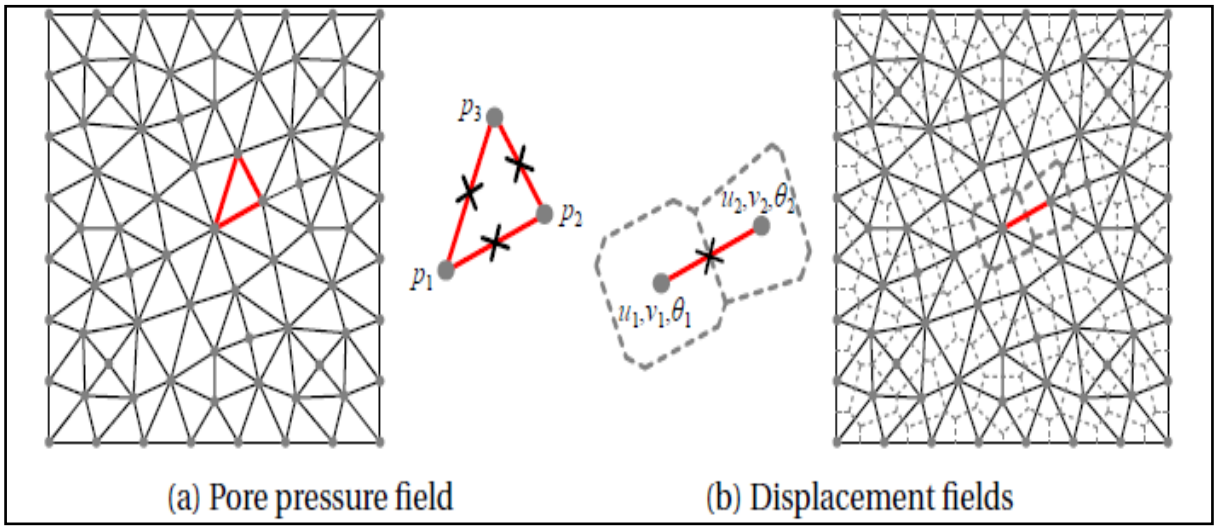

Soutenue le 17 septembre 2019
Spécialité : Mécanique Numérique : Unité de recherche en Mécanique - Laboratoire Roberval (FRE UTC - CNRS 2012)

D2502

University of Technology
of Compiègne

University of Sarajevo,
Faculty of Civil Engineering

EMINA HADŽALIĆ

ANALYSIS OF PORE PRESSURE INFLUENCE ON FAILURE MECHANISMS IN STRUCTURAL SYSTEMS

Doctoral thesis

17/09/2019

Spécialité : Mécanique Numérique

Supervisors:

Prof. Adnan IBRAHIMBEGOVIC, PhD
University of Technology of Compiègne, France

Prof. Samir DOLAREVIĆ, PhD
University of Sarajevo, Faculty of Civil Engineering, BIH

Sarajevo & Compiègne, September 17, 2019

University of Technology
of Compiègne

University of Sarajevo,
Faculty of Civil Engineering

This doctoral thesis is prepared in accordance with doctorate co-supervision agreement between University of Technology of Compiègne, Sorbonne University Alliance, France and University of Sarajevo, Faculty of Civil Engineering, Bosnia and Herzegovina.

The doctoral thesis is defended on September 17, 2019. at the University of Sarajevo, Faculty of Civil Engineering, before the following committee:

1. Prof. Adnan IBRAHIMBEGOVIC, PhD, University of Technology of Compiègne, France
2. Prof. Samir DOLAREVIĆ, PhD, University of Sarajevo, Faculty of Civil Engineering, BiH
3. Prof. Željana NIKOLIĆ, PhD, University of Split, Faculty of Civil Engineering, Architecture and Geodesy, Croatia
4. Prof. José Luis PÉREZ APARICIO, PhD, Universitat Politècnica de València, Escuela Técnica Superior de Ingeniería del Diseño, Spain
5. Emeritus Prof. Muhamed ZLATAR, PhD, University of Sarajevo, Faculty of Civil Engineering, BiH
6. Prof. Abdellatif OUASHINE, PhD, University of Technology of Compiègne, France
7. Prof. Hermann G. MATTHIES, PhD, TU Braunschweig, Germany
8. Prof. Ivica KOŽAR, PhD, University of Rijeka, Faculty of Civil Engineering, Croatia

This doctoral thesis contains:

Pages:	183
Figures:	126
Tables:	11
Equations:	192
References:	157
Appendices:	-

"Remember to celebrate milestones as you prepare for the road ahead."

— Nelson Mandela

To my family…

ACKNOWLEDGEMENTS

The work on this thesis has been supported by the University of Sarajevo, Faculty of Civil Engineering and the French Government scholarship for doctoral level. These supports are gratefully acknowledged.

I would like to express my warmest thanks

To my supervisors:

- *professor Adnan Ibrahimbegovic, for the patient guidance, immense knowledge generously shared, continuous support, encouragement and motivation throughout this journey, which helped me to move forward and to grow, not just as a researcher but as a person. I would also like to thank his wife Nita, who is always very kind and welcoming, and with whom I shared many laughs.*

- *professor Samir Dolarević, for persistent help and support in every situation, whether it was about research or personal struggles.*

To the reviewers of the thesis, professor Željana Nikolić and professor José Luis Pérez Aparicio, and the members of the jury, emeritus professor Muhamed Zlatar, professor Abdellatif Ouashine, professor Hermann G. Matthies and professor Ivica Kožar for careful reading and constructive comments. I am deeply grateful to emeritus professor Muhamed Zlatar for his constant support from the very beginning of my academic and research career.

To madam Catherine Palpant from the Department of Culture and Scientific Cooperation, French Embassy in Bosnia and Herzegovina and madam Željka Divković from Campus France office in Bosnia and Herzegovina, for their immense support.

To all my friends and colleagues at the Faculty of Civil Engineering, University of Sarajevo for their help, many constructive discussions, and for all funny talks we shared throughout this period.

To the wonderful new friends I met during my PhD studies at UTC. Thanks to Tea and Ivan for always being there for me, my Sarita and Milan for all their support

and encouragement, Pablito - FEAP guru for his friendship, patience and selfless help with FEAP and also thanks to Abir, Adela, Xuan Nam, Andjelka and Mijo for all the fun we had on this journey.

To all my friends and especially my best friend Lejla, for all supporting words and encouragement.

And finally, to my family. Thank you for everything. Without you, this would not be possible.

ABSTRACT

Title: Analysis of pore pressure influence on failure mechanisms in structural systems

This thesis studies the issue of the overall safety of structures built of heterogeneous and pore-saturated materials under extreme loads in application to fluid-structure interaction problems, such as the dam-reservoir interaction. We propose a numerical model of interaction capable of predicting main tendencies and overall behavior of pore-saturated dam structure interacting with the reservoir in failure analyses of practical interest. The proposed numerical model is first presented in two-dimensional (2D) framework and later extended to three-dimensional (3D) framework.

We consider the structure built of porous cohesive material. We assume that the external fluid in interaction with the structure acts as a source of pore saturation. We model the response of the pore-saturated structure with the coupled discrete beam lattice model based on Voronoi cell representation of domain with inelastic Timoshenko beam finite elements enhanced with additional kinematics in terms of embedded strong discontinuities acting as cohesive links. The coupling between the solid phase and the pore fluid is handled with Biot's porous media theory, and Darcy's law governing the pore fluid flow. The numerical consideration of internal coupling results with an additional pressure-type degree of freedom placed at each node of the Timoshenko beam finite element, which is later used at the fluid-structure interface.

The confined conditions met for external fluid placed in the reservoir enable the modeling of external fluid motion with the acoustic wave theory. For the numerical representation of the external fluid limited to small (irrotational) motion, we choose a Lagrangian formulation and the mixed displacement/pressure based finite element approximation. The end result are the displacement and pressure degrees of freedom per node of external fluid finite elements, which allows for the issue of the fluid-structure interface to be solved in an efficient and straightforward

manner by directly connecting the structure and external fluid finite elements at common nodes. As a result, all computations can be performed in a fully monolithic manner.

All numerical implementations and computations are performed with the research version of the computer code FEAP (Finite Element Analysis Program). The proposed numerical models of structure, external fluid and ultimately numerical model of interaction are validated in the linear elastic regime of structure response by comparing computed results against reference values obtained either with analytical solutions or continuum models. The numerical simulations in the nonlinear regime of structure response are performed with the aim to demonstrate the proposed coupled discrete beam lattice model capabilities to capture complete macro-scale response and failure mechanisms in pore-saturated structures. Finally, the proposed numerical model of interaction ability to deal with the progressive localized failure of a dam structure built of porous cohesive material under dam-reservoir interaction for a particular loading program was tested. To account for the temperature effects, the thermal coupling is introduced in the numerical model of the structure.

Keywords: cohesive discrete beam lattice model, Timoshenko beam, embedded discontinuity, coupling, pressure, porous medium, Biot's theory, acoustic wave theory, mixed displacement/pressure approximation, fluid-structure interaction, failure analysis, overall safety, temperature

RÉSUMÉ

Titre: Analyse des mécanismes de rupture des systèmes structurels en poro-plasticité

Cette thèse porte sur la sécurité globale des structures en matériaux hétérogènes saturés soumis à des charges extrêmes, et est appliquée à des problèmes d'interaction fluide-structure, tels que l'interaction barrage-réservoir. Un modèle numérique d'interaction est proposé pour prédire les principales tendances et le comportement général d'un barrage en matériau saturé en interaction avec le réservoir dans des analyses de défaillance d'intérêt pratique. Le modèle numérique proposé est d'abord présenté dans un cadre bidimensionnel (2D), puis étendu à un cadre tridimensionnel (3D).

La structure est considérée comme un milieu poreux saturé constitué d'un matériau cohésif. On suppose que le fluide externe en interaction avec la structure agit comme une source de saturation des pores. La réponse de la structure en matériau saturé est décrite avec un modèle lattice discrete couplé de type poutre, basé sur la discrétisation du domaine avec la tessellation de Voronoï, où les liens cohésifs sont représentés par des poutres de Timoshenko non linéaires avec un champ de déplacements enrichi en termes de discontinuités fortes. Le couplage entre la phase solide et le fluide dans les pores est traité avec la théorie de Biot et la loi de Darcy décrivant l'écoulement d'un fluide à travers d'un milieu poreux. La prise en compte numérique du couplage interne ajoute un degré de liberté supplémentaire du type pression à chaque nœud de l'élément fini de Timoshenko, qui est ensuite utilisé pour résoudre les problèmes d'interface entre la structure et le fluide.

On considère que le fluide externe dans le réservoir est limité à des petits mouvements, ce qui nous permet de le modéliser avec la théorie des ondes acoustiques. Pour cela, la formulation lagrangienne avec l'approximation mixte déplacement-pression est choisie. Le traitement de l'interface fluide-structure dans le modèle numérique d'interaction est résolu d'une manière simple et efficace. Notamment,

les éléments finis de la structure et du fluide externe partagent les mêmes degrés de liberté dans les nœuds communs, permettant ainsi la résolution du système d'équations avec une approche de calcul monolithique.

Toutes les implémentations et les simulations numériques sont effectués avec la version recherche du code informatique FEAP (Finite Element Analysis Program). Les modèles numériques proposés pour la structure, le fluide externe et le modèle d'interaction sont validés dans le régime élastique linéaire en comparant les résultats calculés avec les valeurs de référence obtenues soit avec des solutions analytiques, soit avec des modèles continus. Les simulations numériques dans le régime non linéaire ont comme but de démontrer les capacités du modèle proposé de capturer la réponse complète à l'échelle macro et les mécanismes de rupture des structures en matériaux saturés. Enfin, la capacité du modèle d'interaction proposé de traiter la défaillance localisée progressive d'un barrage construit en matériau cohésif poreux sous l'interaction barrage-réservoir a été testé pour un programme de chargement spécifique. Pour prendre en compte les effets de la température, le couplage thermique est introduit dans le modèle numérique de la structure.

Mots clés: modèle lattice discrete cohésif de type poutre, poutre de Timoshenko, discontinuité intégrée, couplage, pression, milieu poreux, théorie de Biot, théorie des ondes acoustiques, approximation mixte déplacement-pression, interaction fluide-structure, analyse de défaillance, sécurité globale, température

SAŽETAK

Naslov: Analiza uticaja pornog pritiska na mehanizme loma konstruktivnih sistema

Ova doktorska teza analizira problem globalne sigurnosti konstrukcija od heterogenih i zasićenih materijala izloženih djelovanju ekstremnih opterećenja, s primjenom na probleme interakcije fluida i konstrukcije kao što je slučaj interakcije brana-rezervoar. U tezi je predložen numerički model s kojim je moguće predvidjeti glavne tendencije i globalno ponašanje konstrukcije brane izgrađene od zasićenog materijala u interakciji sa rezervoarom u analizama sloma od praktičnog interesa. Predloženi numerički model je najprije predstavljen kao dvodimenzionalan, a zatim proširen dodavanjem treće dimenzije.

Konstrukcija se posmatra kao zasićena porozna sredina izgrađena od kohezivnog materijala. Pretpostavlja se da vanjski fluid u interakciji sa konstrukcijom djeluje kao izvor poro-zasićenja. Odgovor konstrukcije od zasićenog materijala je modeliran diskretnim rešetkastim modelom koji je baziran na idealizaciji domene Voronoi ćelijama, sa nelinearnim Timoshenko-vim grednim konačnim elementima s obogaćenim poljem pomjeranja u vidu ugrađenih jakih diskontinuiteta kao kohezivnim vezama. Interakcija između čvrste faze i fluida u porama materijala je u modelu definisana sa Biot-ovom teorijom i Darcy-evim zakonom tečenja fluida. Numerička implementacija problema unutrašnje interakcije rezultuje sa dodatnim stepenom slobode kretanja - porni pritisak po svakom čvoru konačnog elementa Timoshenkove grede, koji se kasnije koristi za rješavanje problema sučelja između konstrukcije i fluida.

Malo pomjeranje vanjskog fluida u rezervoaru omogućuje modeliranje vanjskog fluida sa akustičnom teorijom. Za numeričko modeliranje malih pomjeranja vanjskog fluida, izabrana je Lagrange-ova formulacija i mješovita pomjeranje/pritisak aproksimacija. Problem zajedničkog sučelja konstrukcije i fluida u numeričkom modelu interakcije je jednostavno riješen direktnim povezivnjem konačnih elemenata konstrukcije i konačnih elemenata vanjskog fluida koji dijele iste stepene

slobode kretanja u zajedničkim čvorovima, što omogućava monolitan pristup rješavanju rezultujućeg sistema jednačina.

Sva numerička implementacija i numerički proračuni su urađeni u istraživačkoj verziji kompjuterskog koda FEAP (Finite Element Analysis Program). Predloženi numerički modeli konstrukcije, vanjskog fluida kao i numerički model interakcije su validirani u linearno elastičnom području odgovora konstrukcije poređenjem izračunatih rezultata sa referentnim vrijednostima dobivenim analitičkim rješenjima ili na modelima kontinuuma. Numeričke simulacije u nelinearnom području odgovora konstrukcije su sprovedene s ciljem demonistriranja mogućnosti predloženog modela konstrukcije da predvidi kompletan odgovor i mehanizme loma u konstrukciji izgrađenoj od zasićenog materijala. Konačno, testirana je mogućnost predloženog modela interakcije da opiše progresivni lokalizirani lom u konstrukciji brane izgrađene od kohezivnog zasićenog materijala u uslovima interakcije sa rezervoarom za određeni program opterećenja. S ciljem analiziranja uticaja temperature, u numerički model konstrukcije je uvedeno temperaturno polje.

Ključne riječi: kohezivni diskretni gredni rešetkasti model, Timoshenko-va greda, ugrađeni diskontinuitet, kuplovanje, pritisak, porozna sredina, Biot-ova teorija, akustična teorija, mješovita pomjeranje/pritisak aproksimacija, interakcija fluid-konstrukcija, analiza sloma, globalna sigurnost, temperatura

LIST OF PUBLICATIONS

JOURNALS

1. E. Hadzalic, A. Ibrahimbegovic and S. Dolarevic. Failure mechanisms in coupled soil-foundation systems, *Coupled Systems Mechanics*, 7(1):27–42, 2018.

2. E. Hadzalic, A. Ibrahimbegovic and M. Nikolic. Failure mechanisms in coupled poro-plastic medium, *Coupled Systems Mechanics*, 7(1):43–59, 2018.

3. E. Hadzalic, A. Ibrahimbegovic and S. Dolarevic. Fluid-structure interaction system predicting both internal pore pressure and outside hydrodynamic pressure, *Coupled Systems Mechanics*, 7(6):649-668, 2018.

4. E. Hadzalic, A. Ibrahimbegovic and S. Dolarevic. Theoretical formulation and seamless discrete approximation for localized failure of saturated poro-plastic structure interacting with reservoir, *Computers & Structures*, 214:73-93, 2019.

CONFERENCES AND WORKSHOPS

1. E. Hadzalic, A. Ibrahimbegovic, S. Dolarevic and M. Nikolic. Macroscale response of dry and saturated soil subjected to footing load, ECCOMAS MSF 2017 Thematic conference, 20-22 September 2017, Ljubljana, Slovenia.

2. A. Ibrahimbegovic, E. Hadzalic, E. Karavelic and M. Nikolic. Failure mechanisms in heterogeneous poro-plasticity media in application to FSI problems, ECCM6/ECFD7, 11-15 June 2018, Glasgow, UK.

3. E. Hadzalic, A. Ibrahimbegovic and S. Dolarevic. Novel method for acoustic fluid-structure interaction in application to overall safety of structures in

quasi-static setting, CILAMCE Congress, 11-14 November 2018, Paris/Compiègne, France.

4. E. Hadzalic, A. Ibrahimbegovic and S. Dolarevic and M. Nikolic. Seamless model for fluid-structure interaction predicting overall safety of dam structure under reservoir interaction, ECCOMAS MSF 2019 Thematic conference, 18-20 September 2019, Sarajevo, Bosnia and Herzegovina, accepted abstract.

5. Meca-Math Workshop, Poster: Acoustic fluid-structure interaction, 17-19 April 2018, Compiègne, France.

TABLE OF CONTENTS

CHAPTER 1

INTRODUCTION

OUTLINE

1.1 Motivation

This research is motivated by the practical considerations of localized failure in structures built of heterogeneous and pore-saturated materials under extreme loads. Namely, the presence of the pore fluid can determine the final response and in many cases increase the risk of the ultimate failure of the pore-saturated structure. Examples of this happening can be found widely in everyday engineering practice, whether it is a landslide triggered due to heavy rain in a slope that was once stable, liquefaction phenomena occurring as a result of the pore fluid presence in combination with extreme dynamic loading, fracturing and collapse of the dams resulting from the combined influences of poor monitoring and accidental loads, or issue of sound design of floating wind turbines (Figure 1.1).

(a) Landslide on Cecil Lake Road

(Source: *www.rncan.gc.ca/dangers-naturels/glissements-de-terrain → Photo by R. Couture (CGC)*, 2017)

(b) Liquefaction at Niigata

(Source: *en.wikipedia.org → Japan National Committee on Earthquake Engineering, Proceedings of the 3rd World Conference in Earthquake Engineering, Volume III, pp s.78-s.105.*)

(c) Teton dam failure

(Source: *en.wikipedia.org → www.usbr.gov/dataweb/assets/images/Teton2.jpg, 1976*)

(d) Floating wind turbine

(Source: *IDEOL*)

Figure 1.1 Examples of structures with significant influence of pore fluid presence

Some of the mentioned problems are of great importance in Bosnia and Herzegovina, such as landslides or issue of structural integrity and durability of dams. The frequent occurrence of landslides or rock avalanches is due to the geology of the terrain with a lot of clayey soils and climate with a lot of heavy rains in spring

and autumn. The heavy rains in May 2014 triggered around 3000 landslides (Figure 1.2), resulting in casualties and massive impact on the already weak economy.

(a) Landslide in the village Šerići

(Source: *www.youtube.com*)

(b) Landslide in the village Željezno polje

(Source: *rtvslon.ba*)

Figure 1.2 Activated landslides in Bosnia and Herzegovina after heavy rains in 2014

The majority of dams in Bosnia and Herzegovina are built in the pre-war period, at least 30 years ago with most of them still operating at full capacity. Due to the poor maintenance and monitoring, the issue of the overall safety and durability of these structures is raised. Even in the developed countries where the maintenance and monitoring of dam structures are obligatory, the accidents that can pose a threat to structural integrity can occur. One recent example is the dam in Oroville, California, where in the spillway of the dam one large macro-crack formed suddenly due to severe erosion, raising a fear that a whole structure might ultimately collapse. In underdeveloped countries, this issue is even more pronounced. The recent failure of the Patel dam in Kenya, resulting with a death toll of 41 and hundreds of people forced to leave a completely devastated area, raised the question about the current state of the infrastructure in the country.

(a) Eroded overflow spillway of Oroville Dam, California

(Source: *en.wikipedia.org* → California Department of Water Resources, 2017)

(b) Broken banks of the Patel dam, Kenya

(Source: *naplesherald.com* → Copyright 2018. The Associated Press)

Figure 1.3 Failure in dam structure

For inspecting the current state and potential risk of failure of pore-saturated structures, aside from experimental results and in-situ data measurements, numerical models and numerical simulations can serve as a powerful tool. To achieve the goal of providing an overall safety assessment of pore-saturated structures under extreme loads, the numerical model has to provide a realistic description of the nonlinear response of the structure. Here, one of the most important features of the model is its ability to predict the true cracking pattern for a particular loading program, where cracks coalescence results with the ultimate failure mode of the structure.

1.2 Aims and scopes

The main scientific aim of this doctoral thesis is to provide a numerical model capable of performing an overall safety assessment of structures built of pore-saturated materials under extreme loads, in application to fluid-structure interaction problems such as dam-reservoir interaction. Namely, our goal is to provide a numerical model for investigating the current state of dam structures, in order to be able to determine the potential risk of failure or severe cracking that can endanger structural integrity, durability, and functionality.

When modeling fluid-structure interaction problems such as dam-reservoir interaction, we have to consider three parts where numerical modeling of each part can be identified as one research aim. The first is the numerical modeling of the structure. The majority of dam structures are built of porous cohesive materials, such as soil, rock, or concrete. The external fluid in interaction with structure acts as a source of external loading and also as a source of pore saturation. The presence of the pore fluid in heterogeneous and porous materials in many cases increases the risk of the final failure. The latter suggests that the numerical model of structure ought to account for the internal fluid-structure interaction. In other words, the structure in fluid-structure interaction ought to be represented in terms of a saturated porous medium. In order to perform the safety analysis, the chosen model of the pore-saturated structure has to be able to capture the true macro-scale response, along with the fracture process zone, and localized failure. In addition, a numerical model has to give an efficient performance in terms of fast convergence rates and efficient computational time.

The second part in numerical modeling of fluid-structure interaction is the numerical modeling of the external fluid. Numerical representation of the external fluid motion has to take into account the confined conditions typically met for the external fluid placed in a reservoir. The third and final part is the issue of the

fluid-structure interface. In other words, how to connect the structure and the external fluid finite elements at the common boundary, which affects the manner (monolithic or partitioned) in which the resulting equations of the fluid-structure system can be solved.

1.3 Literature review

The fluid-structure interaction problems are frequently encountered in engineering practice. These problems range from one extreme where the external fluid is in large overall motion, to another extreme where fluid displacements can be regarded as very small, and the fluid behavior can be described with the acoustic wave theory. In the latter group of acoustic fluid-structure interaction problems fall engineering structures like dams, reservoirs, containers or storage tanks. Concrete, rock or soil (for earth dams) are typically used for constructing many such structures. Both concrete, and especially soil are porous materials in which the presence of the pore fluid influences the final response and in many cases increases the risk of ultimate failure. For example, heavy rain can trigger a landslide in the slope that was once stable due to the reduction in the shear strength of the soil. For rocks, fluid flow can occur through the network of initial discontinuities and thus contribute to the rocks collapse or rock-falls.

In fluid-structure interaction problems, the external fluid acts as a source of loading on the structure and also as a source of pore saturation, keeping the material of the structure fully saturated in every time step. In already damage structure, fluid flow can also occur through cracks which have formed in the structure subjected to extreme loading. In this case, to fully describe the structure part in fluid-structure interaction problems, we ought to have a better numerical formulation of the structure response in terms of a saturated porous medium. In other words, we ought to account for the interaction between the solid phase and pore (internal) fluid and resulting coupling effects.

The pioneering works in the domain of solid phase-pore fluid interaction are Terzaghi's theory of one-dimensional consolidation [1], and Biot's theory of three-dimensional consolidation [2]. Both theories are limited to the case of linear elastic behavior of the material. Biot's porous media theory is further extended to take into account nonlinearities of the material in the pre-peak part of the response [3–5]. Biot's porous media theory has also been extensively used as one of the main ingredients in numerical modeling of response, fracturing, and localized failure in saturated and partially saturated porous media. The successful numerical implementations can be found in works which exploit Extended Finite Element

Method (XFEM) [6–10], Partition-of-Unity Finite Element Method (PUFEM) [11, 12], Embedded Discontinuity Finite Element Method (EDFEM) [13–17], Finite element methods with adaptive remeshing techniques [8, 18–21], Central force lattice model [8, 22, 23], Phase field model [24–27] or Discrete lattice model [28–32]. The solid phase-pore fluid interaction is further extended to account for the temperature effects in the saturated porous media. The pioneering work in the finite element analysis of thermo-hydro-mechanical coupling problem is the work of Aboustit *et al.* [33, 34], followed by the works of [35–40].

The motion of the fluid is, in a general case, described with Navier-Stokes equations [41]. However, the small motion of the fluid in contained conditions, such as reservoirs, water containers or storage tanks, allows us to derive the equations governing the external fluid motion from the acoustic wave theory [42, 43]. In numerical modeling of acoustic fluids by the finite element method, two common approaches are Eulerian and Lagrangian.

In the Eulerian approach, the fluid motion is formulated in terms of fluid pressures, displacement potentials, or velocity potentials as state variables. The fluid finite element formulations falling into this category are the pressure formulation [44], the displacement potential-pressure formulation [45–47], the velocity potential formulation [48, 49] and the velocity potential-density formulation [50]. The Eulerian approach is commonly used in solving fluid-structure systems, in which the behavior of the structure is assumed to be linear or nonlinear [51–60]. However, both the equilibrium condition and the compatibility condition have to be enforced at the fluid-structure interface, because of different state variables in the fluid and the structure.

In the Lagrangian approach, the fluid motion is formulated in terms of nodal displacements [44, 61–68]. The advantage of displacement based formulation is in its finite element implementation because fluid finite elements share the same degrees of freedom as the standard finite elements commonly used in the numerical modeling of the structure. Hence, equilibrium and compatibility conditions are automatically satisfied through element assembly procedure. However, it has been reported that the pure displacement based fluid finite element formulation suffers from the existence of spurious zero-energy deformation modes [63, 69–72]. Various numerical treatments have been proposed with the aim to improve the proposed formulation, such as the penalty method [69], the finite element formulation with rotational constraints and a reduced integration technique [73], and the finite element formulation with a reduced integration technique and element mass projection [72]. With the aim to solve the issue of the existence of spurious modes, the mixed displacement/pressure based fluid finite element formulation is

proposed, with nodal displacements and pressures as unknown variables [74–76]. The Lagrangian approach with displacement variables in both the structure and the fluid is employed in many numerical models of fluid-structure interaction with linear or nonlinear response of structure, such as [53, 77–84].

Beside the Eulerian and Lagrangian approach, an added mass or Westergaard approach is also commonly used for solving fluid-structure systems. The added mass approach, which follows the work of Westergaard [85], is the first and the most simple approach for solving fluid-structure interaction. In this approach, the fluid-structure interaction is solved by adding the fraction of the fluid mass to the structural model. The added mass is typically evaluated based on the assumption of the incompressible fluid. The numerical models of fluid-structure interaction, which exploits an added mass approach can be found in [86–90, 78].

1.4 Thesis overview

In this thesis, we propose a numerical model capable of dealing with nonlinear fluid-structure interaction problems, such as progressive localized failure of a dam structure built of porous cohesive material under dam-reservoir interaction. The numerical model of the structure, the numerical model of external fluid and ultimately the numerical model of interaction are first presented in two-dimensional (2D) framework and later extended to three-dimensional (3D) framework.

We first start with the numerical model of the structure. Here, we assume that the structure is built of porous cohesive material and that the external fluid in interaction with structure acts as a source of pore saturation. For the numerical representation of the pore-saturated structure, we propose the use of coupled discrete beam lattice, which is based on Voronoi cell representation of the domain with inelastic Timoshenko beam finite elements enhanced with additional kinematics in terms of embedded strong discontinuities acting as cohesive links. The internal fluid-structure interaction, i.e., the coupling between the solid phase and pore fluid is introduced through Biot's porous media theory and Darcy's law governing the pore fluid flow, ultimately resulting with an additional pressure-type degree of freedom placed at each node of Timoshenko beam finite element.

Next, we focus on numerical modeling of external fluid and finally fluid-structure interaction. We assume a small motion of the external fluid in confined conditions typically met for fluid placed in a reservoir. We describe the small motion of the external fluid with the acoustic wave theory. We model the external fluid motion with the Lagrangian formulation and mixed displacement/pressure approximation. The finite element approximation for external fluid in combination with coupled

discrete beam lattice model for pore-saturated structure allows for external fluid and structure finite elements to share both the displacement and pressure degrees of freedom at the fluid-structure interface. Thus, the issue of the fluid-structure interface in the numerical model of interaction is solved in a straightforward manner through the element assembly procedure.

The thesis is divided into six chapters. In Chapter 1, we outline the aim of the thesis, together with the motivation for research work and literature review. In Chapter 2, we describe in detail the plane strain coupled discrete beam lattice model of the pore-saturated structure, and we discuss the results of several numerical examples. In Chapter 3, we present the numerical model of external fluid and ultimately numerical model of fluid-structure interaction, and its application through a set of numerical simulations. In Chapter 4, we extend the proposed numerical model of the structure, external fluid, and acoustic fluid-structure interaction to the 3D setting. In Chapter 5, we account for the temperature effects by introducing thermal coupling in the proposed 3D numerical model of the pore-saturated structure. Finally, in Chapter 6, we summarize all the main findings and contributions of the thesis together with the suggestions for future works.

All numerical implementations and computations are performed with the research version of the computer code FEAP (Finite Element Analysis Program), developed by R.L. Taylor [41]. The finite element mesh in numerical examples is generated in GMSH [91], with cross-sectional dimensions of beam finite elements computed by using MATLAB [92].

CHAPTER 2

DISCRETE MODEL OF STRUCTURE BUILT OF SATURATED PORO-PLASTIC MEDIUM

ABSTRACT

In this Chapter, we describe the plane strain coupled discrete beam lattice model of structure built of saturated poro-plastic cohesive material. The coupled discrete beam lattice model is based on Voronoi cell representation of the domain with cohesive links as inelastic Timoshenko beam finite elements enhanced with additional kinematics in terms of embedded strong discontinuities. The coupling between the solid phase and the internal (pore) fluid is governed by Biot's porous media theory and Darcy's law for pore fluid flow. The internal fluid pore pressure field is approximated with CST (Constant Strain Triangle) finite elements, which coincide with Delaunay triangles. By exploiting Hammer quadrature rule for numerical integration on CST finite elements and duality property between Voronoi diagram and Delaunay triangle representations, the proposed formulation results with an additional pressure-type degree of freedom placed at each node of Timoshenko beam finite element. The application of the model is illustrated through several numerical simulations.

OUTLINE

2.1 Introduction

In this Chapter, we describe the plane strain coupled discrete beam lattice model used in this thesis for numerical modeling of response and localized failure in structures built of saturated porous cohesive materials. The theoretical formulation for the pore-saturated structure is based upon Biot's porous media theory extended to localized poro-plasticity. The internal fluid-structure interaction, i.e., the interaction between the solid phase and the pore fluid is handled by using a judicious combination of lattice models for structure cracking and finite element approximation for internal (pore) fluid flow.

The outline of the Chapter is as follows: In Section 2.2, we briefly describe Biot's porous media theory. In Section 2.3, we provide a detailed description of discrete lattice models and their application in numerical modeling of response and localized failure in structures. We also explain in detail the manner in which the internal fluid-structure interaction is numerically treated. In Section 2.4, we present a finite element formulation of the proposed coupled discrete lattice model, together with the computational procedure. The finite element formulation is given in fully dynamics framework, which can be easily adjusted for quasi-static simplification of structure built of a saturated porous medium, or dry medium. In Section 2.5, we present results of several numerical simulations with the aim to validate the proposed coupled discrete beam lattice model and to demonstrate its capabilities to capture the response and localized failure in pore-saturated structures, where the cracks coalescence results with the ultimate failure modes. In Section 2.6, we give concluding remarks.

2.2 Biot's porous media theory

In Biot's porous media theory, the equations governing the coupled problem are derived by combining equilibrium and continuity equations [2]. In a dynamic setting, we consider the equation of motion instead of the equilibrium equation. In deriving the strong form of the equations of motion, we use the d'Alembert principle. The main idea behind the d'Alembert principle is that a motion of a solid body in each time step can be described by the equilibrium equations, which includes an additional external load in terms of the inertia force. Thus, the strong form of equations of motion is written as

$$\nabla \cdot \boldsymbol{\sigma} + \mathbf{b} - \rho \mathbf{a} = \mathbf{0} \tag{2.1}$$

where $\boldsymbol{\sigma}$ is the total stress tensor, **b** are the body forces vector, **a** is the solid phase acceleration vector and ρ is the mass density of the mixture assumed to be constant, which is defined as $\rho = (1-n)\rho_s + n\rho_f$, with n as the porosity, ρ_s as the mass density of solid phase and ρ_f as the mass density of pore fluid.

In the formulation of the coupled problem, Biot's theory exploits Terzaghi's principle of effective stresses, which states that the total normal stress is equal to the sum of the effective stress carried by the solid phase, and the pore pressure carried by the fluid in pores. Terzaghi's principle of effective stresses is written as

$$\boldsymbol{\sigma} = \boldsymbol{\sigma}' - \mathbf{I}bp \tag{2.2}$$

where $\boldsymbol{\sigma}'$ is the effective stress tensor, **I** is the second order identity tensor, p is the pore pressure assumed positive in compression, and b is Biot's constant defined as $b = 1 - K_t/K_s$, with K_t and K_s as the bulk moduli of the porous skeleton and the solid phase, respectively. If the material grains are assumed to be incompressible, then Biot's constant is equal to $b = 1$.

The continuity equation for pore fluid flow is written as

$$\dot{\zeta} + \nabla \cdot \mathbf{q} = 0 \tag{2.3}$$

where ζ is the variation of the fluid content, and **q** is the fluid flux.

The variation of the fluid content ζ is written as

$$\zeta = \frac{1}{M}p + b\nabla \cdot \mathbf{u} \tag{2.4}$$

where **u** is the displacement of the solid phase, and M is Biot's modulus, defined as $1/M = (b-n)/K_s + n/K_f$, with K_f as the bulk modulus of the pore fluid. If the material grains and the pore fluid are assumed to be incompressible, then Biot's modulus is $M \to \infty$ $(1/M \to 0)$.

According to Darcy's law, the fluid flux **q** is equal to

$$\mathbf{q} = -\frac{k}{\gamma_f}\nabla p \tag{2.5}$$

where k is the coefficient of permeability of the isotropic porous medium, and γ_f is the specific weight of the fluid.

By combining Equations (2.3-2.5), a new form of continuity equation can be written as

$$\frac{1}{M}\dot{p} + b\nabla \cdot \dot{\mathbf{u}} - \nabla \cdot \left(\frac{k}{\gamma_f}\nabla p\right) = 0 \tag{2.6}$$

2.3 Discrete model of structure

In everyday engineering practice, the response of the structure built of heterogeneous materials is usually computed with homogenized, continuum type of numerical models with strength and deformability defined at the macro-scale, in which the domain is meshed with two-dimensional (2D) or three-dimensional (3D) finite elements. The main advantage of these models is in a relatively simple and efficient way of predicting the main tendencies and overall behavior of heterogeneous materials in failure analyses of interest for engineering practice. However, the use of 2D or 3D finite elements can be challenging when trying to numerically represent the inelastic behavior, and especially cracking and localized failure in the structure built of heterogeneous materials. Successful numerical implementations of strain localization phenomenon can be found in [93–104].

Contrary to the continuum type of numerical models, in discrete lattice models the domain is meshed with one-dimensional (1D) finite elements. The use of 1D, instead of 2D or 3D elements, has its advantages in terms of numerical implementation of different kind of phenomena commonly observed in heterogeneous materials, improving rates of convergence, and decreasing computational time.

For the numerical representation of the structure, we use a cohesive discrete lattice model based on Voronoi cell representation of the domain. Here, the domain is divided into a set of regions or Voronoi cells, with the property that all points in one Voronoi cell are closest to the center of that cell than to the center of any other cell. From the aspect of structural modeling, each Voronoi cell can be identified as a part of the material held together with the adjacent parts by cohesive links. Thus, in discrete lattice models, the macro-scale response of the structure is obtained on the mesh of cohesive links, whose behavior we model with 1D finite elements.

The construction of the discrete lattice model is carried out in a very efficient manner by exploiting the duality property between Voronoi diagram and Delaunay triangulation. The end result of the Delaunay triangulation performed on a given domain is a mesh of triangles. Every edge of triangle connects the centers of two adjacent Voronoi cells and is perpendicular to the edge shared between these two cells (Figure 2.1). Thus, we place along each edge of the triangle a cohesive link, whose behavior we model with the 1D finite element. The cross-sectional height of each finite element is then equal to the length of the edge shared between two adjacent Voronoi cells. What needs to be emphasized is that the center of each finite element is located at the edge shared between two adjacent Voronoi cells. This is a very convenient property for simulating crack propagation in materials. Namely, failure in a cohesive link can be interpreted as a formation of a crack in

the structure. If we identify Voronoi cells as parts of the material held together by cohesive links, then cracks can occur only at their interconnection.

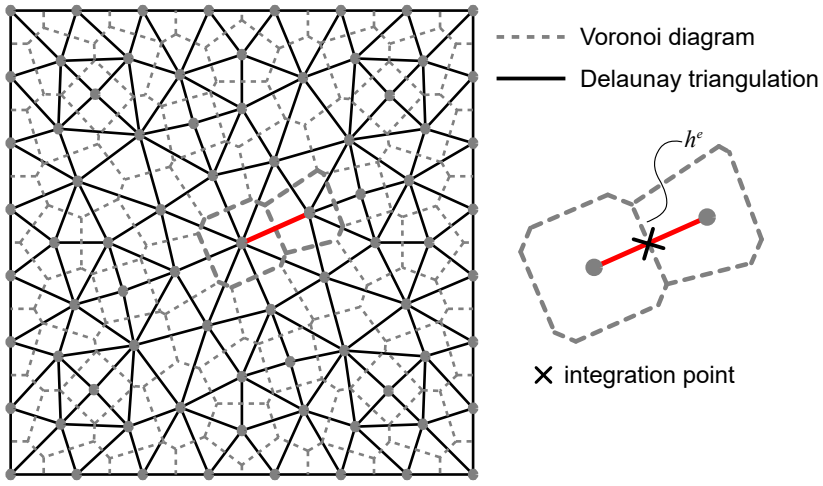

Figure 2.1 Voronoi diagram and Delaunay triangulation

The first advantage of the discrete lattice model based on Voronoi cell representation of the domain with irregular lattice geometry is in its ability to reproduce the linear elastic response of an equivalent continuum model. The confirmed relations between linear elastic parameters of a single lattice and a continuum model depend whether the discrete model is with regular or irregular lattice geometry and whether it is based on spring or beam lattice network. More details can be found in works [105–110].

The successful application of discrete lattice models in numerical modeling of inelastic response and localized failure in materials rests on the idea of multi-scale modeling. Namely, by appropriate numerical modeling of the micro-scale represented by cohesive links, we can obtain the true macro-scale response of the structure. The discrete lattice models with geometrically exact shear deformable beams acting as cohesive links have been used for modeling dynamic fracture of structures built of brittle material [111]. In this discrete model, fracture criterion is stated in terms of strains with two possible modes of fracture, the separation between two adjacent cells and the relative bending deformation. The fracture limits for both modes are assumed to follow Gaussian random distribution. The discrete lattice models with truss bar elements capable of representing the response of a two-phase material [112], have been used in numerical modeling of the response and fracturing in concrete [113, 114]. The truss bar elements enhanced with additional kinematics in terms of embedded strong discontinuity were able to model the crack formation and propagation in mode I, that relates to crack opening. Beside mode I, the crack can also propagate in mode II that relates to crack sliding.

To be able to capture both mode I and mode II of failure, Timoshenko beam finite elements with an embedded strong discontinuity in both axial and transverse direction have been proposed instead of truss bar elements. The discrete lattice models with enhanced Timoshenko beam finite elements have been successfully used to describe the response and fracturing in rocks, both in 2D and 3D setting [115–118]. In the discrete lattice model proposed in [115], a distinction between two phases has been made. Phase I is an intact rock which is not likely to fail. This phase is represented with standard linear elastic Timoshenko beam finite element. Phase II represents a weak phase or initial discontinuities in rocks. Inelastic Timoshenko beam finite elements with enhanced kinematics are used to model this phase.

Our final goal in this thesis is to tackle the acoustic fluid-structure interaction problems. In the acoustic fluid-structure interaction problems on hand, the external fluid acts both as a source of the loading on the structure, and also as a source of the pore saturation. For a better numerical description of the underlying phenomena, we ought to model the structure as a saturated porous medium. In this thesis, for the numerical representation of the pore-saturated structures, we generalize the development of the coupled discrete beam lattice model presented in [32, 118], extending its ability to deal with the nonlinear response and localized failure in pore-saturated structures in acoustic fluid-structure interaction problems of our interest. The proposed coupled discrete beam lattice model is an extension of the discrete beam lattice model with enhanced Timoshenko beam finite elements as cohesive links presented in [115, 118], with Biot's porous media theory governing the coupling between the solid phase and pore fluid as a new ingredient.

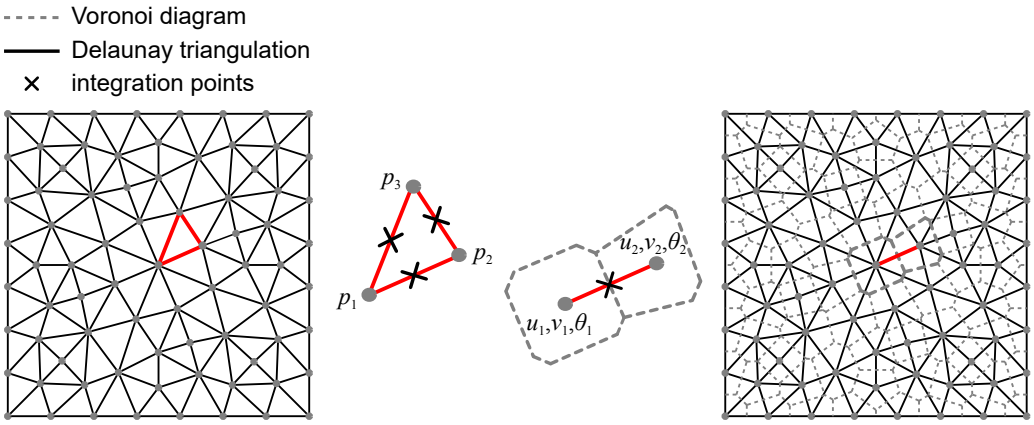

(a) Pore pressure field (b) Displacement fields

Figure 2.2 Discretization of displacement and pore pressure fields

The internal fluid flow in the proposed model of the pore-saturated structure is spread across the mesh of triangles (CST - Constant Strain Triangle finite elements)

that coincides with the mesh of triangles obtained by Delaunay triangulation (Figure 2.2a). Hammer quadrature rule [119] for numerical integration, allows for simplification of the numerical implementation of the coupling. Namely, Hammer quadrature rule positions the integration points at the center of each edge of the triangle. The positions of these integration points coincide with the positions of the integration points for Timoshenko beam finite elements used for representing the mechanical response (Figure 2.2b). For the numerical integration, a single Gauss point placed at the center of the Timoshenko beam finite element is used. This allows us to simplify the data exchange. The database management is also kept simple by treating the pressure degree of freedom as an additional degree of freedom per node of a Timoshenko beam finite element (Figure 2.3).

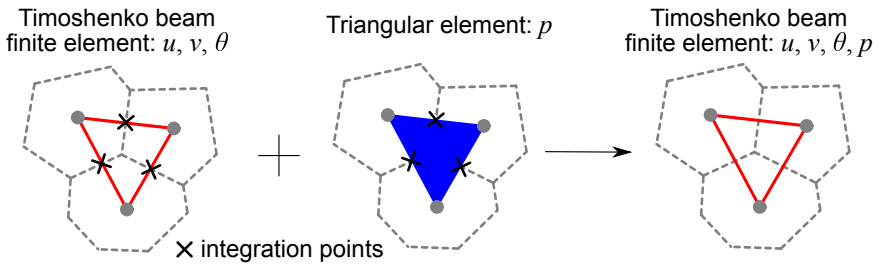

Figure 2.3 Displacement and pore pressure fields finite element approximations

This point of view is also in agreement with the discretization of continuum problem by Hrennikoff framework method using beam along element edges [120], which is the same as our cohesive links, in the elastic regime. It is important to note that such a point of view (although more sound) does not change anything in our implementation since we use Hammer integration points at the mid-point of each element edge for a 3-node CST triangle. The choice of this kind eliminates the contribution of the third node and leaves the contribution of two nodes that correspond to the Timoshenko beam finite element.

Different types of failure mechanisms in different materials are, among others, the result of material heterogeneities, loading, and boundary conditions. Because of this, in the coupled discrete beam lattice model used in this thesis, we allow for all Timoshenko beams to fail [121–123].

To the best of author's knowledge, the literature search did not reveal any confirmed relations between elastic properties of the continuum model and Timoshenko beam lattice in discrete models based on Voronoi cell discretization. However, from the condition that no stiffness is gained or lost compared to the continuum, linear elastic parameters of the discrete lattice model (lattice Young's modulus and Poisson's ratio) can be easily identified from standard experimental tests in combination with numerical tests, shown in Figures 2.4a and 2.4b.

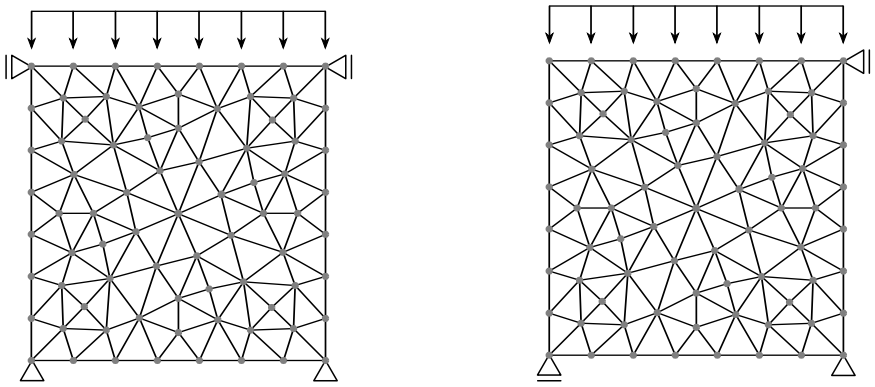

(a) Young's modulus (b) Poisson's ratio

Figure 2.4 Numerical tests for identification of linear elastic parameters of discrete lattice model: boundary conditions

Next, we give an overview of the finite element formulation of the plane strain coupled discrete beam lattice model.

2.4 Finite element formulation

The starting point for our work on coupled discrete beam lattice model of pore-saturated structure is the Timoshenko beam finite element presented in [115, 32, 118]. The detailed descriptions of various numerical procedures and numerical solutions used in the finite element formulation of the Timoshenko beam finite element on hand can be found in [124].

2.4.1 Kinematics

Consider a straight plane Timoshenko beam finite element of length L^e and cross-sectional area A^e. The element has two nodes, and three degrees of freedom per node: axial displacement, transverse displacement, and rotation of cross-section. Displacement fields are interpolated with standard linear interpolation functions, written as

$$\mathbf{u} = \mathbf{N}_u^s \bar{\mathbf{u}} \tag{2.7}$$

where

$$\begin{aligned} &\mathbf{u}^{\mathsf{T}} = \left\{u,\ v,\ \theta\right\};\quad \bar{\mathbf{u}}^{\mathsf{T}} = \left\{u_1,\ v_1,\ \theta_1,\ u_2,\ v_2,\ \theta_2\right\};\\ &\mathbf{N}_u^s = \begin{bmatrix} N_1 & 0 & 0 & N_2 & 0 & 0\\ 0 & N_1 & 0 & 0 & N_2 & 0\\ 0 & 0 & N_1 & 0 & 0 & N_2 \end{bmatrix};\quad \left\{N_1, N_2\right\} = \left\{1-\tfrac{x}{L^e}, \tfrac{x}{L^e}\right\} \end{aligned} \tag{2.8}$$

For simplicity, we considered the shape functions for a Timoshenko beam placed along the global coordinate x axis, which can be easily adapted to any arbitrary element orientation by using a local element frame.

For geometrically linear Timoshenko beam, strain fields are defined as

$$\varepsilon_{xx} = \frac{du}{dx}; \quad \gamma_{xy} = \frac{dv}{dx} - \theta; \quad \kappa_z = \frac{d\theta}{dx} \tag{2.9}$$

where ε_{xx} is the axial strain, γ_{xy} is the shear strain and κ_z is the curvature. In what is to follow, we will denote these strains with the following symbols ε, γ and κ.

Following the standard finite element procedure, strain fields are interpolated as

$$\boldsymbol{\epsilon} = \mathbf{B}_u^s \bar{\mathbf{u}} \tag{2.10}$$

where

$$\begin{aligned} &\boldsymbol{\epsilon}^{\mathsf{T}} = \left\{\varepsilon,\ \gamma,\ \kappa\right\}; \\ &\mathbf{B}_u^s = \begin{bmatrix} B_1 & 0 & 0 & B_2 & 0 & 0 \\ 0 & B_1 & -N_1 & 0 & B_2 & -N_2 \\ 0 & 0 & B_1 & 0 & 0 & B_2 \end{bmatrix}; \quad \left\{B_1, B_2\right\} = \left\{\tfrac{dN_1}{dx}, \tfrac{dN_2}{dx}\right\} = \left\{-\tfrac{1}{L^e}, \tfrac{1}{L^e}\right\} \end{aligned} \tag{2.11}$$

For modeling crack formation in mode I and mode II, i.e., the softening behavior, localization limiter based on embedded strong discontinuity is employed [124–126]. Namely, strong discontinuities are introduced in displacement fields in the axial and transverse direction (Figure 2.5), which are now represented as a sum of a regular part and the discontinuous part. The discontinuous part is represented as a product of an interpolation function M and parameter α, which represents the displacement jump located at the center of the element.

The enhanced displacement fields are interpolated as

$$\mathbf{u} = \mathbf{N}_u^s \bar{\mathbf{u}} + \mathbf{M}\boldsymbol{\alpha} \tag{2.12}$$

where

$$\begin{aligned} &\boldsymbol{\alpha}^{\mathsf{T}} = \left\{\alpha^u,\ \alpha^v,\ 0\right\}; \\ &\mathbf{M} = \begin{bmatrix} M & 0 & 0 \\ 0 & M & 0 \\ 0 & 0 & 0 \end{bmatrix}; \quad M = H_{\bar{x}} - N_2; \quad H_{\bar{x}} = \begin{cases} 0, & x \le \bar{x} \\ 1, & x > \bar{x} \end{cases} \end{aligned} \tag{2.13}$$

Here, α^u and α^v represent displacement jumps in axial and transverse direction.

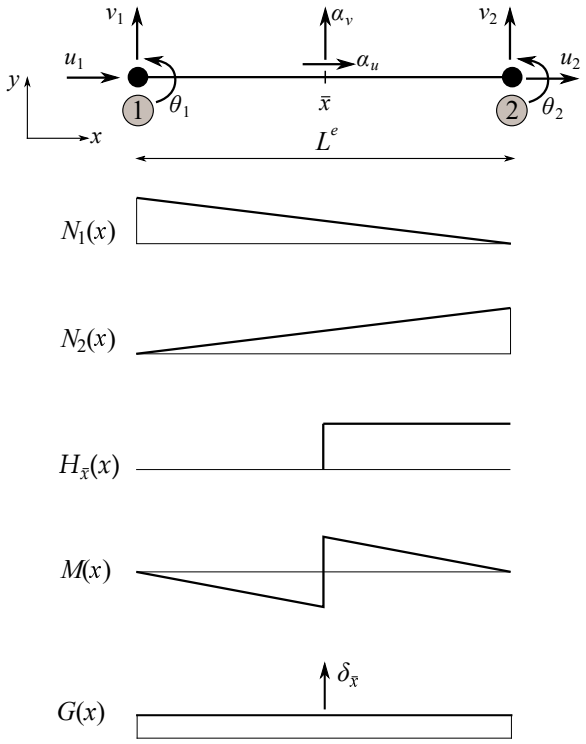

Figure 2.5 Timoshenko beam finite element: interpolation functions

The finite element implementation procedure for the localization limiter based on embedded strong discontinuity fits well within the framework of incompatible mode method [124]. Namely, the parameter α can be interpreted as an incompatible mode parameter, which can be statically condensed on the element level, so that on the global level only remaining unknowns are nodal displacements.

The enhanced strain fields are interpolated as

$$\boldsymbol{\epsilon} = \mathbf{B}_u^s \bar{\mathbf{u}} + \mathbf{G}\boldsymbol{\alpha} \tag{2.14}$$

where

$$\mathbf{G} = \begin{bmatrix} G & 0 & 0 \\ 0 & G & 0 \\ 0 & 0 & 0 \end{bmatrix}; \quad G = \frac{dM}{dx} = \begin{cases} \bar{G}, & x \in [0,\bar{x}) \cup x \in (\bar{x}, L^e] \\ \bar{G} + \delta_{\bar{x}}, & x = \bar{x} \end{cases} \tag{2.15}$$

where $\bar{G} = -\frac{1}{L^e}$, and $\delta_{\bar{x}}$ is the Dirac function

$$\delta_{\bar{x}} = \begin{cases} 0, & x \in [0,\bar{x}) \cup x \in (\bar{x}, L^e] \\ \infty, & x = \bar{x} \end{cases} \tag{2.16}$$

The pore pressure field is approximated with CST finite elements (Figure 2.6). The finite element approximation for the pore pressure field is written as

$$p = \mathbf{N}_p^s \bar{\mathbf{p}} \tag{2.17}$$

where

$$\begin{aligned}
&\bar{\mathbf{p}}^{\mathsf{T}} = \left\{ p_1,\, p_2,\, p_3 \right\}; \\
&\mathbf{N}_p^s = \left\{ N_1^p,\, N_2^p,\, N_3^p \right\}; \quad N_1^p = \frac{1}{2A}\left[(x_2 y_3 - x_3 y_2) + (y_2 - y_3)x + (x_3 - x_2)y \right] \\
&\qquad\qquad N_2^p = \frac{1}{2A}\left[(x_3 y_1 - x_1 y_3) + (y_3 - x_1)x + (x_1 - x_3)y \right] \\
&\qquad\qquad N_3^p = \frac{1}{2A}\left[(x_1 y_2 - x_2 y_1) + (y_1 - x_2)x + (x_2 - y_1)y \right]
\end{aligned} \tag{2.18}$$

where A is the area of the triangular element, x,y, are global coordinates and x_i, y_i are nodal coordinates of CST element.

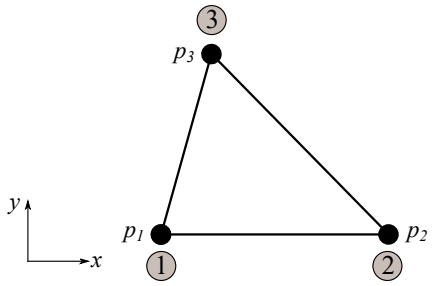

Figure 2.6 CST finite element

The time derivatives of displacement and pore pressure fields are written as

$$\begin{aligned}
&\dot{\mathbf{u}} = \mathbf{N}_u^s \dot{\bar{\mathbf{u}}}; \quad \dot{p} = \mathbf{N}_p^s \dot{\bar{\mathbf{p}}} \\
&\ddot{\mathbf{u}} = \mathbf{N}_u^s \ddot{\bar{\mathbf{u}}}; \quad \ddot{p} = \mathbf{N}_p^s \ddot{\bar{\mathbf{p}}}
\end{aligned} \tag{2.19}$$

2.4.2 Continuity equation and equations of motion

2.4.2.1 Continuity equation

The coupling of the mechanics and the pore fluid flow occurs through the axial direction of the Timoshenko beam finite element. The continuity equation for fluid flow through the porous body is written as

$$\frac{1}{M}\dot{p} + b\dot{\varepsilon} - \frac{k}{\gamma_f}\nabla \cdot (\nabla p) = 0 \tag{2.20}$$

The weak from of the continuity equation is obtained through the principle of virtual works, written as

$$\int_{\Omega^e_{CST}} \delta p \Big[\frac{1}{M} \dot{p} - \frac{k}{\gamma_f} \nabla \cdot (\nabla p) \Big] d\Omega + \int_0^{L^e} \delta p^{\backslash} b \dot{\varepsilon} dx = 0 \tag{2.21}$$

where δp is the virtual pore pressure field interpolated in the same manner as the real pore pressure field

$$\begin{aligned} \delta p &= \mathbf{N}^s_p \delta \bar{\mathbf{p}}; \;\; \delta \bar{\mathbf{p}}^{\mathsf{T}} = \Big\{ \delta p_1, \delta p_2, \delta p_3 \Big\}; \\ p^{\backslash} &= \mathbf{N}^s_{up} \bar{\mathbf{p}}^{\backslash}; \;\; \mathbf{N}^s_{up} = \Big\{ N_1, N_2 \Big\}; \;\; \bar{\mathbf{p}}^{\backslash \mathsf{T}} = \Big\{ p_1, p_2 \Big\}; \\ \delta p^{\backslash} &= \mathbf{N}^s_{up} \delta \bar{\mathbf{p}}^{\backslash}; \;\; \delta \bar{\mathbf{p}}^{\backslash \mathsf{T}} = \Big\{ \delta p_1, \delta p_2 \Big\} \end{aligned} \tag{2.22}$$

2.4.2.2 Equations of motion

In deriving the weak form of the equations of motion, we use the d'Alembert principle, which is a dynamic analog to the principle of virtual work in the quasi-static setting [124]. The main idea behind the d'Alembert principle is that a motion of a solid body in each time step can be described by the equilibrium equation, which includes an additional external load in terms of the inertia force. Here, we assume that the coupling of the mechanics and the internal fluid flow occurs through the axial direction of the Timoshenko beam finite element. Thus, the strong form of the equations of motion for a Timoshenko beam is written as

$$-\rho A^e \frac{\partial^2 u}{\partial t^2} + \frac{\partial N}{\partial x} + n(x,t) = 0 \tag{2.23}$$

$$-\rho A^e \frac{\partial^2 v}{\partial t^2} + \frac{\partial V}{\partial x} + q(x,t) = 0 \tag{2.24}$$

$$-\rho I^e \frac{\partial^2 \theta}{\partial t^2} + \frac{\partial M}{\partial x} + V + m(x,t) = 0 \tag{2.25}$$

where ρ is the mass density, A^e and I^e are the cross-sectional properties of Timoshenko beam: area and second moment of inertia of a cross-section, n, q and m are the distributed external loads, and $N = N' - bp^{\backslash} A^e$, $V = V'$ and $M = M'$ are the total axial force, the shear force and the bending moment, respectively. The superscript $'$ denotes effective force.

The weak form of equations of motion for Timoshenko beam finite element is derived from the d'Alembert principle, which states that the virtual work of internal forces is equal to the virtual work of external forces, which include the

inertia force. The virtual displacements are imaginary displacements which are kinematically admissible and small enough so that virtual strains can be regarded as infinitesimal. The virtual displacement fields and virtual pore pressure field refer to a particular deformed configuration and thus are not time-dependent. The virtual displacement and virtual strain fields are interpolated in the same manner as the real displacement and real strain fields, written as

$$\delta \mathbf{u} = \mathbf{N}_u^s \delta \bar{\mathbf{u}} + \mathbf{M} \delta \boldsymbol{\alpha} \tag{2.26}$$

$$\delta \boldsymbol{\epsilon} = \mathbf{B}_u^s \delta \bar{\mathbf{u}} + \mathbf{G} \delta \boldsymbol{\alpha} \tag{2.27}$$

where

$$\begin{aligned} \delta \mathbf{u}^{\mathsf{T}} &= \left\{ \delta u,\, \delta v,\, \delta \theta \right\}; \qquad \delta \bar{\mathbf{u}}^{\mathsf{T}} = \left\{ \delta u_1,\, \delta v_1,\, \delta \theta_1,\, \delta u_2,\, \delta v_2,\, \delta \theta_2 \right\}; \\ \delta \boldsymbol{\alpha}^{\mathsf{T}} &= \left\{ \delta \alpha^u,\, \delta \alpha^v,\, 0 \right\}; \quad \delta \boldsymbol{\epsilon}^{\mathsf{T}} = \left\{ \delta \varepsilon,\, \delta \gamma,\, \delta \kappa \right\} \end{aligned} \tag{2.28}$$

The virtual work of external forces is computed as

$$\begin{aligned} G^{ext,e} &= \delta \bar{\mathbf{u}}^{\mathsf{T}} \mathbf{f}^{ext,e} - \int_0^{L^e} \left(\delta u \rho A^e \ddot{u} + \delta v \rho A^e \ddot{v} + \delta \theta \rho I^e \ddot{\theta} \right) dx \\ &= \delta \bar{\mathbf{u}}^{\mathsf{T}} \mathbf{f}^{ext,e} - \delta \bar{\mathbf{u}}^{\mathsf{T}} \mathbf{f}^{acc,e} \end{aligned} \tag{2.29}$$

where

$$\mathbf{f}^{acc,e} = \int_0^{L^e} \mathbf{N}_u^{s,\mathsf{T}} \ddot{\boldsymbol{\sigma}} \, dx; \quad \ddot{\boldsymbol{\sigma}}^{\mathsf{T}} = \left\{ \rho A^e \ddot{u}, \rho A^e \ddot{v}, \rho I^e \ddot{\theta} \right\} \tag{2.30}$$

The virtual work of internal forces for Timoshenko finite beam finite element is equal to

$$G^{int,e} = \int_0^{L^e} \left(\mathbf{B}_u^s \delta \bar{\mathbf{u}} \right)^{\mathsf{T}} \boldsymbol{\sigma} \, dx + \int_0^{L^e} \left(\mathbf{G} \delta \boldsymbol{\alpha} \right)^{\mathsf{T}} \boldsymbol{\sigma}_u \, dx \tag{2.31}$$

where

$$\begin{aligned} \boldsymbol{\sigma}^{\mathsf{T}} &= \left\{ N, V, M \right\} = \left\{ N' - bp^{\backprime} A^e, V', M' \right\}; \\ \boldsymbol{\sigma}^{\mathsf{T}} &= \boldsymbol{\sigma}_u^{\mathsf{T}} - \boldsymbol{\sigma}_p^{\mathsf{T}}; \\ \boldsymbol{\sigma}_u^{\mathsf{T}} &= \left\{ N', V', M' \right\}; \;\; \boldsymbol{\sigma}_p^{T} = \left\{ bp^{\backprime} A^e, 0, 0 \right\} \end{aligned} \tag{2.32}$$

The virtual work of internal forces consists of two parts. The first is the virtual work of internal forces in the bulk part of the element (part of the element outside the discontinuity), and the second is the virtual work of internal forces acting at the discontinuity, written as

$$G^{int,e} = \delta\bar{\mathbf{u}}^{\mathsf{T}}\mathbf{f}^{int,e} + \delta\boldsymbol{\alpha}^{\mathsf{T}}\mathbf{h}^{e} \tag{2.33}$$

where $\mathbf{f}^{int,e}$ is the internal force vector, and $\mathbf{h}^{e}$ is the residual vector due to discontinuity, computed as

$$\begin{aligned}
&\mathbf{f}^{int,e} = \int_0^{L^e} \mathbf{B}_u^{s,\mathsf{T}}\boldsymbol{\sigma}\,dx = \mathbf{f}^{int,e}(\boldsymbol{\sigma}_u) - \mathbf{f}^{int,e}(\boldsymbol{\sigma}_p);\\
&\mathbf{h}^{e} = \int_0^{L^e} \mathbf{G}^{\mathsf{T}}\boldsymbol{\sigma}_u dx = \int_0^{L^e} \bar{\mathbf{G}}^{\mathsf{T}}\boldsymbol{\sigma}_u dx + \mathbf{t}; \quad \bar{\mathbf{G}} = \begin{bmatrix} \bar{G} & 0 & 0\\ 0 & \bar{G} & 0\\ 0 & 0 & 0 \end{bmatrix}; \quad \mathbf{t}^{\mathsf{T}} = \left\{ t^u, t^v, 0 \right\}
\end{aligned} \tag{2.34}$$

Here, $\mathbf{t}$ is the internal force vector acting at the discontinuity.

By exploiting the principle of virtual work we obtain

$$0 = G^{int,e} - G^{ext,e} = \delta\bar{\mathbf{u}}^{\mathsf{T}}(\mathbf{f}^{int,e} - \mathbf{f}^{ext,e} + \mathbf{f}^{acc,e}) + \delta\boldsymbol{\alpha}^{\mathsf{T}}\mathbf{h}^{e} \tag{2.35}$$

The previous equation is satisfied if

$$\mathbf{f}^{acc,e} + \mathbf{f}^{int,e} - \mathbf{f}^{ext,e} = \mathbf{0} \tag{2.36}$$

$$\mathbf{h}^{e} = \mathbf{0} \tag{2.37}$$

The Equation (2.36) relates to the bulk part of the element, and the Equation (2.37) relates to the discontinuity.

The internal force vector $\mathbf{t}$ acting at the discontinuity is computed from the following conditions

$$\left.\begin{aligned} \mathbf{h}^{\mathbf{e}} &= 0\\ \int_0^{L^e} \bar{G}\,dx = \int_0^{L^e} -\frac{1}{L^e}dx &= -1 \end{aligned}\right\} \Rightarrow \mathbf{t} = \begin{bmatrix} 1 & 0 & 0\\ 0 & 1 & 0\\ 0 & 0 & 0 \end{bmatrix} \int_0^{L^e} \boldsymbol{\sigma}_u dx \tag{2.38}$$

2.4.3 Constitutive model

The pre-peak response of the Timoshenko beam finite element in both axial and transverse direction is described with the elasto-viscoplastic constitutive model with implemented linear hardening [124], and Fredrick-Armstrong nonlinear kinematic hardening law [127]. The post-peak response of the element is described with exponential softening. The behavior of the element in bending is purely linear elastic.

2.4.3.1 Plasticity model

The proposed model of plasticity is described with [124]

1. Additive decomposition of the total strain into elastic and viscoplastic part, with only the elastic part influencing the value of the stresses

$$\begin{aligned} \varepsilon &= \varepsilon^e + \varepsilon^{vp} \\ \gamma &= \gamma^e + \gamma^{vp} \\ \kappa &= \kappa^e \end{aligned} \tag{2.39}$$

2. Strain energy function in terms of strains and internal variables, plastic deformations ε^{vp}, γ^{vp} and strain-like hardening variables $\bar{\xi}^u$, $\bar{\xi}^v$

$$\begin{aligned} \bar{\psi}^u\left(\varepsilon, \varepsilon^{vp}, \bar{\xi}^u\right) &= \frac{1}{2}\left(\varepsilon - \varepsilon^{vp}\right) EA^e\left(\varepsilon - \varepsilon^{vp}\right) + \frac{1}{2}\bar{\xi}^u H^u_{lh} A^e \bar{\xi}^u \\ \bar{\psi}^v\left(\gamma, \gamma^{vp}, \bar{\xi}^v\right) &= \frac{1}{2}\left(\gamma - \gamma^{vp}\right) k_c GA^e\left(\gamma - \gamma^{vp}\right) + \frac{1}{2}\bar{\xi}^v H^v_{lh} A^e \bar{\xi}^v \end{aligned} \tag{2.40}$$

   where E is Young's modulus, $G = \frac{E}{2(1+\nu)}$ is the shear modulus with ν as Poisson's ratio, H^u_{lh}, H^v_{lh} are the linear hardening moduli and k_c is the shear correction factor. For rectangular cross-sections shear correction factor is equal to $k_c = 5/6$.

3. Yield function in terms of stresses (or stress resultants), stress-like hardening variables $\bar{q}^u$, $\bar{q}^v$, and back-stress variables $\bar{\chi}^u$, $\bar{\chi}^v$

$$\begin{aligned} \bar{\phi}^u\left(N', \bar{\chi}^u, \bar{q}^u\right) &= \left|N' - \bar{\chi}^u A^e\right| - \left(N_y - \bar{q}^u A^e\right) \leq 0 \\ \bar{\phi}^v\left(V', \bar{\chi}^v, \bar{q}^v\right) &= \left|V' - \bar{\chi}^v A^e\right| - \left(V_y - \bar{q}^v A^e\right) \leq 0 \end{aligned} \tag{2.41}$$

   where N_y, V_y are the elastic (yield) limits.
   The stress resultant values N', V' and M' are computed from the elastic part

of total deformation, as

$$\begin{aligned} N' &= EA^e\left(\varepsilon - \varepsilon^{vp}\right) \\ V' &= k_c GA^e\left(\gamma - \gamma^{vp}\right) \\ M' &= EI^e\kappa \end{aligned} \tag{2.42}$$

where the area A^e and second moment of inertia I^e for rectangular cross-sections with cross-sectional width equal to one and cross-sectional height equal to h^e are $A^e = h^e$, $I^e = (h^e)^3/12$.

Remark: We note that, in a general case, the element local coordinate axis x does not pass through the center of gravity of the cross-section (Figure 2.7). In what is to follow, we will neglect the additional coupling between axial and bending strains as a result of the eccentricity e_c.

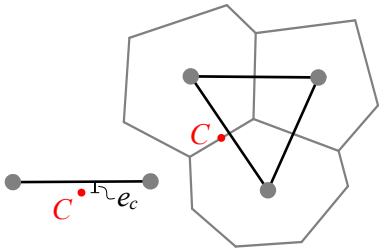

Figure 2.7 Eccentricity of the center of the gravity

The stress-like hardening variables $\bar{q}^u$, $\bar{q}^v$ handle the plasticity threshold evolution as a result of accumulated plastic deformations. For linear hardening, the stress-like hardening variables are given as

$$\begin{aligned} \bar{q}^u &= -H^u_{lh}\bar{\xi}^u \\ \bar{q}^v &= -H^v_{lh}\bar{\xi}^v \end{aligned} \tag{2.43}$$

In experiments with cyclic loading, it has been observed that in a typical cycle with a load reversal, the plasticity threshold limit is reduced from the previous value. This phenomenon is called the Bauschinger effect. To track the change in the value of the plasticity threshold limit with respect to the previous plastic state, back-stress variable $\bar{\chi}$ is introduced. We employ Fredrick-Armstrong nonlinear kinematic hardening law [127], which we can write as

$$\begin{aligned} \dot{\bar{\chi}}^u &= H^u_{lk}\dot{\varepsilon}^{vp} - H^u_{nlk}\dot{\bar{\xi}}^u\bar{\chi}^u \\ \dot{\bar{\chi}}^v &= H^v_{lk}\dot{\gamma}^{vp} - H^v_{nlk}\dot{\bar{\xi}}^v\bar{\chi}^v \end{aligned} \tag{2.44}$$

where H^u_{lk}, H^v_{lk} are the kinematic hardening moduli, and H^u_{nlk}, H^v_{nlk} are the non-dimensional material parameters that characterize the nonlinear kinematic hardening behavior.

3. The evolution equations for internal variables ϵ^{vp}, γ^{vp} and $\bar{\xi}^u$, $\bar{\xi}^v$ obtained through the principle of maximum plastic dissipation and Kuhn-Tucker optimality conditions

$$\begin{aligned} \dot{\varepsilon}^{vp} &= \dot{\bar{\gamma}}^u sign(N' - \bar{\chi}^u A^e); \;\; \dot{\bar{\xi}}^u = \dot{\bar{\gamma}}^u; \;\; \dot{\bar{\gamma}}^u \geq 0 \\ \dot{\gamma}^{vp} &= \dot{\bar{\gamma}}^v sign(V' - \bar{\chi}^v A^e); \;\; \dot{\bar{\xi}}^v = \dot{\bar{\gamma}}^v; \;\; \dot{\bar{\gamma}}^v \geq 0 \end{aligned} \tag{2.45}$$

where $\bar{\gamma}^u$, $\bar{\gamma}^v$ are the plastic multipliers whose values are equal to

$$\begin{aligned} \dot{\bar{\gamma}}^u &= \frac{\langle \bar{\phi}^u(N', \bar{\chi}^u, \bar{q}^u) \rangle}{\eta^u} \\ \dot{\bar{\gamma}}^v &= \frac{\langle \bar{\phi}^v(V', \bar{\chi}^v, \bar{q}^v) \rangle}{\eta^v} \end{aligned} \tag{2.46}$$

where η^u, η^v are the viscosity parameters.

2.4.3.2 Exponential softening

Once the element enters the softening phase, the jump in displacement is activated. All plastic deformation from that point on remains localized at the discontinuity, whereas the bulk part of the element elastically unloads. The exponential softening is described with

1. The yield function defined in terms of stresses (or stress resultants), and dual variables $\bar{\bar{q}}^u$, $\bar{\bar{q}}^v$

$$\begin{aligned} \bar{\bar{\phi}}^u\left(t^u, \bar{\bar{q}}^u\right) &= |t^u| - \left(N_f - \bar{\bar{q}}^u A^e\right) \leq 0 \\ \bar{\bar{\phi}}^v\left(t^v, \bar{\bar{q}}^v\right) &= |t^v| - \left(V_f - \bar{\bar{q}}^v A^e\right) \leq 0 \end{aligned} \tag{2.47}$$

where N_f, V_f are the fracture limits, and $\bar{\bar{q}}^u$, $\bar{\bar{q}}^v$ are the stress-like softening variables that for exponential softening take the following form

$$\begin{aligned} \bar{\bar{q}}^u &= \frac{N_f}{A^e}\left(1 - exp\left(-\bar{\bar{\xi}}^u \frac{(N_f/A^e)}{G^u_f}\right)\right) \\ \bar{\bar{q}}^v &= \frac{V_f}{A^e}\left(1 - exp\left(-\bar{\bar{\xi}}^v \frac{(V_f/A^e)}{G^v_f}\right)\right) \end{aligned} \tag{2.48}$$

where G_f^u, G_f^v are the fracture energies, and $\bar{\bar{\xi}}^u$, $\bar{\bar{\xi}}^v$ are the strain-like softening variables. The stress resultant values in the bulk part of an element in the softening phase, which determine the value of internal forces at the discontinuity t^u, t^v are computed as

$$\begin{aligned} N' &= EA^e\left(\varepsilon - \varepsilon^{vp} + \bar{G}\alpha^u\right) \\ V' &= k_c GA^e\left(\gamma - \gamma^{vp} + \bar{G}\alpha^v\right) \end{aligned} \tag{2.49}$$

2. The evolution equations for internal variables α^u, α^v and $\bar{\bar{\xi}}^u$, $\bar{\bar{\xi}}^v$ with the loading/unloading conditions obtained through the principle of maximum plastic dissipation and Kuhn-Tucker optimality conditions [124]

$$\begin{aligned} &\dot{\alpha}^u = \dot{\bar{\bar{\gamma}}}^u sign(t^u);\ \ \dot{\bar{\bar{\xi}}}^u = \dot{\bar{\bar{\gamma}}}^u;\ \ \dot{\bar{\bar{\gamma}}}^u \geq 0;\ \ \bar{\bar{\phi}}^u \leq 0;\ \ \dot{\bar{\bar{\gamma}}}^u \bar{\bar{\phi}}^u = 0 \\ &\dot{\alpha}^v = \dot{\bar{\bar{\gamma}}}^v sign(t^v);\ \ \dot{\bar{\bar{\xi}}}^v = \dot{\bar{\bar{\gamma}}}^v;\ \ \dot{\bar{\bar{\gamma}}}^v \geq 0;\ \ \bar{\bar{\phi}}^v \leq 0;\ \ \dot{\bar{\bar{\gamma}}}^v \bar{\bar{\phi}}^v = 0 \end{aligned} \tag{2.50}$$

where $\bar{\bar{\gamma}}^u$, $\bar{\bar{\gamma}}^v$ are the plastic multipliers whose values are obtained from the consistency conditions

$$\begin{aligned} \dot{\bar{\bar{\gamma}}}^u \dot{\bar{\bar{\phi}}}^u = 0 \\ \dot{\bar{\bar{\gamma}}}^v \dot{\bar{\bar{\phi}}}^v = 0 \end{aligned} \tag{2.51}$$

2.4.4 Computational procedure

The end result of the finite element discretization procedure is two sets of equations. The first is the first order differential evolution equations for internal variables defined locally (on the element level) at each Gauss quadrature point, and the second is the second order differential equations in time governing the coupled problem defined globally. The solution of these equations is computed at discrete pseudo-time steps $t_1, t_2, ..., t_n$ by using the operator split solution procedure [124]. Here, the solution procedure is divided into the local phase and the global phase, which are treated separately. In the local phase, the solution of evolution equations is computed by using implicit backward Euler time integration scheme. The unknown values of displacement jumps are statically condensed on the element level from the condition that the residual at the discontinuity is equal to zero. In the global phase, the solution in terms of the unknown nodal displacements and pore pressures is computed in a fully monolithic manner using Newmark time-integration scheme and Newton's iterative method.

Following the standard finite element discretization procedure, the system of equations governing the coupled problem for single Timoshenko beam finite element is written as

$$\mathbf{M}^e_{uu}\ddot{\mathbf{u}} + \mathbf{f}^{int,e}(\boldsymbol{\sigma}_u) - \mathbf{K}^e_{up}\bar{\mathbf{p}}^{\backslash} = \mathbf{f}^{ext,e} \tag{2.52}$$

$$\mathbf{K}^{e,\mathsf{T}}_{up}\dot{\mathbf{u}} + \mathbf{D}^e_{pp}\dot{\bar{\mathbf{p}}}^{\backslash} + \mathbf{K}^e_{pp}\bar{\mathbf{p}}^{\backslash} = \mathbf{q}^{ext,e} \tag{2.53}$$

where $\mathbf{M}^e_{uu}$ is the mass matrix, $\mathbf{f}^{int,e}(\boldsymbol{\sigma}_u)$ is the internal load vector resulting from displacements (i.e. effective stresses), $\mathbf{K}^e_{up}$ is the coupling matrix, $\mathbf{D}^e_{pp}$ is the compressibility matrix, $\mathbf{K}^e_{pp}$ is the permeability matrix, and $\mathbf{f}^{e,ext}$ and $\mathbf{q}^{e,ext}$ are the load vectors. The matrices $\mathbf{K}^e_{up}$, $\mathbf{D}^e_{pp}$ and $\mathbf{K}^e_{pp}$ are computed as

$$\begin{aligned}
\mathbf{K}^e_{up} &= \int_0^{L^e} \mathbf{B}^{s,\mathsf{T}}_{up}\, b\mathbf{N}^s_{up}\, dx; \qquad \mathbf{B}^s_{up} = \begin{bmatrix} B_1 & 0 & 0 & B_2 & 0 & 0 \end{bmatrix} \\
\mathbf{D}^e_{pp} &= \int_{\Omega^e_{CST}} \mathbf{N}^{s,\mathsf{T}}_p \frac{1}{M} \mathbf{N}^s_p\, d\Omega; \qquad \mathbf{K}^e_{pp} = \int_{\Omega^e_{CST}} (\nabla \mathbf{N}^s_p)^{\mathsf{T}} \frac{k}{\gamma_f} \nabla \mathbf{N}^s_p\, d\Omega
\end{aligned} \tag{2.54}$$

Here we note that in the global system of equations (Equations 2.52 and 2.53) we take the parts of the $\mathbf{D}^e_{pp}$, and $\mathbf{K}^e_{pp}$ matrices (Equation 2.54) that correspond to the nodes of Timoshenko beam finite element.

The Timoshenko beam finite element mass matrix $\mathbf{M}^e$ in Equation (2.52) is obtained by distributing the total mass of an element to nodes (Figure 2.8), resulting in a diagonally lumped mass matrix, written as [111]

$$\mathbf{M}^e_{uu} = \frac{1}{2}\rho\, diag\left(A_{tot},\, A_{tot},\, I^e,\, A_{tot},\, A_{tot},\, I^e\right) \tag{2.55}$$

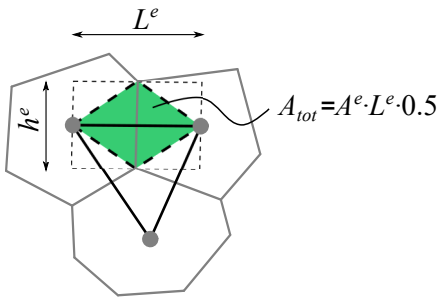

Figure 2.8 Timoshenko beam finite element lumped mass matrix computation

The solution of the coupled problem at the global level in terms of unknown values of nodal displacements and pore pressures is preceded by the solution for the unknown values of internal variables at the local (element) level.

2.4.4.1 Local phase: bulk

Computational procedure for proposed plasticity model is as follows

Start with the best iterative values of nodal displacements, then

- Assume elastic trial step

$$\bar{\gamma}^{u,trial}_{n+1} = 0 \Rightarrow \begin{cases} \varepsilon^{vp,trial}_{n+1} = \varepsilon^{vp}_{n} \\ \bar{\xi}^{u,trial}_{n+1} = \bar{\xi}^{u}_{n} \end{cases} ; \quad \bar{\gamma}^{v,trial}_{n+1} = 0 \Rightarrow \begin{cases} \gamma^{vp,trial}_{n+1} = \gamma^{vp}_{n} \\ \bar{\xi}^{v,trial}_{n+1} = \bar{\xi}^{v}_{n} \end{cases}$$

- Calculate trial values of resultant forces, stress-like hardening variables and back-stress variables

$$\Rightarrow \begin{cases} N'^{trial}_{n+1} = EA^e\left(\varepsilon^{(i)}_{n+1} - \varepsilon^{vp}_{n}\right) \\ \bar{q}^{u,trial}_{n+1} = -H^u_{lh}\bar{\xi}^u_n \\ \bar{\chi}^{u,trial}_{n+1} = H^u_{lk}\varepsilon^{vp}_n - H^u_{nlk}\bar{\xi}^u_n\bar{\chi}^u_n \end{cases} ; \quad \Rightarrow \begin{cases} V'^{trial}_{n+1} = k_c GA^e\left(\gamma^{(i)}_{n+1} - \gamma^{vp}_{n}\right) \\ \bar{q}^{v,trial}_{n+1} = -H^v_{lh}\bar{\xi}^v_n \\ \bar{\chi}^{v,trial}_{n+1} = H^v_{lk}\gamma^{vp}_n - H^v_{nlk}\bar{\xi}^v_n\bar{\chi}^v_n \end{cases}$$

- Calculate trial values of yield functions

$$\bar{\phi}^{u,trial}_{n+1} = \left|N'^{trial}_{n+1} - \bar{\chi}^{u,trial}_{n+1}A^e\right| - \left(N_y - \bar{q}^{u,trial}_{n+1}A^e\right)$$
$$\bar{\phi}^{v,trial}_{n+1} = \left|V'^{trial}_{n+1} - \bar{\chi}^{v,trial}_{n+1}A^e\right| - \left(V_y - \bar{q}^{v,trial}_{n+1}A^e\right)$$

→ if $\bar{\phi}^{u,trial}_{n+1} \leq 0$ the current step in axial direction is indeed elastic, and the values of internal variables, stress-like hardening variable and back-stress variable at time step t_{n+1} are

$$\bar{\gamma}^{u}_{n+1} = 0 \Rightarrow \begin{cases} \varepsilon^{vp}_{n+1} = \varepsilon^{vp}_{n}; \quad \bar{q}^{u}_{n+1} = \bar{q}^{u,trial}_{n+1} \\ \bar{\xi}^{u}_{n+1} = \bar{\xi}^{u}_{n}; \quad \bar{\chi}^{u}_{n+1} = \bar{\chi}^{u,trial}_{n+1} \end{cases}$$

The value of elasto-plastic tangent modulus $C^{ep,u}$ at time step t_{n+1} is

$$C^{ep,u}_{n+1} = E$$

if $\bar{\phi}^{u,trial}_{n+1} > 0$ the current step in axial direction is plastic, and the values of internal variables, stress-like hardening variable and back-stress

variable at time step t_{n+1} are

$$\bar{\gamma}^u_{n+1} = \frac{\bar{\phi}^{u,trial}_{n+1}}{A^e\left(E + H^u_{lh} + H^u_{lk} - H^u_{nlk}\bar{\chi}^u_n + \frac{\eta^u}{\Delta t}\right)}$$

$$\Rightarrow \begin{cases} \varepsilon^{vp}_{n+1} = \varepsilon^{vp}_n + \bar{\gamma}^u_{n+1} sign\left(N'^{trial}_{n+1} - \bar{\chi}^{u,trial}_{n+1} A^e\right) \\ \bar{\xi}^u_{n+1} = \bar{\xi}^u_n + \bar{\gamma}^u_{n+1} \\ \bar{q}^u_{n+1} = \bar{q}^u_n - H^u_{lh}\bar{\gamma}^u_{n+1} \\ \bar{\chi}^u_{n+1} = \bar{\chi}^u_n + H^u_{lk}\bar{\gamma}^u_{n+1} sign\left(N'^{trial}_{n+1} - \bar{\chi}^{u,trial}_{n+1} A^e\right) - H^u_{nlk}\bar{\gamma}^u_{n+1}\bar{\chi}^u_n \end{cases}$$

where Δt is the time increment.
The value of elasto-plastic tangent modulus $C^{ep,u}$ at time step t_{n+1} is

$$C^{ep,u}_{n+1} = \frac{E\left(H^u_{lh} + H^u_{lk} - H^u_{nlk}\bar{\chi}^u_{n+1} + \frac{\eta^u}{\Delta t}\right)}{E + H^u_{lh} + H^u_{lk} - H^u_{nlk}\bar{\chi}^u_{n+1} + \frac{\eta^u}{\Delta t}}$$

→ if $\bar{\phi}^{v,trial}_{n+1} \leq 0$ the current step in transverse direction is indeed elastic, and the values of internal variables, stress-like hardening variable and back-stress variable at time step t_{n+1} are

$$\bar{\gamma}^v_{n+1} = 0 \Rightarrow \begin{cases} \gamma^{vp}_{n+1} = \gamma^{vp}_n; \quad \bar{q}^v_{n+1} = \bar{q}^{v,trial}_{n+1} \\ \bar{\xi}^v_{n+1} = \bar{\xi}^v_n; \quad \bar{\chi}^v_{n+1} = \bar{\chi}^{v,trial}_{n+1} \end{cases}$$

The value of elasto-plastic tangent modulus $C^{ep,v}$ at time step t_{n+1} is

$$C^{ep,v}_{n+1} = k_c G$$

if $\bar{\phi}^{v,trial}_{n+1} > 0$ the current step in transverse direction is plastic, and the values of internal variables, stress-like hardening variable and back-stress variable at time step t_{n+1} are

$$\bar{\gamma}^v_{n+1} = \frac{\bar{\phi}^{v,trial}_{n+1}}{A^e\left(k_c G + H^v_{lh} + H^v_{lk} - H^v_{nlk}\bar{\chi}^v_n + \frac{\eta^v}{\Delta t}\right)}$$

$$\Rightarrow \begin{cases} \gamma^{vp}_{n+1} = \epsilon^{vp}_n + \bar{\gamma}^v_{n+1} sign\left(V'^{trial}_{n+1} - \bar{\chi}^{v,trial}_{n+1} A^e\right) \\ \bar{\xi}^v_{n+1} = \bar{\xi}^v_n + \bar{\gamma}^v_{n+1} \\ \bar{q}^v_{n+1} = \bar{q}^v_n - H^v_{lh}\bar{\gamma}^v_{n+1} \\ \bar{\chi}^v_{n+1} = \bar{\chi}^v_n + H^v_{lk}\bar{\gamma}^v_{n+1} sign\left(V'^{trial}_{n+1} - \bar{\chi}^{v,trial}_{n+1} A^e\right) - H^v_{nlk}\bar{\gamma}^v_{n+1}\bar{\chi}^v_n \end{cases}$$

The value of elasto-plastic tangent modulus $C^{ep,v}$ at time step t_{n+1} is

$$C^{ep,v}_{n+1} = \frac{k_c G\left(H^v_{lh} + H^v_{lk} - H^v_{nlk}\bar{\chi}^v_{n+1} + \frac{\eta^v}{\Delta t}\right)}{k_c G + H^v_{lh} + H^v_{lk} - H^v_{nlk}\bar{\chi}^v_{n+1} + \frac{\eta^v}{\Delta t}}$$

2.4.4.2 Local phase: discontinuity

Computational procedure for exponential softening is as follows

Start with the best iterative values of nodal displacements, then

- Assume elastic trial step

$$\bar{\bar{\gamma}}^{u,trial}_{n+1} = 0 \Rightarrow \begin{cases} \alpha^{u,trial}_{n+1} = \alpha^u_n \\ \bar{\bar{\xi}}^{u,trial}_{n+1} = \bar{\bar{\xi}}^u_n \end{cases}; \quad \bar{\bar{\gamma}}^{v,trial}_{n+1} = 0 \Rightarrow \begin{cases} \alpha^{v,trial}_{n+1} = \alpha^v_n \\ \bar{\bar{\xi}}^{v,trial}_{n+1} = \bar{\bar{\xi}}^v_n \end{cases}$$

- Calculate trial value of internal forces acting at discontinuity and stress-like softening variables

$$\Rightarrow \begin{cases} t^{u,trial}_{n+1} = EA^e\left(\varepsilon^{(i)}_{n+1} - \varepsilon^{vp} + \bar{G}\alpha^u_n\right) \\ \bar{\bar{q}}^{u,trial}_{n+1} = \dfrac{N_f}{A^e}\left(1 - exp\left(-\bar{\bar{\xi}}^u_n \dfrac{(N_f/A^e)}{G^u_f}\right)\right) \end{cases}$$

$$\Rightarrow \begin{cases} t^{v,trial}_{n+1} = k_c GA^e\left(\gamma^{(i)}_{n+1} - \gamma^{vp} + \bar{G}\alpha^v_n\right) \\ \bar{\bar{q}}^{v,trial}_{n+1} = \dfrac{V_f}{A^e}\left(1 - exp\left(-\bar{\bar{\xi}}^v_n \dfrac{(V_f/A^e)}{G^v_f}\right)\right) \end{cases}$$

- Calculate trial value of yield functions

$$\bar{\bar{\phi}}^{u,trial}_{n+1} = \left|t^{u,trial}_{n+1}\right| - \left(N_f - \bar{\bar{q}}^{u,trial}_{n+1}A^e\right)$$
$$\bar{\bar{\phi}}^{v,trial}_{n+1} = \left|t^{v,trial}_{n+1}\right| - \left(V_f - \bar{\bar{q}}^{v,trial}_{n+1}A^e\right)$$

  → if $\bar{\bar{\phi}}^{u,trial}_{n+1} \leq 0$ the current step in axial direction is indeed elastic, and the values of internal variables at time step t_{n+1} remain the same as at time step t_n

$$\bar{\bar{\gamma}}^u_{n+1} = 0 \Rightarrow \begin{cases} \alpha^u_{n+1} = \alpha^u_n \\ \bar{\bar{\xi}}^u_{n+1} = \bar{\bar{\xi}}^u_n \\ \bar{\bar{q}}^u_{n+1} = \bar{\bar{q}}^{u,trial}_{n+1} \end{cases}$$

if $\bar{\bar{\phi}}^{u,trial}_{n+1} > 0$ the current step is in axial direction is plastic, and the values of internal variables needs to be updated in order to ensure the plastic admissibility of stress. The values of internal variables for exponential softening at time step t_{n+1} are computed iteratively from the condition

$$\bar{\bar{\phi}}^{u}_{n+1} \leq tol$$

The values of internal variables at time step t_{n+1} and iteration (j) are

$$\Delta\bar{\bar{\gamma}}^{u,(j)}_{n+1} = \frac{\bar{\bar{\phi}}^{u,(j)}_{n+1}}{A^e\left(-\bar{G}E + K^{u,(j)}_{\alpha}\right)} \Rightarrow \begin{cases} \alpha^{u,(j+1)}_{n+1} = \alpha^{u,(j)}_{n+1} + \Delta\bar{\bar{\gamma}}^{u,(j)}_{n+1} sign\left(t^{u,trial}_{n+1}\right) \\ \bar{\bar{\xi}}^{u,(j+1)}_{n+1} = \bar{\bar{\xi}}^{u,(j)}_{n+1} + \Delta\bar{\bar{\gamma}}^{u,(j)}_{n+1} \end{cases}$$

where

$$K^{u,(j)}_{\alpha} = -\frac{(N_f/A^e)^2}{G^u_f}\left(exp\left(-\bar{\bar{\xi}}^{u,(j)}\frac{(N_f/A^e)}{G^u_f}\right)\right)$$

$$t^{u,(j)}_{n+1} = EA^e\left(\epsilon^{(i)}_{n+1} - \epsilon^{vp} + \bar{G}\alpha^{u,(j)}_{n}\right)$$

$$\bar{\bar{q}}^{u,(j)}_{n+1} = \frac{N_f}{A^e}\left(1 - exp\left(-\bar{\bar{\xi}}^{u,(j)}_{n+1}\frac{(N_f/A^e)}{G^u_f}\right)\right)$$

→ if $\bar{\bar{\phi}}^{v,trial}_{n+1} \leq 0$ the current step in transverse direction is indeed elastic, and the values of internal variables at time step t_{n+1} are

$$\bar{\bar{\gamma}}^{v}_{n+1} = 0 \Rightarrow \begin{cases} \alpha^{v}_{n+1} = \alpha^{v}_{n} \\ \bar{\bar{\xi}}^{v}_{n+1} = \bar{\bar{\xi}}^{v}_{n} \\ \bar{\bar{q}}^{v}_{n+1} = \bar{\bar{q}}^{v,trial}_{n+1} \end{cases}$$

if $\bar{\bar{\phi}}^{v,trial}_{n+1} > 0$ the current step in transverse direction is plastic. The values of internal variables for exponential softening at time step t_{n+1} are computed iteratively from the condition

$$\bar{\bar{\phi}}^{v}_{n+1} \leq tol$$

The values of internal variables at time step t_{n+1} and iteration (j) are

$$\Delta\bar{\bar{\gamma}}^{v,(j)}_{n+1} = \frac{\bar{\bar{\phi}}^{v,(j)}_{n+1}}{A^e\left(-\bar{G}Gk_c + K^{v,(j)}_{\alpha}\right)} \Rightarrow \begin{cases} \alpha^{v,(j+1)}_{n+1} = \alpha^{v,(j)}_{n+1} + \Delta\bar{\bar{\gamma}}^{v,(j)}_{n+1} sign\left(t^{v,trial}_{n+1}\right) \\ \bar{\bar{\xi}}^{v,(j+1)}_{n+1} = \bar{\bar{\xi}}^{v,(j)}_{n+1} + \Delta\bar{\bar{\gamma}}^{v,(j)}_{n+1} \end{cases}$$

where

$$K_{\alpha}^{v,(j)} = -\frac{(V_f/A^e)^2}{G_f^v}\Big(exp\Big(-\bar{\bar{\xi}}^{v,(j)}\frac{(V_f/A^e)}{G_f^v}\Big)\Big)$$
$$t_{n+1}^{v,(j)} = k_c G A^e\Big(\gamma_{n+1}^{(i)} - \gamma^{vp} + \bar{G}\alpha_n^{v,(j)}\Big)$$
$$\bar{\bar{q}}_{n+1}^{v,(j)} = \frac{V_f}{A^e}\Big(1 - exp\Big(-\bar{\bar{\xi}}_{n+1}^{v,(j)}\frac{(V_f/A^e)}{G_f^u}\Big)\Big)$$

2.4.4.3 Global phase

The computation of internal variables in the local phase is followed by the global phase. The global phase of the computation is performed by means of Newton's iterative method. Based on the converged values of internal variables, the values of internal forces are computed and compared with the values of external forces to check whether the equilibrium is satisfied. The equilibrium condition is written as

$$\mathop{\mathbb{A}}_{e=1}^{n_{elem}}\Big[\mathbf{f}^{ext} - \mathbf{f}^{int,(i)} - \mathbf{f}^{acc,(i)}\Big]_{n+1}^{e} < \mathbf{tol} \tag{2.56}$$

If the previous condition is satisfied, the computation for new time-step is performed. If not, new iterative values of unknown nodal displacements and pore pressures are to be computed.

The global phase of the computation is solved using Newmark time-integration scheme, which solves the second-order transient problem in the following manner [41]

$$\mathbf{R}_{n+1} = \mathbf{F}_{n+1} - \mathbf{P}\big(\mathbf{u}_{n+1}, \dot{\mathbf{u}}_{n+1}, \ddot{\mathbf{u}}_{n+1}\big) = \mathbf{0} \tag{2.57}$$

where

$$\begin{aligned}\mathbf{u}_{n+1} &= \mathbf{u}_n + \Delta t\dot{\mathbf{u}}_n + \Delta t^2\big[(0.5-\beta)\ddot{\mathbf{u}}_n + \beta\ddot{\mathbf{u}}_{n+1}\big]\\ \dot{\mathbf{u}}_{n+1} &= \dot{\mathbf{u}}_n + \Delta t\big[(1-\gamma)\ddot{\mathbf{u}}_n + \gamma\ddot{\mathbf{u}}_{n+1}\big]\end{aligned} \tag{2.58}$$

in which β and γ are parameters controlling stability and numerical dissipation, and Δt is the time increment.

For a time step t_{n+1} and iteration i, the global system of equations to be solved is written as

$$\mathop{\mathbb{A}}_{e=1}^{n_{elem}}\left\{\begin{bmatrix}\frac{1}{\beta\Delta t^2}\mathbf{M}_{uu} + \bar{\mathbf{K}}_{uu} & -\mathbf{K}_{up}\\ \frac{\gamma}{\beta\Delta t}\mathbf{K}_{up}^{\mathsf{T}} & \frac{\gamma}{\beta\Delta t}\mathbf{D}_{pp} + \mathbf{K}_{pp}\end{bmatrix}_{n+1}^{e,(i)}\begin{Bmatrix}\Delta\bar{\mathbf{u}}\\ \Delta\bar{\mathbf{p}}\end{Bmatrix}_{n+1}^{e,(i)} = \begin{Bmatrix}\mathbf{r}_u\\ \mathbf{r}_p\end{Bmatrix}_{n+1}^{e,(i)}\right\} \tag{2.59}$$

where $\bar{\mathbf{K}}^{e}_{uu}$ is the element tangent stiffness matrix, and $\mathbf{r}^{e,(i)}_{u,n+1}$ and $\mathbf{r}^{e,(i)}_{p,n+1}$ are residuals pertaining to the solid and the pore fluid part.

After solving the global system of equations, the new iterative values of unknown fields are updated as

$$\begin{aligned}\bar{\mathbf{u}}^{(i+1)}_{n+1} &= \bar{\mathbf{u}}^{(i)}_{n+1} + \Delta\bar{\mathbf{u}}^{(i)}_{n+1} \\ \bar{\mathbf{p}}^{(i+1)}_{n+1} &= \bar{\mathbf{p}}^{(i)}_{n+1} + \Delta\bar{\mathbf{p}}^{(i)}_{n+1}\end{aligned} \tag{2.60}$$

In each iteration, the tangent stiffness matrix for every element is constructed. The tangent stiffness matrix of an element is obtained by linearization of Equations (2.36) and (2.37) with respect to nodal displacements and displacement jumps.

If the element is elasto-viscoplastic then only Equation (2.36) with respect to nodal displacements is linearized since the jump in displacement is not yet activated. The element tangent stiffness matrix is defined as

$$\bar{\mathbf{K}}^{e,(i)}_{uu,n+1} = \mathbf{K}^{e,(i)}_{uu,n+1} = \left(\frac{\partial \mathbf{f}^{int}(\boldsymbol{\sigma}_u)}{\delta\bar{\mathbf{u}}}\right)^{e,(i)}_{n+1} = \int_0^{L^e} \mathbf{B}^{s,\mathsf{T}}_u \mathbf{C}^{ep,(i)}_{n+1} \mathbf{B}^{s}_u dx \tag{2.61}$$

Elasto-viscoplastic tangent matrix is written as

$$\mathbf{C}^{ep,(i)}_{n+1} = \begin{bmatrix} C^{ep,u}_{n+1}A^e & 0 & 0 \\ 0 & C^{ep,v}_{n+1}A^e & 0 \\ 0 & 0 & EI^e \end{bmatrix} \tag{2.62}$$

where $C^{ep,u}_{n+1}$ and $C^{ep,v}_{n+1}$ are elasto-plastic tangent moduli for axial and transverse direction.

If the element is in the softening then both Equations (2.36) and (2.37) are linearized. The element tangent stiffness matrix is obtained by performing static condensation procedure in which the unknown values of displacement jumps are eliminated from the condition that the residual at the discontinuity is equal to zero. The statically condensed element tangent stiffness matrix is written as

$$\bar{\mathbf{K}}^{e,(i)}_{uu,n+1} = \hat{\mathbf{K}}^{e,(i)}_{uu,n+1} = \left[\mathbf{K}^{e,(i)}_{uu,n+1} - \mathbf{F}^{e,(i)}_{n+1}\left(\mathbf{H}^{e,(i)}_{n+1} + \mathbf{K}_{\alpha}\right)^{-1}\left(\mathbf{F}^{e,(i),\mathsf{T}}_{n+1} + \mathbf{K}_{d}\right)\right] \tag{2.63}$$

where

$$\mathbf{K}^{e,(i)}_{uu,n+1} = \left(\frac{\partial \mathbf{f}^{int}(\boldsymbol{\sigma}_u)}{\delta\bar{\mathbf{u}}}\right)^{e,(i)}_{n+1} = \int_0^{L^e} \mathbf{B}^{s,\mathsf{T}}_u \mathbf{C}^{ep,(i)}_{n+1} \mathbf{B}^{s}_u dx$$

$$\mathbf{F}^{e,(i)}_{n+1} = \left(\frac{\partial \mathbf{f}^{int}(\boldsymbol{\sigma}_u)}{\delta\boldsymbol{\alpha}}\right)^{e,(i)}_{n+1} = \int_0^{L^e} \mathbf{B}^{s,\mathsf{T}}_u \mathbf{C}^{ep,(i)}_{n+1} \bar{\mathbf{G}} dx$$

$$\left(\mathbf{F}^{\mathsf{T}}+\mathbf{K_d}\right)_{n+1}^{e,(i)}=\left(\frac{\partial \mathbf{h}}{\delta \bar{\mathbf{u}}}\right)_{n+1}^{e,(i)}=\int_0^{L^e}\bar{\mathbf{G}}^{\mathsf{T}}\mathbf{C}_{n+1}^{ep,(i)}\mathbf{B}_u^s dx+\mathbf{K}_d$$

$$\left(\mathbf{H}+\mathbf{K}_\alpha\right)_{n+1}^{e,(i)}=\left(\frac{\partial \mathbf{h}}{\delta \boldsymbol{\alpha}}\right)_{n+1}^{e,(i)}=\int_0^{L^e}\bar{\mathbf{G}}^{\mathsf{T}}\mathbf{C}_{n+1}^{ep,(i)}\bar{\mathbf{G}}dx+\mathbf{K}_\alpha \tag{2.64}$$

If the current step in the softening is elastic, then

$$\mathbf{K}_d=\mathbf{C}^*\mathbf{B}_u^s;\quad \mathbf{K}_\alpha=\mathbf{0};\quad \mathbf{C}^*=\begin{bmatrix} EA^e & 0 & 0\\ 0 & k_cGA^e & 0\\ 0 & 0 & 0\end{bmatrix} \tag{2.65}$$

Else, if the current step in the softening is plastic, then

$$\mathbf{K}_d=\mathbf{0};\quad \mathbf{K}_\alpha=\begin{bmatrix} K_\alpha^u A^e & 0 & 0\\ 0 & K_\alpha^v A^e & 0\\ 0 & 0 & 0\end{bmatrix} \tag{2.66}$$

Remark 1: When computing the element tangent stiffness matrix all different combinations that can occur, have to be taken into account. For example, in axial direction softening can occur while in transverse direction element is elasto-viscoplastic. After the appropriate tangent stiffness matrix for every element is constructed, an assembly procedure to take into account the contribution of every element to global equilibrium is performed. We note that in the assembly procedure denoted by operator $\mathbb{A}$, the local-global transformation procedure is included.

Remark 2: We note that the equal order of finite element interpolation (linear interpolation) is used for both the displacement and pore pressure fields. If the undrained limit state is considered, with permeability and compressibility matrix equal to zero, then this kind of approximation (unless stabilization techniques are implemented [128]) can cause stability issues and finite elements which satisfy Babuska-Brezzi condition [129, 130], or Zienkiewicz-Taylor mixed patch test [131] should be used (e.g., see [132]). However, if the undrained limit state is not considered (as is in our case), then equal order of interpolation for unknown fields is justified [5, 133].

Remark 3: In quasi-static setting, with inertial effects being negligible, the resulting set of equations on the global level are the first order differential equations in time. The global phase of computation under quasi-static assumptions is solved using Newton's iterative method and backward Euler scheme which solves the first order transient problem in the following manner [41]

$$\mathbf{R}_{n+1} = \mathbf{F}_{n+1} - \mathbf{P}\big(\mathbf{u}_{n+1}, \dot{\mathbf{u}}_{n+1}\big) = \mathbf{0} \tag{2.67}$$

where

$$\dot{\mathbf{u}}_{n+1} = \frac{1}{\Delta t}\big[\mathbf{u}_{n+1} - \mathbf{u}_n\big] \tag{2.68}$$

For a time step t_{n+1} and iteration i, the global system of equations to be solved under the quasi-static assumption is written as

$$\mathop{\mathbb{A}}_{e=1}^{n} \left\{ \begin{bmatrix} \bar{\mathbf{K}}_{uu} & -\mathbf{K}_{up} \\ \frac{1}{\Delta t}\mathbf{K}_{up}^{\mathsf{T}} & \frac{1}{\Delta t}\mathbf{D}_{pp} + \mathbf{K}_{pp} \end{bmatrix}^{e,(i)}_{n+1} \begin{Bmatrix} \Delta\bar{\mathbf{u}} \\ \Delta\bar{\mathbf{p}}^{\backprime} \end{Bmatrix}^{e,(i)}_{n+1} = \begin{Bmatrix} \mathbf{r}_u \\ \mathbf{r}_p \end{Bmatrix}^{e,(i)}_{n+1} \right\} \tag{2.69}$$

Remark 4: In numerical simulations of structures built of dry material in quasi-static setting, the global system of equations is reduced to the system of algebraic equilibrium equations. The global phase of computation is solved using Newton's iterative method. For a time step t_{n+1} and iteration i, the global system of equations to be solved under the quasi-static assumption is written as

$$\mathop{\mathbb{A}}_{e=1}^{n} \left\{ \bar{\mathbf{K}}^{e,(i)}_{uu,n+1} \Delta\bar{\mathbf{u}}^{e,(i)}_{n+1} = \{\mathbf{r}_u\}^{e,(i)}_{n+1} \right\} \tag{2.70}$$

For solving the global phase, the arc-length method can also be used in which both the current values of external load and displacements are sought iteratively.

Remark 5: We note that the boundary conditions in the numerical test for identification of lattice Young's modulus shown in Figure 2.4a, correspond to the conditions of constrained lateral deformations. The conditions of constrained later deformations are typically met in the oedometer test, which is commonly used in soil mechanics to determine the consolidation characteristics of soils. In the oedometer test the movement of the sample is allowed only in the vertical direction, which makes this test very useful for obtaining the value of constrained (oedometer) elastic modulus.

The relation between the oedometer elastic modulus E_{oed} and Young's modulus E for continuum can be derived by exploiting Hooke's law. Hooke's law for isotropic material in three dimensions with ν as Poisson's ratio is written as

$$\begin{bmatrix} \sigma_{11} \\ \sigma_{22} \\ \sigma_{33} \\ \sigma_{23} \\ \sigma_{13} \\ \sigma_{12} \end{bmatrix} = \frac{E}{(1+\nu)(1-2\nu)} \begin{bmatrix} 1-\nu & \nu & \nu & 0 & 0 & 0 \\ \nu & 1-\nu & \nu & 0 & 0 & 0 \\ \nu & \nu & 1-\nu & 0 & 0 & 0 \\ 0 & 0 & 0 & \frac{1-2\nu}{2} & 0 & 0 \\ 0 & 0 & 0 & 0 & \frac{1-2\nu}{2} & 0 \\ 0 & 0 & 0 & 0 & 0 & \frac{1-2\nu}{2} \end{bmatrix} \begin{bmatrix} \varepsilon_{11} \\ \varepsilon_{22} \\ \varepsilon_{33} \\ \varepsilon_{23} \\ \varepsilon_{13} \\ \varepsilon_{12} \end{bmatrix} \tag{2.71}$$

where $\boldsymbol{\sigma}$ is the stress vector and $\boldsymbol{\varepsilon}$ is the strain vector.

Hence, the oedometer elastic modulus E_{oed} and Young's modulus E for continuum are related by

$$E_{oed} = E\frac{(1-\nu)}{(1+\nu)(1-2\nu)} \tag{2.72}$$

The ratio between the oedometer modulus E_{oed} and Young's modulus E for different values of Poisson's ratio are shown in Table 2.1.

Table 2.1 Oedometer vs. Young's modulus for different values of Poisson's ratio

Poisson's ratio ν	Oedometer modulus/Young's modulus E_{oed}/E
0	1
0.1	1.02
0.2	1.11
0.3	1.35
0.4	2.14
0.45	3.79

2.5 Numerical results

In this section, we present the results of several numerical simulations, which serve to illustrate the coupled discrete beam lattice model performance. All numerical implementations and computations are performed with the research version of the computer code FEAP, developed by R.L. Taylor [41]. In all numerical simulations, the finite element mesh is generated by using Delaunay triangulation and GMSH software [91]. The cross-sectional properties of the Timoshenko beam finite elements are computed from the Voronoi diagram by using MATLAB software [92].

2.5.1 Illustrative examples

In this section, we demonstrate the capabilities of the proposed discrete beam lattice model on a set of illustrative examples for a structure with very small water content (i.e., structure built of dry, non-porous material). We describe in details the phases of the macro-scale response of the structure computed with the proposed model. Namely, we aim to demonstrate the idea of multi-scale modeling. In other words, we aim to show that with the appropriate modeling of the micro-scale, we are able to capture the true response of the structure on the macro-scale level.

2.5.1.1 Hardening response of discrete beam lattice model

In our first example, we observe a cantilever beam modeled with a single Timoshenko beam finite element, shown in Figure 2.9a. The material parameters of the Timoshenko beam finite element are: Young's modulus $E = 10^5$ kPa, the yield limit $\sigma_y = 10$ kPa, the linear hardening modulus $H_{lh} = 10^3$ kPa, the linear hardening modulus $H_{lk} = 10^3$ kPa, the nonlinear hardening parameter $H_{nlk} = 10^2$, and the viscosity parameter $\eta = 10^3$ kPa s.

We subject the beam to the increasing triangular pulse load program (Figure 2.9b), with the aim to investigate the influence of different types of hardening phenomena on the final response. From the results shown in Figure 2.10, we can see that the proposed viscoplastic Timoshenko beam finite element with nonlinear kinematic hardening is able to capture the Bauschinger effect, ratcheting behavior of the material, and also the rate-dependency of the response.

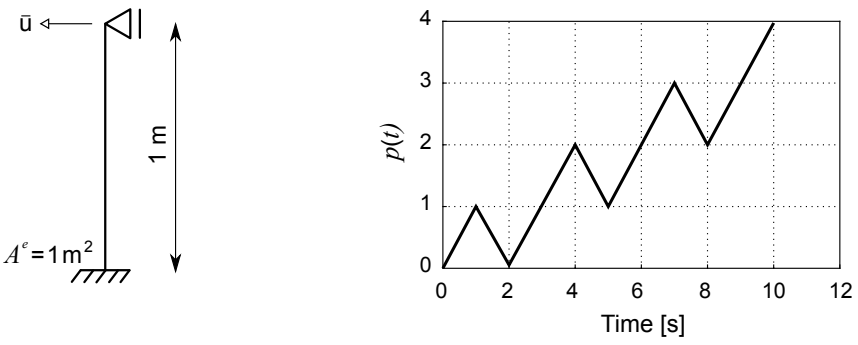

(a) Problem statement (b) Triangular pulse loading program

Figure 2.9 Nonlinear cantilever beam

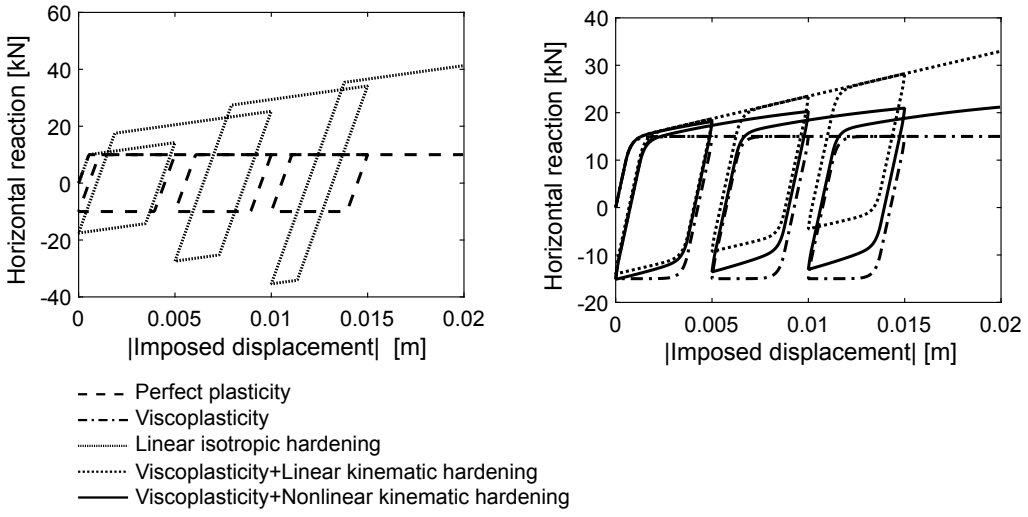

Figure 2.10 Nonlinear cantilever beam: computed results

Next, we subject a single column filled-in by Voronoi cells to the hysteresis loading program. We qualitatively investigate the influence of the chosen ratio between the yield stress in compression and tension for a Timoshenko beam finite element on the final shape of the computed hysteresis curve. The geometry of the column and boundary conditions are shown in Figure 2.11a. The finite element mesh and Voronoi diagram are shown in Figures 2.11b-2.11c.

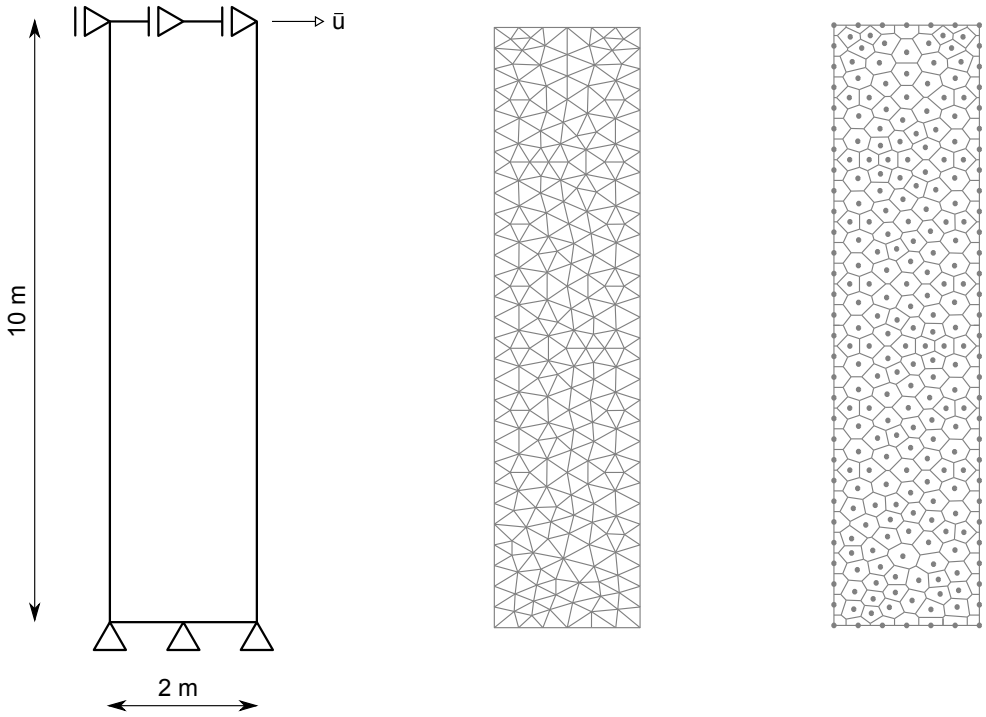

(a) Problem statement (b) Finite element mesh (c) Voronoi diagram

Figure 2.11 Nonlinear column

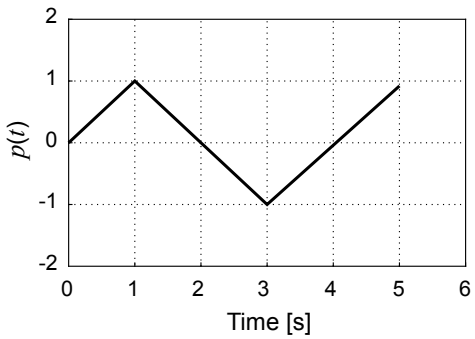

Figure 2.12 Hystersis loading program

The computation is performed by imposing horizontal displacements on the top base of the column, following the loading program shown in Figure 2.12. The material parameters of the Timoshenko beam finite element are: Young's modulus

$E = 10^4$ MPa, the yield limit $\sigma_y = 1$ MPa, the linear hardening modulus $H_{lh} = 10^3$ MPa, the linear kinematic hardening modulus $H_{lk} = 10^3$ MPa, the nonlinear hardening parameter $H_{nlk} = 10^2$, and the viscosity parameter $\eta = 10^3$ MPa s.

The computed force-displacement curve for the case when the ratio between yield stress values in compression and tension is equal to 1 is shown in Figure 2.13a. We can see that the computed hysteresis curve is of a similar shape as the one obtained in the cyclic loading experiments with materials such as steel. In Figure 2.13b, we can see that for the case when the same ratio is equal to 10, the shape of the computed hysteresis curve corresponds to the one observed in the experiments with materials such as concrete.

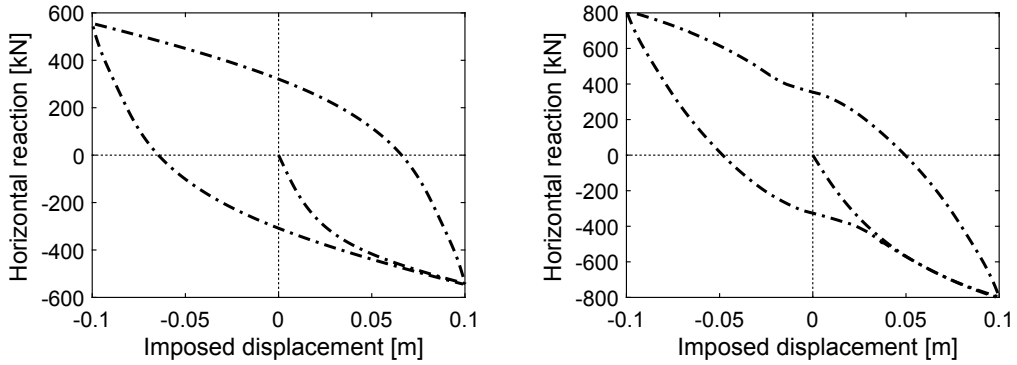

(a) $\sigma_{y,c}/\sigma_{y,t} = 1$ (b) $\sigma_{y,c}/\sigma_{y,t} = 10$

Figure 2.13 Nonlinear column: computed hysteresis loops

2.5.1.2 Hardening and softening response of discrete beam lattice model

The macro-scale response of structure built of cohesive heterogeneous material, such as rock or concrete, can be divided into three phases. The first phase is the linear elastic phase with no cracks occurring in the structure. The second phase represents the fracture process zone where cracks start to form and propagate, resulting in a loss of stiffness, but the load carrying capacity of the structure still increases. In the third phase, cracks coalescence results in an ultimate failure mode. Namely, after reaching the ultimate load value, one large macro-crack is starting to form and propagate, leading to a complete failure of the structure.

The constitutive model chosen for the Timoshenko beam finite element in combination with the enhanced kinematics in terms of embedded strong discontinuities in the axial and transverse direction can indeed capture all three phases of the macro-scale response. With the aim of illustrating these phases, we perform a numerical simulation of uniaxial tension test on a rock specimen in the quasi-static

framework. We perform uniaxial tension test by imposing uniform vertical displacements on the top base of the specimen while keeping the bottom base fixed in the horizontal and vertical direction (Figure 2.14a). The global phase of computation under the quasi-static assumption is solved by using Newton's iterative method in combination with the line search algorithm [134] (see **Remark 4**).

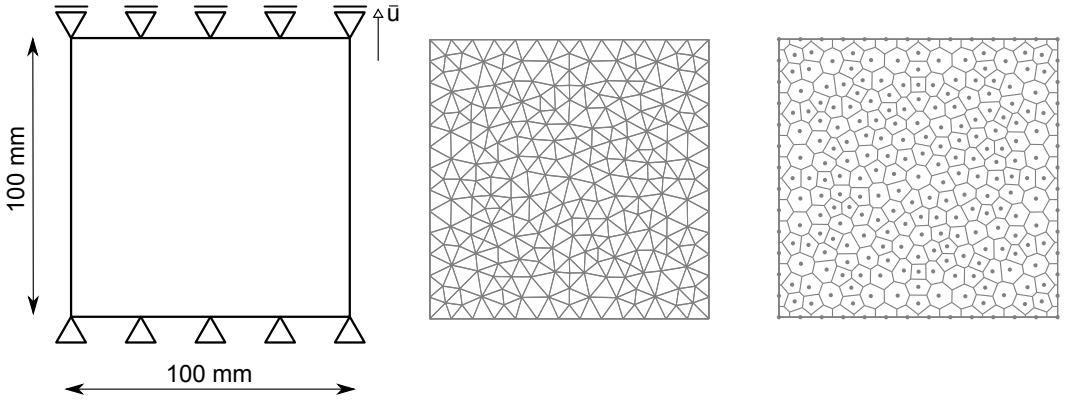

(a) Problem statement (b) Finite element mesh (c) Voronoi diagram

Figure 2.14 Uniaxial tension test

Table 2.2 Uniaxial tension test: material parameters of the finite element

Young's modulus [MPa]	Poisson's ratio [/]	Yield limit [MPa]	Hardening modulus [MPa]	Fracture limit [MPa]	Fracture energy [N/mm]
$E = 10000$	$\nu = 0.2$	$\sigma_{y,t} = 18$	$H_{lh,t} = 1000$	$\mu_{G,t} = 22$ $\sigma_{G,t} = 1$	$G_{f,t} = 15$
		$\sigma_{y,c} = 180$	$H_{lh,c} = 1000$	$\mu_{G,c} = 220$ $\sigma_{G,c} = 10$	$G_{f,c} = 300$
		$\sigma_{y,s} = 22$	$H_{lh,s} = 1000$	$\mu_{G,s} = 26$ $\sigma_{G,s} = 1$	$G_{f,s} = 150$

The geometry of the specimen and boundary conditions are shown in Figure 2.14a. The finite element mesh and Voronoi diagram are shown in Figures 2.14b and 2.14c. The material parameters of Timoshenko beam finite elements are shown in Table 2.2. To take into account material heterogeneities, the ultimate values of stresses are randomly assigned to every finite element using Gaussian random distribution defined with mean μ_G and standard deviation σ_G (with σ_G^2 as the variance). The probability density function (PDF) of Gaussian random distribution of Gaussian random variable X is written as (Figure 2.15)

$$f(x|\mu_G, \sigma_G) = \frac{1}{\sigma_G\sqrt{2\pi}} e^{-\frac{1}{2}\frac{(x-\mu_G)^2}{\sigma_G^2}} \tag{2.73}$$

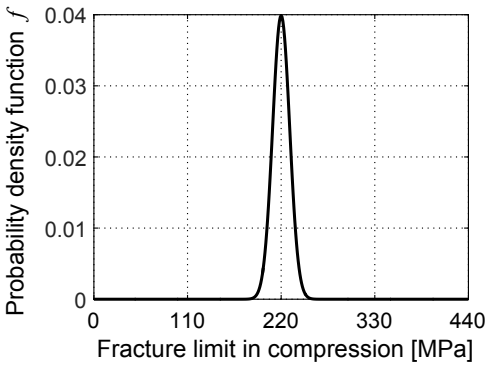

Figure 2.15 PDF of Gaussian random distribution of fracture limit in compression

The three phases of response are indicated in the computed force-displacement diagram, shown in Figure 2.16. With the aim of comparing results with experimental observations, we note that that the failure in a cohesive link can be interpreted as a formation of a crack on a macro-scale level. The first phase of the computed macro-scale response is a linear elastic phase, where none of the cohesive links have entered the softening phase of the response. In other words, this can be identified as that no cracks have formed on the macro-scale level (Figure 2.17a). In the second phase, cohesive links start to enter the softening phase of the response in mode I and/or mode II. Observed from the macro-scale, this can be interpreted as the formation of the fracture process zone (Figure 2.17b, broken cohesive links marked red). In the third phase, the coalescence of broken cohesive links in increasing softening (beam elements with increasing values of displacement jumps) results with an ultimate failure mode, which leads to the complete failure of the specimen. The computed ultimate failure mode coincides with the one commonly observed in experimental uniaxial tension test, where one large macro-crack splits the specimen into two parts (Figure 2.17c). Note that in Figures 2.17b and 2.17c results for mode I of cohesive link failure are shown.

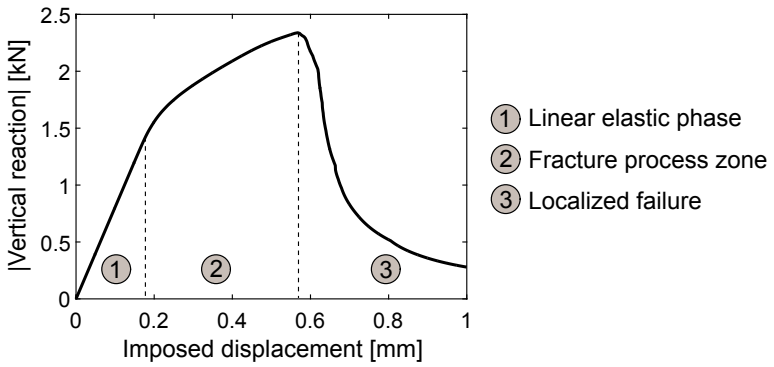

Figure 2.16 Uniaxial tension test: computed results

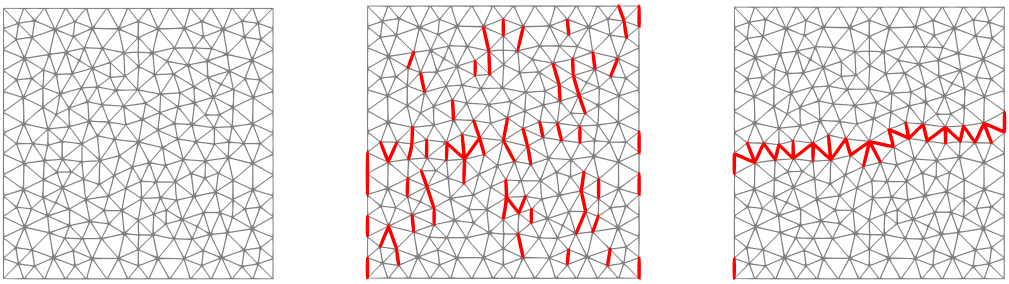

(a) Linear elastic phase (b) Fracture process zone (c) Localized failure

Figure 2.17 Uniaxial tension test: three phases of the macro-scale response

The next several figures illustrate the ultimate failure mode in a uniaxial tension test, captured at the end of the loading program. The computed vertical displacements and the broken cohesive links in increasing softening at the end of the loading program are shown in Figures 2.18a-2.18c. The values of displacement jumps in broken cohesive links are shown in Figures 2.18d and 2.18e.

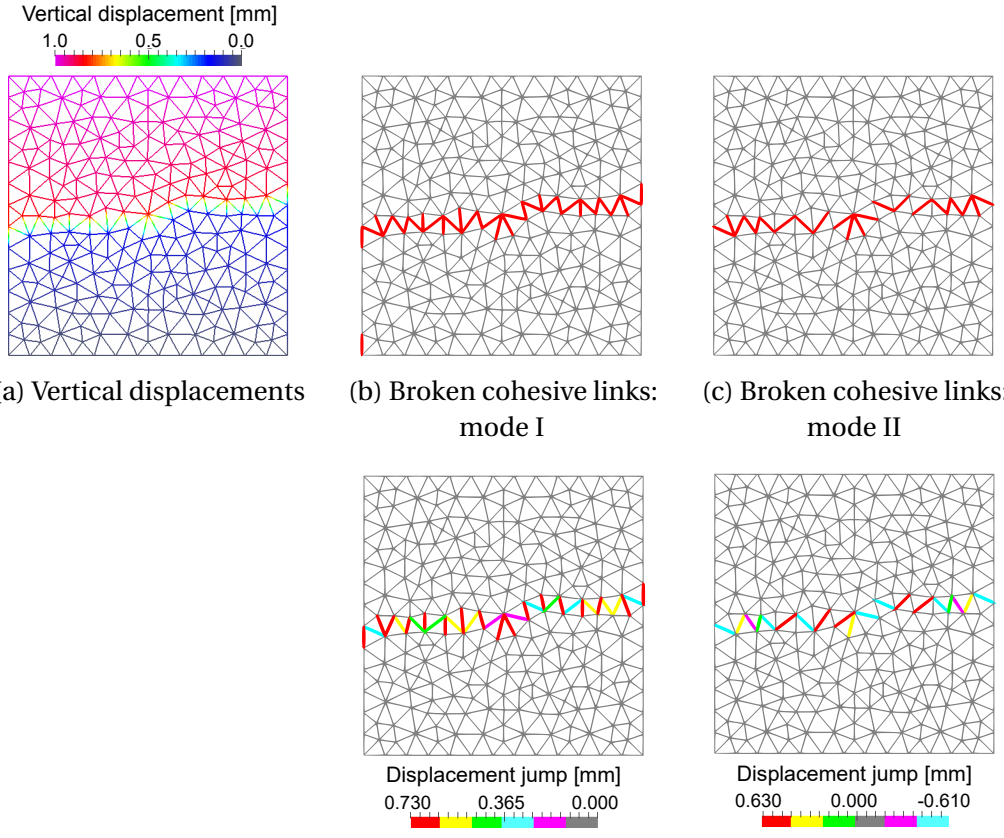

(a) Vertical displacements (b) Broken cohesive links: mode I (c) Broken cohesive links: mode II

(d) Displacement jumps: mode I (e) Displacement jumps: mode II

Figure 2.18 Failure mode for uniaxial tension test

2.5.2 Validation examples

In this section, we aim to validate the coupled discrete beam lattice model of structure built of a saturated porous medium. For the quasi-static case, we compare our results against those computed with a continuum model using commercial software PLAXIS [135]. In PLAXIS, the coupling between the solid phase and the pore fluid is governed by Biot's porous media theory, and the equal order of interpolation for both the displacement and pressure fields is available. For such comparison, we choose 15-node triangular elements with fourth-order polynomial interpolations. For the dynamic case, we compare the computed results against the reference values provided in [136].

2.5.2.1 Quasi-static case

First, we observe a saturated poro-elastic column, and we perform a numerical simulation of a one-dimensional plane strain consolidation test. The stress state in this example can be regarded as homogeneous. Second, we observe a saturated soil subjected to footing load, which results in a heterogeneous stress state. In both examples, the corresponding linear elastic parameters of the continuum model are identified by exploiting the property that the discrete beam lattice model based on Voronoi cell representation of the domain can reproduce the linear elastic response of an equivalent continuum model.

→ Saturated poro-elastic column

The geometry and the boundary conditions of the saturated poro-elastic column are shown in Figure 2.19a. The linear elastic parameters of the Timoshenko beam finite element are: Young's modulus $E = 40$ MPa and Poisson's ratio $\nu = 0$. Because we observe a problem of one-dimensional consolidation, Poisson's ratio in a continuum model is taken as $\nu = 0$. The identified corresponding oedometer modulus of a continuum model is $E_{oed} = 33.91$ MPa (which is equal to Young's modulus E since $\nu = 0$). The coefficient of permeability is $k = 10^{-2}$ m/s, the specific weight of the water is $\gamma_w = 10$ kN/m^3, Biot's constant is $b = 1$ and Biot's modulus is $M = 1.7$ GPa, for both discrete and continuum model.

With the aim of inspecting the possible mesh dependency of the results, we perform a computation with a discrete model for two different mesh densities: coarse with 336 Timoshenko beam finite elements (Figure 2.19b), and fine with 1281 Timoshenko beam finite elements (Figure 2.19c). The loading program is shown in Figure 2.20. The time step is set to $\Delta t = 0.01$ s. The computation in a continuum model is performed on a mesh of 1190 triangular elements.

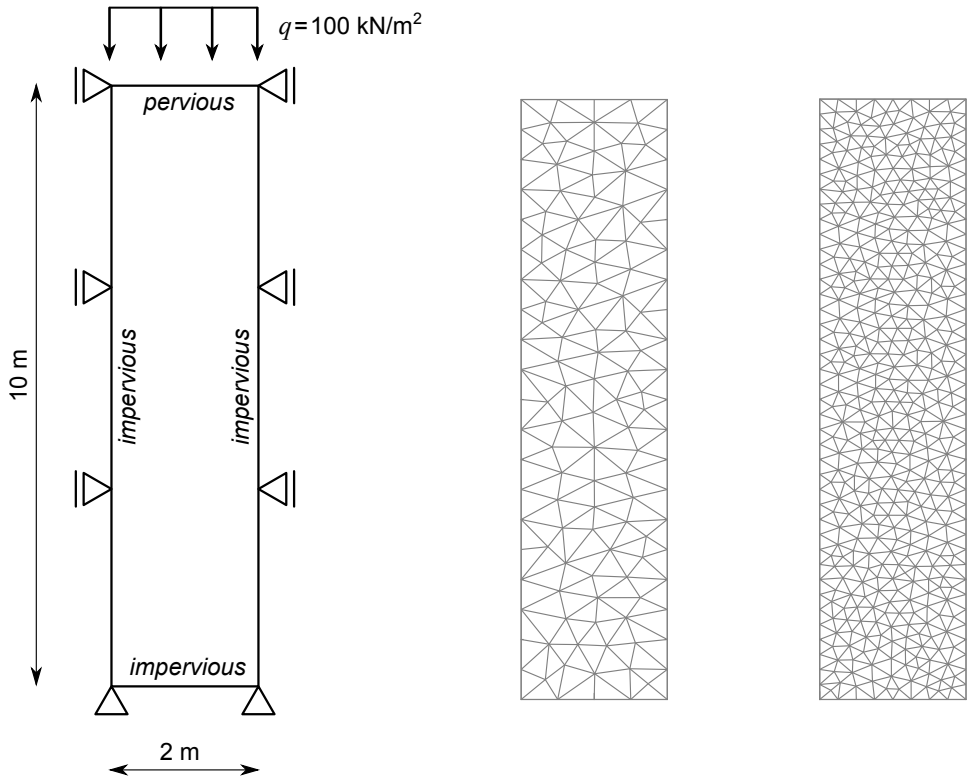

(a) Problem statement (b) Coarse mesh (c) Fine mesh

Figure 2.19 Saturated poro-elastic column

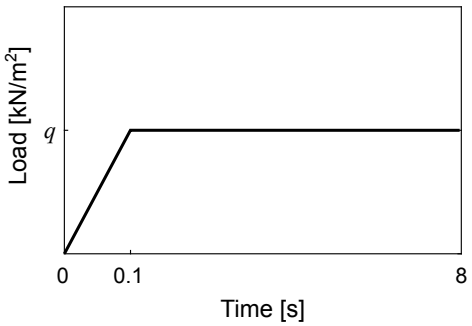

Figure 2.20 Saturated poro-elastic column: loading program

The computed time evolutions of vertical displacement of the column top and the excess pore pressure at the bottom of the column are shown in Figures 2.21a and 2.21b. We can conclude that the results obtained with the discrete model show an excellent agreement with the results obtained with a continuum model. The computed results are practically mesh independent. What is important to emphasize is that the coefficient of permeability of a coupled discrete beam lattice model matches that of an equivalent continuum model. Hence, it can be easily identified from standard experimental tests.

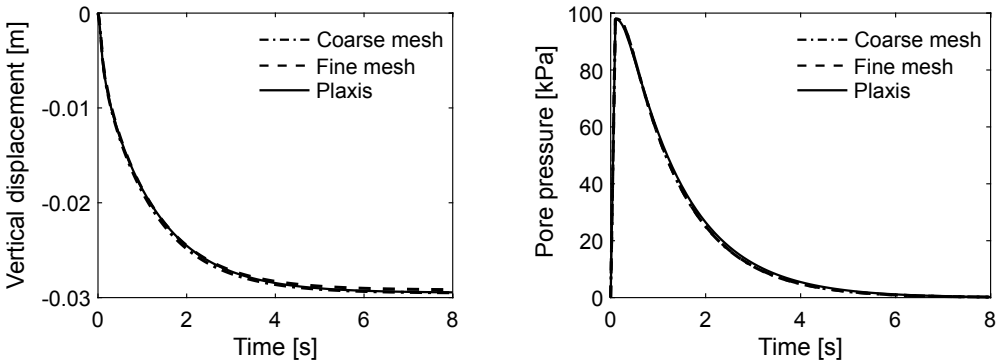

(a) Vertical displacement of column top

(b) Excess pore pressure at column bottom

Figure 2.21 Saturated poro-elastic column: computed results

The consolidation represents the time change in the volume of the sample due to the change in effective stresses. After excess pore pressures drop to zero, there is no more change in effective stresses, and we can state that the consolidation process has ended. From Figure 2.21b, we can conclude that as the value of excess pore pressure approaches zero, the value of vertical displacement approaches constant value marking the end of the consolidation (Figure 2.21a). The distributions of vertical displacements and excess pore pressures at the end of the loading program are shown in Figures 2.22a and 2.22b.

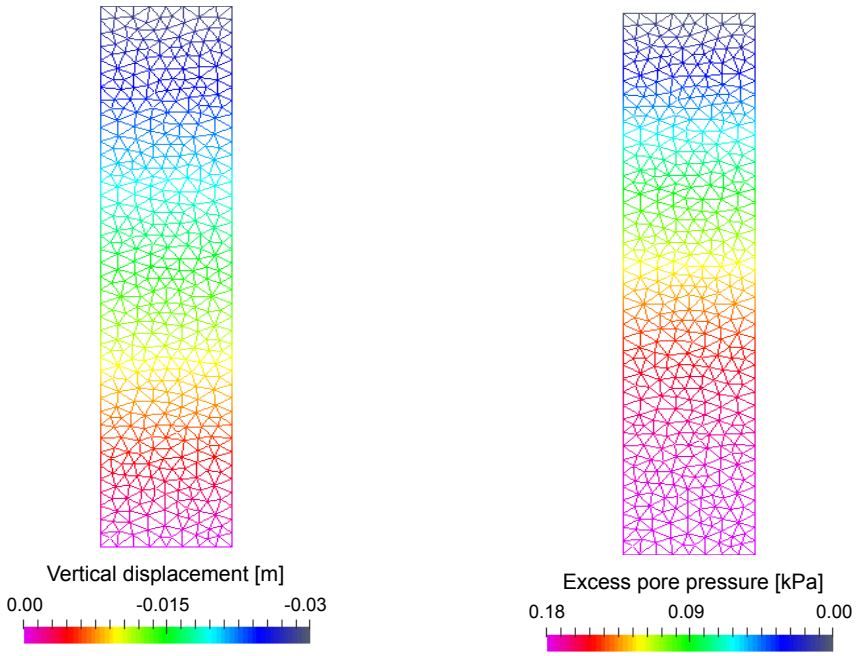

(a) Vertical displacements

(b) Excess pore pressures

Figure 2.22 Saturated poro-elastic column: computed results

We repeat the computation with a discrete model with the ramp loading reaching its maximum value at $t = 1$ s. The computed results are shown in Figures 2.23a and 2.23b. We compare computed results against those shown in Figures 2.21a and 2.21b. From Figure 2.23b, we can conclude that the maximum value of excess pore pressure is, as expected, greater in the case of higher loading rate. This observation is in accordance with Terzaghi's principle of effective stresses. In the case of undrained conditions, where water is not allowed to drain, the total applied force will be carried by the water in the pores because the water is assumed to be much stiffer than the porous skeleton. If the water is allowed to drain, then the part of the force will be carried by the solid phase and part by the water in the pores. In the case of a higher loading rate, the water has less time to drain; hence, the maximum value of excess pore pressure is greater than in the case of lower loading rate.

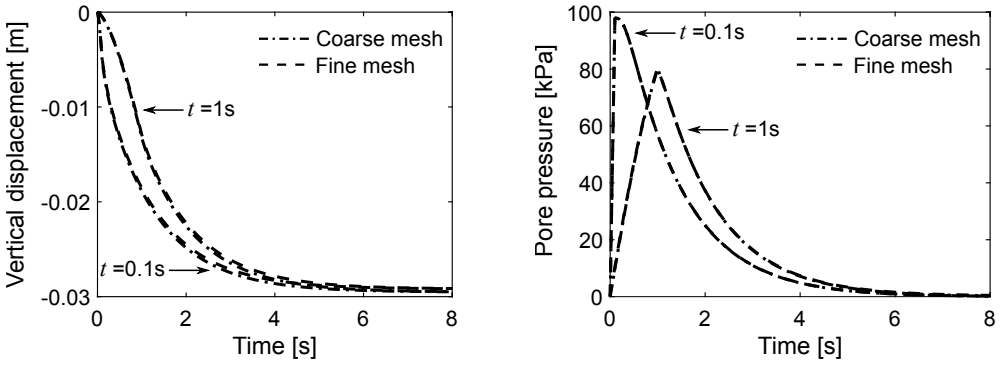

(a) Vertical displacement of column top

(b) Excess pore pressure at column bottom

Figure 2.23 Comparison of loading rates

→ Footing on soil stratum

The geometry and the boundary conditions of the observed problem, and the loading program are shown in Figures 2.24a and 2.24b. The linear elastic parameters of the Timoshenko beam finite element are: Young's modulus $E = 40$ MPa, and Poisson's ratio $\nu = 0$. The identified oedometer modulus of a continuum model is $E_{oed} = 33.91$ MPa, and Poisson's ratio $\nu = 0.188$. The coefficient of permeability is $k = 10^{-3}$ m/day, the specific weight of the water is $\gamma_w = 10$ kN/m^3, Biot's constant is $b = 1$ and Biot's modulus is $M = 1.3$ GPa, for both discrete and continuum model.

As in the previous example, we perform the computation for two different mesh densities: coarse with 401 Timoshenko beam finite elements (Figure 2.25a) and fine with 1570 Timoshenko beam finite elements (Figure 2.25b). The time step is set to $\Delta t = 0.1$ day. The computation in a continuum model is performed for 1126 triangular elements.

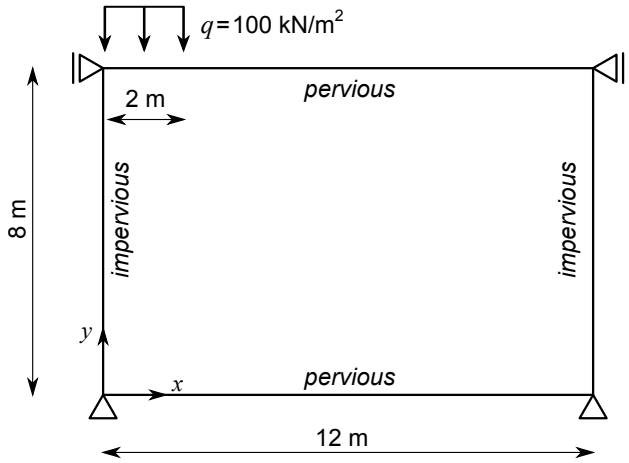

(a) Problem statement

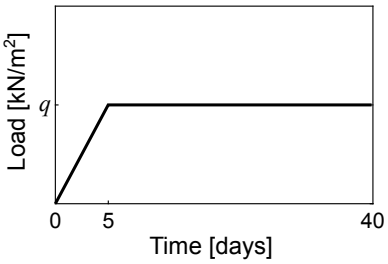

(b) Loading program

Figure 2.24 Footing on soil stratum

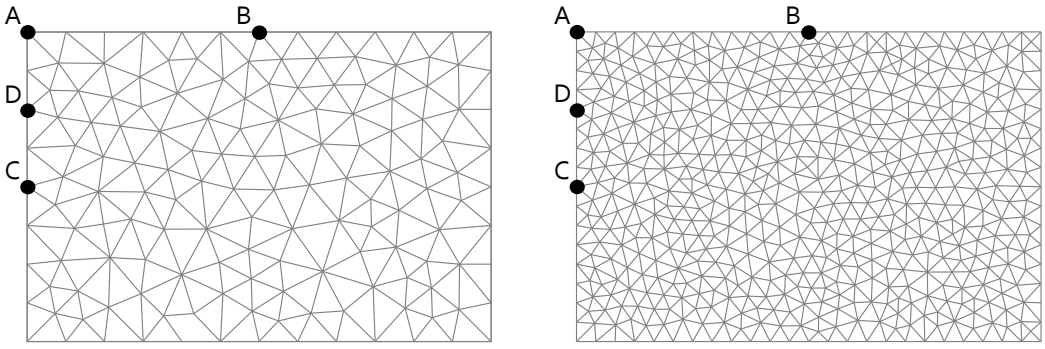

(a) Coarse mesh

(b) Fine mesh

Figure 2.25 Finite element mesh densities

The computed time evolution of vertical displacements at point A(0,8) and B(6,8), and excess pore pressures at points C(0,4) and D(0,6) are shown in Figures 2.26a, 2.27a and 2.28a. We can observe a good match between the results obtained with the discrete and continuum model, with the results being practically mesh independent.

Next, we introduce the nonlinearities in the discrete and continuum model in order to investigate the influence of the nonlinear behavior on the computed displacement and excess pore pressure fields. We perform the computation in the continuum model for a Mohr-Coulomb constitutive law, with strength parameters: cohesion $c = 15$ kPa, and angle of internal friction $\phi = 20°$. Contrary to the linear elastic parameters of discrete lattice model, other lattice parameters such as the yield and fracture limits have to be identified through more elaborate parameter identification procedures, such as the probability based ones [137–139]. Here, we follow a simpler approach. Namely, we identify the nonlinear parameters of the

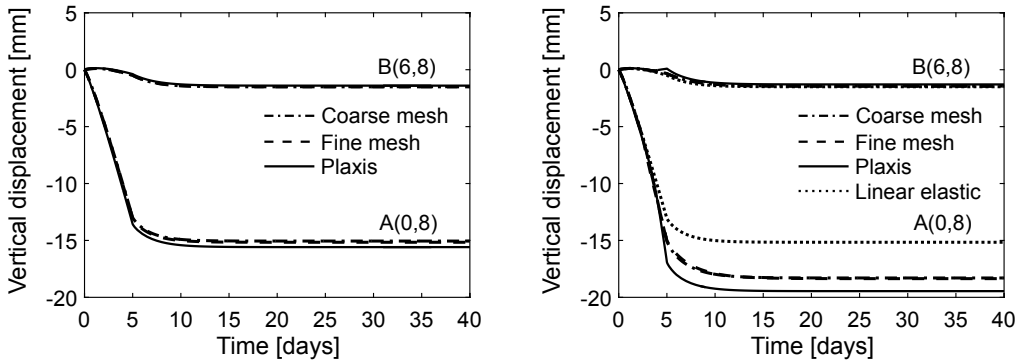

(a) Linear behavior (b) Nonlinear behavior

Figure 2.26 Computed vertical displacements

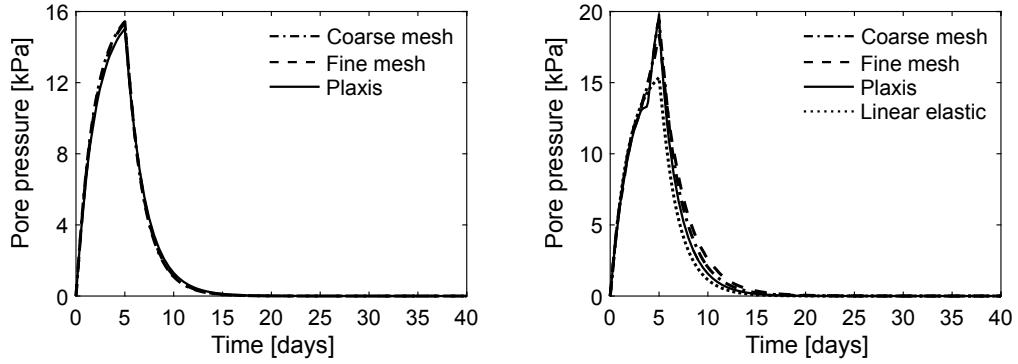

(a) Linear behavior (b) Nonlinear behavior

Figure 2.27 Computed excess pore pressure at point C(0,4)

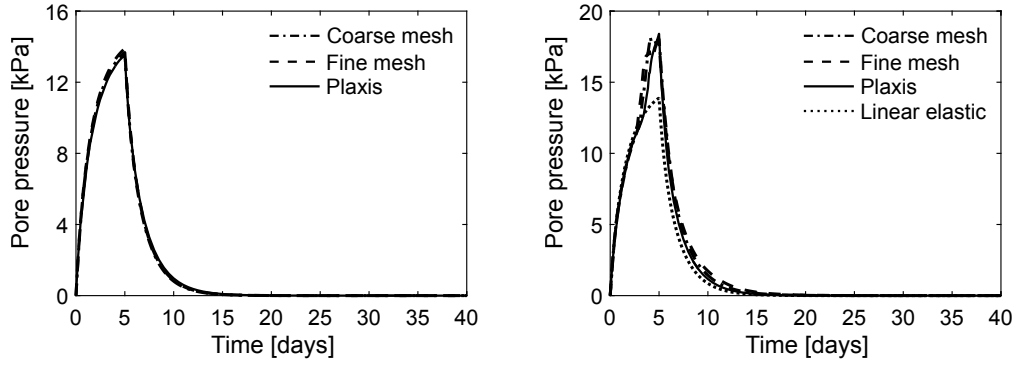

(a) Linear behavior (b) Nonlinear behavior

Figure 2.28 Computed excess pore pressure at point D(0,6)

Timoshenko beam finite elements by simply matching the curves (vertical reaction-vertical displacement at point A), computed with the discrete and continuum model for the case of dry material. The identified yield and fracture limits in tension, compression and shear are: $\sigma_{y,t} = 4.7$ kPa; $\sigma_{y,c} = 47$ kPa; $\sigma_{y,s} = 40$ kPa; $\sigma_{f,t} = 4.8$

kPa; $\sigma_{f,c} = 48$ kPa; $\sigma_{f,s} = 42$ kPa. The fracture energies in tension, compression and shear are: $G_{f,t} = 0.1$ MN/m; $G_{f,c} = 10$ MN/m; $G_{f,s} = 1$ MN/m. The identified linear hardening modulus is $H_{lh} = 1100$ kPa.

The computed time evolution of vertical displacements at points A and B, and excess pore pressures at points C and D are shown in Figures 2.26b, 2.27b and 2.28b. We observe a good match between the results computed with the discrete and continuum model, with the results being practically mesh independent. We can conclude that nonlinear behavior results in an increase in the values of computed vertical displacements and excess pore pressures, as previously observed in [5, 140]. The excess pore pressure fields at $t = 5$ days computed with the continuum and discrete model are shown in Figures 2.29a-2.29c.

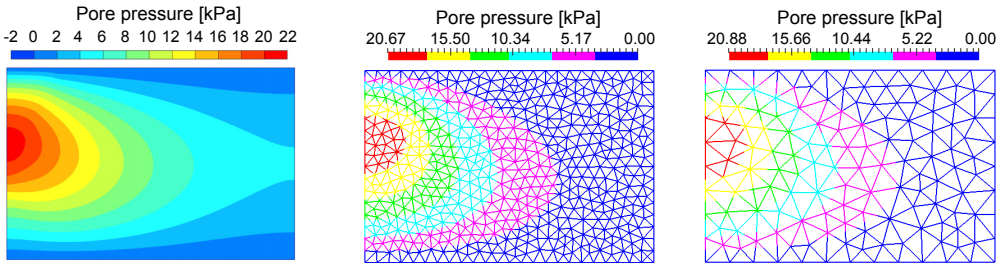

(a) Continuum model

(b) Discrete model: fine mesh

(c) Discrete model: coarse mesh

Figure 2.29 Nonlinear behavior, computed excess pore pressure field

2.5.2.2 Dynamic case

In this example, we perform a validation computation of the proposed discrete model of a saturated porous medium in a dynamic setting, where we compare the computed results against the reference values provided in [136]. We observe a saturated poro-elastic column (Figure 2.30a) subjected to step and sinusoidal loading (Figures 2.31a and 2.31b), defined with following expressions

$$F = 3\ [\text{kN/m}^2]$$

$$F = 3[1 - \cos(\omega t)]\ [\text{kN/m}^2];\ \omega = 75\ s^{-1}$$

The computation in a continuum model is performed for Lame's parameters $\lambda_L = 5.5833$ MPa, and $\mu_L = 8.3750$ MPa, which correspond to Young's modulus $E = 20.1$ MPa, and Poisson's ratio $\nu = 0.2$. By exploiting the property that discrete lattice model based on Voronoi cell representation of domain with irregular lattice geometry can reproduce the linear elastic response of an equivalent continuum

model, we identify the corresponding Timoshenko beam linear elastic parameters to be: Young's modulus $E = 23.71$ MPa, and Poisson's ratio $\nu = 0$. The specific weight of water is $\gamma_w = 10$ kN/m^3, the mass density of mixture is $\rho = 1670$ kg/m^3, the coefficient of permeability is $k = 10^{-2}$ m/s, Biot's constant is $b = 1$ and Biot's modulus is $1/M \to 0$, for both continuum and discrete model. The time step is set to $\Delta t = 0.001$ s.

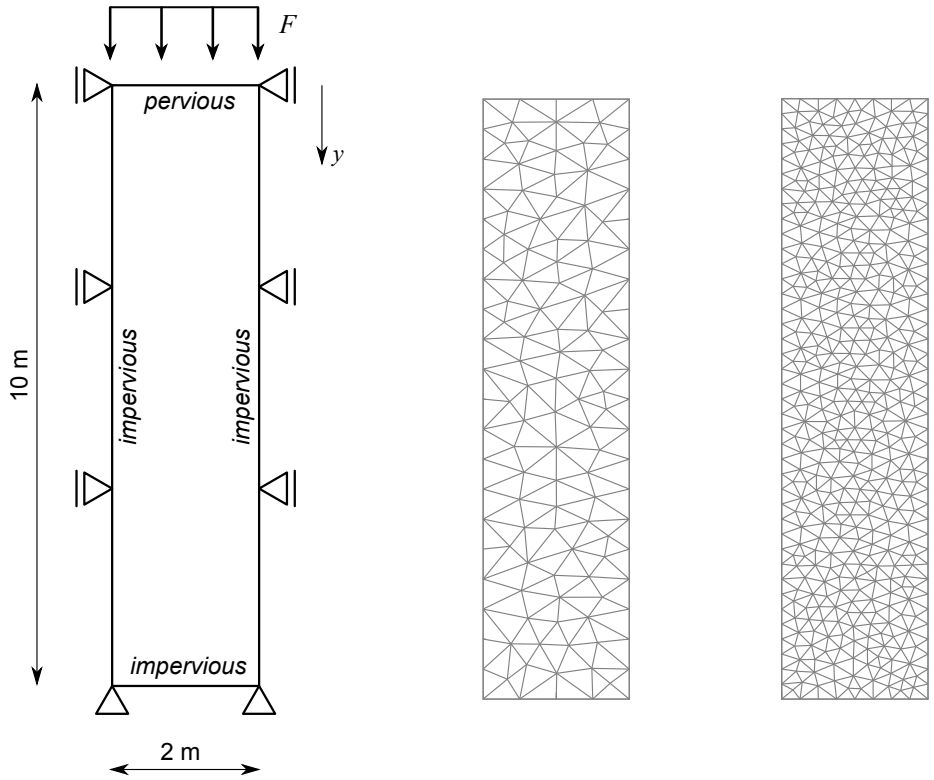

(a) Problem statement (b) Coarse mesh (c) Fine mesh

Figure 2.30 Saturated poro-elastic column, dynamic case

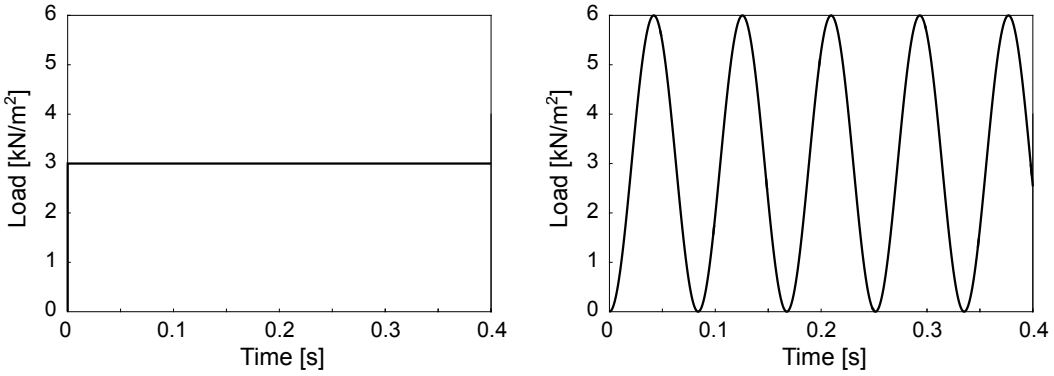

(a) Step loading program (b) Sinusoidal loading program

Figure 2.31 Saturated poro-elastic column, dynamic case: loading programs

With the aim of inspecting the possible mesh dependency of the results, we perform a computation with a discrete model for two mesh densities: coarse with 336 Timoshenko beam finite elements (Figure 2.30b), and fine with 1281 Timoshenko beam finite elements (Figure 2.30c).

The computed results in terms of the time evolution of vertical displacement of the column top, and excess pore pressures are shown in Figures 2.32a-2.32c. We can conclude that a good match between the computed results and reference values is obtained, with the results being practically mesh independent.

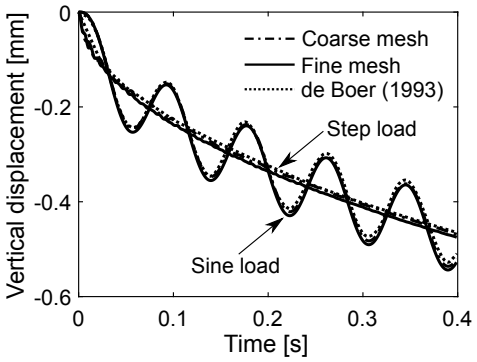

(a) Vertical displacement of column top

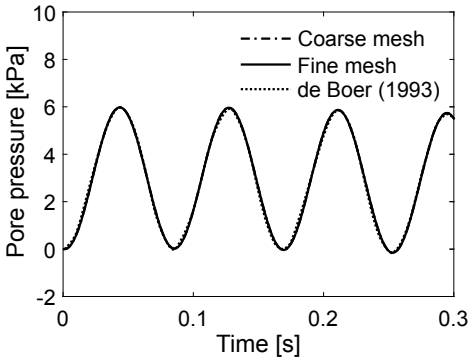

(b) Excess pore pressure at $y = 6$ m

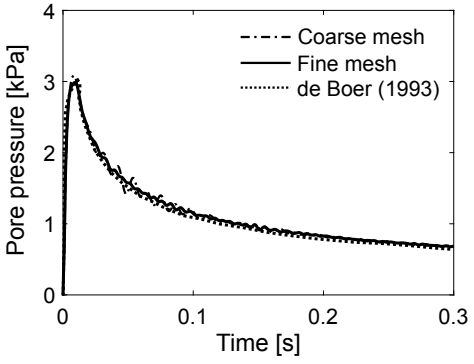

(c) Excess pore pressure at $y = 1$ m

Figure 2.32 Saturated poro-elastic column, dynamic case: computed results

2.5.3 Plane strain compression test

With the aim to investigate the influence of coupling effects on the failure mechanisms in a saturated porous medium, we simulate a plane strain compression test on a water-saturated specimen. The geometry of the specimen and boundary conditions are shown in Figure 2.33a. The finite element mesh and Voronoi discretization are shown in Figures 2.33b and 2.33c.

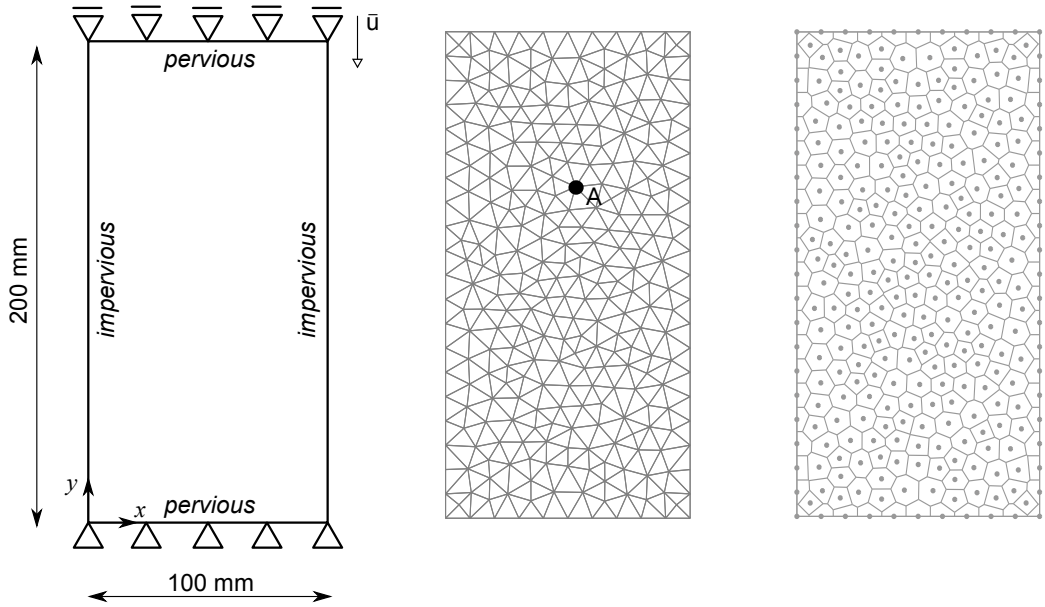

(a) Problem statement (b) Finite element mesh (c) Voronoi diagram

Figure 2.33 Plane strain compression test

Table 2.3 Compression test: material parameters of the finite element

Young's modulus [kPa]	Poisson's ratio [/]	Yield limit [kPa]	Hardening modulus [kPa]	Fracture limit [kPa]	Fracture energy [kN/m]
$E = 20000$	$\nu = 0.2$	$\sigma_{y,t} = 10$	$H_{lh,t} = 2000$	$\mu_{G,t} = 12$ $\sigma_{G,t} = 1$	$G_{f,t} = 20$
		$\sigma_{y,c} = 100$	$H_{lh,c} = 2000$	$\mu_{G,c} = 120$ $\sigma_{G,c} = 10$	$G_{f,c} = 100$
		$\sigma_{y,s} = 12$	$H_{lh,s} = 2000$	$\mu_{G,s} = 15$ $\sigma_{G,s} = 1$	$G_{f,s} = 100$

The material parameters of the Timoshenko beam finite element are shown in Table 2.3. The ultimate values of stresses are randomly assigned to every finite element using Gaussian random distribution. The ultimate shear stress for each Timoshenko beam finite element is defined with Mohr-Coulomb law, written as

$$\sigma^*_{f,s} = \begin{cases} \sigma_{f,s} + |\sigma'| \cdot \tan\phi, & \sigma' < 0 \\ \sigma_{f,s}, & \sigma' \geq 0 \end{cases} \tag{2.74}$$

where $\sigma_{f,s}$ is the ultimate shear stress independent of the normal effective stress (i.e. cohesion, c), ϕ is the angle of internal friction of material and σ' is the effective normal stress in the element, assumed negative in compression.

The angle of internal friction is selected as $\phi = 11°$. The coefficient of permeability is $k = 10^{-7}$ m/s, the specific weight of the water is $\gamma_w = 10$ kN/m^3, Biot's constant is $b = 1$ and Biot's modulus is $1/M \to 0$.

Our goal is to capture the post-peak response and the failure mechanisms in a water-saturated specimen. For this reason, the test is performed with vertical displacements imposed on the top base of the specimen with a constant rate. We assume that the inertial effects are negligible. To investigate the coupling effects, vertical displacements are imposed with two different rates: $v = 1 \cdot 10^{-6}$ m/s and $v = 8 \cdot 10^{-6}$ m/s. The time step is set to $\Delta t = 1$ s.

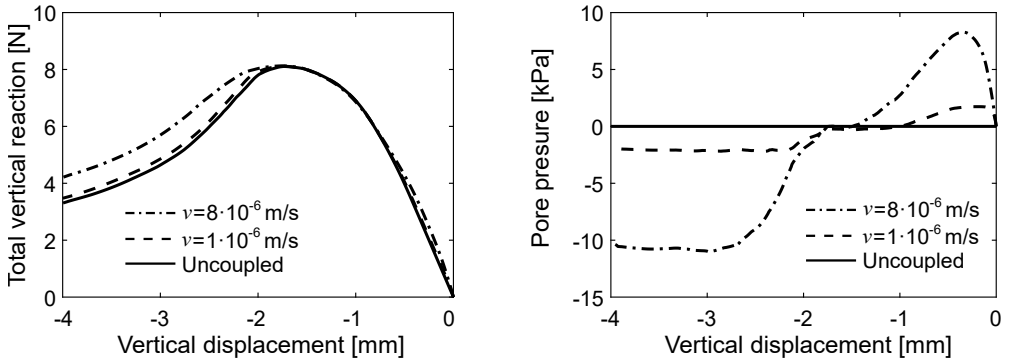

(a) Total vertical reaction (b) Excess pore pressure at point A

Figure 2.34 Computed results, different displacement rates

We monitor the time evolution of the excess pore pressures at point A(53.16, 136.21)[m]. The macro-scale responses of the specimen upon reaching the ultimate load value for different displacement rates do not differ significantly despite different values of generated excess pore pressures (Figure 2.34a). As in the accordance with Equation 2.20, the higher displacement rate leads to a greater increase in the values of excess pore pressures than in the case of the lower displacement rate (Figure 2.34b). After initial contraction, the specimen begins to exhibit dilative behavior. The dilative behavior leads to the decrease in the value of excess pore pressures and the evolution of the negative excess pore pressures (Figures 2.35a and 2.35b). Significant coupling effects are observed in the post-peak part of the response, where the higher displacement rate results in a greater value of total vertical reaction. After the ultimate load level is reached, the stiffness of the specimen decreases and one large macro-crack is starting to form, leading to the complete failure of the specimen. The distribution of vertical displacements and the broken cohesive links in increasing softening at the end of the loading program for $k = 1 \cdot 10^{-7}$ m/s, $v = 1 \cdot 10^{-6}$ m/s are shown in Figures 2.36a-2.36c.

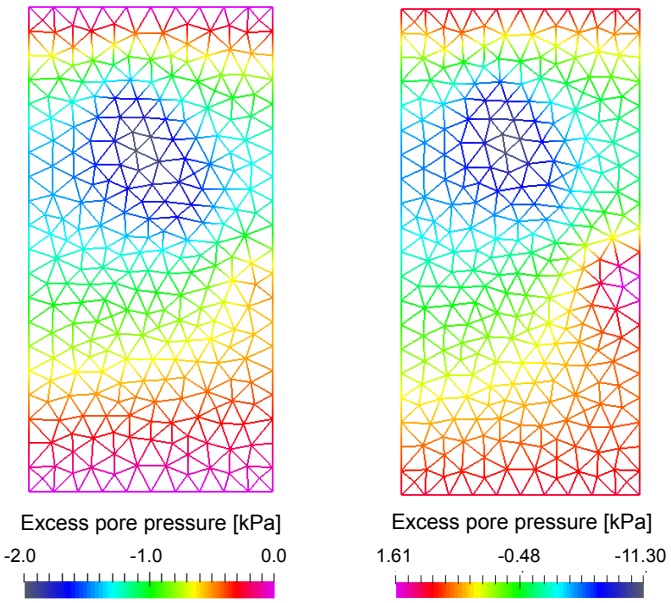

(a) $v = 1 \cdot 10^{-6}$ m/s (b) $v = 8 \cdot 10^{-6}$ m/s

Figure 2.35 Excess pore pressure at the end of the loading program

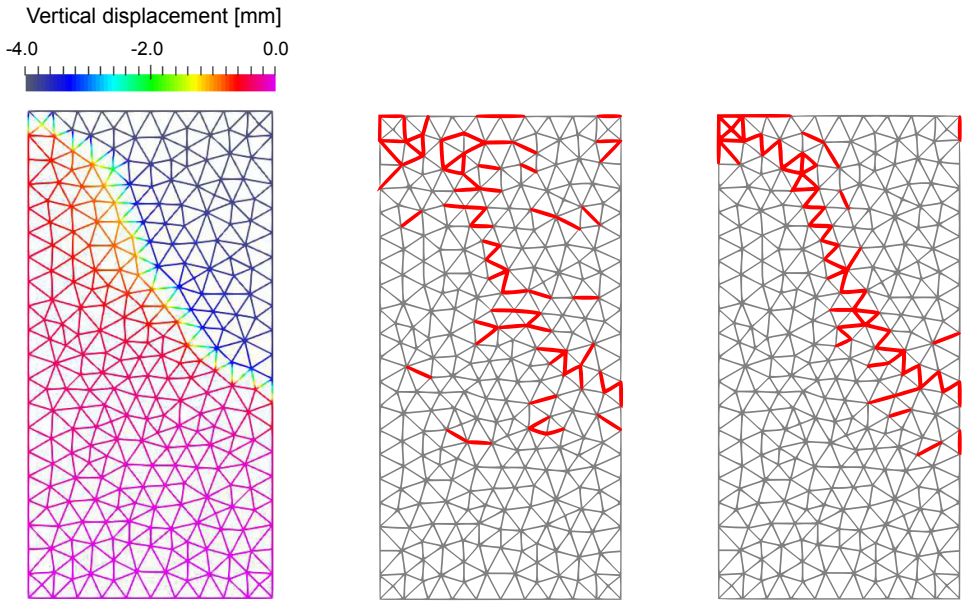

(a) Vertical displacement (b) Broken cohesive links: mode I (c) Broken cohesive links: mode II

Figure 2.36 Failure mode for plane strain compression test

We also preform the computation for $v = 1 \cdot 10^{-6}$ m/s for two different values of coefficient of permeability: $k = 1 \cdot 10^{-7}$ m/s and $k = 1 \cdot 10^{-8}$ m/s. The computed results are shown in Figures 2.37a and 2.37b. As in accordance with Equation 2.20,

the lower value of the coefficient of permeability leads to a greater increase in the values of excess pore pressures.

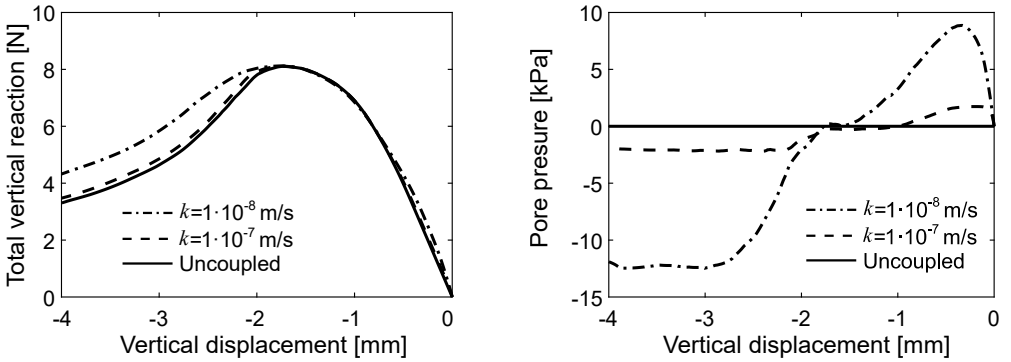

(a) Total vertical reaction (b) Excess pore pressure at point A

Figure 2.37 Computed results, different permeabilities

2.5.4 Coupled soil-foundation system

In this numerical example, we simulate the response of water-saturated soil under the rigid footing. The geometry and boundary conditions are shown in Figure 2.38a. The finite element mesh and Voronoi discretization are shown in Figures 2.38b and 2.38c.

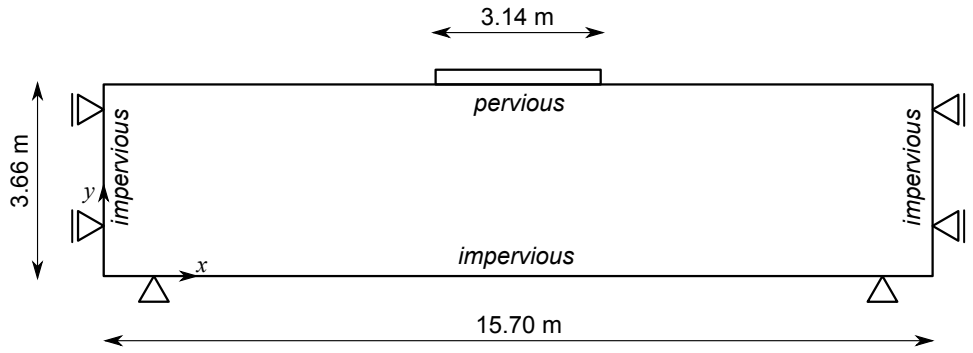

(a) Problem statement

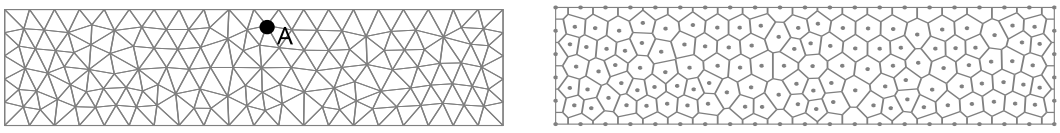

(b) Finite element mesh (c) Voronoi diagram

Figure 2.38 Coupled soil-foundation system

The material parameters of the Timoshenko beam finite element are shown in Table 2.4. The ultimate shear stress for each Timoshenko beam finite element is

defined with Mohr-Coulomb law (Equation 2.74). The internal angle of friction is selected as $\phi = 17°$. The coefficient of permeability is $k = 10^{-6}$ m/s, the specific weight of the water is $\gamma_w = 10$ kN/m^3, Biot's constant is $b = 1$ and Biot's modulus is $1/M \to 0$.

Table 2.4 Coupled soil-foundation system: material parameters of the finite element

Young's modulus [MPa]	Poisson's ratio [/]	Yield limit [MPa]	Hardening modulus [MPa]	Fracture limit [MPa]	Fracture energy [GN/m]
$E = 160$	$\nu = 0.3$	$\sigma_{y,t} = 0.03$ $\sigma_{y,c} = 0.30$ $\sigma_{y,s} = 0.07$	$H_{lh,t} = 60$ $H_{lh,c} = 60$ $H_{lh,s} = 60$	$\sigma_{f,t} = 0.09$ $\sigma_{f,c} = 0.90$ $\sigma_{f,s} = 0.13$	$G_{f,t} = 0.6$ $G_{f,c} = 60$ $G_{f,s} = 30$

We simulate the response of the rigid footing by imposing uniform vertical displacements with a constant rate along the length of the footing. We assume that the inertial effects are negligible. To investigate the coupling effects, we perform the computation for two different displacements rates: $v = 2 \cdot 10^{-5}$ m/s and $v = 5 \cdot 10^{-5}$ m/s. The time step is set to $\Delta t = 1$ s.

The computed results are shown in Figures 2.39a and 2.39b. We can conclude that the macro-scale response prior to reaching the ultimate load value is significantly influenced by the coupling effects (Figure 2.39a). The material under the footing exhibits contractive behavior, as shown in the computed excess pore pressures at point A(8.26,3.15)[m] (Figure 2.39b). Higher displacement rate causes the generation of higher values of excess pore pressures, which leads to an increase in the value of total vertical reaction (see Equation 2.2). However, for a higher rate, the softening part of the response begins at the smaller value of vertical displacement. In the post-peak part of the response, computed responses for different

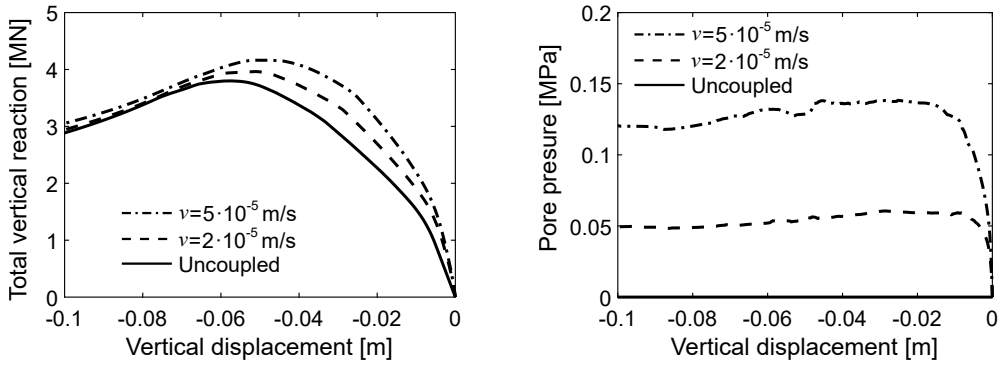

(a) Total vertical reaction

(b) Excess pore pressure at point A

Figure 2.39 Computed results, different displacement rates

displacement rates do not differ significantly from the uncoupled response. The failure mechanism formed under the footing, shown in Figure 2.40, coincides with the commonly observed shape of the failure wedge. The distributions of vertical displacements and excess pore pressures at the end of the loading program for $k = 1 \cdot 10^{-6}$ m/s, $v = 2 \cdot 10^{-5}$ m/s are shown in Figures 2.40c and 2.40d.

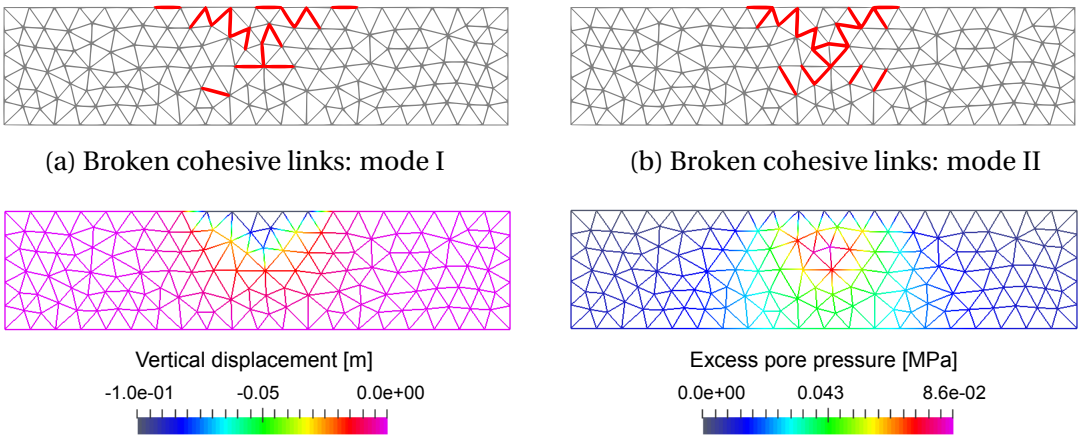

(a) Broken cohesive links: mode I

(b) Broken cohesive links: mode II

(c) Vertical displacements

(d) Excess pore pressures

Figure 2.40 Failure mode for coupled soil-foundation system

We repeat the computation for $v = 5 \cdot 10^{-5}$ m/s for two different values of coefficient of permeability: $k = 1 \cdot 10^{-5}$ m/s and $k = 1 \cdot 10^{-6}$ m/s. A higher coefficient of permeability means that the soil is more permeable and that water is able to drain faster. This leads to the generation of lower values of excess pore pressures (Figure 2.41b) and a decrease in the value of total reaction compared to the less permeable soil (Figure 2.41a), as in accordance with Equations 2.2 and 2.20.

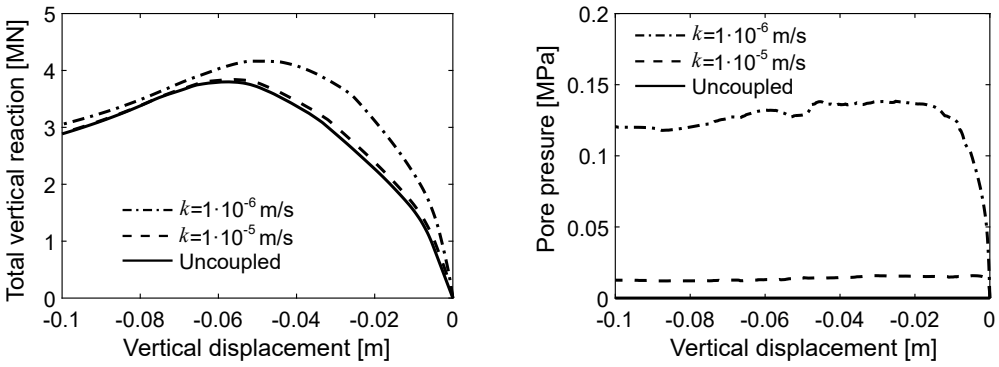

(a) Total vertical reaction

(b) Excess pore pressure at point A

Figure 2.41 Computed results, different permeabilities

2.6 Concluding remarks

In this Chapter, we used coupled discrete beam lattice model based on Voronoi cell representation of domain with cohesive links as inelastic Timoshenko beam finite elements with enhanced kinematics to simulate the response and localized failure in pore-saturated structures. The coupling between the solid phase and internal pore fluid is handled with Biot's porous media theory, and Darcy's law governing the pore fluid flow. The pore fluid flow is approximated with CST finite elements, which coincide with Delaunay triangles. The numerical implementation of internal fluid-structure interaction is simplified by exploiting Hammer quadrature rule for numerical integration on CST finite elements and duality between the Voronoi diagram and Delaunay triangle representations, which results in an additional, pressure-type degree of freedom placed at each node of Timoshenko beam finite element.

The advantage of discrete models is that the true failure modes are captured with 1D finite elements, which ensures relatively simple and efficient numerical implementation of the model. We have shown that by appropriate modeling the micro-scale, the coupled discrete beam lattice model is able to predict complete macro-scale response including both the pre-peak and the post-peak behavior and to capture true failure mechanisms in structures built of dry or pore-saturated materials subjected to extreme loads. Thus, we can obtain the ultimate load value in (much) more solvable manner, without any ambiguity between the (potential) lack of convergence and real peak resistance.

The linear elastic parameters of the model can be identified from standard experimental tests. The validation computations show that the coefficient of permeability of the coupled discrete beam lattice model closely matches that of an equivalent continuum model, thus can also be obtained directly as a result of standard experimental tests conducted on concrete, rock or soil specimens. Other parameters of the Timoshenko beam finite element have to be identified through more elaborate parameter identification procedures such as the probability based ones, where material heterogeneities can also play a role.

The proposed coupled discrete beam lattice model shows an efficient performance in terms of fast convergence rates and efficient computational time. In Table 2.5), we give the residual and energy convergence rates for a typical time step in the post-peak part of the response of the soil subjected to footing load. The computational time depends on the density of the mesh, the loading program, the loading rate, and the selected time step. For the case of coupled soil-foundation system ($k = 1 \cdot 10^{-6}$ m/s), the computational time for loading rate $v = 5 \cdot 10^{-5}$ m/s

is 236.15s, and for loading rate $v = 2 \cdot 10^{-5}$ m/s is 556.34s (Processor: Intel Core i7-3632QM/2.2GHz, RAM 8.00GB, FEAP: single-core).

Table 2.5 Coupled soil foundation-system ($k = 1 \cdot 10^{-6}$ m/s, $v = 5 \cdot 10^{-5}$ m/s), convergence rates for time step: 4000

Iteration	Residual norm	Energy norm
1	$6.7516 \cdot 10^{-03}$	$4.9926 \cdot 10^{-07}$
2	$3.9441 \cdot 10^{-03}$	$1.6061 \cdot 10^{-07}$
3	$6.3604 \cdot 10^{-04}$	$4.0685 \cdot 10^{-09}$
4	$4.0008 \cdot 10^{-05}$	$9.1335 \cdot 10^{-11}$
5	$4.3019 \cdot 10^{-06}$	$1.0264 \cdot 10^{-13}$
6	$2.8904 \cdot 10^{-11}$	$3.5076 \cdot 10^{-23}$

CHAPTER 3

ACOUSTIC FLUID-STRUCTURE INTERACTION

ABSTRACT

In this Chapter, we propose a novel approach for dealing with acoustic fluid-structure interaction nonlinear problems, such as progressive localized failure of a dam structure built of porous cohesive material in interaction with reservoir under extreme static and/or dynamic loads. The main original aspects of the proposed approach concern ability to deal with the loss of structural integrity in fluid-structure interaction problems, as well as a seamless discretization between structure and external fluid achieved by using a judicious combination of a lattice model for the pore-saturated structure and finite element approximation for external fluid. Namely, the interaction of structure built of a poro-plastic medium is here restricted to acoustic fluids, which allows to use Lagrangian formulation for the small motion of the external fluid and mixed discrete approximation resulting with the same displacement pressure degrees of freedom and seamless approximation between structure and fluid. The latter is justified for the small motion of the external fluid confined in the reservoir and simplification of the acoustic wave theory for irrotational flows and quasi-incompressible fluids. The application of the model is illustrated through several numerical simulations.

OUTLINE

3.1 Introduction

In this Chapter, we propose a novel approach for numerical modeling of fluid-structure interaction nonlinear problems [141–143]. The main original aspects are the proposed approach capabilities to carry on with computations of the external fluid interacting with structure undergoing localized failure with cracks and to represent internal fluid (pore) pressure influence on ultimate failure modes with fully saturated cracks. Namely, we generalize the development of the coupled discrete beam lattice model described in Chapter 2, extending its ability to deal with fluid-structure interaction with the emphasis on the numerical representation of the structure response in terms of a saturated porous medium. We limit ourselves to fluid-structure problems under conditions that enable the modeling of the external fluid with the acoustic wave theory. Namely, the latter is justified for the small motion of the external fluid in confined conditions typically met for fluid placed in a reservoir. For the numerical representation of the external fluid motion, we choose a Lagrangian formulation and mixed displacement/pressure based finite element approximation. The coupled discrete model for the structure built of a saturated porous medium in combination with the mixed displacement/pressure based formulation for the external fluid allows for the structure and fluid finite elements to share both the displacement and pressure degrees of freedom at the fluid-structure interface. This permits for the elements to be connected directly at the common nodes without any special numerical treatment of the fluid-structure interface. As a result, the exchange of both the motion and the pressure at the fluid-structure interface is ensured, and all computations can be performed in a fully monolithic manner.

The main benefit of the proposed model is its ability to provide a better numerical representation of the structure in interaction with confined fluids. In previous attempts to model the fluid-structure interaction problems of this kind, the use of pressure degree of freedom at the fluid-structure interface led to a cumbersome exchange of information in terms of added mass. Here, the numerical model of the structure contains pore pressure as an additional degree of freedom per node, which enables direct exchange of the pressures at the fluid-structure interface. With such a numerical model of the structure, we are able to simulate the full saturation of the material of the structure at every time step, with the external fluid acting as the source of pore saturation. In addition, we are able to take into account the inelastic behavior, to predict the crack formation and propagation in saturated materials and quantify overall safety of pore-saturated structures subjected to the extreme loads.

The outline of the Chapter is as follows: In Section 3.2, we present equations governing the external fluid motion derived from acoustic wave theory under small motion hypothesis. We describe mixed displacement/pressure based finite element formulation, and we provide two different finite elements, for the quasi-static case and dynamic case. In Section 3.3, we present the results of several numerical simulations. We simulate acoustic fluid-structure interaction problems in a quasi-static and dynamic setting, respectively. First, we perform validation computations of the proposed external fluid model. Second, we investigate the proposed numerical model of acoustic fluid-structure interaction capabilities to predict hydrostatic and hydrodynamic pressure distributions on the upstream face of the structure, which are in close agreement with analytical solutions. Finally, we focus on the proposed numerical model ability to deal with the loss of structural integrity, ultimately providing the overall safety assessment of the dam structure to potential overload with respect to the fundamental load cases. In Section 3.4, we give concluding remarks.

3.2 External fluid model in mixed Lagrangian formulation

3.2.1 Assumptions and governing equations

We assume a small motion of inviscid, isentropic, and homogeneous fluid with constant density. The fluid motion starts from the rest, the fluid velocities remain small, and the fluid flow is considered to be irrotational as the conditions typically met for fluid placed in a reservoir. The governing momentum and continuity equations derived from acoustic wave theory are written as

$$\rho\dot{\mathbf{v}} + \nabla p = 0 \tag{3.1}$$

$$\nabla \cdot \mathbf{v} + \frac{\dot{p}}{\beta} = 0 \tag{3.2}$$

where $\mathbf{v}$ is the velocity vector, p is the pressure, ρ is the mass density, and β is the bulk modulus of external fluid.

For irrotational flows, the vorticity is constrained to zero

$$\nabla \times \mathbf{v} = 0 \tag{3.3}$$

3.2.2 Mixed displacement/pressure based formulation

Mixed displacement/pressure based finite element formulation for acoustic fluids is based on the analogy with the mixed formulations for nearly incompressible solids [41, 124, 144]. Here, we assume that the fluid motion starts from the rest with the fluid displacements remaining small. Moreover, we follow [69, 73] by assuming that the fluid motion remains irrotational. However, contrary to the penalty-type approach for enforcing irrotational constraint, here we use the mixed variational formulation to achieve the same goal. The main advantage of such an approach is in resulting set of degrees of freedom, featuring both fluid displacements and pressure, and providing a seamless connection to the poro-plasticity formulation described in Chapter 2. The resulting variational formulation is equivalent to [74–76], and can be written as

$$\Pi_f^e = \int_{\Omega_f^e} \left[-\frac{p^2}{2\beta} - p\big(\nabla\cdot\mathbf{u}\big) - \frac{\boldsymbol{\Lambda}\cdot\boldsymbol{\Lambda}}{2\vartheta} + \boldsymbol{\Lambda}\cdot\big(\nabla\times\mathbf{u}\big) - \mathbf{u}\cdot\mathbf{f}^b \right] d\Omega \tag{3.4}$$

where p is the pressure, $\mathbf{u}$ is the displacement vector, and $\boldsymbol{\Lambda}$ is the 'vorticity moment' or Lagrangian multiplier enforcing zero vorticity in terms of perturbed Lagrangian with ϑ as the penalty parameter. The parameter β is the bulk modulus of the external fluid, and $\mathbf{f}^b$ is the external load vector, that next to the body forces also includes inertia force $-\rho\ddot{\mathbf{u}}$.

The corresponding weak form is obtained from the first variation of Equation (3.4) and is written as

$$\begin{aligned}\int_{\Omega_f^e} \Big[\delta p\Big(-\frac{1}{\beta}p - \nabla\cdot\mathbf{u}\Big) + \Big(-p\big(\nabla\cdot\delta\mathbf{u}\big) + \boldsymbol{\Lambda}\big(\nabla\times\delta\mathbf{u}\big) - \delta\mathbf{u}\cdot\mathbf{f}^b\Big) \\ + \delta\boldsymbol{\Lambda}\Big(-\frac{1}{\vartheta}\boldsymbol{\Lambda} + \nabla\times\mathbf{u}\Big)\Big] d\Omega = 0\end{aligned} \tag{3.5}$$

We further ought to introduce the finite element approximations for the displacements, pressure, and 'vorticity moment'. For a typical finite element, we have

$$\begin{aligned}&\mathbf{u} = \mathbf{N}_u^f\bar{\mathbf{u}}; \quad p = \mathbf{N}_p^f\bar{\mathbf{p}}; \quad \boldsymbol{\Lambda} = \mathbf{N}_\lambda^f\bar{\boldsymbol{\lambda}} \\ &\mathbf{u} = \mathbf{N}_u^f\ddot{\bar{\mathbf{u}}}; \quad p = \mathbf{N}_p^f\ddot{\bar{\mathbf{p}}}; \quad \boldsymbol{\Lambda} = \mathbf{N}_\lambda^f\ddot{\bar{\boldsymbol{\lambda}}} \\ &\nabla\cdot\mathbf{u} = (\nabla\cdot\mathbf{N}_u^f)\,\bar{\mathbf{u}} = \mathbf{V}^f\bar{\mathbf{u}} \\ &\nabla\times\mathbf{u} = (\nabla\times\mathbf{N}_u^f)\,\bar{\mathbf{u}} = \mathbf{D}^f\bar{\mathbf{u}}\end{aligned} \tag{3.6}$$

where $\mathbf{N}_u^f$, $\mathbf{N}_p^f$, and $\mathbf{N}_\lambda^f$ are interpolation matrices, $\bar{\mathbf{u}}$ is the vector of unknown nodal displacements, $\bar{\mathbf{p}}$ is the vector of unknown nodal pressures, and $\bar{\boldsymbol{\lambda}}$ is the vector of unknown nodal 'vorticity moments'.

The end result of the finite element discretization procedure is the following system of equations governing the discrete problem

$$\mathop{\mathbb{A}}_{e=1}^{n_{elem}} \left\{ \begin{bmatrix} \mathbf{A}_{uu} & \mathbf{0} & \mathbf{0} \\ \mathbf{0} & \mathbf{0} & \mathbf{0} \\ \mathbf{0} & \mathbf{0} & \mathbf{0} \end{bmatrix}^e \begin{Bmatrix} \ddot{\bar{\mathbf{u}}} \\ \ddot{\bar{\mathbf{p}}} \\ \ddot{\bar{\boldsymbol{\lambda}}} \end{Bmatrix}^e + \begin{bmatrix} \mathbf{0} & \mathbf{L}_{up} & \mathbf{L}_{u\lambda} \\ \mathbf{L}_{up}^\mathsf{T} & \mathbf{L}_{pp} & \mathbf{0} \\ \mathbf{L}_{u\lambda}^\mathsf{T} & \mathbf{0} & \mathbf{L}_{\lambda\lambda} \end{bmatrix}^e \begin{Bmatrix} \bar{\mathbf{u}} \\ \bar{\mathbf{p}} \\ \bar{\boldsymbol{\lambda}} \end{Bmatrix}^e = \begin{Bmatrix} \mathbf{f}^f \\ \mathbf{0} \\ \mathbf{0} \end{Bmatrix}^e \right\} \tag{3.7}$$

where

$$\begin{aligned} \mathbf{A}_{uu}^e &= \int_{\Omega_f^e} \rho \mathbf{N}_u^{f,T} \mathbf{N}_u^f d\Omega; \\ \mathbf{L}_{up}^e &= -\int_{\Omega_f^e} \mathbf{V}^{f,T} \mathbf{N}_p^f d\Omega; \qquad \mathbf{L}_{u\lambda}^e = \int_{\Omega_f^e} \mathbf{D}^{f,T} \mathbf{N}_\lambda^f d\Omega \\ \mathbf{L}_{pp}^e &= -\int_{\Omega_f^e} \frac{1}{\beta} \mathbf{N}_p^{f,T} \mathbf{N}_p^f d\Omega; \quad \mathbf{L}_{\lambda\lambda}^e = -\int_{\Omega_f^e} \frac{1}{\vartheta} \mathbf{N}_\lambda^{f,T} \mathbf{N}_\lambda^f d\Omega \end{aligned} \tag{3.8}$$

The 'vorticity moment' degree of freedom can be statically condensed on the element level so that the only unknown variables remaining on the global level are displacements and pressures.

The strong form of the governing equations follows from Equation (3.5)

$$\nabla p + \nabla \times \boldsymbol{\Lambda} - \mathbf{f}^b = 0 \tag{3.9}$$

$$\nabla \cdot \mathbf{u} + \frac{p}{\beta} = 0 \tag{3.10}$$

$$\nabla \times \mathbf{u} - \frac{\boldsymbol{\Lambda}}{\vartheta} = 0 \tag{3.11}$$

Based on previously made assumptions, we note that Equations (3.9-3.10) are penalized version of the strong form described in (3.1-3.3).

3.2.3 Finite element approximation post-processing

Mixed displacement/pressure based finite element formulation, in combination with the proper choice of finite elements that satisfy the inf-sup condition, has shown to be a very efficient tool when dealing with nearly incompressible behavior of acoustic fluids in the frequency or dynamic analysis. The range of elements satisfying the inf-sup condition can be found in literature [144–147].

In our numerical simulations of fluid-structure interaction in the dynamic setting for the external fluid domain we choose linear finite element approximations for the displacements, with constant approximations for the pressure and the 'vorticity moment'. In other words, for the discretization of the external fluid domain, we use the **Q4-P1-Λ1** finite element depicted in Figure 3.1.

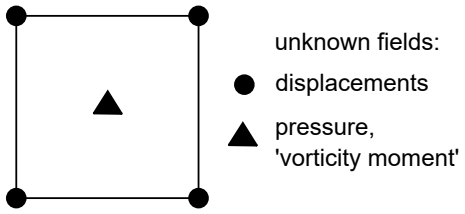

Figure 3.1 Finite element approximation for external fluid, dynamic case: **Q4-P1-Λ1**

For the purpose of solving the global system of equations, we can statically condense (e.g., [124]) the pressure and the 'vorticity moment' unknowns at the element level. We can then obtain the values of the pressures and the 'vorticity moments' from the computed values of displacements. However, our goal is to directly connect the external fluid finite elements with structure finite elements at the common nodes in order to ensure the direct exchange of both the motion and the pressure at the fluid-structure interface. This is achieved by reconstructing the pressure field for the external fluid finite elements, by extrapolating the pressure computed inside an element to the nodes of a **Q4** finite element used for the displacement approximation. In particular, the pressure at each node is evaluated as an average value of the pressures computed in the finite elements that share that node, as shown in Figure 3.2.

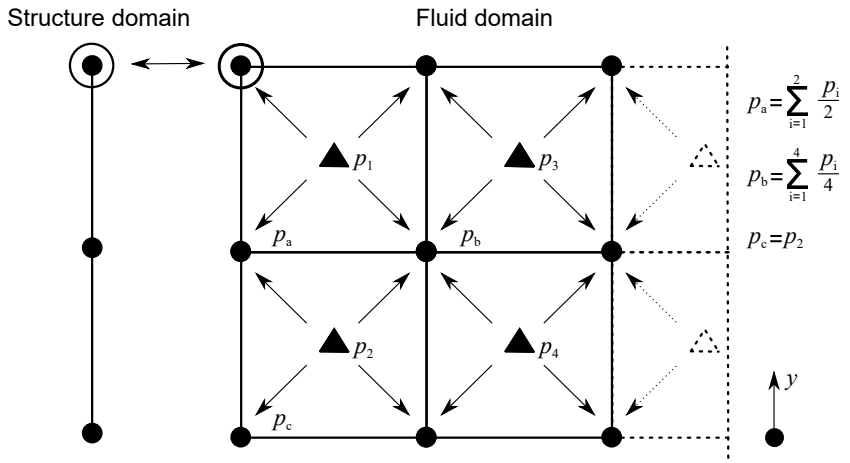

Figure 3.2 Extrapolation of the pressures

For the mesh of regular elements, the error in the value of the pressure computed in this manner is only limited to the finite elements located at the bottom (and/or top, depending on the boundary conditions) of the mesh. The error in the computed pressure increases if the size of the finite elements varies along the y-coordinate. However, by increasing the density of the mesh, the error can be decreased to better control the accuracy. The proposed approach enables us to compute the displacements, pressure, and 'vorticity moment' on a **Q4**-**P1**-**Λ1** finite element by performing the static condensation process. With such a post-processing procedure, we obtain the '**Q4**-**P4**' finite element, which we can then use for direct transfer at the fluid-structure interface.

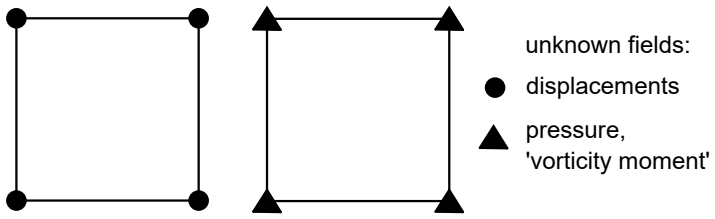

Figure 3.3 Finite element approximation for external fluid, quasi-static case: **Q4**-**P4**-**Λ4**

In our numerical simulations of fluid-structure interaction in the quasi-static setting (negligible inertial effects) for the external fluid domain, we will use a finite element with the same order of interpolation for the displacement, pore pressures and 'vorticity moment'. More precisely, we choose **Q4**-**P4**-**Λ4** finite element (Figure 3.3). For our problem of interest, where we consider the external fluid as a source of the saturation and the loading on the structure, this is the most practical choice. Namely, by statically condensing 'vorticity moment' on the element level, we directly obtain '**Q4**-**P4**' finite element, without any post-processing procedures needed. The finite element approximation of this kind is predictive enough for delivering the solution in terms of proper treatment of the fluid-structure interface, as it will be shown in the numerical simulations.

Remark 1: We note that practically same results for the quasi-static dam-reservoir interaction presented in this thesis (section 3.3.1.2) can be obtained by using **Q4**-**P1**-**Λ1** instead of **Q4**-**P4**-**Λ4** finite elements. However, in this case, a small mass has to be added in the external fluid model.

Remark 2: In general case, the penalty parameter ϑ in mixed $\mathbf{u}-p-\mathbf{\Lambda}$ formulation is a numerically large value ranging from $10^2\beta \leq \vartheta \leq 10^6\beta$. By assigning a numerically small value to a ϑ, the $\mathbf{u}-p$ formulation is obtained [75].

3.3 Numerical results

In this section, we present the results of several numerical simulations, which serve to illustrate the capabilities of the proposed numerical approach for dealing with acoustic fluid-structure interaction problems. All numerical implementations and computations are performed with the research version of the computer code FEAP, developed by R.L. Taylor [41]. In all numerical simulations, the finite element mesh is generated by using Delaunay triangulation and GMSH software [91]. The cross-sectional properties of the Timoshenko beam finite elements are computed from the Voronoi diagram by using MATLAB software [92].

3.3.1 Quasi-static case

3.3.1.1 Rigid and flexible water container

The first example presents a simple validation computation of the proposed numerical model of acoustic fluid-structure interaction in the quasi-static setting. Namely, we study a concrete water container with the geometry shown in Figure 3.4a.

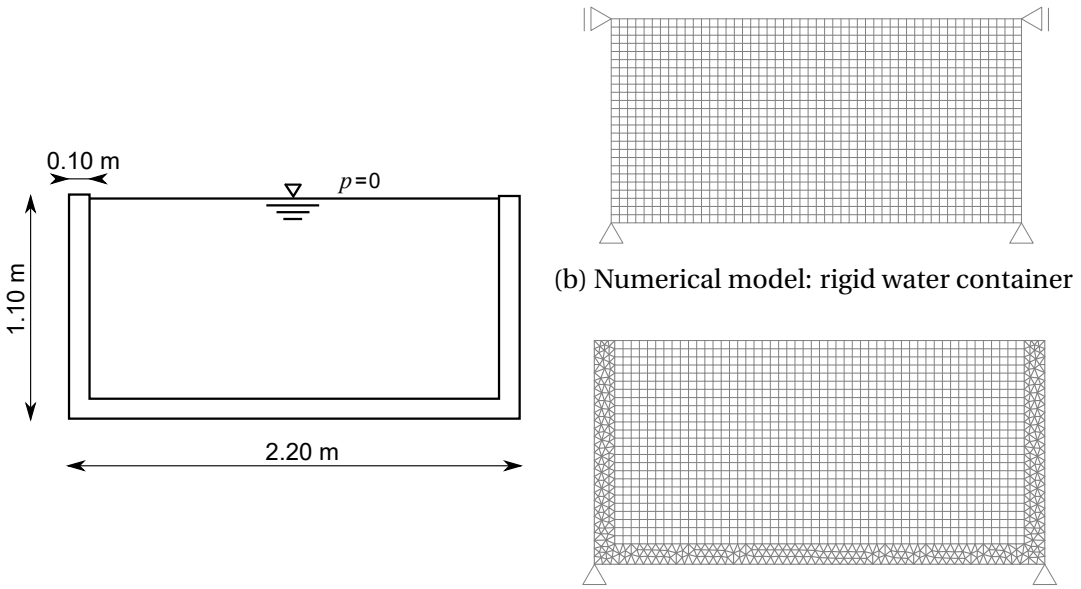

(a) Geometry

(b) Numerical model: rigid water container

(c) Numerical model: flexible water container

Figure 3.4 Water container

First, we assume that the walls and the slab of the container are rigid. We obtain the pressure field on a mesh of adequately constrained fluid finite elements (Figure 3.4b). Next, we assume that the walls and the slab are linear elastic and flexible.

We obtain the pressure field on a numerical model in which the structure domain is meshed with one-dimensional linear elastic Timoshenko beam finite elements (Figures 3.4c). In all computations, the value of pressure at the free surface is $p = 0$. Young's modulus for the Timoshenko beam finite element is $E = 10^4$ MPa. The coefficient of permeability is $k = 10^{-6}$ m/s, Biot's constant is $b = 1$ and Biot's modulus is $1/M \to 0$. The specific weight of the water is $\gamma_w = 10$ kN/m^3. The bulk modulus of the outside water is $\beta = 10^3$ MPa. The value of penalty parameter is $\vartheta = 10^{-5}\beta$.

We compare computed results against the analytical distribution of hydrostatic pressure. We present the results of numerical computations in the next several figures. From Figure 3.5, we can conclude that the proposed numerical model of acoustic fluid-structure interaction predicts correct hydrostatic pressure distribution on the wall of the container. The distributions of hydrostatic pressures in the case of a rigid and flexible container are shown in Figures 3.6a-3.6c. We can conclude that the results are mesh independent.

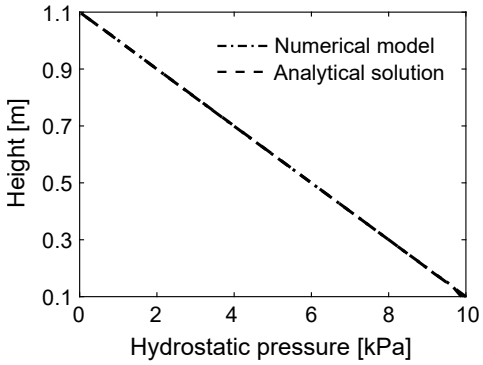

Figure 3.5 Hydrostatic pressure distribution on the wall of container

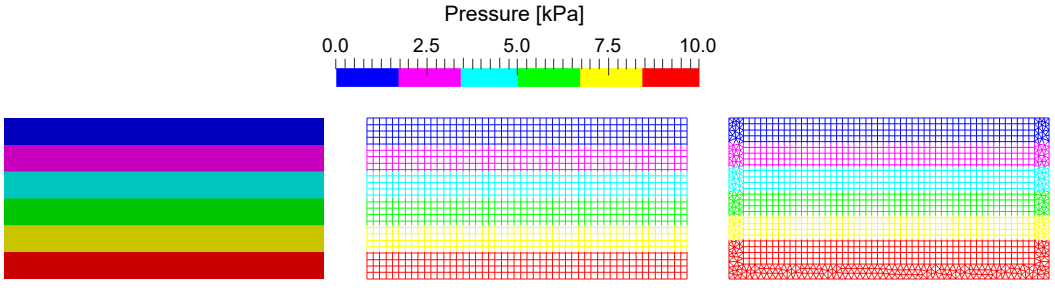

(a) Rigid container: 1 element (b) Rigid container (c) Flexible container

Figure 3.6 Water container: computed results

3.3.1.2 Dam-reservoir system

In this numerical example, we observe a small-sized dam subjected to the self-weight and the hydrostatic loading. shown in Figure 3.7. The finite element mesh and Voronoi discretization of the structure domain are shown in Figures 3.8a and 3.8b. The loading program is shown in Figure 3.8c. The specific weight of the dam material is $\gamma_s = 20$ kN/m^3, and the specific weight of the water is $\gamma_w = 10$ kN/m^3. We first apply an increase of the self-weight to simulate the construction of the dam, followed by the hydrostatic loading of the external reservoir.

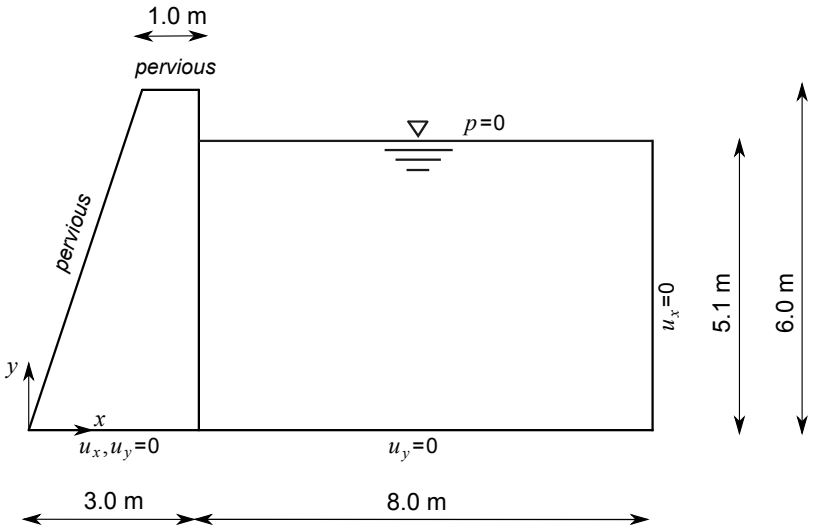

Figure 3.7 Geometry of dam-reservoir system, quasi-static case

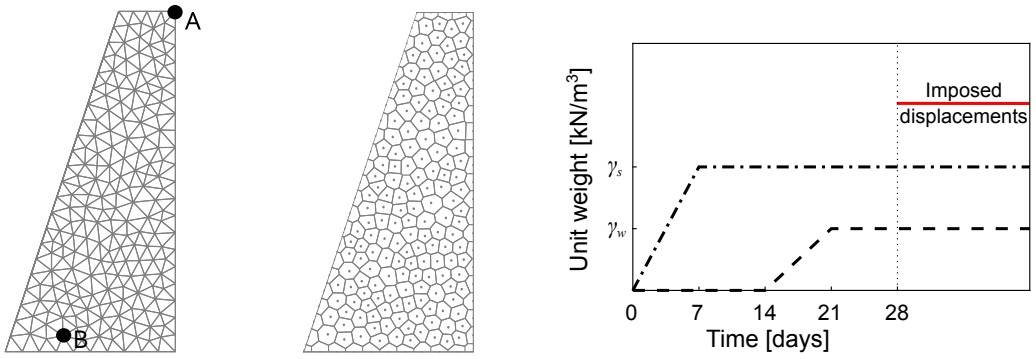

(a) Finite element mesh (b) Voronoi diagram (c) Loading program

Figure 3.8 Dam-reservoir system, quasi-static case

In the final part of this analysis, we would like to illustrate the capability of the proposed approach to represent the localized failure, where the cracks coalescence results with the ultimate failure mode. In this manner, we seek to investigate the

safety factor of the complete dam structure, which (contrary to usual factors for different materials) ought to be defined for particular load pattern. This is done by computing the maximum overload that can be applied on top of (already) acting self-weight and hydrostatic pressure of the external reservoir. The computation is carried out by imposed displacement, bringing the dam structure each time to the ultimate state of localized failure. We present both results computed for either horizontal or vertical overload, quantifying the localized failure brought by increasing horizontal or vertical load, respectively.

We start by assuming that the behavior of the dam remains linear elastic, and we apply first the self-weight and then the hydrostatic loading. Here, we analyze in detail the results of the fluid-structure interaction obtained with the mixed displacement/pressure based external fluid finite element formulation. Next, we assume that the behavior of the dam is inelastic. We introduce yield and fracture limits for Timoshenko beam finite elements to take into account the possibility of plastic zones and cracks formation as a result of combined body and hydrostatic loading. Finally, we determine the admissible horizontal and vertical overloads of the dam by imposing corresponding displacements on the top base of the dam until ultimate failure. In the first two computation phases, application of the self-weight and hydrostatic loading, the time step is set to $\Delta t = 0.1$ day. In the final stage of localized failure, the time step is set to $\Delta t = 1$ s.

→ Linear elastic behavior

Young's modulus and Poisson's ratio of the Timoshenko beam finite element are $E = 10^4$ MPa and $\nu = 0$. The coefficient of permeability is $k = 10^{-7}$ m/s, Biot's constant is $b = 1$ and Biot's modulus is $M = 10^6$ MPa. The bulk modulus of the outside water is $\beta = 10^3$ MPa. The value of penalty parameter is $\vartheta = 10^{-5}\beta$. We compare the results obtained with the mixed displacement/pressure based finite element formulation of fluid motion against analytical values.

Figure 3.9a show the contours for the computed pressure field in the reservoir and in a porous medium from which the dam is built, by using a numerical model of acoustic fluid-structure interaction. The results are practically identical with the analytical solution for the hydrostatic pressure distribution (Figure 3.9b). From the computed excess pore pressure distribution inside the dam, we can conclude that the water in the dam reservoir can keep the porous material from which the dam is built fully saturated in every time step, which is confirmed by the results in Figure 3.10a showing the time evolution of total excess pore pressure at the bottom of the dam with respect to applied loading.

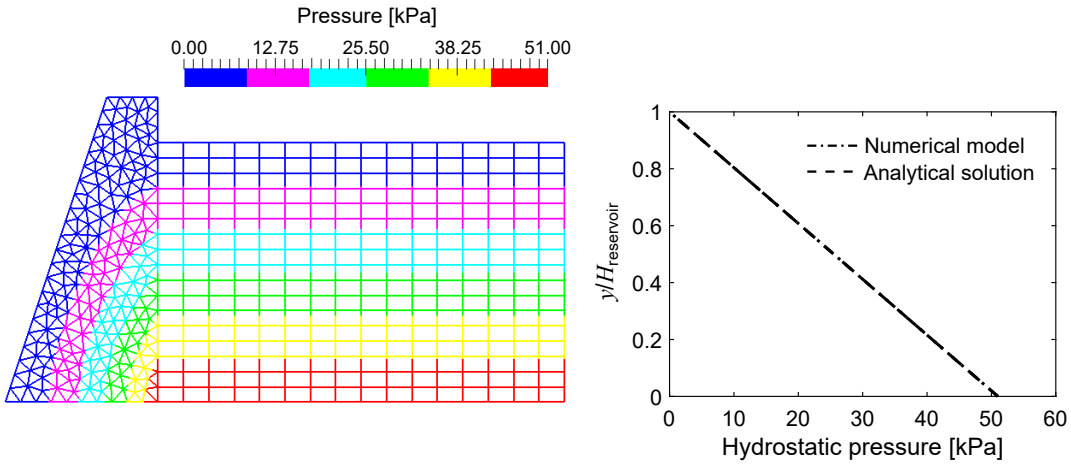

(a) Pressure and pore pressure distribution

(b) Pressure distribution

Figure 3.9 Linear elastic behavior: computed results

Next, we inspect other aspects of fluid-structure interaction, such as the values of total vertical and horizontal reactions, and displacements of the dam.

In Figures 3.10b and 3.10c, the total vertical and horizontal reaction at the bottom of the dam are shown. In mixed displacement/pressure formulation, where common nodes share both displacements and pressures, we have the transfer of both forces and pressures which gives the total value of horizontal reaction equal to the resultant force of the hydrostatic pressures. The total vertical reaction is equal to the total weight of the dam. Here, we have an additional vertical reaction from the hydrostatic loading as a result of common nodes. This additional value changes and approaches zero as the size of the fluid finite element approaches zero.

The horizontal displacement of the tip of the dam → point A(3, 6)[m] gives additional insight into the results of fluid-structure interaction. From Figure 3.10d, we can see that the total horizontal displacement of the tip of the dam, after hydrostatic loading has been applied is a sum of displacements due to self-weight, hydrostatic forces and hydrostatic pressures. We can verify this if we perform the uncoupled computation of the structure response (Biot's constant $b = 0 \rightarrow$ matrix $\mathbf{K}^e_{up}$ is a null matrix) for the hydrostatic loading case. This way, we can obtain the displacements of the dam only from hydrostatic forces exerted on the structure. To validate our results, we perform an uncoupled computation on a model of a dam alone, where we apply hydrostatic loading in terms of equivalent nodal horizontal forces. We can conclude that the value of horizontal displacement for the uncoupled fluid-structure interaction case and the case of the dam alone are practically the same (Figure 3.10e). Next, we subtract the value of displacements for the cou-

pled and uncoupled case (Figure 3.10f). The resulting values of displacements are due to the coupling between the solid and fluid phase (see Equation 2.20).

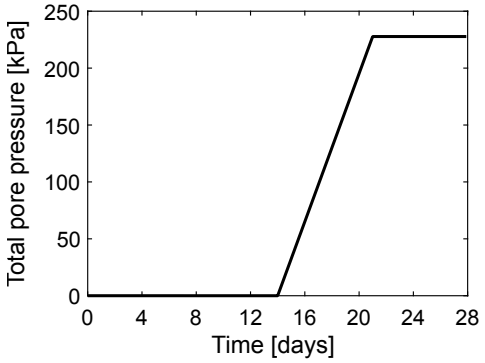

(a) Total excess pore pressure

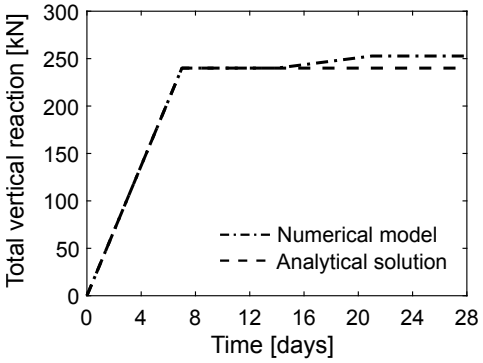

(b) Total vertical reaction

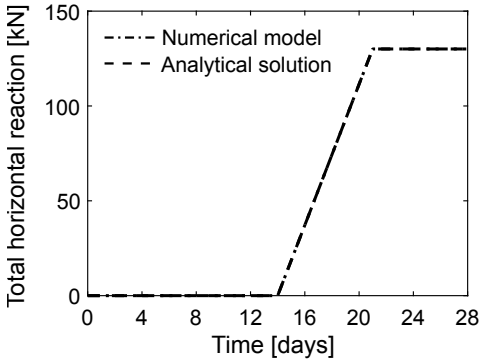

(c) Total horizontal reaction

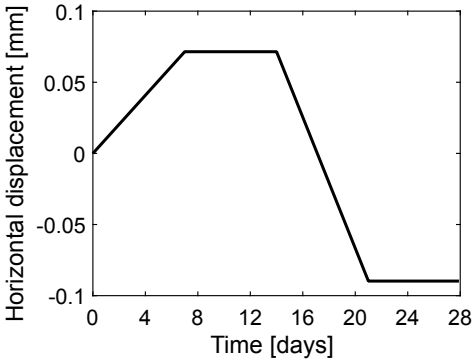

(d) Horizontal displacement at point A

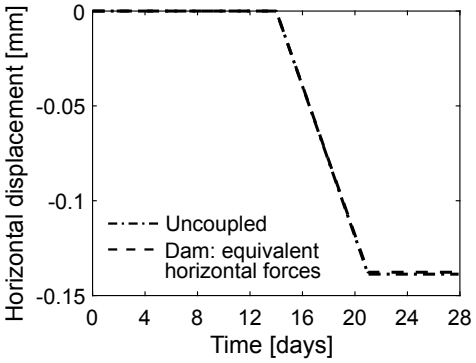

(e) Horizontal displacement at point A resulting from hydrostatic forces

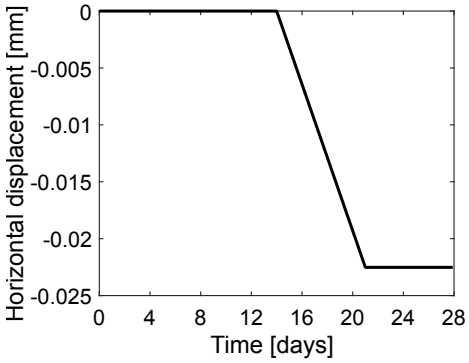

(f) Horizontal displacement at point A resulting from hydrostatic pressures

Figure 3.10 Linear elastic behavior: computed results

To summarize, the proposed numerical model of acoustic-fluid structure interaction results in a full fluid-structure interaction problem, where both the influence of the hydrostatic forces and the hydrostatic pressures on the response of the dam are included.

→ Inelastic behavior

In this case, we admit that due to the self-weight and the hydrostatic loading, plastic zones and cracks can form in the dam. Thus, we introduce yield and fracture limits for the Timoshenko beam finite element in tension, compression and shear: $\sigma_{y,t} = 0.015$ MPa; $\sigma_{y,c} = 0.20$ MPa; $\sigma_{y,s} = 0.015$ MPa; $\sigma_{f,t} = 0.02$ MPa; $\sigma_{f,c} = 0.30$ MPa; $\sigma_{f,s} = 0.02$ MPa. The fracture energies in tension, compression and shear are: $G_{f,t} = 0.01$ GN/m; $G_{f,c} = 0.1$ GN/m; $G_{f,s} = 0.01$ GN/m. The linear hardening modulus is $H_{lh} = 10^3$ MPa.

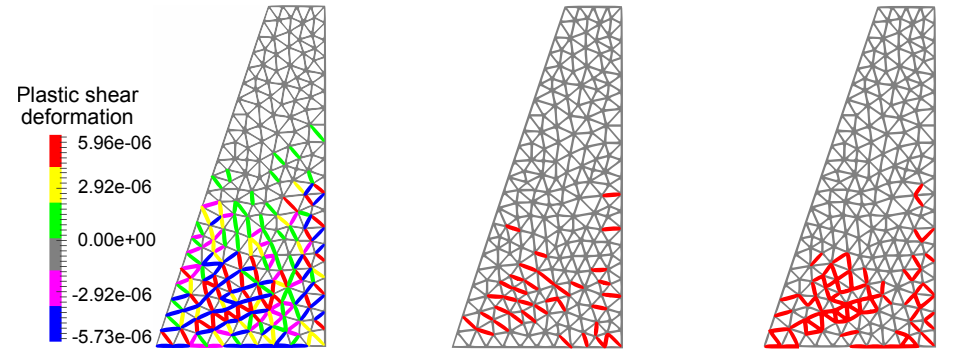

(a) Plastic shear deformation (b) Broken cohesive links: mode I (c) Broken cohesive links: mode II

Figure 3.11 Inelastic behavior: broken cohesive links and plastic zones

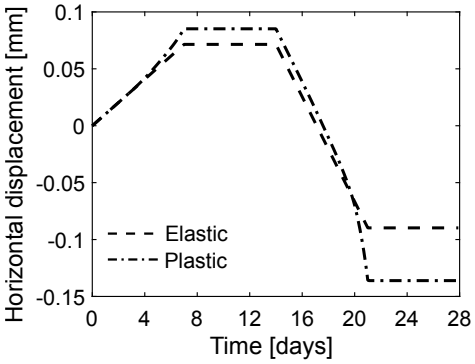

Figure 3.12 Inelastic behavior: horizontal displacement at point A

Elements in which plasticity has occurred are shown in Figure 3.11a, where we can see that a large area of the domain has become plastic. In Figures 3.11b and 3.11c, broken cohesive links in the dam at the end of the loading program are shown. These broken cohesive links (marked red) represent Timoshenko beam finite elements that had entered softening phase of the response in mode I, and mode II. The plastic zones and broken cohesive links result in the less stiff response

of the dam. This leads to an increase in the value of horizontal displacement of the tip of the dam, compared to the linear elastic case (Figure 3.12).

→ Localized failure analysis of dam structure for either horizontal or vertical overload

The self-weight and the hydrostatic loading are considered as the fundamental load cases acting upon the dam, which must be used for the structure design. During the dam life cycle, one can imagine occasional extreme loads that can threaten structure integrity and lead to localized failure. Here, we want to quantify the remaining resistance to possible overload (on top of dam dead-load and reservoir pressure) that can be applied on the dam leading to the complete failure. The overload of this kind can be interpreted as the structure safety factor, which has to be properly taken into account in the design process. In particular, we carry on such a safety factor computation by computing the final failure mode for either applied horizontal or vertical overloads.

First, we compute the value of the admissible horizontal overload by imposing horizontal displacements with a constant rate of $1 \cdot 10^{-3}$ mm/s on the top base of the dam, applied after the loading program shown in Figure 3.8c. The computed value of horizontal overload that dam can withstand until the complete failure is 8.3810 kN (see Figure 3.13a). It is important to note fairly low safety since the self-weight and hydrostatic loading resulted in the total horizontal reaction equal to 130.05 kN (Figure 3.10c). Namely, for this particular geometry and the mechanical properties of the dam, we can state that the factor of safety of the dam against failure is 1.06. In other words, an increase in the value of the horizontal load in the amount of 6% will result in the failure of the dam. The excess pore pressure at point B(1.0175, 0.2776)[m] is shown in Figure 3.13b. The deformed configuration of the dam and the broken cohesive links in increasing softening at the end of the

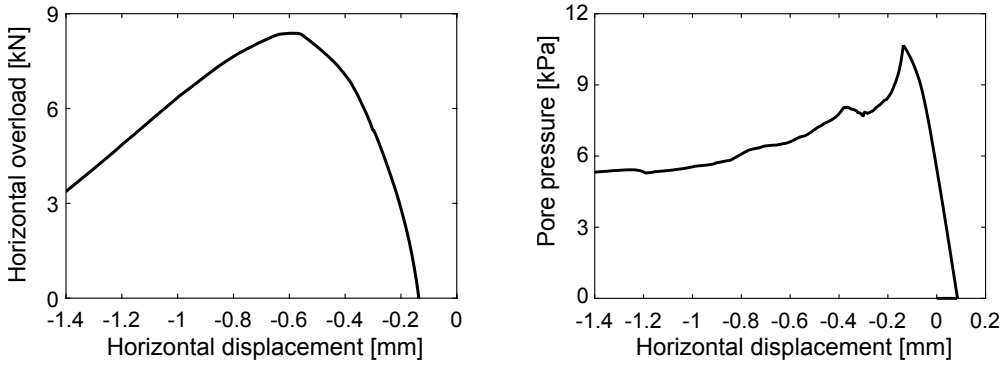

(a) Horizontal overload (b) Excess pore pressure at point B

Figure 3.13 Horizontal overload: computed results

loading program are shown in Figures 3.14a-3.14c. After the horizontal overload level is reached, one large macro-crack starts to form and propagate resulting in the decrease in the load carrying capacity of the dam (Figures 3.14d and 3.14e).

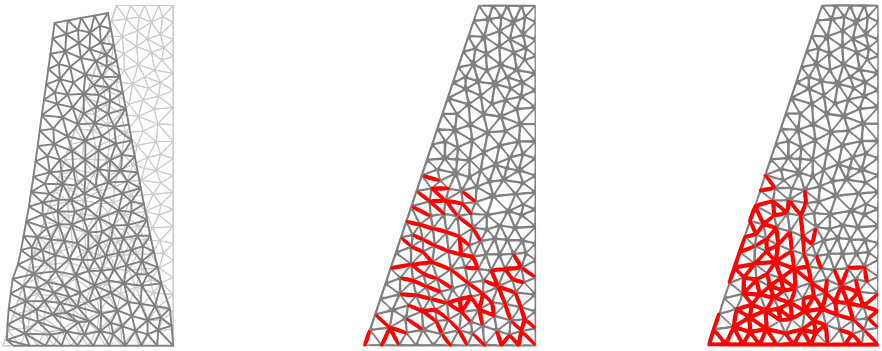

(a) Deformed configuration (b) Broken cohesive links: mode I (c) Broken cohesive links: mode II

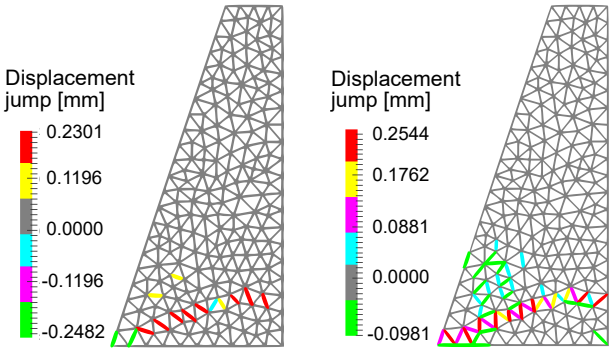

(d) Displacement jumps: mode I (e) Displacement jumps: mode II

Figure 3.14 Failure mode for horizontal overload

We also perform the uncoupled computation of the structure response (Biot's constant $b = 0 \rightarrow$ matrix $\mathbf{K}^e_{up}$ is a null matrix), in order to investigate the influence

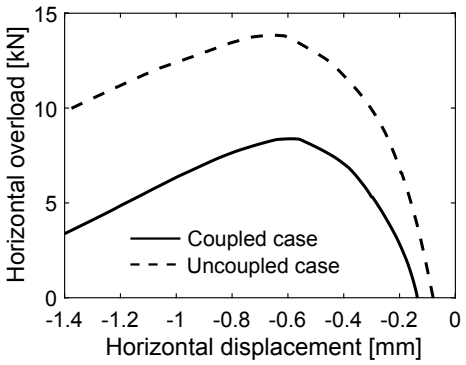

Figure 3.15 Comparison of horizontal overloads

of pore fluid presence on the computed value of admissible horizontal overload. The uncoupled computation results in a higher value of the computed horizontal overload (13.8381 kN) compared to the coupled case, as shown in Figure 3.15. Namely, the failure mode for horizontal overload brought by imposed horizontal displacements on the top base of the dam results in a decrease in the value of the admissible horizontal overload compared to the uncoupled case.

Second, we compute the value of the admissible vertical overload by imposing vertical displacements with a constant rate of $1 \cdot 10^{-3}$ mm/s on the top base of the dam. The corresponding vertical force evolution and the loading program are shown in Figure 3.8c. The computed admissible vertical overload force is much bigger with 140.0553 kN (Figure 3.16a). The total vertical reaction resulting from the self-weight and hydrostatic loading is 252.7516 kN (Figure 3.10b). Thus, we can state that the factor of safety of the dam against failure is 1.55, for this particular geometry and the mechanical properties of the dam. The excess pore pressure at point B(1.0175, 0.2776)[m] is shown in Figure 3.16b. The deformed configuration of the dam is shown in Figure 3.17a. The broken cohesive links in increasing softening at the end of the loading program are shown in Figures 3.17b-3.17c. The values of displacement jumps in the broken cohesive links are shown in Figures 3.17d and 3.17e.

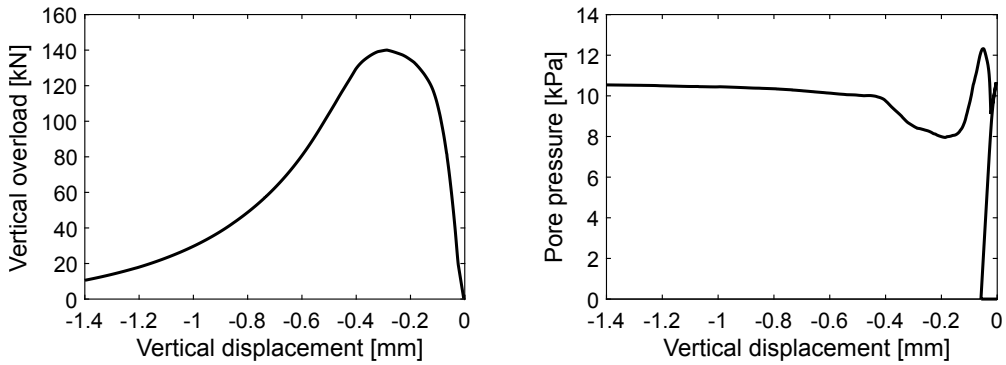

(a) Vertical overload

(b) Excess pore pressure at point B

Figure 3.16 Vertical overload: computed results

We also perform the uncoupled computation of admissible vertical overload by setting Biot's constant $b = 0$. The computed results are shown in Figure 3.18. The computed vertical overload for the uncoupled case does not differ significantly compared to the coupled case (141.3855 kN). Namely, the localized failure brought by imposed vertical displacements on the top base of the dam occurs near the top base of the dam (Figure 3.17a) and does not affect the computed value of vertical

overload significantly. Slight difference in computed results is observed in the post-peak part of the response.

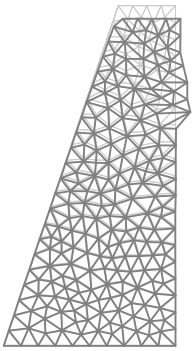

(a) Deformed configuration

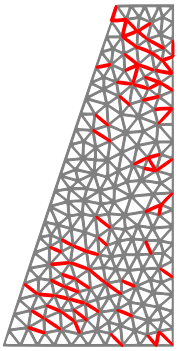

(b) Broken cohesive links: mode I

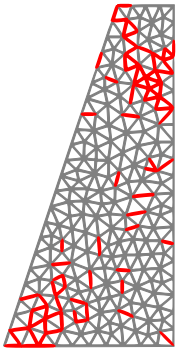

(c) Broken cohesive links: mode II

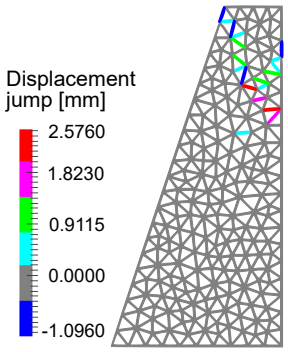

(d) Displacement jumps: mode I

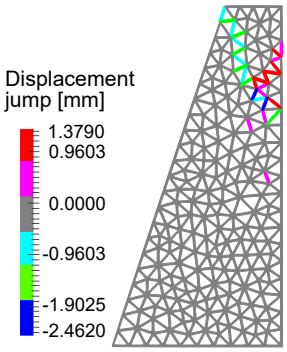

(e) Displacement jumps: mode II

Figure 3.17 Failure mode for vertical overload

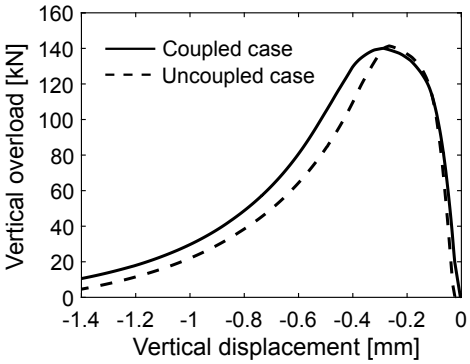

Figure 3.18 Comparison of vertical overloads

3.3.2 Dynamic case

3.3.2.1 Analytical solutions for hydrodynamic pressures

When the fluid-structure systems, such as dam-reservoir are subjected to extreme dynamic loads brought by for example seismic ground movement, next to the hydrostatic pressures and forces, additional hydrodynamic pressures and forces are exerted on the upstream face of the structure. Their values and distribution have to be quantified either with analytical solutions proposed in the literature or with numerical methods, in order to provide the sound design of the structure.

The problem of evaluating the value and the distribution of the hydrodynamic pressure was first examined in the work of Westergaard who provided a solution for the case of a rigid dam with vertical upstream face subjected to horizontal harmonic ground motion [85], followed by von Kármán who provided the solution very close to Westergard's using linear momentum balance principle [148]. Later, Chwang and Housner, also using the momentum method, derived the analytical solution for the general case of an inclined upstream face of the dam subjected to constant horizontal acceleration [149]. In the second part of his work, Chwang derived the analytical solution using two-dimensional potential flow theory [150]. In addition to the inclined upstream face of the dam, Liu proposed an analytical solution for the sloped reservoir base [151].

→ Westergaard's solution

Westergaard [85] is the first who studied the problem of evaluating the value and distribution of hydrodynamic pressure exerted on the upstream face of the dam. His work was focused on the simple two-dimensional dam-reservoir system subjected to the horizontal harmonic ground motion (Figure 3.19). The dam was assumed to be rigid with vertical upstream face, and the length of the reservoir was assumed to be infinite. Westergaard derived an analytical solution for the hydrodynamic pressure distribution in terms of series of sine functions. Maximum hydrodynamic pressure distribution on the vertical upstream face of the rigid dam, according to Westergaard, is described with the following expression

$$\begin{aligned} p &= \frac{8a_0\rho H}{\pi^2}\sum_{1,3,5,\ldots}^{n}\frac{1}{n^2 c_n}\sin\left(\frac{n\pi y}{2H}\right) \\ c_n &= \sqrt{1-\frac{16\rho H^2}{n^2 g K T^2}} \end{aligned} \tag{3.12}$$

where a_0 is the maximum horizontal acceleration of the foundation, ρ is the density of the retained water, H is the depth of the reservoir, K is the bulk modulus of water, and T is the period of the horizontal acceleration of the foundation.

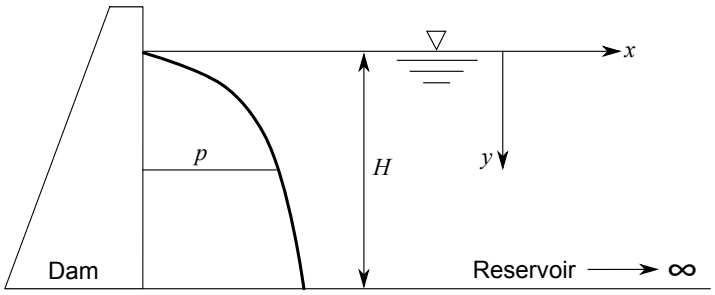

Figure 3.19 Dam-reservoir system studied by Westergaard [85]

Based on the previous solution, Westergaard proposed a simpler expression which results in a parabolic distribution of the hydrodynamic pressures

$$p = 0.875\rho a_0 \sqrt{Hy} \tag{3.13}$$

This expression, even though represents a conservative approximation, gives satisfactory results and is widely used in everyday engineering practice.

According to Westergaard, the total horizontal force exerted on the vertical, upstream face of the dam is equal to

$$F = F_x = 0.543\rho a_0 H^2 \tag{3.14}$$

→ Von Kármán's solution

An analytical solution very close to Westergaard's was derived by von Kármán. In his work, von Kármán [148] exploited linear momentum-balance principle and derived an expression for hydrodynamic pressure distribution which reads as

$$p = 0.707\rho a_0 \sqrt{Hy} \tag{3.15}$$

According to von Kármán, the total horizontal force exerted on the vertical, upstream face of the dam is equal to

$$F = F_x = 0.555\rho a_0 H^2 \tag{3.16}$$

→ Chwang's solution

For a general case of a rigid dam with an inclined upstream face with a constant slope subjected to uniform horizontal acceleration a_0 (Figure 3.20), Chwang and Housner [149] derived analytical solution using the momentum balance method proposed by von Kármán. The fluid in the reservoir is assumed to be incompressible and inviscid.

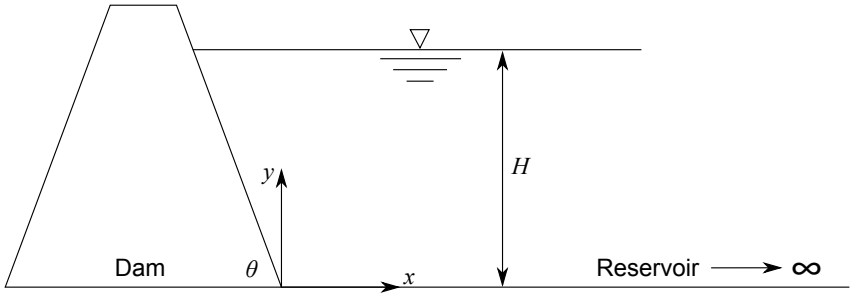

Figure 3.20 Dam-reservoir system studied by [149] and [150]

In their analytical solution, as in the Westergaard's and von Kármán 's solutions, the value of hydrodynamic pressures ranges from zero at the top of the reservoir to maximum at the bottom of the reservoir. Chwang, in the second part of his work [150], derived an exact solution for hydrodynamic pressure distribution using two-dimensional potential flow theory. Here, except for the case of the vertical upstream face, the maximum value of hydrodynamic pressure does not occur at the bottom of the reservoir but is moved up to a certain distance.

The hydrodynamic pressure distribution on the inclined upstream face is described with the following expression

$$p = C_p \rho a_0 H \tag{3.17}$$

where C_p is the pressure coefficient. The values of the pressure coefficient for different angles of inclination are shown in Figure 3.21, for both methods. The expression for computing the values of pressure coefficient can be found in [149] and [150].

The total horizontal and vertical force exerted on the inclined upstream face of the dam are equal to

$$\begin{aligned} F_x &= C_x \rho a_0 H^2 \\ F_y &= C_y \rho a_0 H^2 \end{aligned} \tag{3.18}$$

where C_x and C_y are force coefficients. The values of force coefficients for different angles of inclination are shown in Figure 3.22, for both methods. The expressions for computing the values of force coefficient can be found in [149] and [150].

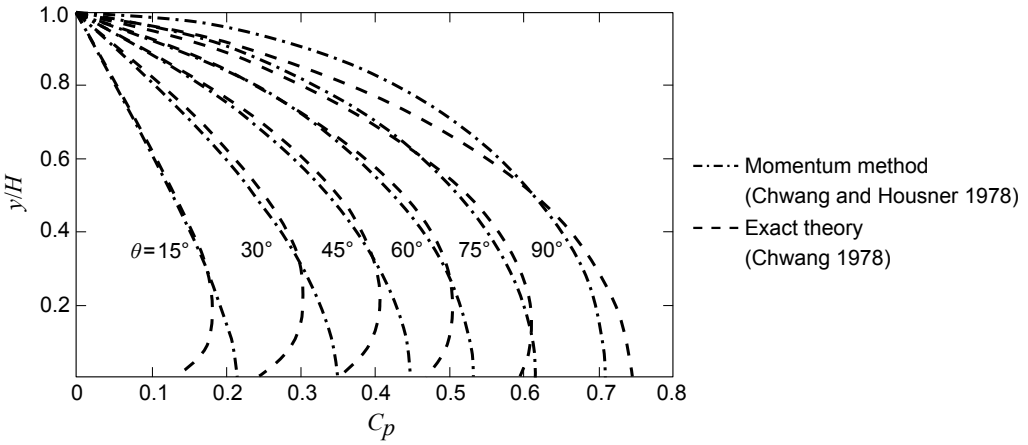

Figure 3.21 Pressure coefficient provided by [149] and [150], Adapted from "Hydrodynamic pressures on sloping dams during earthquakes. Part 2. Exact theory", by A.T. Chwang, 1978, *The Journal of Fluid Mechanics*, 87(2), pp. 347. Copyright 1978 Cambridge University Press, Adapted with permission

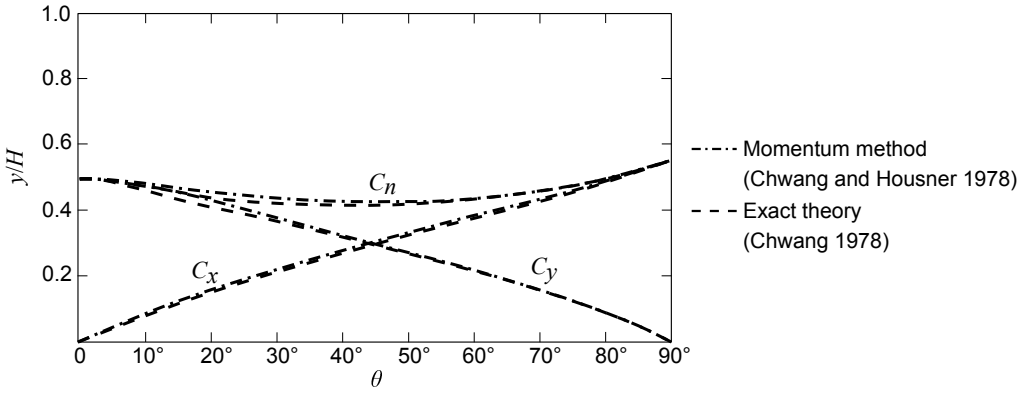

Figure 3.22 Force coefficient provided by [149] and [150], Adapted from "Hydrodynamic pressures on sloping dams during earthquakes. Part 2. Exact theory", by A.T. Chwang, 1978, *The Journal of Fluid Mechanics*, 87(2), pp. 347. Copyright 1978 Cambridge University Press, Adapted with permission

For the case of the vertical upstream face, the exact method gives the value of force coefficient $C_x = 0.543$ which is the same as Westergaard's solution, and the momentum method gives the value $C_x = 0.555$ which is the same as von Kármán's solution. The comparison between the analytical solutions for hydrodynamic pressure distribution on the vertical upstream face of the dam is shown in Figure 3.23.

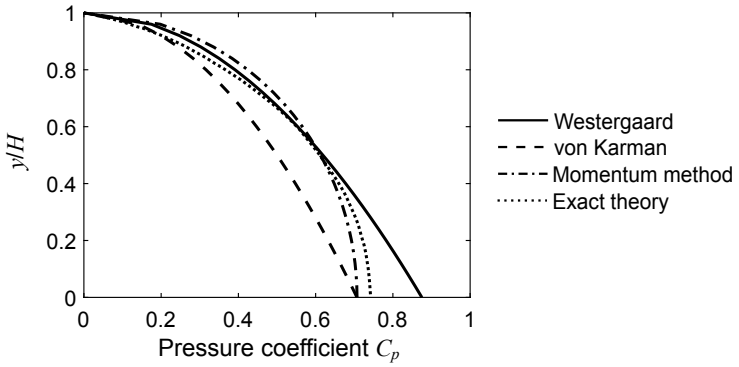

Figure 3.23 Comparison of analytical solutions for vertical upstream face ($\theta = 90°$)

3.3.2.2 Modal analysis of rigid cavity problem

In this example, we perform the modal analysis of the rigid cavity problem in order to validate the proposed external fluid model, which is based on **Q4**-**P1**-Λ**1** finite element. The geometry and the boundary conditions of the problem are shown in Figure 3.24. The density of the fluid is $\rho = 1000$ kg/m^3, the bulk modulus is $\beta = 115.6$ MPa, and the penalty parameter is $\vartheta = 10^3\beta$.

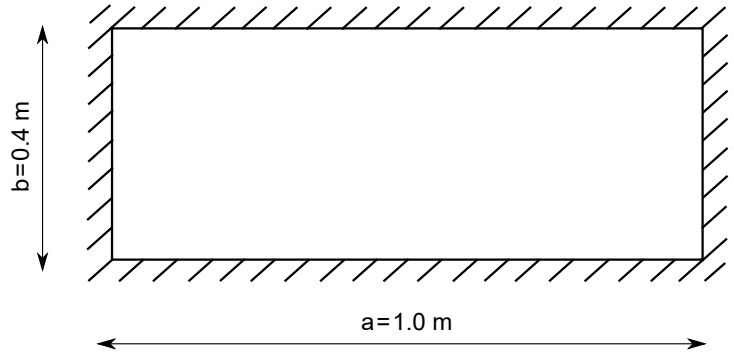

Figure 3.24 Rigid cavity problem: problem statement

We compare the computed values of the first four frequencies against those provided in [69] and [75], which are computed from analytical solution defined with following expression

$$\omega = c\pi\sqrt{\left(\frac{n}{a}\right)^2 + \left(\frac{m}{b}\right)^2} \tag{3.19}$$

where n, m are integers, and c is the acoustic wave speed.

The computed values of first four frequencies are shown in Table 3.1. We can conclude that by increasing the mesh density, the results obtained with **Q4**-**P1**-Λ**1** approach the analytical solution.

Table 3.1 Rigid cavity problem: computed frequencies

Mesh density	Frequency [Hz]			
4x3	174.4	374.9	444.6	463.0
8x6	171.1	348.8	429.9	459.3
32x24	170.1	340.5	425.3	457.8
64x48	170.0	340.1	425.1	457.8
Analytical solution	170.0	340.0	425.0	457.7

3.3.2.3 Linear elastic separator wall

In this example, we observe a linear elastic separator wall 12 m high, and 1.2 m thick. The configuration of the problem is shown in Figure 3.25. Young's modulus and Poisson's ratio of the Timoshenko beam finite element are $E = 10^4$ MPa and $\nu = 0$. The mass density is $\rho_s = 2000$ kg/m^3. The coefficient of permeability is $k = 10^{-6}$ m/s, Biot's constant is $b = 1$ and Biot's modulus is $1/M \to 0$. The mass density of external fluid (water) is $\rho_f = 1000$ kg/m^3, and the bulk modulus is $\beta = 10^5$ MPa. We note that in this particular simulation of acoustic fluid-structure interaction, the boundary and loading conditions imposed on the external fluid allow for the vorticity constraint to be completely omitted without any influence on the computed results.

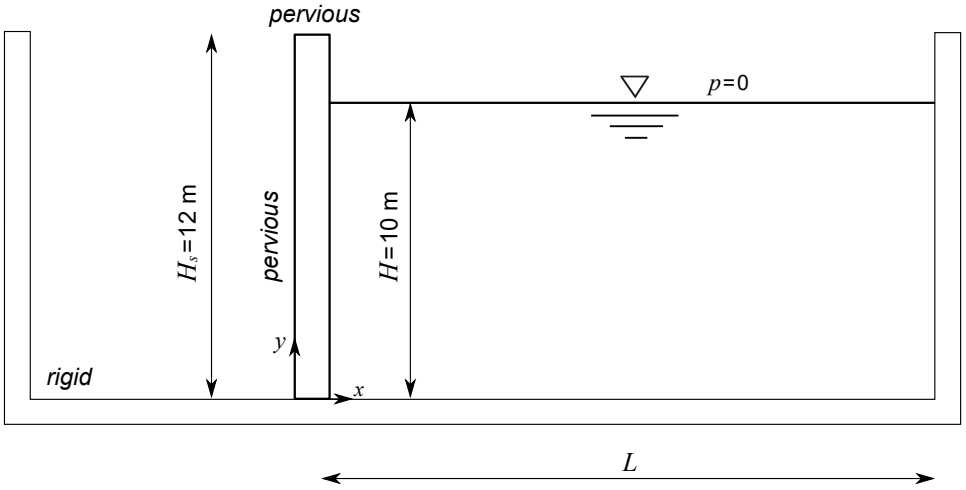

Figure 3.25 Linear elastic separator wall: problem statement

We subject the separator wall and the contained fluid to a horizontal ground acceleration reaching its maximum value of $a_0 = 1$ m/s^2 at $t = 1$s, after which is kept constant (Figure 3.26). According to [152], we model the horizontal ground movement in terms of equivalent horizontal forces. Here, we consider a system

with a fixed base, and we apply at every node of the finite element mesh an equivalent force with a value equal to the product of the corresponding mass and the imposed base acceleration. We compare the computed results against those provided by Chwang [150], with the aim to validate the proposed model for predicting hydrodynamic pressures and hydrodynamic forces exerted on the upstream face of the structure.

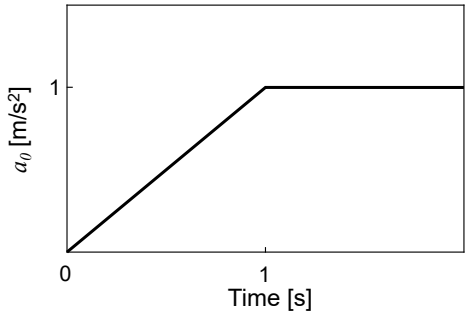

Figure 3.26 Linear elastic separator wall: loading program

We present the results for hydrodynamic pressures distribution in terms of the pressure coefficient C_p. The pressure p is then equal to $p = C_p \rho a_0 H$, where ρ is the mass density of the external fluid, a_0 is the horizontal acceleration, and H is the height of the reservoir. The computed values of the pressure coefficient for different values of L/H ratio are shown in Figure 3.27a. We can conclude that the values of hydrodynamic pressure depend on the length of the fluid domain, because of the influence of boundary effects at the infinity. For values of L/H ratio greater than 3, results do not differ significantly and approach the analytical solution provided by Chwang [150].

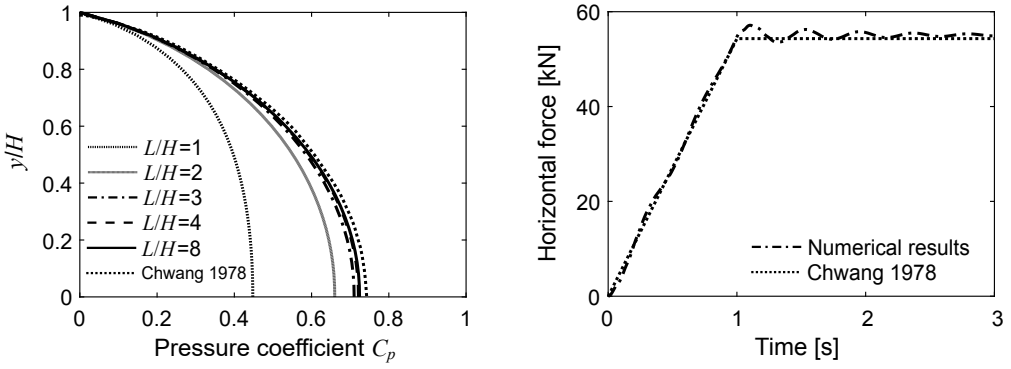

(a) C_p for different L/H ratios

(b) Horizontal force $L/H = 8$

Figure 3.27 Linear elastic separator wall: computed results

We also investigate the influence of the fluid acting as a source of additional forces on the structure. We compare the reference value of total horizontal force exerted on the vertical upstream face of the structure provided by Chwang [150] against the computed value of horizontal force. The value of horizontal force is computed on a numerical model of acoustic fluid-structure interaction, in which only the reservoir was subjected to horizontal ground acceleration. The results are shown in Figure 3.27b. We can conclude that as the oscillations of the separator wall are being damped, the computed results approach the reference value. This confirms that with the proposed model we are able to ensure the direct transfer of both forces and pressures at the fluid-structure interface. It should be noted that no artificial damping (e.g., Rayleigh damping) is added in the numerical model of the fluid-structure interaction. The damping in the numerical model results solely from the equations governing the coupled problem. The hydrodynamic pressure distribution in the fluid domain, and pore pressure distribution in the separator wall for $L/H = 4$ are shown in Figure 3.28.

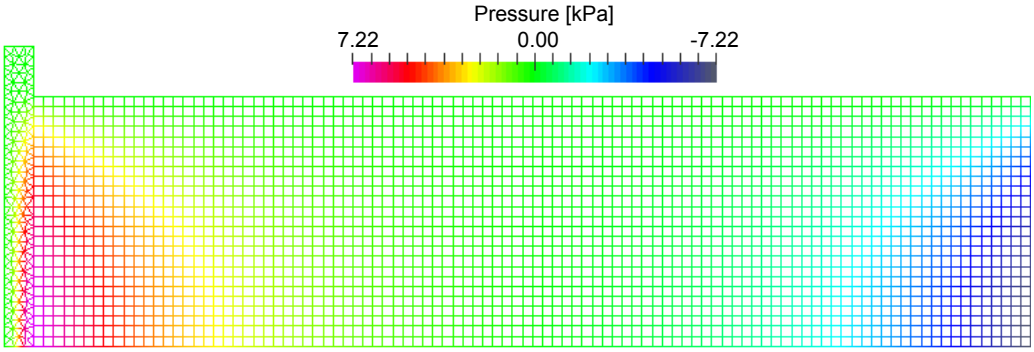

Figure 3.28 Pressure and pore pressure distribution: $L/H = 4$

3.3.2.4 Dam-reservoir system

In this example, we observe a small-size gravity dam, shown in Figure 3.29. The length of the reservoir is chosen as $L = 20.40$ m in order to eliminate the influence of the boundary effects. First, we assume that the response of dam remains linear elastic, and we subject the dam-reservoir system to a horizontal ground acceleration reaching its maximum value of $a_0 = 1$ m/s^2 at $t = 1$s, which is then kept constant (Figure 3.30a). The time step is set to $\Delta t = 0.01$ s. The horizontal ground movement is modeled in terms of equivalent horizontal forces acting on the system with fixed base [152]. We compare computed results against analytical solutions provided by Chwang [150].

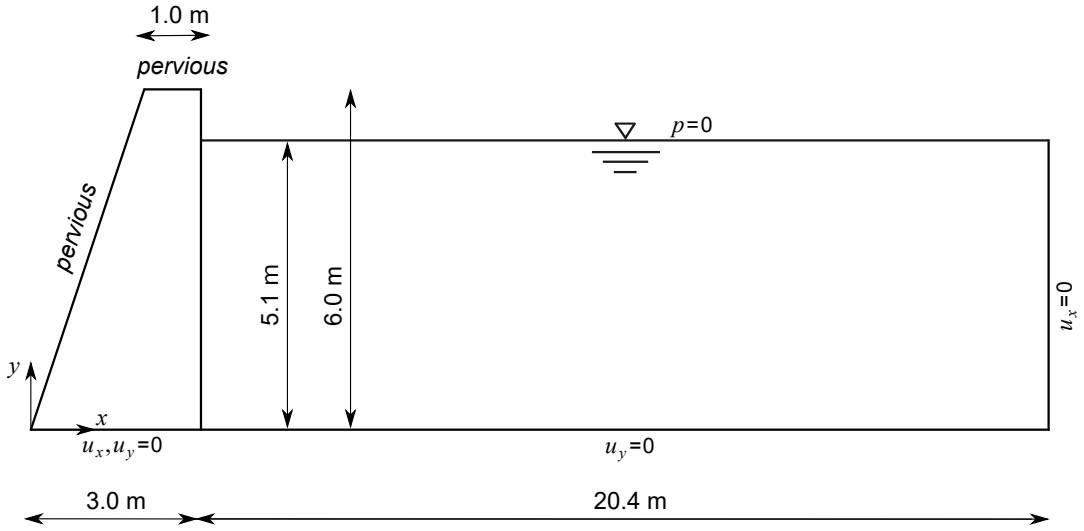

Figure 3.29 Geometry of dam-reservoir system, dynamic case

Next, we aim to determine the horizontal overload dam can withstand until ultimate failure. Here, we perform a nonlinear dynamic analysis following the loading program shown in Figure 3.30b. First, we apply self-weight followed by the hydrostatic loading of the external reservoir. Finally, we subject the dam-reservoir system to the linear increasing horizontal ground acceleration with a constant rate of 2 m/s^2 /1s, until the ultimate state of localized failure. The specific weight of the dam material is $\gamma_s = 20$ kN/m^3, and the specific weight of the water is $\gamma_w = 10$ kN/m^3.

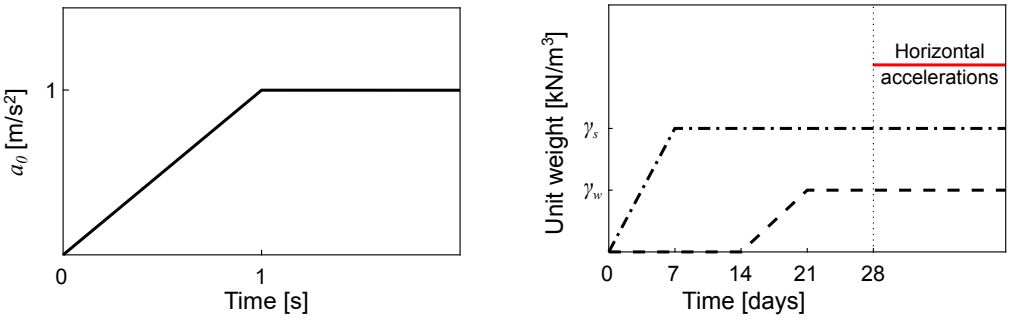

(a) Validation analysis

(b) Localized failure analysis

Figure 3.30 Dam-reservoir system, dynamic case: loading programs

In the first two computation phases, application of the self-weight and hydrostatic loading, the time step is set to $\Delta t = 0.1$ day. In the final stage of localized failure, the initial time step is set to $\Delta t = 0.001$ s. Prior to reaching the ultimate value of horizontal overload, the time step is reduced to $\Delta t = 0.0001$ s. Throughout this numerical example, the vorticity constraint is completely omitted.

→ Linear elastic behavior

Young's modulus and Poisson's ratio of the Timoshenko beam finite element are $E = 10^4$ MPa and $\nu = 0$. The coefficient of permeability is $k = 10^{-7}$ m/s, Biot's constant is $b = 1$ and Biot's modulus is $M = 10^6$ MPa. The bulk modulus of the outside water is $\beta = 10^3$ MPa.

We compare the computed values of hydrodynamic pressure and hydrodynamic force exerted on the wall against analytical solutions provided by Chwang [150]. The computed results for the vertical upstream face are shown in Figures 3.31a and 3.31b. We can conclude that a good match between computed hydrodynamic pressures and hydrodynamic forces, and analytical values is obtained.

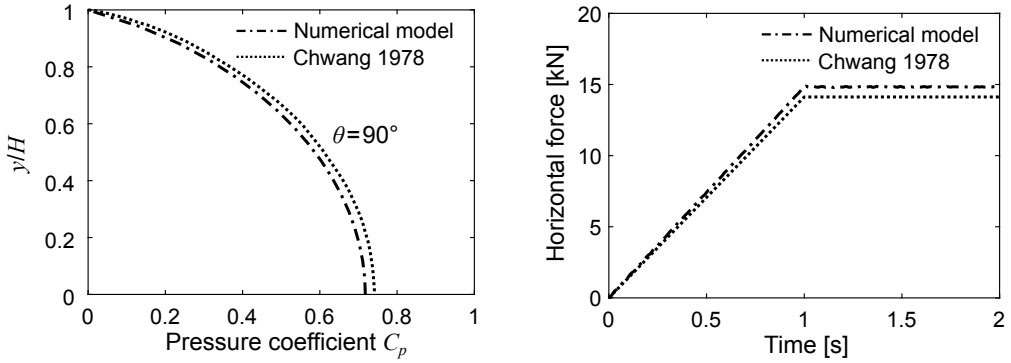

(a) Pressure coefficient (b) Horizontal hydrodynamic force

Figure 3.31 Linear elastic behavior: computed results, Θ = 90°

We also perform the computation for the upstream face of the dam inclined with a constant slope Θ = 75°. The computed hydrodynamic pressure distribution is shown in Figure 3.32a and the computed horizontal and vertical hydrodynamic force exerted on the upstream face of the dam are shown in Figure 3.32b. We can conclude that computed results closely match analytical solutions.

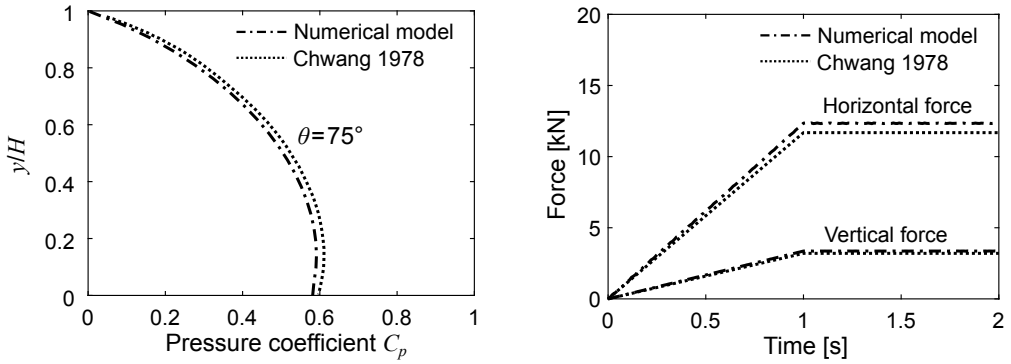

(a) Pressure coefficient (b) Hydrodynamic forces

Figure 3.32 Linear elastic behavior: computed results, Θ = 75°

The hydrodynamic pressure distribution in the reservoir, and excess pore pressure distribution in the body of the dam at $t = 2$ s and at $t = 10$ s for vertical upstream face are shown in Figures 3.33a and 3.33b, and in Figures 3.34a and 3.34b for inclined upstream face.

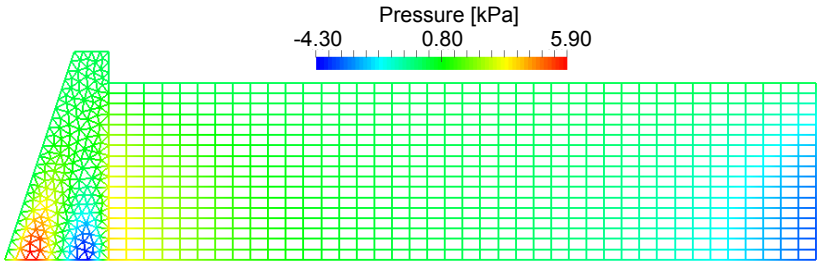

(a) $t = 2$ s

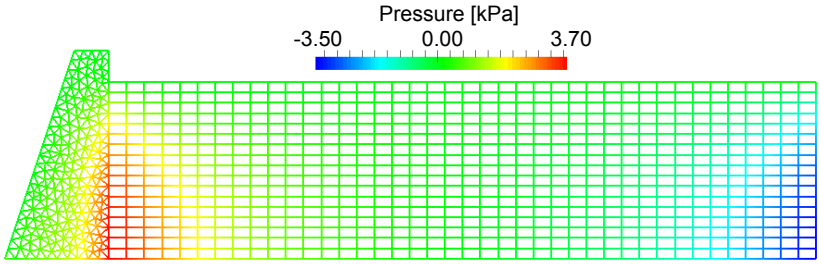

(b) $t = 10$ s

Figure 3.33 Pressure and excess pore pressure distribution: $\Theta = 90°$

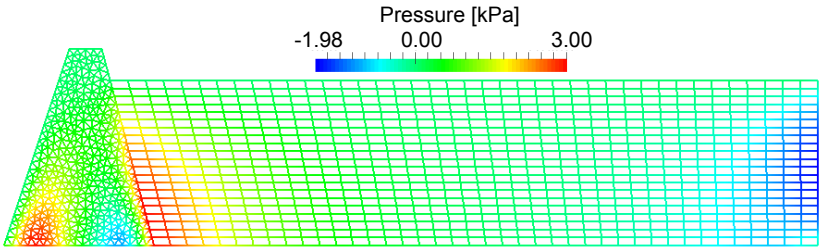

(a) $t = 2$ s

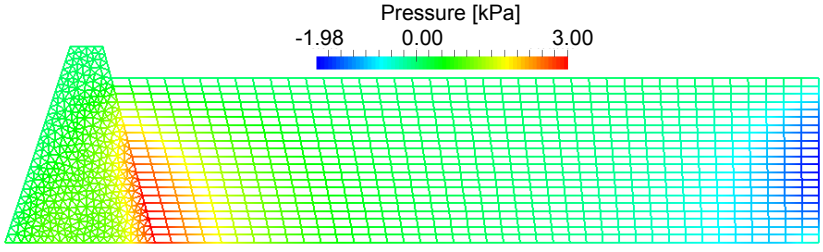

(b) $t = 10$ s

Figure 3.34 Pressure and excess pore pressure distribution: $\Theta = 75°$

→ Localized failure analysis of dam structure

In this section, we perform a nonlinear dynamic analysis, following the loading program shown in Figure 3.30b, with the aim to determine the horizontal overload, which results with the localized failure of dam structure. We introduce yield and fracture limits for the Timoshenko beam finite element in tension, compression and shear: $\sigma_{y,t}$ = 0.015 MPa; $\sigma_{y,c}$ = 0.20 MPa; $\sigma_{y,s}$ = 0.015 MPa; $\sigma_{f,t}$ = 0.02 MPa; $\sigma_{f,c}$ = 0.30 MPa; $\sigma_{f,s}$ = 0.02 MPa. The fracture energies in tension, compression and shear are: $G_{f,t}$ = 0.01 GN/m; $G_{f,c}$ = 0.1 GN/m; $G_{f,s}$ = 0.01 GN/m. The linear hardening modulus is $H_{lh} = 10^3$ MPa, linear kinematic hardening modulus is $H_{lk} = 10^3$ MPa, nonlinear hardening parameter is $H_{nlk} = 10^2$, and the viscosity parameter is η = 10 MPa s.

We present computed results with respect to computed horizontal displacement of the tip of the dam → point A(3, 6)[m]. The computed ultimate value of horizontal overload that results with the ultimate state of localized failure of dam structure is 92.8187 kN, which corresponds to the horizontal ground acceleration of 2.466 m/s^2 (Figure 3.35a). The self-weight and hydrostatic loading resulted in the total horizontal reaction equal to 130.05 kN. We can conclude that for this particular geometry and mechanical properties, the computed factor of safety of the dam subjected to combined quasi-static and extreme dynamic loads is 1.71. The excess pore pressure at point B(1.0175, 0.2776)[m] is shown in Figure 3.35b. The deformed configuration of the dam, and the broken cohesive links in increasing softening at the end of the loading program are shown in Figures 3.36a-3.36c. The values of displacement jumps in the broken cohesive links are shown in Figures 3.36d and 3.36e.

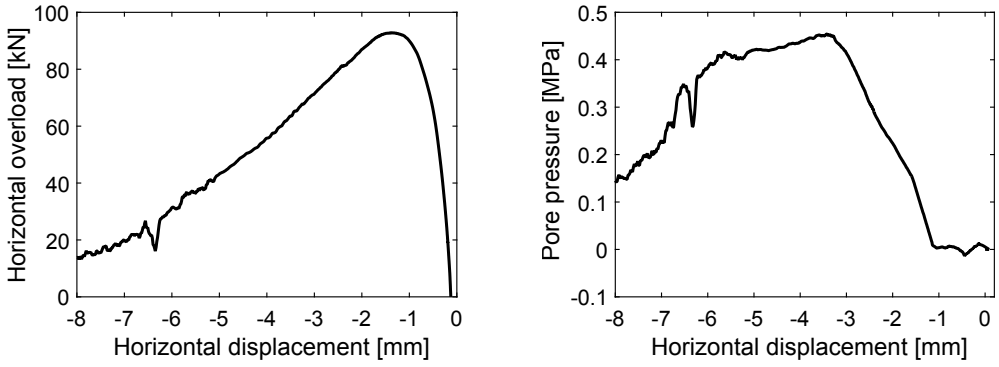

(a) Horizontal overload (b) Excess pore pressure at point B

Figure 3.35 Horizontal overload, dynamic case: computed results

We also perform the uncoupled computation of the structure response. The uncoupled computation results in a much lower value of the computed horizontal

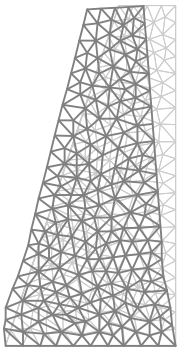

(a) Deformed configuration

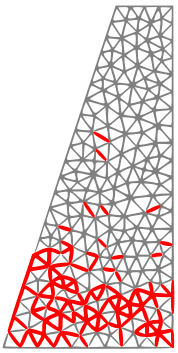

(b) Borken cohesive links: mode I

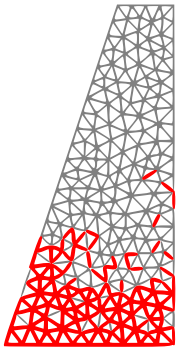

(c) Broken cohesive links: mode II

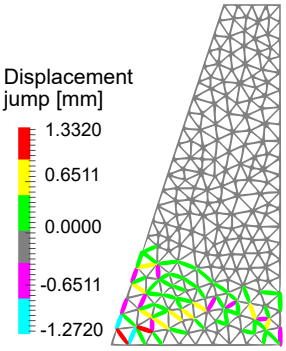

(d) Displacement jumps: mode I

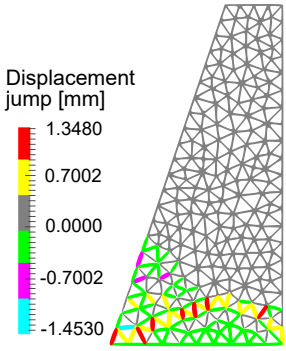

(e) Displacement jumps: mode II

Figure 3.36 Failure mode for horizontal overload, dynamic case

overload (33.8414 kN) compared to the coupled case, as shown in Figure 3.37. Namely, the failure mode for horizontal overload brought by imposed horizontal ground acceleration modeled in terms of equivalent horizontal forces results in an increase in the value of the admissible horizontal overload compared to the uncoupled case.

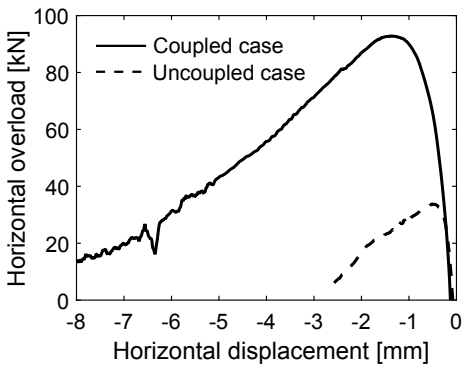

Figure 3.37 Comparison of horizontal overloads, dynamic case

3.4 Concluding remarks

In this Chapter, we presented a novel approach to numerical modeling of the acoustic fluid-structure interaction nonlinear problems. The structure is represented in terms of a saturated porous medium. The structure response is modeled with coupled discrete beam lattice model, which is based on Voronoi cell representation with inelastic Timoshenko beam finite elements enhanced with additional kinematics as cohesive links. The internal coupling is handled with Biot's porous media theory. The motion of the external fluid in interaction with the structure is described with the Lagrangian formulation and mixed displacement/pressure based finite element approximation. The main advantage of the proposed numerical model for acoustic fluid-structure interaction is in the resulting set of degrees of freedom per node of structure and external fluid finite elements, which permits for the elements to be connected directly at the common nodes without any need for special numerical consideration of the fluid-structure interface. As a result, the direct exchange of both motion and the pressure at the common boundary is ensured, and all unknown fields can be computed in a fully monolithic manner.

We have confirmed through numerical simulations that the proposed numerical model of interaction is capable of predicting both the hydrostatic and hydrodynamic pressures and forces exerted on the upstream face of the structure in close agreement with analytical solutions. In addition, we are able to model the formation of cracks and plastic zones in the structure subjected to fundamental load cases, such as the self-weight and hydrostatic loading.

Finally, we have illustrated the proposed model ability to represent localized failure modes, and thus quantify the overall safety of the dam structure to potential overload with respect to the fundamental load cases. The computation of this kind in a quasi-static setting is performed by imposing either horizontal or vertical displacement upon the dam deformed configuration, which is obtained under the dead-load and reservoir pressure. In a dynamic setting, the localized failure of dam structure is brought by subjecting the dam-reservoir system to the linear increasing horizontal ground acceleration, which is modeled in terms of equivalent horizontal forces. We have shown qualitatively how different types of failure modes affect the computed value of admissible overload compared to the uncoupled case of structure response. Namely, for different types of loading programs, the presence of the pore fluid can increase or decrease the computed value of admissible overload. Thus, the ability of the proposed formulation to quantify the overall structure safety for a particular loading program is very important from the standpoint of

engineering practice dealing with issues of the structure design, both in terms of the structural integrity and structural durability.

For a more detailed explanation of computed admissible overload for a particular loading program, we go back to Terzaghi's principle of effective stresses (see Chapter 2), which states that the total normal stress is equal to the sum of effective stress carried by the solid phase, and pore pressure carried by the pore fluid. We can rewrite this principle in terms of total reaction, which we can interpret as the ultimate load value structure can withstand until failure. Namely, the total reaction in the coupled model R^c at each time step is equal to the sum of contributions of effective reaction carried by the solid phase R^e, and the reaction carried by the fluid in pores R^p, written as

$$R^c = R^e + R^p$$

For uncoupled model, the total reaction R^{uc} is equal to

$$R^{uc} = R^e$$

In our case, we can state that the reaction R^e obtains approximately the same value regardless of the structure response being coupled or uncoupled. To explain this, we return to Mohr-Coulomb's law, which states that the strength of the material depends on the cohesion and the friction, and that friction is directly proportional to the effective normal stress. The strength of cohesive materials, such as rocks or concrete, dominantly depends on the value of cohesion and contribution of the friction is not as significant. This is the case in our proposed coupled discrete beam lattice model, which makes this model suitable for cohesive types of materials. The fracture limits in tension, compression, and shear define the ultimate load level structure can withstand until ultimate failure for a particular loading program, and this part is constant regardless of the structure response being coupled or uncoupled. An increase in the ultimate load value can be obtained if the Mohr-Coulomb's law is implemented for defining the fracture limit in shear (see Section 2.5.3). Thus, if the latter is not implemented, we can state that the contribution of the solid phase to the total value of the total reaction is constant. Hence, the value of the total reaction changes due to the contribution of the pore fluid. Depending on the time evolution of the pore pressures in the body of the dam for different types of failure modes, the contribution of the pore fluid can increase or decrease the total reaction compared to the uncoupled case.

The proposed model of interaction, even when pushed to the extreme while computing the final phase of localized failure, exhibits good performance in terms of fast convergence rates and efficient computational time. In Tables 3.2 and 3.3, we give the residual and energy convergence rates for a typical time step per each computation phase of localized failure analysis of pore-saturated dam structure under horizontal overload in a quasi-static setting. The computational times for horizontal and vertical overloads in a quasi-static setting with included first two computation phases are 720.83 s, and 815.52 s, respectively. The computational time for horizontal overload in a dynamic setting is 1050.07 s (Processor: Intel Core i7-3632QM/2.2GHz, RAM 8.00GB, FEAP: single-core).

Table 3.2 Convergence rates: residual norm for selected time steps

Iteration	Self-weight phase Time step: 50	Hydrostatic loading phase Time step: 180	Localized failure Time step: 1610
1	$2.4177 \cdot 10^{-04}$	$3.4008 \cdot 10^{-04}$	$1.2834 \cdot 10^{-02}$
2	$5.4542 \cdot 10^{-04}$	$4.6168 \cdot 10^{-04}$	$8.8185 \cdot 10^{-04}$
3	$2.0887 \cdot 10^{-05}$	$1.7170 \cdot 10^{-05}$	$4.4117 \cdot 10^{-04}$
4	$8.7336 \cdot 10^{-16}$	$1.6796 \cdot 10^{-13}$	$1.3242 \cdot 10^{-04}$
5			$2.5074 \cdot 10^{-05}$
6			$1.0504 \cdot 10^{-04}$
7			$3.9459 \cdot 10^{-07}$
8			$2.0083 \cdot 10^{-13}$

Table 3.3 Convergence rates: energy norm for selected time steps

Iteration	Self-weight phase Time step: 50	Hydrostatic loading phase Time step: 180	Localized failure Time step: 1610
1	$9.7579 \cdot 10^{-10}$	$8.2718 \cdot 10^{-09}$	$2.6056 \cdot 10^{-08}$
2	$7.6616 \cdot 10^{-11}$	$9.7831 \cdot 10^{-11}$	$5.8175 \cdot 10^{-10}$
3	$8.2985 \cdot 10^{-14}$	$2.7183 \cdot 10^{-14}$	$1.4944 \cdot 10^{-10}$
4	$3.5316 \cdot 10^{-35}$	$1.0109 \cdot 10^{-29}$	$5.8688 \cdot 10^{-12}$
5			$7.2201 \cdot 10^{-13}$
6			$6.4927 \cdot 10^{-13}$
7			$2.3475 \cdot 10^{-17}$
8			$6.3199 \cdot 10^{-29}$

CHAPTER 4

EXTENSION TO 3D CASE

ABSTRACT

In this Chapter, we extend the proposed two-dimensional (2D) numerical model of acoustic fluid-structure interaction to the three-dimensional (3D) setting. The 3D numerical model of interaction inherits all the main features and benefits of the 2D model, with modifications that arise due to the added dimension of the model. The structure response is described with coupled discrete beam lattice model of structure built of saturated poro-plastic cohesive material. The small motion of external fluid motion in contained conditions is described with acoustic wave theory and modeled with the Lagrangian formulation and mixed displacement/pressure based finite element approximation. The finite element representations of the structure and the external fluid allow for the issue of the fluid-structure interface to be solved through element assembly procedure. The application of the model is illustrated through several numerical simulations.

OUTLINE

4.1 Introduction

In this Chapter, we extend the two-dimensional (2D) numerical models of pore-saturated structure, external fluid and ultimately acoustic fluid-structure interaction previously presented in Chapters 2 and 3 to three-dimensional (3D) setting.

The outline of the Chapter is as follows: In Section 4.2, we describe the main features of the coupled discrete beam lattice model of the structure in a 3D setting. In Section 4.3, we present the finite element formulation of the proposed coupled discrete beam lattice model, together with the computational procedure. The finite element formulation is given in fully dynamics framework, which can be easily adjusted for quasi-static simplification. In Section 4.4, we provide finite element approximation for external fluid. In Section 4.5, we present the results of several numerical simulations. First, we simulate the response of the structure alone, with the aim to validate the proposed model of the structure and to demonstrate its capabilities to deal with nonlinear behavior and progressive localized failure in structures built of saturated poro-plastic cohesive material. Second, we simulate the response of dam structure under reservoir interaction. In Section 4.6, we give concluding remarks.

4.2 Discrete model of structure

For the numerical representation of the structure built of a saturated poro-plastic medium, we extend the proposed 2D plane strain coupled discrete beam lattice model to the 3D setting. For the construction of the discrete lattice model in the 3D framework, we use the same procedure described previously in Chapter 2, Section 2.3. Namely, the construction of the model is performed by exploiting the duality property between the Voronoi cell representation and Delaunay tetrahedralization of the domain (Figure 4.1). The end result of Delaunay tetrahedralization is the mesh of tetrahedra. Every edge of tetrahedra connects the centers of two adjacent Voronoi cells and is perpendicular to the polygon shared between these two cells. We place along each edge of tetrahedra a cohesive link, whose behavior we model with the 1D finite element. The cross-section of each finite element is the polygon shared between two adjacent cells. In general case, the polygonal cross-section for every finite element is of a different shape. To simplify the matter, we replace the polygonal cross-section for every finite element with an equivalent circular cross-section (Figure 4.1). Namely, we compute the diameter of an equivalent circular cross-section from the condition that the area of the polygon obtained from Voronoi cell representation is equal to the area of a circular cross-section.

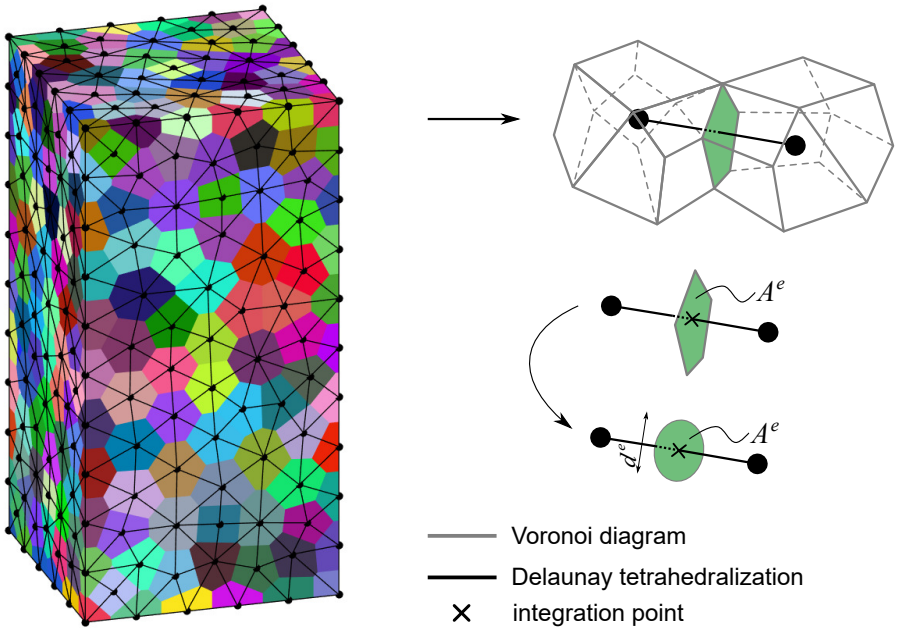

Figure 4.1 Voronoi diagram and Delaunay tetrahedralization

The behavior of cohesive links is again modeled with inelastic Timoshenko beam finite elements with enhanced kinematics [117, 118]. For the 3D case of discrete beam lattice model, Timoshenko beam finite element is enhanced with additional kinematics in terms of embedded discontinuities in axial and both transverse directions. Thus, enhanced Timoshenko beam finite element is, in addition to the mode I and mode II, capable of modeling crack formation in mode III as well. Mode I relates to crack opening, mode II relates to in-plane crack sliding, and mode III relates to the out-of-plane shear sliding. It is important to note that linear elastic parameters of Timoshenko beam finite element, Young's modulus and Poisson's ratio can be identified in the same manner as previously noted in Chapter 2, Section 2.3.

In a 3D numerical model of structure built of a saturated poro-plastic medium, we spread the pore fluid flow across the mesh of tetrahedra (Tet4 - linear tetrahedral finite elements) that coincides with the mesh of tetrahedra obtained by Delaunay tetrahedralization of the domain. For numerical integration on tetrahedral finite elements, we choose nodal point rule which positions the integration points at every node of tetrahedra [153]. The integration rule of this kind eliminates the contribution of two nodes and leaves the contribution of the two nodes that correspond to the Timoshenko beam finite element. This allows us to treat the pore pressure as an additional degree of freedom placed at each node of the Timoshenko beam finite element, which we later use for the fluid-structure interface (Figure 4.2).

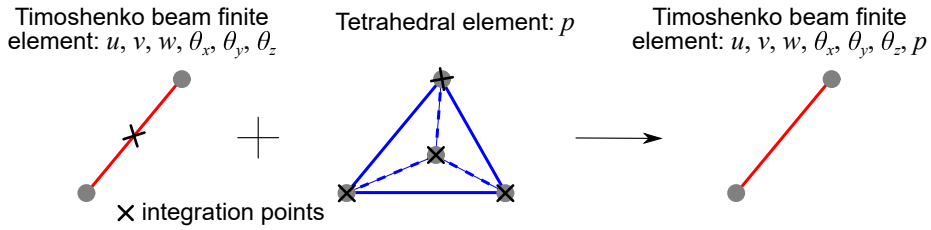

Figure 4.2 Displacement and pore pressure fields finite element approximations, 3D case

Next, we give an overview of the finite element formulation of the coupled discrete beam lattice model of pore-saturated structures in a 3D setting. The starting point for our work on the proposed model is the Timoshenko beam finite element presented in [117, 32, 118].

4.3 Finite element formulation

4.3.1 Kinematics

Consider a straight Timoshenko beam finite element of length L^e and cross-sectional area A^e. All equations for Timoshenko beam finite element are expressed in a local coordinate frame, which can be easily adapted to the global frame by using standard local-global transformation (Figure 4.3).

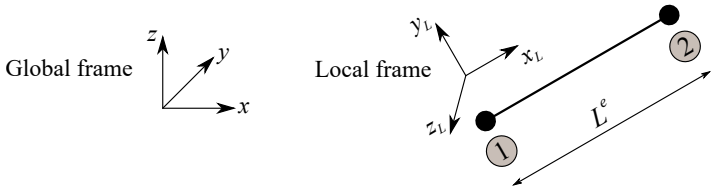

Figure 4.3 Local and global coordinate frame

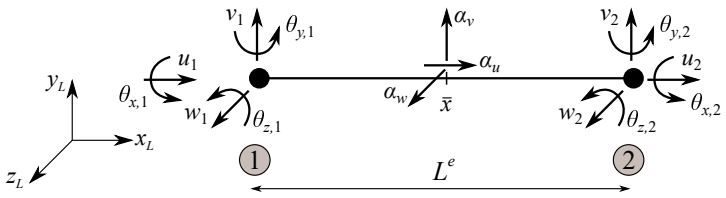

Figure 4.4 Timoshenko beam finite element in 3D framework

The element has two nodes, and six degrees of freedom per node: axial displacement u along local x axis, transverse displacements v and w along local y and z axes, and rotations of cross-section θ_x, θ_y, θ_z around local x, y, z axes, respectively

(Figure 4.4). For simplicity, we considered a Timoshenko beam placed along the global x axis. The displacement fields are enhanced in axial and both transverse directions with embedded strong discontinuities in order to model all three modes of crack formation (Figure 4.5). The enhanced displacement fields are interpolated as

$$\mathbf{u} = \mathbf{N}_u^s \bar{\mathbf{u}} + \mathbf{M}\boldsymbol{\alpha} \tag{4.1}$$

where

$$\mathbf{u}^\mathsf{T} = \left\{u,\ v,\ w,\ \theta_x,\ \theta_y,\ \theta_z\right\};$$

$$\bar{\mathbf{u}}^\mathsf{T} = \left\{u_1,\ v_1,\ w_1,\ \theta_{x,1},\ \theta_{y,1},\ \theta_{z,1},\ u_2,\ v_2,\ w_2,\ \theta_{y,2},\ \theta_{z,2}\right\};$$

$$\mathbf{N}_u^s = \begin{bmatrix} N_1 & 0 & 0 & 0 & 0 & 0 & N_2 & 0 & 0 & 0 & 0 & 0 \\ 0 & N_1 & 0 & 0 & 0 & 0 & 0 & N_2 & 0 & 0 & 0 & 0 \\ 0 & 0 & N_1 & 0 & 0 & 0 & 0 & 0 & N_2 & 0 & 0 & 0 \\ 0 & 0 & 0 & N_1 & 0 & 0 & 0 & 0 & 0 & N_2 & 0 & 0 \\ 0 & 0 & 0 & 0 & N_1 & 0 & 0 & 0 & 0 & 0 & N_2 & 0 \\ 0 & 0 & 0 & 0 & 0 & N_1 & 0 & 0 & 0 & 0 & 0 & N_2 \end{bmatrix}; \quad \left\{N_1, N_2\right\} = \left\{1 - \tfrac{x}{L^e},\ \tfrac{x}{L^e}\right\};$$

$$\mathbf{M} = \begin{bmatrix} M & 0 & 0 & 0 & 0 & 0 \\ 0 & M & 0 & 0 & 0 & 0 \\ 0 & 0 & M & 0 & 0 & 0 \\ 0 & 0 & 0 & 0 & 0 & 0 \\ 0 & 0 & 0 & 0 & 0 & 0 \\ 0 & 0 & 0 & 0 & 0 & 0 \end{bmatrix}; \quad \boldsymbol{\alpha}^\mathsf{T} = \left\{\alpha^u,\ \alpha^v,\ \alpha^w,\ 0,\ 0,\ 0\right\} \tag{4.2}$$

Here, α^u, α^v and α^w represent displacement jumps in axial, in-plane transverse and out-of-plane transverse direction.

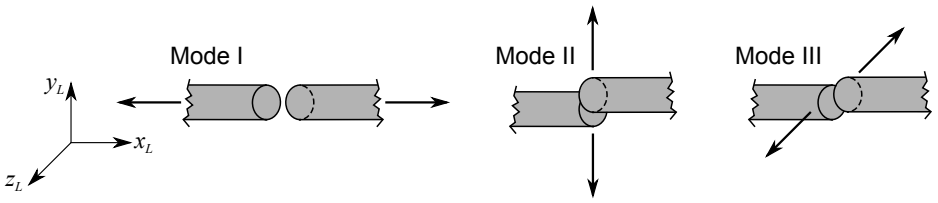

Figure 4.5 Three modes of crack formation

The enhanced strain fields are interpolated as

$$\boldsymbol{\epsilon} = \mathbf{B}_u^s \bar{\mathbf{u}} + \mathbf{G}\boldsymbol{\alpha} \tag{4.3}$$

where

$$\boldsymbol{\epsilon}^\mathsf{T} = \left\{\varepsilon_{xx},\ \gamma_{xy},\ \gamma_{xz},\ \kappa_x,\ \kappa_y,\ \kappa_z\right\} \Rightarrow \begin{cases} \varepsilon_{xx} = \dfrac{du}{dx} & \kappa_x = \dfrac{d\theta_x}{dx} \\ \gamma_{xy} = \dfrac{dv}{dx} - \theta_z & \kappa_y = \dfrac{d\theta_y}{dx} \\ \gamma_{xz} = \dfrac{dw}{dx} + \theta_y & \kappa_z = \dfrac{d\theta_z}{dx} \end{cases};$$

$$\mathbf{B}_u^s = \begin{bmatrix} B_1 & 0 & 0 & 0 & 0 & 0 & B_2 & 0 & 0 & 0 & 0 & 0 \\ 0 & B_1 & 0 & 0 & 0 & -N_1 & 0 & B_2 & 0 & 0 & 0 & -N_2 \\ 0 & 0 & B_1 & 0 & N_1 & 0 & 0 & 0 & B_2 & 0 & N_2 & 0 \\ 0 & 0 & 0 & B_1 & 0 & 0 & 0 & 0 & 0 & B_2 & 0 & 0 \\ 0 & 0 & 0 & 0 & B_1 & 0 & 0 & 0 & 0 & 0 & B_2 & 0 \\ 0 & 0 & 0 & 0 & 0 & B_1 & 0 & 0 & 0 & 0 & 0 & B_2 \end{bmatrix}; \quad \begin{aligned} \left\{B_1, B_2\right\} &= \left\{\tfrac{dN_1}{dx}, \tfrac{dN_2}{dx}\right\} \\ &= \left\{-\tfrac{1}{L^e}, \tfrac{1}{L^e}\right\}; \end{aligned}$$

$$\mathbf{G} = \begin{bmatrix} G & 0 & 0 & 0 & 0 & 0 \\ 0 & G & 0 & 0 & 0 & 0 \\ 0 & 0 & G & 0 & 0 & 0 \\ 0 & 0 & 0 & 0 & 0 & 0 \\ 0 & 0 & 0 & 0 & 0 & 0 \\ 0 & 0 & 0 & 0 & 0 & 0 \end{bmatrix} \tag{4.4}$$

where ε_{xx} is the axial strain, γ_{xy}, γ_{xz} are the shear strains, and κ_x, κ_y, κ_z are the curvatures. In what is to follow, we will denote these strains with following symbols ε, γ_y, γ_z, κ_x, κ_y and κ_z.

The pore pressure field is approximated with tetrahedral finite elements with four nodes (Figure 4.6). The finite element approximation for the pore pressure field is written as

$$p = \mathbf{N}_p^s \bar{\mathbf{p}} \tag{4.5}$$

where

$$\bar{\mathbf{p}}^{\mathsf{T}} = \left\{p_1,\, p_2,\, p_3,\, p_4\right\};$$

$$\mathbf{N}_p^s = \left\{N_1^p,\, N_2^p,\, N_3^p,\, N_4^p\right\};\quad N_i^p = \frac{a_i + b_i x + c_i y + d_i z}{6V},\quad i = 1,4;$$

$$6V = det\begin{vmatrix} 1 & x_1 & y_1 & z_1 \\ 1 & x_2 & y_2 & z_2 \\ 1 & x_3 & y_3 & z_3 \\ 1 & x_4 & y_4 & z_4 \end{vmatrix};\qquad a_1 = det\begin{vmatrix} x_2 & y_2 & z_2 \\ x_3 & y_3 & z_3 \\ x_4 & y_4 & z_4 \end{vmatrix};\qquad b_1 = -det\begin{vmatrix} 1 & y_2 & z_2 \\ 1 & y_3 & z_3 \\ 1 & y_4 & z_4 \end{vmatrix};$$

$$c_1 = -det\begin{vmatrix} x_2 & 1 & z_2 \\ x_3 & 1 & z_3 \\ x_4 & 1 & z_4 \end{vmatrix};\qquad d_1 = -det\begin{vmatrix} x_2 & y_2 & 1 \\ x_3 & y_3 & 1 \\ x_4 & y_4 & 1 \end{vmatrix};\qquad (4.6)$$

$$etc.$$

where V is the volume of the tetrahedral element, x,y,z are global coordinates, x_i, y_i, z_i are nodal coordinates of tetrahedral element, and constants a_{2-4}, b_{2-4}, c_{2-4}, d_{2-4} are defined by cyclic interchange of the subscripts in the order $1,2,3,4$.

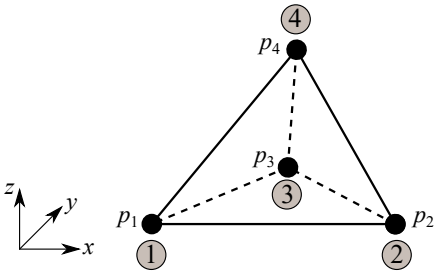

Figure 4.6 Linear tetrahedral finite element

The time derivatives of displacement and pore pressure fields are written as

$$\dot{\mathbf{u}} = \mathbf{N}_u^s \dot{\mathbf{u}};\quad \dot{p} = \mathbf{N}_p^s \dot{\mathbf{p}}$$
$$\ddot{\mathbf{u}} = \mathbf{N}_u^s \ddot{\mathbf{u}};\quad \ddot{p} = \mathbf{N}_p^s \ddot{\mathbf{p}} \qquad (4.7)$$

4.3.2 Continuity equation and equations of motion

4.3.2.1 Continuity equation

The coupling of the mechanics and the pore fluid flow occurs through the axial direction of the Timoshenko beam finite element. The continuity equation for fluid

flow through the porous body is written as

$$\frac{1}{M}\dot{p} + + b\dot{\varepsilon} - \frac{k}{\gamma_f}\nabla\cdot(\nabla p) = 0 \tag{4.8}$$

The weak from of the continuity equation is obtained through the principle of virtual works, written as

$$\int_{\Omega^e_{Tet4}} \delta p\Big[\frac{1}{M}\dot{p} - \frac{k}{\gamma_f}\nabla\cdot(\nabla p)\Big]d\Omega + \int_0^{L^e} \delta p^{\backprime} b\dot{\varepsilon}\,dx = 0 \tag{4.9}$$

where δp is the virtual pore pressure field interpolated in the same manner as the real pore pressure field

$$\begin{aligned}
&\delta p = \mathbf{N}^s_p \delta\bar{\mathbf{p}};\;\; \delta\bar{\mathbf{p}}^{\mathsf{T}} = \Big\{\delta p_1,\, \delta p_2,\, \delta p_3,\, \delta p_4\Big\};\\
&p^{\backprime} = \mathbf{N}^s_{up}\bar{\mathbf{p}}^{\backprime};\;\; \mathbf{N}^s_{up} = \Big\{N_1,\, N_2\Big\};\;\; \bar{\mathbf{p}}^{\backprime\mathsf{T}} = \Big\{p_1,\, p_2\Big\};\\
&\delta p^{\backprime} = \mathbf{N}^s_{up}\delta\bar{\mathbf{p}}^{\backprime};\;\; \delta\bar{\mathbf{p}}^{\backprime\mathsf{T}} = \Big\{\delta p_1,\, \delta p_2\Big\}
\end{aligned} \tag{4.10}$$

4.3.2.2 Equations of motion

The strong form of the equations of motion for a 3D Timoshenko beam with a circular cross-section is written as

$$-\rho A^e\frac{\partial^2 u}{\partial t^2} + \frac{\partial N}{\partial x} + n(x,t) = 0 \tag{4.11}$$

$$-\rho A^e\frac{\partial^2 v}{\partial t^2} + \frac{\partial V_y}{\partial x} + q_y(x,t) = 0 \tag{4.12}$$

$$-\rho A^e\frac{\partial^2 w}{\partial t^2} + \frac{\partial V_z}{\partial x} + q_z(x,t) = 0 \tag{4.13}$$

$$-\rho I^e_{pol}\frac{\partial^2\theta_x}{\partial t^2} + \frac{\partial M_x}{\partial x} + m_x(x,t) = 0 \tag{4.14}$$

$$-\rho I^e_{yy}\frac{\partial^2\theta_y}{\partial t^2} + \frac{\partial M_y}{\partial x} - V_z + m_y(x,t) = 0 \tag{4.15}$$

$$-\rho I^e_{zz}\frac{\partial^2\theta_z}{\partial t^2} + \frac{\partial M_z}{\partial x} + V_y + m_z(x,t) = 0 \tag{4.16}$$

where ρ is the mass density, A^e is the are of a cross-section, I^e_{yy}, I^e_{zz} are the second moments of inertia of a cross-section, I^e_{pol} is the polar moment of inertia of a cross-section, n, q_y, q_z, m_x, m_y and m_z are the distributed external loads, and $N = N' - bp^{\backprime}A^e$ is the total axial force, $V_y = V'_y$, $V_z = V'_z$ are the shear forces, $M_x = M'_x$

is the torsion moment, $M_y = M'_y$, $M_z = M'_z$ are the bending moments (Figure 4.7). The superscript $'$ denotes effective force. Here, we assume that the coupling of the mechanics and the internal fluid flow occurs through the axial direction of the Timoshenko beam finite element.

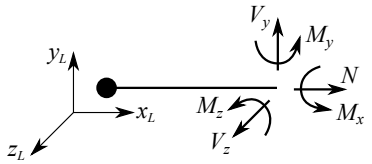

Figure 4.7 Stress resultants

The weak form of equations of motion for Timoshenko beam finite element is derived from the d'Alembert principle. The virtual displacement and virtual strain fields are interpolated in the same manner as the real displacement and real strain fields, written as

$$\delta \mathbf{u} = \mathbf{N}_u^s \delta \bar{\mathbf{u}} + \mathbf{M} \delta \boldsymbol{\alpha} \tag{4.17}$$

$$\delta \boldsymbol{\epsilon} = \mathbf{B}_u^s \delta \bar{\mathbf{u}} + \mathbf{G} \delta \boldsymbol{\alpha} \tag{4.18}$$

where

$$\begin{aligned}
\delta \mathbf{u}^{\mathsf{T}} &= \left\{ \delta u,\, \delta v,\, \delta w,\, \delta \theta_x,\, \theta_y,\, \delta \theta_z \right\}; \\
\delta \bar{\mathbf{u}}^{\mathsf{T}} &= \left\{ \delta u_1,\, \delta v_1,\, \delta w_1,\, \delta \theta_{x,1},\, \delta \theta_{y,1},\, \delta \theta_{z,1},\, \delta u_2,\, \delta v_2,\, \delta w_2,\, \delta \theta_{x,2},\, \delta \theta_{y,2},\, \delta \theta_{z,2} \right\}; \\
\delta \boldsymbol{\alpha}^{\mathsf{T}} &= \left\{ \delta \alpha^u,\, \delta \alpha^v,\, \delta \alpha^w,\, 0,\, 0,\, 0 \right\}; \\
\delta \boldsymbol{\epsilon}^{\mathsf{T}} &= \left\{ \delta \varepsilon,\, \delta \gamma_y,\, \delta \gamma_z,\, \delta \kappa_x,\, \delta \kappa_y,\, \delta \kappa_z \right\}
\end{aligned} \tag{4.19}$$

The virtual work of external forces is computed as

$$G^{ext,e} = \delta \bar{\mathbf{u}}^{\mathsf{T}} \mathbf{f}^{ext,e} - \delta \bar{\mathbf{u}}^{\mathsf{T}} \mathbf{f}^{acc,e} \tag{4.20}$$

where

$$\begin{aligned}
\mathbf{f}^{acc,e} &= \int_0^{L^e} \mathbf{N}_u^{s,\mathsf{T}} \ddot{\boldsymbol{\sigma}}\, dx; \\
\ddot{\boldsymbol{\sigma}}^{\mathsf{T}} &= \left\{ \rho A^e \ddot{u}, \rho A^e \ddot{v}, \rho A^e \ddot{w}, \rho I_{pol}^e \ddot{\theta}_x, \rho I_{yy}^e \ddot{\theta}_y, \rho I_{zz}^e \ddot{\theta}_z \right\}
\end{aligned} \tag{4.21}$$

The virtual work of internal forces for Timoshenko finite beam finite element is equal to

$$G^{int,e} = \int_0^{L^e} \left(\mathbf{B}_u^s \delta\bar{\mathbf{u}}\right)^\mathsf{T} \boldsymbol{\sigma}\, dx + \int_0^{L^e} \left(\mathbf{G}\delta\boldsymbol{\alpha}\right)^\mathsf{T} \boldsymbol{\sigma}_u dx \tag{4.22}$$

where

$$\begin{aligned}
&\boldsymbol{\sigma}^\mathsf{T} = \left\{N, V_y, V_z, M_x, M_y, M_z\right\} = \left\{N' - bp\backslash A^e, V_y', V_z', M_x', M_y', M_z'\right\};\\
&\boldsymbol{\sigma}^\mathsf{T} = \boldsymbol{\sigma}_u^\mathsf{T} - \boldsymbol{\sigma}_p^\mathsf{T};\\
&\boldsymbol{\sigma}_u^\mathsf{T} = \left\{N', V_y', V_z', M_x', M_y', M_z'\right\};\ \ \boldsymbol{\sigma}_p^\mathsf{T} = \left\{bp\backslash A^e, 0, 0, 0, 0, 0\right\}
\end{aligned} \tag{4.23}$$

The virtual work of internal forces consists of two parts. The first is the virtual work of internal forces in the bulk part of the element (part of the element outside the discontinuity), and the second is the virtual work of internal forces acting at the discontinuity, written as

$$G^{int,e} = \delta\bar{\mathbf{u}}^T \mathbf{f}^{int,e} + \delta\boldsymbol{\alpha}^T \mathbf{h}^e \tag{4.24}$$

where $\mathbf{f}^{int,e}$ is the internal force vector, and $\mathbf{h}^e$ is the residual vector due to discontinuity, computed as

$$\begin{aligned}
&\mathbf{f}^{int,e} = \int_0^{L^e} \mathbf{B}_u^{s,\mathsf{T}} \boldsymbol{\sigma}\, dx = \mathbf{f}^{int,e}(\boldsymbol{\sigma}_u) - \mathbf{f}^{int,e}(\boldsymbol{\sigma}_p);\\
&\mathbf{h}^e = \int_0^{L^e} \mathbf{G}^\mathsf{T} \boldsymbol{\sigma}_u dx = \int_0^{L^e} \bar{\mathbf{G}}^\mathsf{T} \boldsymbol{\sigma}_u dx + \mathbf{t};\quad \bar{\mathbf{G}} = \begin{bmatrix} \bar{G} & 0 & 0 & 0 & 0 & 0\\ 0 & \bar{G} & 0 & 0 & 0 & 0\\ 0 & 0 & \bar{G} & 0 & 0 & 0\\ 0 & 0 & 0 & 0 & 0 & 0\\ 0 & 0 & 0 & 0 & 0 & 0\\ 0 & 0 & 0 & 0 & 0 & 0 \end{bmatrix};\\
&\qquad\qquad \mathbf{t}^\mathsf{T} = \left\{t^u, t^v, t^w, 0, 0, 0\right\}
\end{aligned} \tag{4.25}$$

Here, $\mathbf{t}$ is the internal force vector acting at the discontinuity.

By exploiting the principle of virtual work we obtain

$$0 = G^{int,e} - G^{ext,e} = \delta\bar{\mathbf{u}}^\mathsf{T}(\mathbf{f}^{int,e} - \mathbf{f}^{ext,e} + \mathbf{f}^{acc,e}) + \delta\boldsymbol{\alpha}^\mathsf{T}\mathbf{h}^e \tag{4.26}$$

Previous equation is satisfied if

$$\mathbf{f}^{acc,e} + \mathbf{f}^{int,e} - \mathbf{f}^{ext,e} = \mathbf{0} \tag{4.27}$$

$$\mathbf{h}^{e} = \mathbf{0} \tag{4.28}$$

The Equation (4.27) relates to the bulk part of the element, and the Equation (4.28) relates to the discontinuity.

The internal force vector **t** acting at the discontinuity is computed from the following conditions

$$\left.\begin{aligned} \mathbf{h^e} &= 0 \\ \int_0^{L^e} \bar{G} dx = \int_0^{L^e} -\frac{1}{L^e} dx &= -1 \end{aligned}\right\} \Rightarrow \mathbf{t} = \begin{bmatrix} 1&0&0&0&0&0 \\ 0&1&0&0&0&0 \\ 0&0&1&0&0&0 \\ 0&0&0&0&0&0 \\ 0&0&0&0&0&0 \\ 0&0&0&0&0&0 \end{bmatrix} \int_0^{L^e} \boldsymbol{\sigma}_u dx \tag{4.29}$$

4.3.3 Constitutive model

The pre-peak response of the 3D Timoshenko beam finite element in axial, and both transverse directions is described with the elasto-viscoplastic constitutive model with implemented linear hardening [124], and Fredrick-Armstrong non-linear kinematic hardening law [127]. The post-peak response of the element is described with exponential softening. The behavior of the element in bending and torsion is purely linear elastic.

4.3.3.1 Plasticity model

The proposed model of plasticity is described with [124]

1. Additive decomposition of the total strain into elastic and viscoplastic part, with only the elastic part influencing the value of the stresses

$$\begin{aligned} \varepsilon = \varepsilon^e + \varepsilon^{vp} \quad & \kappa_x = \kappa_x^e \\ \gamma_y = \gamma_y^e + \gamma_y^{vp} \quad & \kappa_y = \kappa_y^e \\ \gamma_z = \gamma_z^e + \gamma_z^{vp} \quad & \kappa_z = \kappa_z^e \end{aligned} \tag{4.30}$$

2. Strain energy function in terms of strains and internal variables, plastic deformations ϵ^{vp}, γ_y^{vp}, γ_z^{vp} and strain-like hardening variables $\bar{\xi}^u$, $\bar{\xi}^v$, $\bar{\xi}^w$

$$\begin{aligned}
\bar{\psi}^u\left(\varepsilon,\varepsilon^{vp},\bar{\xi}^u\right) &= \frac{1}{2}\left(\varepsilon-\varepsilon^{vp}\right)EA^e\left(\varepsilon-\varepsilon^{vp}\right)+\frac{1}{2}\bar{\xi}^u H_{lh}^u A^e\bar{\xi}^u \\
\bar{\psi}^v\left(\gamma_y,\gamma_y^{vp},\bar{\xi}^v\right) &= \frac{1}{2}\left(\gamma_y-\gamma_y^{vp}\right)k_cGA^e\left(\gamma_y-\gamma_y^{vp}\right)+\frac{1}{2}\bar{\xi}^v H_{lh}^v A^e\bar{\xi}^v \\
\bar{\psi}^w\left(\gamma_z,\gamma_z^{vp},\bar{\xi}^w\right) &= \frac{1}{2}\left(\gamma_z-\gamma_z^{vp}\right)k_cGA^e\left(\gamma_z-\gamma_z^{vp}\right)+\frac{1}{2}\bar{\xi}^w H_{lh}^w A^e\bar{\xi}^w
\end{aligned} \tag{4.31}$$

   where for circular cross-sections shear correction factor is equal to $k_c = 9/10$.

3. Yield function in terms of stresses (or stress resultants), stress-like hardening variables $\bar{q}^u$, $\bar{q}^v$, $\bar{q}^w$ and back-stress variables $\bar{\chi}^u$, $\bar{\chi}^v$, $\bar{\chi}^w$

$$\begin{aligned}
\bar{\phi}^u\left(N',\bar{\chi}^u,\bar{q}^u\right) &= |N'-\bar{\chi}^u A^e| - \left(N_y-\bar{q}^u A^e\right)\le 0 \\
\bar{\phi}^v\left(V_y',\bar{\chi}^v,\bar{q}^v\right) &= |V_y'-\bar{\chi}^v A^e| - \left(V_{y,y}-\bar{q}^v A^e\right)\le 0 \\
\bar{\phi}^w\left(V_z',\bar{\chi}^w,\bar{q}^w\right) &= |V_z'-\bar{\chi}^w A^e| - \left(V_{z,y}-\bar{q}^w A^e\right)\le 0
\end{aligned} \tag{4.32}$$

   where N_y, $V_{y,y}$, $V_{z,y}$ are the elastic (yield) limits.
   The stress resultant values N', V_y', V_z', M_x', M_y' and M_z' are computed from the elastic part of total deformation. For a circular cross-section for which the element local coordinate axis x coincides with the center of gravity, the stress resultant values are computed as

$$\begin{aligned}
N' &= EA^e\left(\varepsilon-\varepsilon^{vp}\right) & M_x' &= GI_{pol}^e\kappa_x \\
V_y' &= k_cGA^e\left(\gamma_y-\gamma_y^{vp}\right) & M_y' &= EI_{yy}^e\kappa_y \\
V_z' &= k_cGA^e\left(\gamma_z-\gamma_z^{vp}\right) & M_z' &= EI_{zz}^e\kappa_y
\end{aligned} \tag{4.33}$$

   where the area A^e, the second moments of inertia I_{yy}^e, I_{zz}^e and the polar moment of inertia I_{pol}^e for circular cross-sections with diameter equal to d^e are $A^e = (d^e)^2\pi/4$, $I_{yy}^e = I_{zz}^e = I^e = (d^e)^4\pi/64$, $I_{pol}^e = (d^e)^4\pi/32$.

   The stress-like hardening variables $\bar{q}^u$, $\bar{q}^v$, $\bar{q}^w$ for linear hardening are given as

$$\begin{aligned}
\bar{q}^u &= -H_{lh}^u\bar{\xi}^u \\
\bar{q}^v &= -H_{lh}^v\bar{\xi}^v \\
\bar{q}^w &= -H_{lh}^w\bar{\xi}^w
\end{aligned} \tag{4.34}$$

For Fredrick-Armstrong nonlinear kinematic hardening law [127], the back-stress variables $\bar{\chi}_u$, $\bar{\chi}_v$, $\bar{\chi}_w$ are computed as

$$\begin{aligned}\dot{\bar{\chi}}^u &= H^u_{lk}\dot{\varepsilon}^{vp} - H^u_{nlk}\dot{\bar{\xi}}^u\bar{\chi}^u \\ \dot{\bar{\chi}}^v &= H^v_{lk}\dot{\gamma}^{vp}_y - H^v_{nlk}\dot{\bar{\xi}}^v\bar{\chi}^v \\ \dot{\bar{\chi}}^w &= H^w_{lk}\dot{\gamma}^{vp}_z - H^w_{nlk}\dot{\bar{\xi}}^w\bar{\chi}^w\end{aligned} \tag{4.35}$$

3. The evolution equations for internal variables ϵ^{vp}, γ^{vp}_y, γ^{vp}_z and $\bar{\xi}^u$, $\bar{\xi}^v$, $\bar{\xi}^w$

$$\begin{aligned}\dot{\varepsilon}^{vp} &= \dot{\bar{\gamma}}^u sign(N' - \bar{\chi}^u A^e); \quad \dot{\bar{\xi}}^u = \dot{\bar{\gamma}}^u; \quad \dot{\bar{\gamma}}^u \geq 0 \\ \dot{\gamma}^{vp}_y &= \dot{\bar{\gamma}}^v sign(V'_y - \bar{\chi}^v A^e); \quad \dot{\bar{\xi}}^v = \dot{\bar{\gamma}}^v; \quad \dot{\bar{\gamma}}^v \geq 0 \\ \dot{\gamma}^{vp}_z &= \dot{\bar{\gamma}}^w sign(V'_z - \bar{\chi}^w A^e); \quad \dot{\bar{\xi}}^w = \dot{\bar{\gamma}}^w; \quad \dot{\bar{\gamma}}^w \geq 0\end{aligned} \tag{4.36}$$

where $\bar{\gamma}^u$, $\bar{\gamma}^v$, $\bar{\gamma}^w$ are the plastic multipliers whose values are equal to

$$\begin{aligned}\dot{\bar{\gamma}}^u &= \frac{\langle \bar{\phi}^u(N', \bar{\chi}^u, \bar{q}^u)\rangle}{\eta^u} \\ \dot{\bar{\gamma}}^v &= \frac{\langle \bar{\phi}^v(V'_y, \bar{\chi}^v, \bar{q}^v)\rangle}{\eta^v} \\ \dot{\bar{\gamma}}^w &= \frac{\langle \bar{\phi}^w(V'_z, \bar{\chi}^w, \bar{q}^w)\rangle}{\eta^w}\end{aligned} \tag{4.37}$$

where η^u, η^v, η^w are the viscosity parameters.

4.3.3.2 Exponential softening

The exponential softening is described with [124]

1. The yield function defined in terms of stresses (or stress resultants), and dual variables $\bar{\bar{q}}^u$, $\bar{\bar{q}}^v$, $\bar{\bar{q}}^w$

$$\begin{aligned}\bar{\bar{\phi}}^u\left(t^u, \bar{\bar{q}}^u\right) &= |t^u| - \left(N_f - \bar{\bar{q}}^u A^e\right) \leq 0 \\ \bar{\bar{\phi}}^v\left(t^v, \bar{\bar{q}}^v\right) &= |t^v| - \left(V_{y,f} - \bar{\bar{q}}^v A^e\right) \leq 0 \\ \bar{\bar{\phi}}^w\left(t^v, \bar{\bar{q}}^w\right) &= |t^w| - \left(V_{z,f} - \bar{\bar{q}}^w A^e\right) \leq 0\end{aligned} \tag{4.38}$$

where N_f, $V_{y,f}$, $V_{z,f}$ are the fracture limits, and $\bar{\bar{q}}^u$, $\bar{\bar{q}}^v$, $\bar{\bar{q}}^w$ are the stress-like softening variables.

The stress-like softening variables for exponential softening take the following form

$$\begin{aligned}
\bar{\bar{q}}^u &= \frac{N_f}{A^e}\Big(1 - exp\Big(-\bar{\bar{\xi}}^u \frac{(N_f/A^e)}{G_f^u}\Big)\Big) \\
\bar{\bar{q}}^v &= \frac{V_{y,f}}{A^e}\Big(1 - exp\Big(-\bar{\bar{\xi}}^v \frac{(V_{y,f}/A^e)}{G_f^v}\Big)\Big) \\
\bar{\bar{q}}^w &= \frac{V_{z,f}}{A^e}\Big(1 - exp\Big(-\bar{\bar{\xi}}^w \frac{(V_{z,f}/A^e)}{G_f^w}\Big)\Big)
\end{aligned} \tag{4.39}$$

where G_f^u, G_f^v, G_f^w are the fracture energies, and $\bar{\bar{\xi}}^u$, $\bar{\bar{\xi}}^v$, $\bar{\bar{\xi}}^w$ are the strain-like softening variables. The stress resultant values in the bulk part of an element in the softening phase, which determine the value of internal forces at the discontinuity t^u, t^v, t^w are computed as

$$\begin{aligned}
N' &= EA^e\big(\varepsilon - \varepsilon^{vp} + \bar{G}\alpha^u\big) \\
V_y' &= k_c GA^e\big(\gamma_y - \gamma_y^{vp} + \bar{G}\alpha^v\big) \\
V_z' &= k_c GA^e\big(\gamma_z - \gamma_z^{vp} + \bar{G}\alpha^w\big)
\end{aligned} \tag{4.40}$$

2. The evolution equations for internal variables α^u, α^v, α^w and $\bar{\bar{\xi}}^u$, $\bar{\bar{\xi}}^v$, $\bar{\bar{\xi}}^w$ with the loading/unloading conditions

$$\begin{aligned}
&\dot{\alpha}^u = \dot{\bar{\bar{\gamma}}}^u sign(t^u); \quad \dot{\bar{\bar{\xi}}}^u = \dot{\bar{\bar{\gamma}}}^u; \quad \dot{\bar{\bar{\gamma}}}^u \geq 0; \quad \bar{\bar{\phi}}^u \leq 0; \quad \dot{\bar{\bar{\gamma}}}^u \bar{\bar{\phi}}^u = 0 \\
&\dot{\alpha}^v = \dot{\bar{\bar{\gamma}}}^v sign(t^v); \quad \dot{\bar{\bar{\xi}}}^v = \dot{\bar{\bar{\gamma}}}^v; \quad \dot{\bar{\bar{\gamma}}}^v \geq 0; \quad \bar{\bar{\phi}}^v \leq 0; \quad \dot{\bar{\bar{\gamma}}}^v \bar{\bar{\phi}}^v = 0 \\
&\dot{\alpha}^w = \dot{\bar{\bar{\gamma}}}^w sign(t^w); \quad \dot{\bar{\bar{\xi}}}^w = \dot{\bar{\bar{\gamma}}}^w; \quad \dot{\bar{\bar{\gamma}}}^w \geq 0; \quad \bar{\bar{\phi}}^w \leq 0; \quad \dot{\bar{\bar{\gamma}}}^w \bar{\bar{\phi}}^w = 0
\end{aligned} \tag{4.41}$$

where $\bar{\bar{\gamma}}^u$, $\bar{\bar{\gamma}}^v$, $\bar{\bar{\gamma}}^w$ are the plastic multipliers whose values are obtained from the consistency conditions

$$\begin{aligned}
\dot{\bar{\bar{\gamma}}}^u \dot{\bar{\bar{\phi}}}^u &= 0 \\
\dot{\bar{\bar{\gamma}}}^v \dot{\bar{\bar{\phi}}}^v &= 0 \\
\dot{\bar{\bar{\gamma}}}^w \dot{\bar{\bar{\phi}}}^w &= 0
\end{aligned} \tag{4.42}$$

4.3.4 Computational procedure

The finite element discretization procedure reduces the nonlinear coupled problem to two sets of equations. The first is the first order differential evolution equations of internal variables defined locally at each Gauss point, and the second is the second order differential equations governing the coupled problem defined globally. The solution of these equations is again computed by using the operator split solution procedure, in the same manner as described in Chapter 2, Section 2.4.4. The solution procedure is split into local and global phase, which are treated separately. In the local phase, the solution of evolution equations is computed by using implicit backward Euler time integration scheme (see Sections 2.4.4.1 and 2.4.4.2). In the global phase, the solution in terms of the unknown nodal displacements and pore pressures is computed in a fully monolithic manner using Newmark time-integration scheme and Newton's iterative method.

The system of equations governing the coupled problem for single Timoshenko beam finite element is written as

$$\mathbf{M}^e_{uu}\ddot{\tilde{\mathbf{u}}} + \mathbf{f}^{int,e}(\boldsymbol{\sigma}_u) - \mathbf{K}^e_{up}\tilde{\mathbf{p}}^{\backslash} = \mathbf{f}^{ext,e} \tag{4.43}$$

$$\mathbf{K}^{e,\mathsf{T}}_{up}\dot{\tilde{\mathbf{u}}} + \mathbf{D}^e_{pp}\dot{\tilde{\mathbf{p}}}^{\backslash} + \mathbf{K}^e_{pp}\tilde{\mathbf{p}}^{\backslash} = \mathbf{q}^{ext,e} \tag{4.44}$$

where $\mathbf{M}^e_{uu}$ is the mass matrix, $\mathbf{f}^{int,e}(\boldsymbol{\sigma}_u)$ is the internal load vector resulting from displacements (i.e. effective stresses), $\mathbf{K}^e_{up}$ is the coupling matrix, $\mathbf{D}^e_{pp}$ is the compressibility matrix, $\mathbf{K}^e_{pp}$ is the permeability matrix, and $\mathbf{f}^{e,ext}$ and $\mathbf{q}^{e,ext}$ are the load vectors. The matrices $\mathbf{K}^e_{up}$, $\mathbf{D}^e_{pp}$ and $\mathbf{K}^e_{pp}$ are computed as

$$\begin{aligned}
\mathbf{K}^e_{up} &= \int_0^{L^e} \mathbf{B}^{s,\mathsf{T}}_{up}\, b\, \mathbf{N}^s_{up}\, dx; \qquad \mathbf{B}^s_{up} = \begin{bmatrix} B_1 & 0 & 0 & 0 & 0 & B_2 & 0 & 0 & 0 & 0 \end{bmatrix} \\
\mathbf{D}^e_{pp} &= \int_{\Omega^e_{Tet4}} \mathbf{N}^{s,\mathsf{T}}_p \frac{1}{M} \mathbf{N}^s_p\, d\Omega; \quad \mathbf{K}^e_{pp} = \int_{\Omega^e_{Tet4}} (\nabla \mathbf{N}^s_p)^{\mathsf{T}} \frac{k}{\gamma_f} \nabla \mathbf{N}^s_p\, d\Omega
\end{aligned} \tag{4.45}$$

Here we note that in the global system of equations (Equation 4.44) we take the parts of the $\mathbf{D}^e_{pp}$, and $\mathbf{K}^e_{pp}$ matrices (Equation 4.45) that correspond to the nodes of Timoshenko beam finite element.

For numerical integration on tetrahedral finite elements, we choose the nodal point integration rule. The nodal point integration rule is a linear order rule, which results with a diagonal form of compressibility matrix $\mathbf{D}^e_{pp}$. However, this does not affect significantly computed results. Namely, the Biot's modulus M in the problems of our interest is always a large number or infinity, which results with the values of entries of a matrix $\mathbf{D}^e_{pp}$ close to zero or zero.

The Timoshenko beam finite element mass matrix $\mathbf{M}^e_{uu}$ in Equation (4.43) is obtained by distributing the total mass of an element to nodes (Figure 4.8), resulting in a diagonally lumped mass matrix, written as

$$\mathbf{M}^e_{uu} = \frac{1}{2}\rho\, diag\big(V_{tot},\, V_{tot},\, V_{tot},\, I^e_{pol},\, I^e,\, I^e,\, V_{tot},\, V_{tot},\, V_{tot},\, I^e_{pol},\, I^e,\, I^e\big) \tag{4.46}$$

where V_{tot} is obtained as one-third of the total volume of the cylinder with a base diameter equal to d^e and height equal to L^e (Figure 4.8).

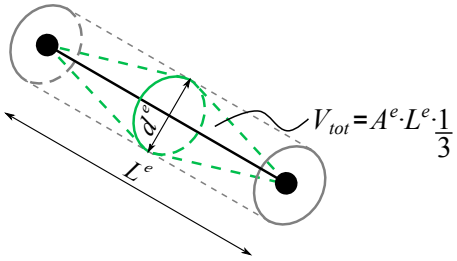

Figure 4.8 Timoshenko beam finite element lumped mass matrix computation in 3D setting

The solution in terms of unknown nodal displacements and pore pressures is computed at discrete pseudo-time steps $t_1, t_2, ..., t_n$ using Newmark time-integration scheme. For a time step t_{n+1} and iteration i, the global system of equations to be solved is written as

$$\mathop{\mathbb{A}}_{e=1}^{n_{elem}} \left\{ \begin{bmatrix} \frac{1}{\beta\Delta t^2}\mathbf{M}_{uu} + \bar{\mathbf{K}}_{uu} & -\mathbf{K}_{up} \\ \frac{\gamma}{\beta\Delta t}\mathbf{K}^{\mathsf{T}}_{up} & \frac{\gamma}{\beta\Delta t}\mathbf{D}_{pp} + \mathbf{K}_{pp} \end{bmatrix}^{e,(i)}_{n+1} \begin{Bmatrix} \Delta\bar{\mathbf{u}} \\ \Delta\bar{\mathbf{p}}' \end{Bmatrix}^{e,(i)}_{n+1} = \begin{Bmatrix} \mathbf{r}_u \\ \mathbf{r}_p \end{Bmatrix}^{e,(i)}_{n+1} \right\} \tag{4.47}$$

where $\bar{\mathbf{K}}^e_{uu}$ is the element tangent stiffness matrix, and $\mathbf{r}^{e,(i)}_{u,n+1}$ and $\mathbf{r}^{e,(i)}_{p,n+1}$ are residuals pertaining to the solid and the pore fluid part.

After solving the global system of equations, the new iterative values of unknown fields are updated as

$$\begin{aligned} \bar{\mathbf{u}}^{(i+1)}_{n+1} &= \bar{\mathbf{u}}^{(i)}_{n+1} + \Delta\bar{\mathbf{u}}^{(i)}_{n+1} \\ \bar{\mathbf{p}}^{(i+1)}_{n+1} &= \bar{\mathbf{p}}^{(i)}_{n+1} + \Delta\bar{\mathbf{p}}^{(i)}_{n+1} \end{aligned} \tag{4.48}$$

The element tangent stiffness matrix $\bar{\mathbf{K}}^e$ depends whether the element is in elasto-viscoplastic or softening part of the response. If the element is elasto-viscoplastic, the tangent stiffness matrix is defined as

$$\bar{\mathbf{K}}^{e,(i)}_{uu,n+1} = \mathbf{K}^{e,(i)}_{uu,n+1} = \int_0^{L^e} \mathbf{B}^{s,\mathsf{T}}_u \mathbf{C}^{ep,(i)}_{n+1} \mathbf{B}^s_u\, dx \tag{4.49}$$

Elasto-plastic tangent matrix is written as

$$\mathbf{C}_{n+1}^{ep,(i)} = \begin{bmatrix} C_{n+1}^{ep,u} A^e & 0 & 0 & 0 & 0 & 0 \\ 0 & C_{n+1}^{ep,v} A^e & 0 & 0 & 0 & 0 \\ 0 & 0 & C_{n+1}^{ep,w} A^e & 0 & 0 & 0 \\ 0 & 0 & 0 & GI_{pol}^e & 0 & 0 \\ 0 & 0 & 0 & 0 & EI^e & 0 \\ 0 & 0 & 0 & 0 & 0 & EI^e \end{bmatrix} \tag{4.50}$$

where $C_{n+1}^{ep,u}$, $C_{n+1}^{ep,v}$ and $C_{n+1}^{ep,w}$ are elasto-plastic tangent moduli for axial and transverse directions. The local phase procedure for computing elasto-plastic tangent moduli is given in Section 2.4.4.1.

If the element is in the softening, the element tangent stiffness matrix is obtained by performing static condensation procedure. The statically condensed element tangent stiffness matrix is written as

$$\bar{\mathbf{K}}_{uu,n+1}^{e,(i)} = \hat{\mathbf{K}}_{uu,n+1}^{e,(i)} = \left[\mathbf{K}_{uu,n+1}^{e,(i)} - \mathbf{F}_{n+1}^{e,(i)} \left(\mathbf{H}_{n+1}^{e,(i)} + \mathbf{K}_{\alpha} \right)^{-1} \left(\mathbf{F}_{n+1}^{e,(i),T} + \mathbf{K}_{d} \right) \right] \tag{4.51}$$

where

$$\begin{aligned} \mathbf{K}_{uu,n+1}^{e,(i)} &= \int_0^{L^e} \mathbf{B}_u^{s,\mathsf{T}} \mathbf{C}_{n+1}^{ep,(i)} \mathbf{B}_u^s dx; \\ \mathbf{F}_{n+1}^{e,(i)} &= \int_0^{L^e} \mathbf{B}_u^{s,\mathsf{T}} \mathbf{C}_{n+1}^{ep,(i)} \bar{\mathbf{G}} dx; \\ \mathbf{H}_{n+1}^{e,(i)} &= \int_0^{L^e} \bar{\mathbf{G}}^{\mathsf{T}} \mathbf{C}_{n+1}^{ep,(i)} \bar{\mathbf{G}} dx \end{aligned} \tag{4.52}$$

The matrices $\mathbf{K}_d$ and $\mathbf{K}_\alpha$ depend on the current step in softening being elastic or plastic. If the current step in the softening is elastic, then

$$\mathbf{K}_d = \mathbf{C}^* \mathbf{B}_u^s; \quad \mathbf{K}_\alpha = \mathbf{0}; \quad \mathbf{C}^* = \begin{bmatrix} EA^e & 0 & 0 & 0 & 0 & 0 \\ 0 & k_c GA^e & 0 & 0 & 0 & 0 \\ 0 & 0 & k_c GA^e & 0 & 0 & 0 \\ 0 & 0 & 0 & 0 & 0 & 0 \\ 0 & 0 & 0 & 0 & 0 & 0 \\ 0 & 0 & 0 & 0 & 0 & 0 \end{bmatrix} \tag{4.53}$$

Else, if the current step in the softening is plastic, then

$$\mathbf{K}_d = \mathbf{0}; \quad \mathbf{K}_\alpha = \begin{bmatrix} K_\alpha^u A^e & 0 & 0 & 0 & 0 & 0 \\ 0 & K_\alpha^v A^e & 0 & 0 & 0 & 0 \\ 0 & 0 & K_\alpha^w A^e & 0 & 0 & 0 \\ 0 & 0 & 0 & 0 & 0 & 0 \\ 0 & 0 & 0 & 0 & 0 & 0 \\ 0 & 0 & 0 & 0 & 0 & 0 \end{bmatrix} \tag{4.54}$$

The local phase procedure for computing matrices K_α^u, K_α^v and K_α^w is given in Chapter 2, Section 2.4.4.2.

4.4 External fluid model

The external fluid model is extended from 2D to the 3D setting. The strong form of governing equations and variational formulation is equivalent to that presented in Chapter 3, Section 3.2.2. The end result of the finite element discretization procedure is the following system of equations governing the small and irrotational motion of the external fluid, written as

$$\mathop{\mathbb{A}}_{e=1}^{n_{elem}} \left\{ \begin{bmatrix} \mathbf{A}_{uu} & \mathbf{0} & \mathbf{0} \\ \mathbf{0} & \mathbf{0} & \mathbf{0} \\ \mathbf{0} & \mathbf{0} & \mathbf{0} \end{bmatrix}^e \begin{Bmatrix} \ddot{\bar{\mathbf{u}}} \\ \ddot{\bar{\mathbf{p}}} \\ \ddot{\bar{\boldsymbol{\lambda}}} \end{Bmatrix}^e + \begin{bmatrix} \mathbf{0} & \mathbf{L}_{up} & \mathbf{L}_{u\lambda} \\ \mathbf{L}_{up}^\mathsf{T} & \mathbf{L}_{pp} & \mathbf{0} \\ \mathbf{L}_{u\lambda}^\mathsf{T} & \mathbf{0} & \mathbf{L}_{\lambda\lambda} \end{bmatrix}^e \begin{Bmatrix} \bar{\mathbf{u}} \\ \bar{\mathbf{p}} \\ \bar{\boldsymbol{\lambda}} \end{Bmatrix}^e = \begin{Bmatrix} \mathbf{f}^f \\ \mathbf{0} \\ \mathbf{0} \end{Bmatrix}^e \right\} \tag{4.55}$$

where

$$\begin{aligned} \mathbf{A}_{uu}^e &= \int_{\Omega_f^e} \rho \mathbf{N}_u^{f,T} \mathbf{N}_u^f d\Omega; \\ \mathbf{L}_{up}^e &= -\int_{\Omega_f^e} \mathbf{V}^{f,T} \mathbf{N}_p^f d\Omega; \qquad \mathbf{L}_{u\lambda}^e = \int_{\Omega_f^e} \mathbf{D}^{f,T} \mathbf{N}_\lambda^f d\Omega \\ \mathbf{L}_{pp}^e &= -\int_{\Omega_f^e} \frac{1}{\beta} \mathbf{N}_p^{f,T} \mathbf{N}_p^f d\Omega; \quad \mathbf{L}_{\lambda\lambda}^e = -\int_{\Omega_f^e} \frac{1}{\vartheta} \mathbf{N}_\lambda^{f,T} \mathbf{N}_\lambda^f d\Omega \end{aligned} \tag{4.56}$$

The 'vorticity moment' degree of freedom can again be statically condensed on the element level so that the only unknown variables remaining on the global level are displacements and pressures.

The finite element approximations for displacements, pressure and 'vorticity moment' are given as

$$\begin{aligned}
&\mathbf{u} = \mathbf{N}_u^f \bar{\mathbf{u}}; \quad p = \mathbf{N}_p^f \bar{\mathbf{p}}; \quad \boldsymbol{\Lambda} = \mathbf{N}_\lambda^f \bar{\boldsymbol{\lambda}} \\
&\mathbf{u} = \mathbf{N}_u^f \ddot{\bar{\mathbf{u}}}; \quad p = \mathbf{N}_p^f \ddot{\bar{\mathbf{p}}}; \quad \boldsymbol{\Lambda} = \mathbf{N}_\lambda^f \ddot{\bar{\boldsymbol{\lambda}}} \\
&\nabla \cdot \mathbf{u} = (\nabla \cdot \mathbf{N}_u^f)\, \bar{\mathbf{u}} = \mathbf{V}^f \bar{\mathbf{u}} \\
&\nabla \times \mathbf{u} = (\nabla \times \mathbf{N}_u^f)\, \bar{\mathbf{u}} = \mathbf{D}^f \bar{\mathbf{u}}
\end{aligned} \tag{4.57}$$

In the 3D numerical model of acoustic fluid-structure interaction, for the external fluid domain, we choose linear finite element approximations (hexahedral finite element with eight nodes) for the displacements, with constant approximations for the pressure and the 'vorticity moment'. In other words, we choose the **Hex8-P1-Λ1** finite element depicted in Figure 4.9. In order to solve the issue of fluid-structure interface, we use the same finite element approximation post-processing procedure previously described in Chapter 3, Section 3.2.3 for the **Q4-P1-Λ1** finite element.

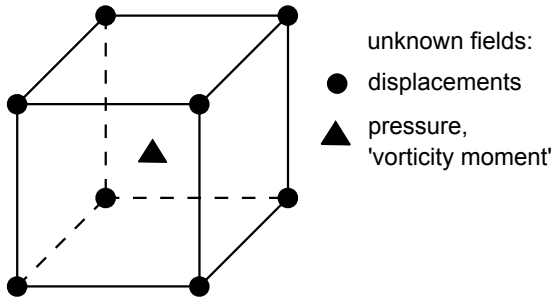

Figure 4.9 Finite element approximation for external fluid in 3D numerical model **Hex8-P1-Λ1**

4.5 Numerical results

In this section, we present the results of several numerical simulations, which serve to illustrate the coupled discrete beam lattice model performance and the capabilities of proposed numerical approach for dealing with acoustic fluid-structure interaction problems in the 3D framework. With the aim of validating and comparing results, the numerical simulations are performed for the numerical examples presented in Chapters 2 and 3, which are extended by adding the third dimension to the model. All numerical implementations and computations are performed with the research version of the computer code FEAP, developed by R.L. Taylor [41].

In all numerical simulations, the finite element mesh is generated by using Delaunay tetrahedralization and GMSH software [91]. The cross-sectional properties of the Timoshenko beam finite elements are computed from the Voronoi diagram by using MATLAB software [92], which uses Qhull code [154].

4.5.1 Saturated poro-elastic column

In this section, we aim to validate the coupled discrete beam lattice model of structure built of a saturated porous medium in the 3D framework. We observe saturated poro-elastic column shown in Figure 4.10a, and we perform a quasi-static one-dimensional consolidation test. We compare our results against those computed with a continuum model using commercial software PLAXIS [135]. In PLAXIS, the coupling between the solid phase and the pore fluid is governed by Biot's porous media theory, and the equal order of interpolation for both the displacement and pressure fields is available. For such comparison, we choose 10-node tetrahedral elements with second-order polynomial interpolations.

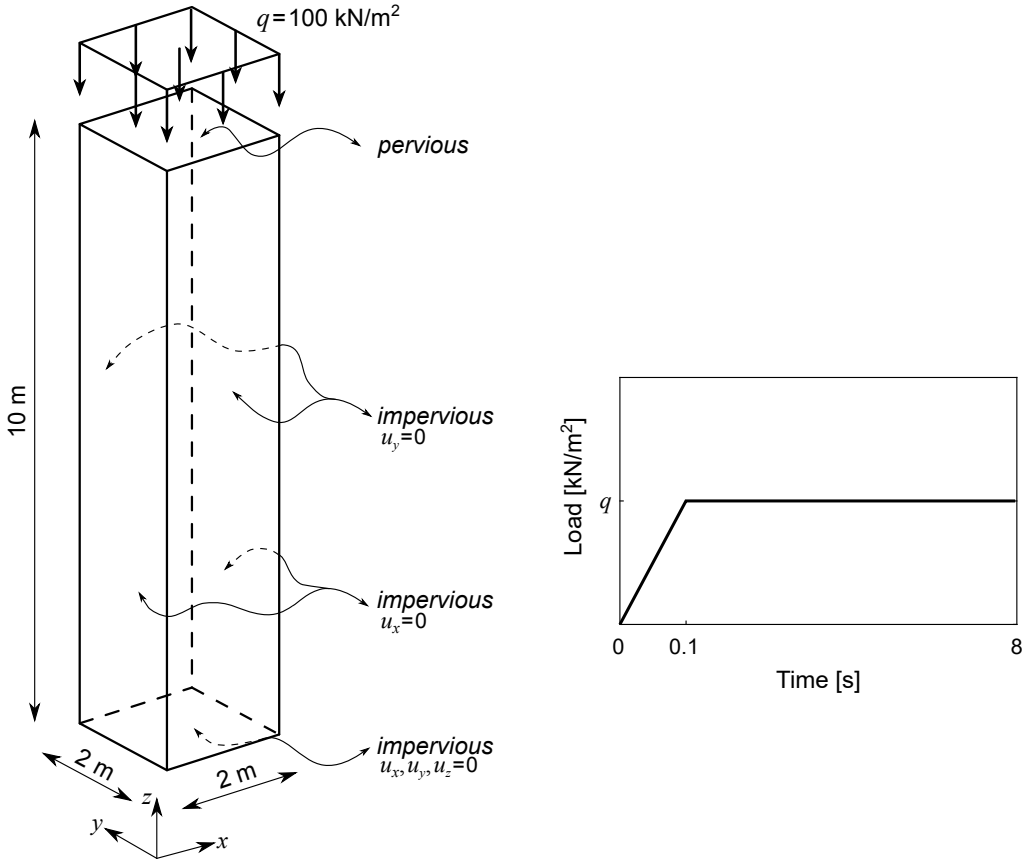

(a) Problem statement (b) Loading program

Figure 4.10 3D Saturated poro-elastic column

The linear elastic parameters of the Timoshenko beam finite element are: Young's modulus $E = 40$ MPa and Poisson's ratio $\nu = 0$. Because we observe a problem of one-dimensional consolidation, Poisson's ratio in a continuum model is taken as $\nu = 0$. The identified oedometer modulus of a continuum model is $E_{oed} = 31.57$ MPa (which is equal to Young's modulus E since $\nu = 0$). The coefficient of permeability is $k = 10^{-2}$ m/s, the specific weight of the water is $\gamma_w = 10$ kN/m^3, Biot's constant is $b = 1$ and Biot's modulus is $M = 1.6$ GPa, for both discrete and continuum model.

The loading program is shown in Figure 4.10b. The time step is set to $\Delta t = 0.01$ s. With the aim of inspecting the possible mesh dependency of the results, we perform computation with a discrete model for two different mesh densities: coarse with 1641 Timoshenko beam finite elements(Figure 4.11a), and fine with 4563 Timoshenko beam finite elements (Figure 4.11b). The computation in a continuum model is performed on a mesh of 4308 tetrahedral elements.

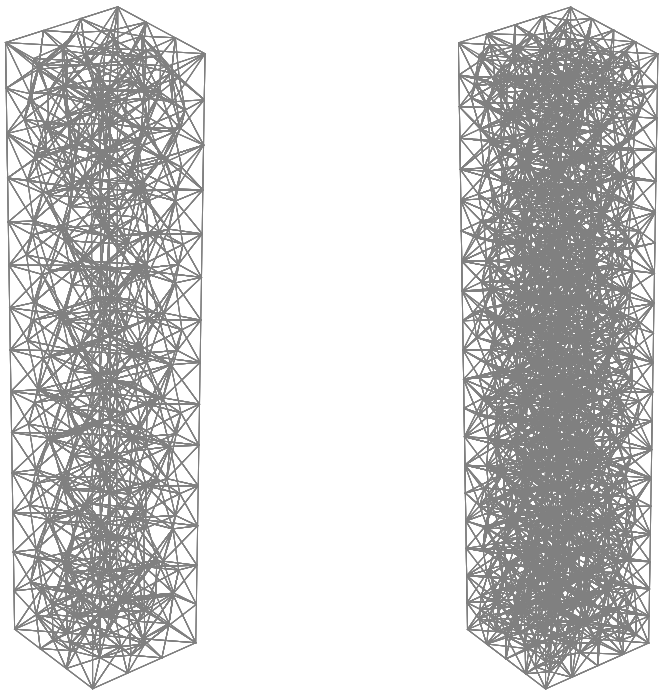

(a) Coarse mesh (b) Fine mesh

Figure 4.11 Finite element mesh densities

The computed time evolutions of vertical displacement of the column top and the excess pore pressure at the bottom of the column are shown in Figures 4.12a and 4.12b. We can conclude that the results obtained with the discrete model show an excellent agreement with the results obtained with a continuum model, with the results being practically mesh independent.

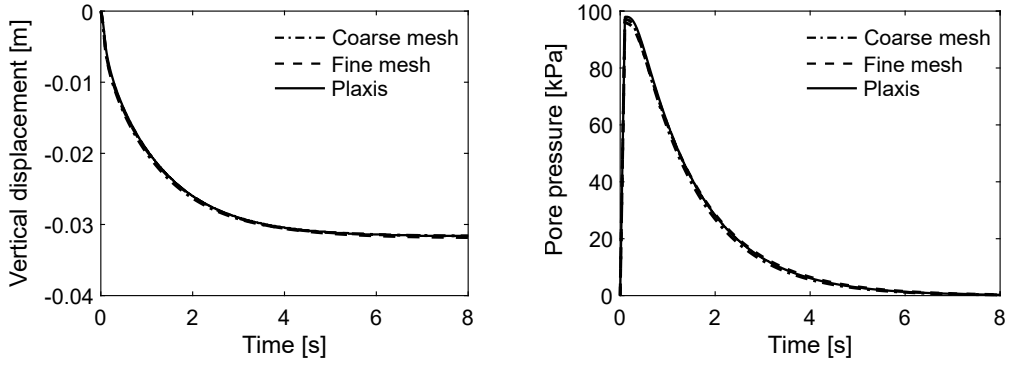

(a) Vertical displacement of column top

(b) Excess pore pressure at column bottom

Figure 4.12 3D Saturated poro-elastic column: computed results

We repeat the computation with a discrete model with the ramp loading reaching its maximum value at $t = 1$ s. The computed results are shown in Figures 4.13a and 4.13b. We compare computed results against those shown in Figures 4.12a and 4.12b. From Figure 4.13b, we can conclude that a higher loading rate result in an increase in the value of excess pore pressure. As the value of excess pore pressure approaches zero, the value of vertical displacement approaches constant value marking the end of the consolidation.

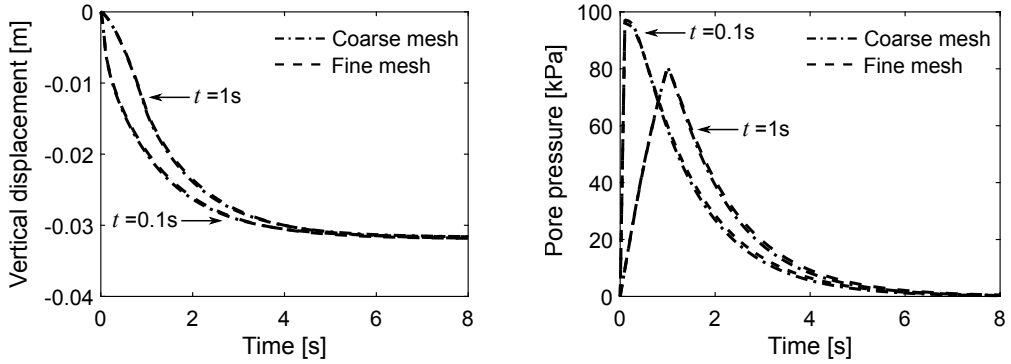

(a) Vertical displacement of column top

(b) Excess pore pressure at column bottom

Figure 4.13 Comparison of loading rates

We note that the identified value of Young's modulus of an equivalent continuum model for 3D case ($E = 31.57$ MPa) is slightly lower than for 2D case ($E = 33.91$ MPa), suggesting that the three-dimensional coupled discrete beam lattice model is slightly more deformable than the two-dimensional model. It is important also to note that for the 3D case as well the coefficient of permeability of a coupled

discrete beam lattice model matches the one of an equivalent continuum model. Hence, it can be easily identified from standard experimental tests.

4.5.2 Compression test

In this section, we perform a compression test on a water-saturated specimen shown in Figure 4.14a, by imposing vertical displacements on the top base of the specimen. The finite element mesh is shown in Figure 4.14b. We assume that the inertial effects are negligible. The material parameters of the Timoshenko beam finite element are shown in Table 4.1. The ultimate values of stresses are randomly assigned to every finite element using Gaussian random distribution (Equation 2.74). The same values of yield shear stress, ultimate shear stress, and fracture energy are selected for both transverse directions (marked with subscript $_s$). The ultimate shear stress is defined with Mohr-Coulomb law. The angle of internal friction is selected as $\phi = 11°$. The coefficient of permeability is $k = 10^{-8}$ m/s, the specific weight of the water is $\gamma_w = 10$ kN/m^3, Biot's constant is $b = 1$ and Biot's modulus is $1/M \to 0$.

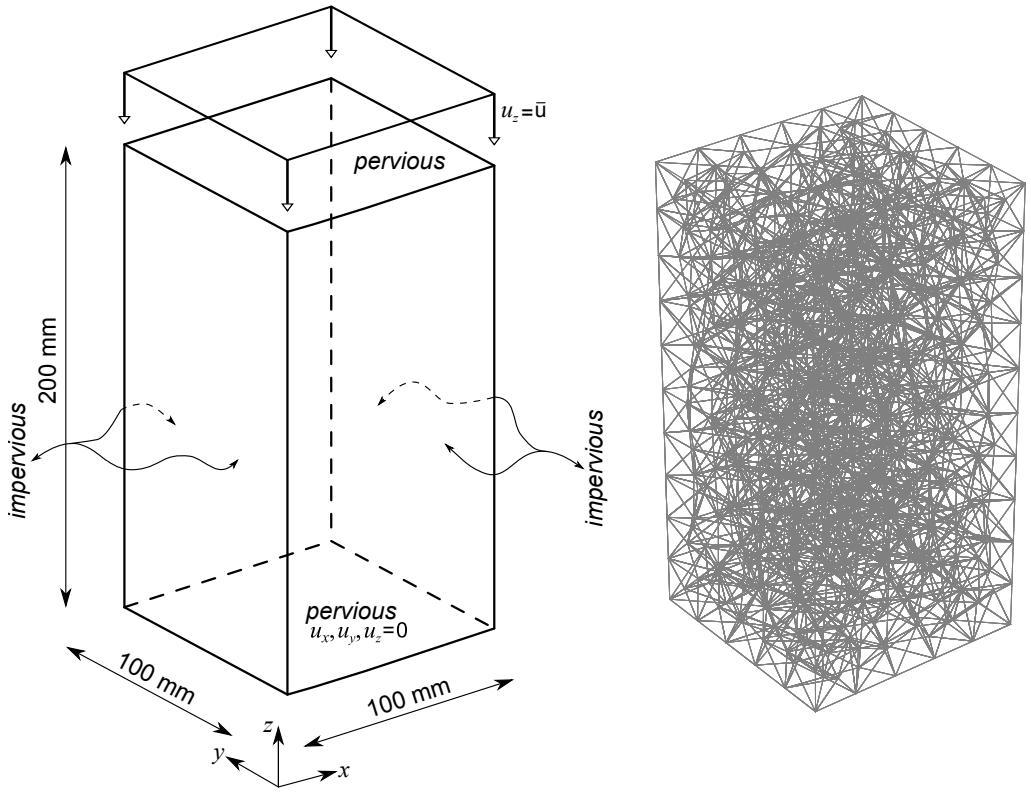

(a) Problem statement (b) Finite element mesh

Figure 4.14 3D Compression test

Table 4.1 3D Compression test: material parameters of the finite element

Young's modulus [kPa]	Poisson's ratio [/]	Yield limit [kPa]	Fracture limit [kPa]	Fracture energy [kN/m]
$E = 20000$	$\nu = 0.2$	$\sigma_{y,t} = 10$	$\mu_{G,t} = 12$ $\sigma_{G,t} = 1$	$G_{f,t} = 20$
		$\sigma_{y,c} = 100$	$\mu_{G,c} = 120$ $\sigma_{G,c} = 10$	$G_{f,c} = 100$
		$\sigma_{y,s} = 12$	$\mu_{G,s} = 15$ $\sigma_{G,s} = 1$	$G_{f,s} = 100$

The linear hardening modulus is $H_{lh} = 2 \cdot 10^3$ kPa, the linear kinematic hardening modulus is $H_{lk} = 2 \cdot 10^3$ kPa, nonlinear hardening parameter is $H_{nlk} = 2 \cdot 10^2$, and the viscosity parameter is $\eta = 20$ kPa s.

We first perform uncoupled computation (Biot's constant $b = 0 \rightarrow$ matrix $\mathbf{K}^e_{up}$ is a null matrix), to simulate the response of dry specimen. We compare the results computed for a 3D model of specimen against those computed for the 2D model of the specimen. For both cases, we present results in terms of average stress, which is obtained as total vertical reaction divided by the area of the specimen (100 mm x 1 mm for 2D case, and 100 mm x 100 mm for 3D case). The comparison of results is shown in Figure 4.15a. We can conclude that the 3D model results in a higher ultimate value of average stress, and higher value of fracture energy needed to drive the specimen to a complete failure.

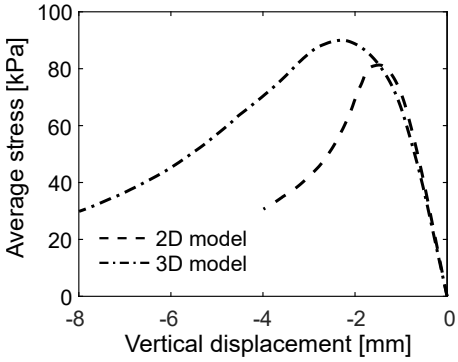

(a) Comparison of responses for 2D and 3D model of dry specimen

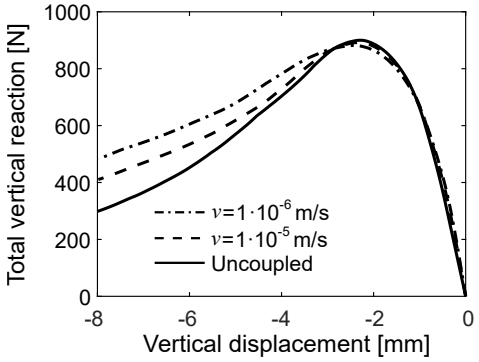

(b) Comparison of responses for different displacement rates, 3D model of saturated specimen

Figure 4.15 Comparison of computed results

Next, we simulate the response of saturated specimen, and we perform the compression test by imposing vertical displacements with a constant rate on the top base of the specimen. With the aim to investigate the coupling effects, we perform

compression test with two displacement rates: $v = 1 \cdot 10^{-5}$ m/s and $v = 1 \cdot 10^{-6}$ m/s. The computed results are shown in Figure 4.15b. The computed macro-scale responses prior to reaching the ultimate load value do not differ significantly. In the post-peak regime, higher displacement rate results in a greater value of total vertical reaction compared to the uncoupled case. After the ultimate load level is reached, one large macro-crack is starting to form, leading to the complete failure of the specimen. The distributions of vertical displacements and excess pore pressures, and the broken cohesive links in increasing softening at the end of the loading program for $v = 1 \cdot 10^{-6}$ m/s are shown in Figures 4.16a and 4.16e.

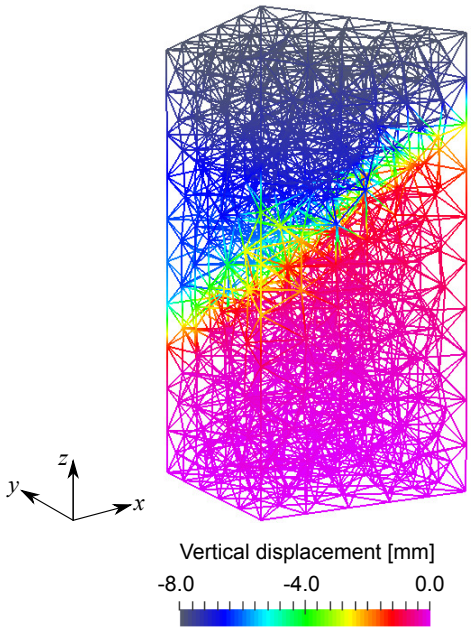

(a) Vertical displacement

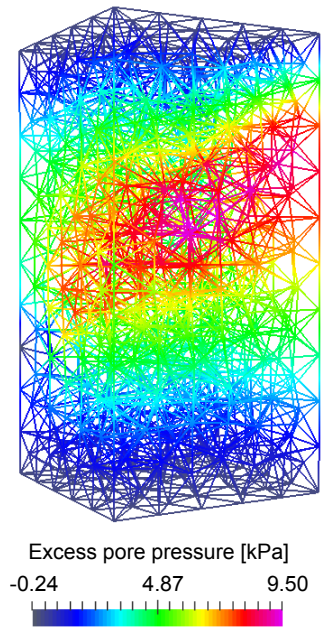

(b) Excess pore pressure

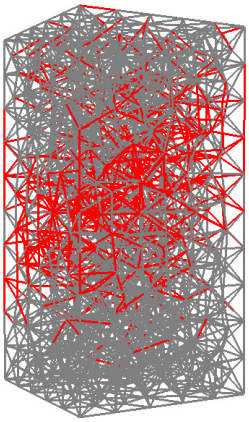

(c) Broken cohesive links: mode I

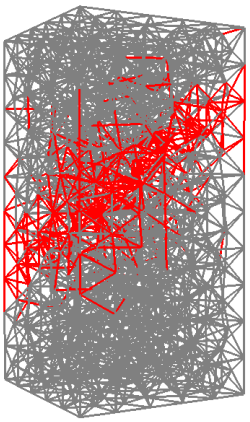

(d) Broken cohesive links: mode II

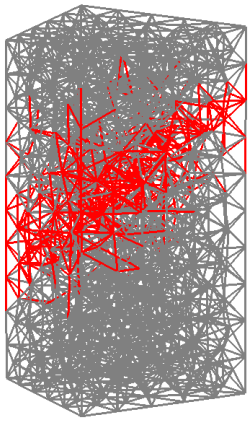

(e) Broken cohesive links: mode III

Figure 4.16 Failure mode for 3D compression test

4.5.3 Dam-reservoir system

In this numerical example, we observe the 3D problem of dam-reservoir interaction. The geometry of the dam-reservoir system is shown in Figure 4.17. The bottom base of the dam is kept fixed, and the movement of the dam in y direction is restrained. We first start by assuming that the behavior of the dam remains linear elastic. Here, we perform numerical simulations with the aim to validate the proposed numerical model ability to predict hydrostatic and hydrodynamic pressure distributions exerted on the upstream face of the dam structure in close agreement with analytical solutions.

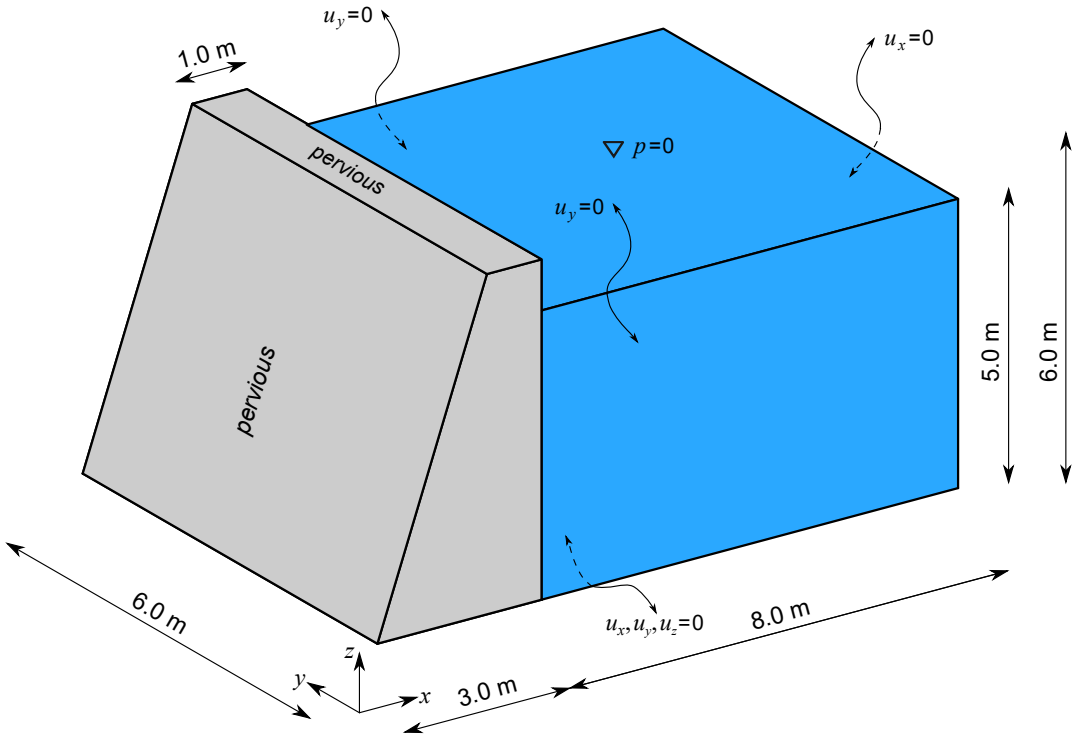

Figure 4.17 Geometry of 3D dam-reservoir system

Next, we perform localized failure analysis with the aim to compute admissible horizontal overload (in x direction) that can be applied on top of (already) acting self-weight and hydrostatic loading. The computation of admissible overload in the quasi-static setting is performed by imposing horizontal displacements on the top base of the dam. The admissible overload in a dynamic setting is computed by subjecting the dam-reservoir system to the linear increasing horizontal ground acceleration, which is modeled in terms of equivalent horizontal forces. Throughout this numerical example, the vorticity constraint is completely omitted.

Remark 1: The finite element mesh of the structure domain is obtained by performing Delaunay tetrahedralization of the domain, which results with the irregular

triangular mesh of Timoshenko beam finite elements on the domain surfaces. With the goal of connecting the structure finite elements with the external fluid finite elements, we impose regular triangular mesh on the fluid-structure boundary. By doing so, we are able to connect structure and external fluid finite elements at the common nodes (Figure 4.18). It is important to note that since we are connecting line elements with volume elements at the fluid-structure boundary, we ensure the exchange of motion and pressure through the common nodes, whereas the compatibility across the surface is not achieved.

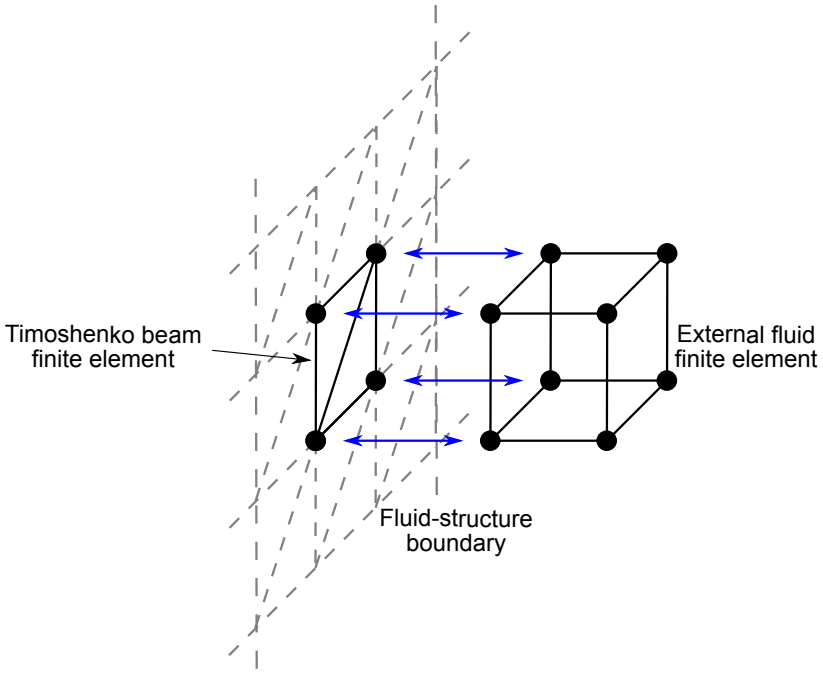

Figure 4.18 Mesh of Timoshenko beam finite elements at fluid-structure boundary

Remark 2: The mesh of the dam structure for the 3D case is coarser than for the 2D case. Namely, the length of a Timoshenko beam finite element in 2D was approximately 0.3 m, whereas in 3D it is approximately 0.5 m, which results in a reservoir height equal to 5.0 m. The reasons for having to choose coarser mesh density for the 3D case are the difficulties when generating the Voronoi diagram and computing the area of each Timoshenko beam finite element, and a significant increase in computational costs for finer meshes.

4.5.3.1 Linear elastic behavior

Young's modulus and Poisson's ratio of the Timoshenko beam finite element are $E = 10^4$ MPa and $\nu = 0$. The coefficient of permeability is $k = 10^{-7}$ m/s, Biot's constant is $b = 1$ and Biot's modulus is $M = 10^6$ MPa. The specific weight of the

dam material is $\gamma_s = 20$ kN/m^3, and the specific weight of the water is $\gamma_w = 10$ kN/m^3. The bulk modulus of the outside water is $\beta = 10^3$ MPa.

→ Hydrostatic pressure distribution

We first apply an increase of the self-weight, followed by the hydrostatic loading of the external reservoir (Figure 4.19). The time step is set to $\Delta t = 0.1$ day. We compare computed results against analytical values.

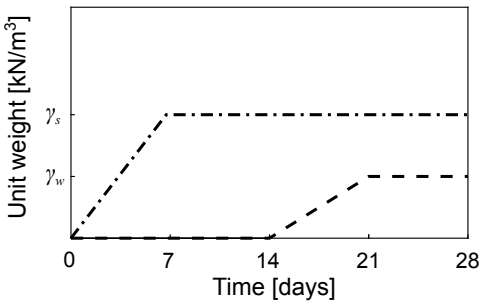

Figure 4.19 Loading program for validation analysis, quasi-static case

The computed pressure field in the reservoir and in the body of the dam is shown in Figure 4.20. We can conclude that the computed hydrostatic pressure distribution on the upstream face of the dam structure closely matches the analytical solution (Figure 4.21a). The difference can be observed only at the bottom of the reservoir, due to the finite element approximation and post-processing procedure for the pressure field in the reservoir (see Chapter 3, Section 3.2.3).

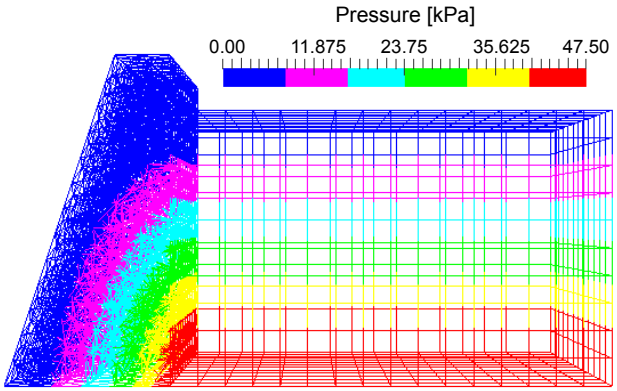

Figure 4.20 Hydrostatic pressure and pore pressure distribution

The total vertical and horizontal reaction at the bottom base of the dam are shown in Figures 4.21b and 4.21c. The total horizontal reaction of 124.93 kN/m' (749.58 kN) is in close agreement with the analytical value of the resultant force of the hydrostatic pressures equal to 125.0 kN/m'. The total vertical reaction closely matches the total weight of the dam. The slight difference in the value of the total

weight of the dam is due to idealizations while computing the cross-sectional area and the corresponding volume of each Timoshenko beam finite element. The additional vertical reaction in the second phase of the loading program is due to the hydrostatic loading as a result of common nodes. This additional value changes and approaches zero as the size of fluid finite element approaches zero. The horizontal displacements (x direction) of the tip of the dam → point A(3, 3, 6)[m] are shown in Figure 4.21d.

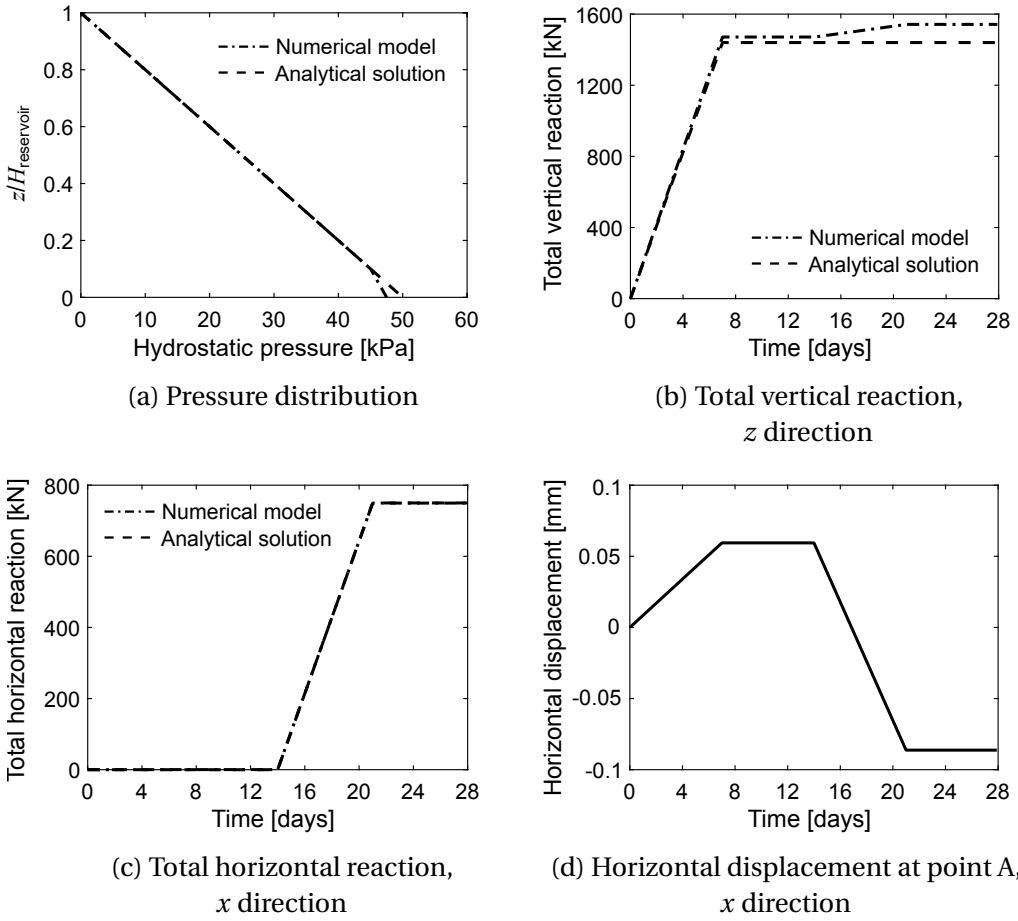

(a) Pressure distribution

(b) Total vertical reaction, z direction

(c) Total horizontal reaction, x direction

(d) Horizontal displacement at point A, x direction

Figure 4.21 Linear elastic behavior, dynamic case: computed results

→ Hydrodynamic pressure distribution

We subject the dam-reservoir system to a horizontal ground acceleration increasing linearly with time and reaching its maximum value of $a_0 = 1$ m/s^2 at $t = 1$s, after which is kept constant (Figure 4.22). The length of the reservoir is chosen as $L = 20.0$ m instead of $L = 8.0$ m in order to eliminate the influence of the boundary effects. The time step is set to $\Delta t = 0.01$ s. We compare computed results against analytical solutions provided by Chwang [150] for the 2D case of dam-reservoir interaction.

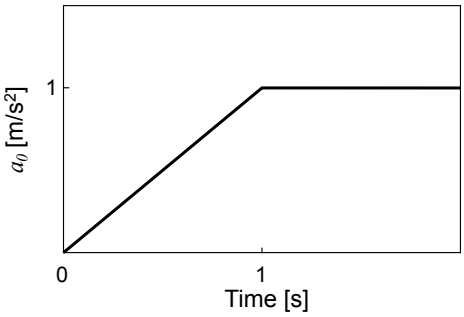

Figure 4.22 Loading program for validation analysis, dynamic case

The computed results are shown in Figures 4.23a and 4.23b. We can conclude that a good match between computed hydrodynamic pressures and hydrodynamic force, and analytical values is obtained. The hydrodynamic pressure distribution in the reservoir, and excess pore pressure distribution in the body of the dam at $t = 2$ s is shown in Figures 4.24.

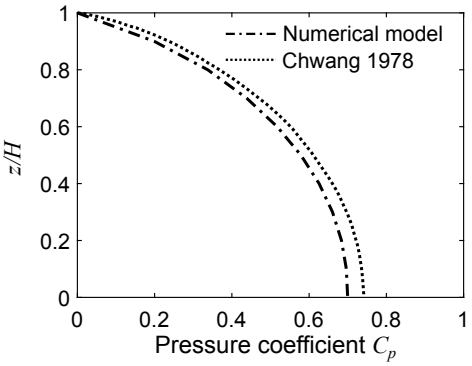

(a) Pressure coefficient

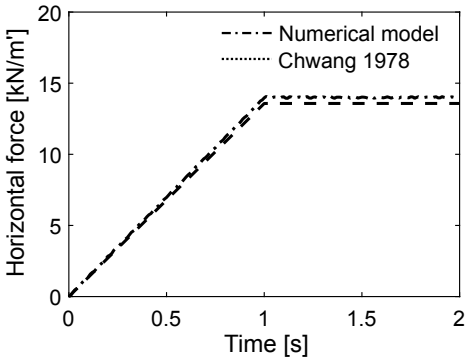

(b) Horizontal hydrodynamic force, x direction

Figure 4.23 Linear elastic behavior, dynamic case: computed results

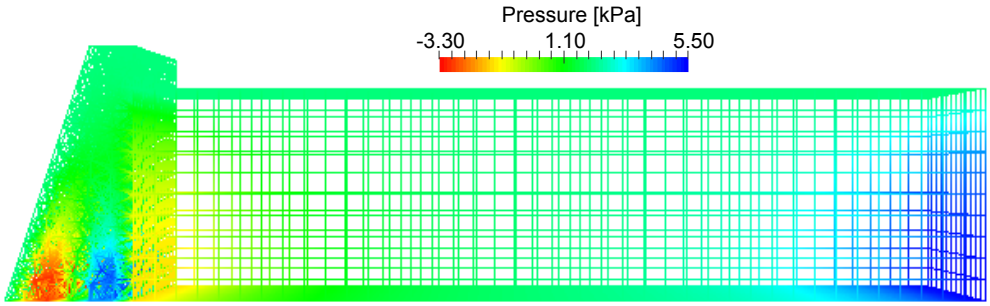

Figure 4.24 Hydrodynamic pressure and pore pressure distribution

4.5.3.2 Localized failure analysis of dam structure

Next, we allow for plastic zones and cracks to form in dam structure by introducing yield and fracture limits for each Timoshenko beam finite element. The same values of yield shear stress, ultimate shear stress, and fracture energy are selected for both transverse directions (marked with subscript $_s$). The yield and fracture limits for the Timoshenko beam finite element in tension, compression and shear: $\sigma_{y,t}$ = 0.015 MPa; $\sigma_{y,c}$ = 0.20 MPa; $\sigma_{y,s}$ = 0.015 MPa; $\sigma_{f,t}$ = 0.02 MPa; $\sigma_{f,c}$ = 0.30 MPa; $\sigma_{f,s}$ = 0.02 MPa. The fracture energies in tension, compression and shear are: $G_{f,t}$ = 0.01 GN/m; $G_{f,c}$ = 0.1 GN/m; $G_{f,s}$ = 0.01 GN/m. The linear hardening modulus is $H_{lh} = 10^3$ MPa.

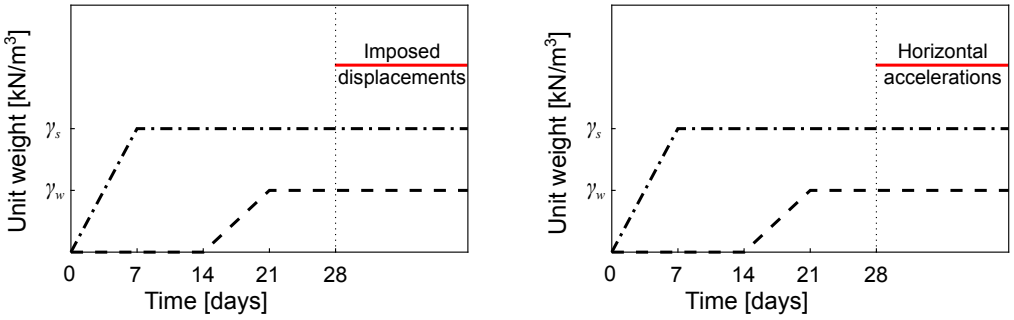

(a) Quasi-static case (b) Dynamic case

Figure 4.25 Localized failure analysis, loading programs

We provide an overall safety assessment of pore-saturated dam structure by performing failure analysis both in a quasi-static and dynamic setting, following the loading programs shown in Figures 4.25a and 4.25b. We first apply an increase of the self-weight, followed by the hydrostatic loading. The time step in the first two computation phases is set to Δt = 0.1 day. In a quasi-static setting, we compute the admissible horizontal overload by imposing horizontal displacements with a constant rate of $1 \cdot 10^{-3}$ mm/s on the top base of the dam. The time step is set to Δt = 1 s. In a dynamic setting, we compute the admissible horizontal overload by subjecting the dam-reservoir system to the linear increasing horizontal ground acceleration with a constant rate of 2 m/s^2 /1s. The initial time step is set to Δt = 0.001 s. Prior to reaching the ultimate value of horizontal overload, the time step is reduced to Δt = 0.0001 s.

→ Quasi-static case

The computed admissible horizontal overload force is 101.2393 kN (16.8732 kN/m') (Figure 4.26). The total horizontal reaction resulting from the self-weight and hydrostatic loading is 749.58 kN (124.93 kN/m'). Hence, we can state that for

this particular geometry and the mechanical properties of the dam, the factor of safety of the dam against failure is 1.14. The broken cohesive links in increasing softening at the end of the loading program are shown in Figures 4.27a-4.27c.

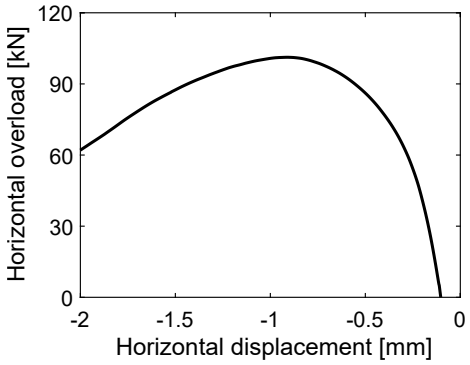

Figure 4.26 Horizontal overload (x direction), quasi-static case

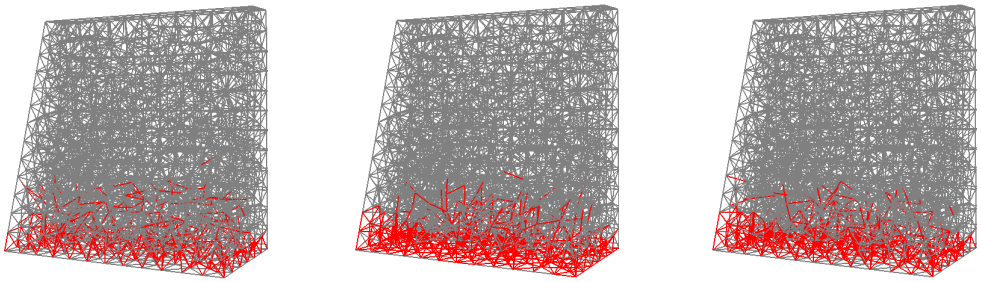

(a) Broken cohesive links: mode I

(b) Broken cohesive links: mode II

(c) Broken cohesive links: mode III

Figure 4.27 Failure mode for horizontal overload, quasi-static case

The computed factor of safety of the dam against failure in a quasi-static setting for 3D dam-reservoir system with reservoir height of 5.0 m is equal to 1.14, whereas for the 2D dam-reservoir system and reservoir height of 5.1 m the computed factor of safety is 1.06.

→ Dynamic case

The computed admissible value of horizontal overload force is 701.7073 kN (116.9512 kN/m'), which corresponds to the horizontal ground acceleration of 3.0746 m/s^2 (Figure 4.28). The self-weight and hydrostatic loading resulted in the total horizontal reaction equal to 749.58 kN (124.93 kN/m'). We can conclude that for this particular geometry and mechanical properties, the computed factor of safety of the dam subjected to combined quasi-static and extreme dynamic loads is 1.94. The broken cohesive links in increasing softening at the end of the loading program are shown in Figures 4.29a-4.29c.

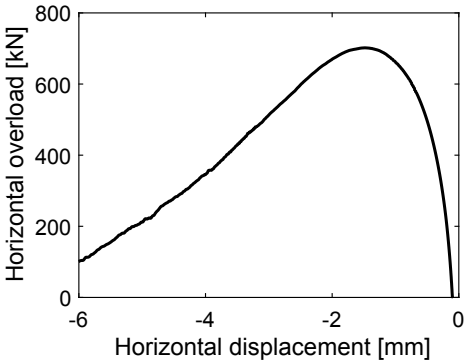

Figure 4.28 Horizontal overload (x direction), dynamic case

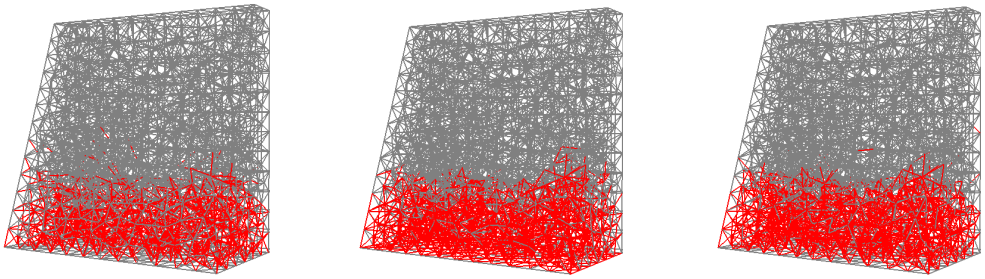

(a) Broken cohesive links: mode I

(b) Broken cohesive links: mode II

(c) Broken cohesive links: mode III

Figure 4.29 Failure mode for horizontal overload, dynamic case

The computed factor of safety of the dam against failure in a dynamic setting for 3D dam-reservoir system with reservoir height of 5.0 m is equal to 1.94, whereas for the 2D dam-reservoir system and reservoir height of 5.1 m the computed factor of safety is 1.71.

4.6 Concluding remarks

In this Chapter, we presented a 3D numerical model of acoustic fluid-structure interaction. The proposed model is an extension of the previously presented 2D numerical model, with modifications that arise due to the added dimension of the model.

First, we have simulated the response of the pore-saturated structure. The results of numerical simulations in the linear elastic regime of structure response confirm that the coefficient of permeability of coupled discrete beam lattice model of pore-saturated structure closely matches that of an equivalent continuum model. The results of numerical simulations in the nonlinear regime of structure response

demonstrate the capabilities of the proposed numerical model to capture inelastic response and localized failure in the pore-saturated structure.

Second, we have simulated dam-reservoir interaction. We have confirmed that the proposed numerical model of acoustic fluid-structure interaction is capable of predicting the hydrostatic and hydrodynamic pressure distributions exerted on the upstream face of the dam structure in close agreement with analytical solutions. Furthermore, we have illustrated the proposed numerical model ability to deal with the progressive localized failure of dam structure by computing the admissible horizontal overload that dam structure can withstand on top of already acting self-weight and hydrostatic pressure.

The proposed 3D numerical model of the structure and numerical model of acoustic fluid-structure interaction exhibit good performance in terms of fast convergence rates. However, the computational time is significantly increased when compared to the 2D case. For instance, the computational time for horizontal overload with included first two computation phases for the 2D case is 720.83 s, and for the 3D case 232566.9 s.

CHAPTER 5

EXTENSION TO NONISOTHERMAL CASE

ABSTRACT

In this Chapter, we account for the thermal effects in the structure built of a saturated porous medium. Namely, we present a coupled discrete beam lattice model of structure built of a nonisothermal saturated porous medium, which is an extension of the coupled discrete beam lattice model proposed in Chapter 4, for the isothermal case. The modifications pertain to the introduction of thermal coupling in the model. The temperature field is approximated with linear tetrahedral finite elements, resulting with an additional temperature degree of freedom placed at each node of the Timoshenko beam finite element. The heat flow in the model is governed by Fourier law for heat conduction. The application of the model is illustrated through several numerical simulations.

OUTLINE

5.1 Introduction

In this Chapter, we account for the thermal effects in the structure built of a saturated porous medium. Temperature changes can induce additional stresses in the structure as a result of restrained movement, which may contribute to cracking. Furthermore, the thermal actions can affect the stiffness and strength properties of the material, which has to be properly accounted for in order to provide a sound design of the structure. To be able to model these phenomena, which influence the overall safety and durability of the structure, we extend the coupled discrete beam lattice model presented in Chapter 4, for the isothermal case to nonisothermal case by introducing the thermal coupling into the model.

The outline of the Chapter is as follows: In Section 5.2, we describe the equations governing the response of the nonisothermal saturated porous medium. In Section 5.3, we present the finite element formulation of the proposed thermo-hydro-mechanical coupled discrete beam lattice model, together with the computational procedure. The finite element formulation is given in fully dynamics framework, which can be easily adjusted for quasi-static simplification. In Section 5.4, we present the results of several numerical simulations with the aim to validate the proposed coupled discrete beam lattice model of structure built of a nonisothermal saturated porous medium, and to demonstrate its capabilities to predict response and cracking in the structure subjected to combined thermal and mechanical loads. In Section 5.5, we give concluding remarks.

5.1.1 Governing equations of nonisothermal saturated porous medium

The equations governing the response of nonisothermal saturated porous medium are derived by combining equilibrium equation imposed on a porous medium, continuity equation imposed on a fluid flow and energy equation imposed on heat flow through such a porous medium [33, 34, 36, 5]. In a dynamic setting, we refer to the equation of motion instead of the equilibrium equation. The isothermal equations of motion and continuity equation are explained in detail in Chapter 2, Section 2.2.

Next, we present the equations governing the response of the nonisothermal saturated porous medium. The governing equations are derived under the assumptions that no phase change occurs and that the thermal equilibrium between the solid phase and the pore fluid is achieved.

5.1.1.1 Equations of motion

The strong form of equations of motion is written as

$$\nabla \cdot \boldsymbol{\sigma} + \mathbf{b} - \rho \mathbf{a} = \mathbf{0} \tag{5.1}$$

where $\boldsymbol{\sigma}$ is the total stress tensor, $\mathbf{b}$ are the body forces vector, $\mathbf{a}$ is the solid phase acceleration vector and ρ is the mass density of the mixture assumed to be constant.

Following Terzaghi's principle of effective stresses, the total stress is decomposed into effective stress and pore pressure, written as

$$\boldsymbol{\sigma} = \boldsymbol{\sigma}' - \mathbf{I} b p \tag{5.2}$$

where $\boldsymbol{\sigma}'$ is the effective stress tensor, $\mathbf{I}$ is the second order identity tensor, p is the pore pressure assumed positive in compression, and b is Biot's constant.

Furthermore, the effective stress tensor can be decomposed into mechanical part $\boldsymbol{\sigma}_u$ resulting from displacements and thermal part $\boldsymbol{\sigma}_T$ resulting from changes in temperature, written as

$$\boldsymbol{\sigma}' = \boldsymbol{\sigma}_u - \boldsymbol{\sigma}_T \tag{5.3}$$

with $\boldsymbol{\sigma}_T$ computed as

$$\boldsymbol{\sigma}_T = \boldsymbol{\beta}_T (T - T_0) \tag{5.4}$$

where $\boldsymbol{\beta}_T$ is the thermal stress tensor for isotropic case defined as $\boldsymbol{\beta}_T = \beta_T \mathbf{I}$, and T_0 is the reference temperature.

5.1.1.2 Continuity equation

The continuity equation for fluid flow through a nonisothermal porous medium is written as

$$\frac{1}{M}\dot{p} + b\nabla \cdot \dot{\mathbf{u}} - \bar{\beta}_{sf}\dot{T} - \nabla \cdot \left(\frac{k}{\gamma_f}\nabla p\right) = 0 \tag{5.5}$$

where M is Biot's modulus, k is the coefficient of permeability of the isotropic porous medium, γ_f is the specific weight of the fluid and $\bar{\beta}_{sf}$ is the thermal expansion coefficient of the mixture defined as $\bar{\beta}_{sf} = (b-n)\bar{\beta}_s + n\bar{\beta}_f$, with $\bar{\beta}_s$ as the thermal expansion coefficient of the solid phase and $\bar{\beta}_f$ as the thermal expansion coefficient of the pore fluid. In the formulation of continuity equation, the temperature dependence of the solid density is neglected.

5.1.1.3 Energy equation

The energy equation for porous medium under the assumption that both the solid phase and pore fluid have the same temperature at the coincident point and with convection ignored is written as

$$\rho C_T \dot{T} + \nabla \cdot \mathbf{q}_T - s = 0 \tag{5.6}$$

where ρC_T is the effective heat capacity defined as $\rho C_T = (1-n)\rho_s C_T^s + n\rho_f C_T^f$, with C_T^s as the heat capacity of the solid phase and C_T^f as the heat capacity of the pore fluid, $\mathbf{q}_T$ is the heat flux and s is the heat source.

The heat flux $\mathbf{q}_T$ is defined with Fourier law for heat conduction, written as

$$\mathbf{q}_T = -k_T \nabla T \tag{5.7}$$

where k_T is the coefficient of thermal conductivity of the isotropic porous medium.

In the formulation of energy equation the convection, the pressure and temperature dependence of the solid and fluid densities, and mechanical contributions to energy balance are neglected. These simplifications are in many cases justified and result in an uncoupled form of the energy equation [5, 36, 155].

5.2 Discrete model of structure

The starting point for our work on coupled discrete beam lattice model of the nonisothermal pore-saturated structure is the model presented in Chapter 4, for the isothermal case. Next, we present the modifications in the finite element formulation that arise due to the introduction of thermal coupling in the model.

5.3 Finite element formulation

5.3.1 Kinematics

The kinematics for inelastic Timoshenko beam finite element, and finite element approximation for pore pressure field are given in Chapter 4, Section 4.3.1. The temperature field is approximated in the same manner as the pore pressure field, using tetrahedral finite elements with four nodes (Figure 5.1).

The finite element approximation for temperature field is written as

$$T = \mathbf{N}_T^s \bar{\mathbf{T}} \tag{5.8}$$

where

$$\bar{\mathbf{T}}^{\mathsf{T}} = \left\{T_1,\, T_2,\, T_3,\, T_4\right\};$$

$$\mathbf{N}_T^s = \left\{N_1^t,\, N_2^t,\, N_3^t,\, N_4^t\right\};\quad N_i^t = \frac{a_i + b_i x + c_i y + d_i z}{6V},\quad i = 1,4;$$

$$6V = det\begin{vmatrix} 1 & x_1 & y_1 & z_1 \\ 1 & x_2 & y_2 & z_2 \\ 1 & x_3 & y_3 & z_3 \\ 1 & x_4 & y_4 & z_4 \end{vmatrix};\qquad a_1 = det\begin{vmatrix} x_2 & y_2 & z_2 \\ x_3 & y_3 & z_3 \\ x_4 & y_4 & z_4 \end{vmatrix};\qquad b_1 = -det\begin{vmatrix} 1 & y_2 & z_2 \\ 1 & y_3 & z_3 \\ 1 & y_4 & z_4 \end{vmatrix};$$

$$c_1 = -det\begin{vmatrix} x_2 & 1 & z_2 \\ x_3 & 1 & z_3 \\ x_4 & 1 & z_4 \end{vmatrix};\qquad d_1 = -det\begin{vmatrix} x_2 & y_2 & 1 \\ x_3 & y_3 & 1 \\ x_4 & y_4 & 1 \end{vmatrix};\qquad (5.9)$$

$$etc.$$

where V is the volume of the tetrahedral element, x,y,z are global coordinates and x_i, y_i, z_i are nodal coordinates of tetrahedral element, and constants a_{2-4}, b_{2-4}, c_{2-4}, d_{2-4} are defined by cyclic interchange of the subscripts in the order $1,2,3,4$.

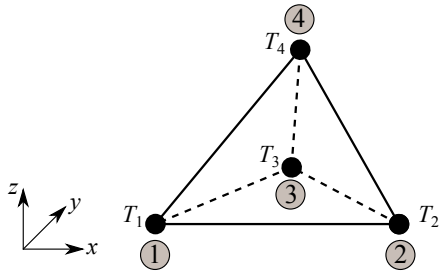

Figure 5.1 Linear tetrahedral finite element

The time derivatives of temperature field are written as

$$\dot{T} = \mathbf{N}_T^s \dot{\bar{\mathbf{T}}};$$
$$\ddot{T} = \mathbf{N}_T^s \ddot{\bar{\mathbf{T}}} \qquad (5.10)$$

5.3.2 Weak form of governing equations

5.3.2.1 Continuity equation

The coupling of the mechanics and the pore fluid flow occurs through the axial direction of the Timoshenko beam finite element. The continuity equation is

written as

$$\frac{1}{M}\dot{p} + b\dot{\varepsilon} - \bar{\beta}_{sf}\dot{T} - \nabla\cdot\left(\frac{k}{\gamma_f}\nabla p\right) = 0 \tag{5.11}$$

By introducing finite element approximations into the weak form of continuity equation and performing standard finite element discretization procedure (Chapter 4, Section 4.3), we obtain

$$\begin{aligned}\int_{\Omega^e_{Tet4}} \left[\left(\mathbf{N}_p^{s,\mathsf{T}}\frac{1}{M}\mathbf{N}_p^s\right)\dot{\bar{\mathbf{p}}} - \left(\mathbf{N}_p^{s,\mathsf{T}}\bar{\beta}_{sf}\mathbf{N}_T^s\right)\dot{\bar{\mathbf{T}}} + \left((\nabla\mathbf{N}_p^s)^{\mathsf{T}}\frac{k}{\gamma_f}\nabla\mathbf{N}_p^s\right)\bar{\mathbf{p}}\right] d\Omega \\ + \int_0^{L^e}\left(\mathbf{N}_{up}^{s,T} b\mathbf{B}_{up}^s\right)\dot{\bar{\mathbf{u}}}\,dx = \mathbf{q}^{ext,e}\end{aligned} \tag{5.12}$$

5.3.2.2 Energy equation

The energy equation is written as

$$\rho C_T\dot{T} - \nabla\cdot\left(k_T\nabla T\right) - s = 0 \tag{5.13}$$

The weak form of energy equation is written as

$$\int_{\Omega^e_{Tet4}} \delta T\left[\rho C_T\dot{T} - k_T\nabla\cdot(\nabla T) - s\right] d\Omega = 0 \tag{5.14}$$

where δT is the virtual temperature field interpolated in the same manner as the real temperature field

$$\begin{aligned}\delta T &= \mathbf{N}_T^s\delta\bar{\mathbf{T}};\ \ \delta\bar{\mathbf{T}}^{\mathsf{T}} = \left\{\delta T_1,\, \delta T_2,\, \delta T_3,\, \delta T_4\right\};\\ p^{\backslash} &= \mathbf{N}_{uT}^s\bar{\mathbf{T}}^{\backslash};\ \ \mathbf{N}_{uT}^s = \left\{N_1,\, N_2\right\};\ \ \bar{\mathbf{T}}^{\backslash\mathsf{T}} = \left\{T_1,\, T_2\right\};\\ \delta T^{\backslash} &= \mathbf{N}_{uT}^s\delta\bar{\mathbf{T}}^{\backslash};\ \ \delta\bar{\mathbf{T}}^{\backslash\mathsf{T}} = \left\{\delta T_1,\, \delta T_2\right\}\end{aligned} \tag{5.15}$$

By introducing finite element approximations into the weak form of continuity equation and performing standard finite element discretization procedure, we obtain

$$\int_{\Omega^e_{Tet4}} \left[\left(\mathbf{N}_T^{s,\mathsf{T}}\rho C_T\mathbf{N}_T^s\right)\dot{\bar{\mathbf{T}}} + \left((\nabla\mathbf{N}_T^s)^{\mathsf{T}}k_T\nabla\mathbf{N}_T^s\right)\bar{\mathbf{T}}\right] d\Omega = \mathbf{s}^{ext,e} \tag{5.16}$$

5.3.2.3 Equations of motion

The derivation of the weak form of equations of motion for the isothermal porous medium is presented in detail in Chapter 4, Section 4.3.2.2. The resulting weak

form of equations of motion for the nonisothermal porous medium is written as

$$\mathbf{f}^{acc,e} + \mathbf{f}^{int,e} - \mathbf{f}^{ext,e} = \mathbf{0} \tag{5.17}$$

$$\mathbf{h}^{e} = \mathbf{0} \tag{5.18}$$

where $\mathbf{f}^{int,e}$ is the vector of inertial forces, $\mathbf{f}^{int,e}$ is the internal force vector, $\mathbf{f}^{acc,e}$ is the external load vector, and $\mathbf{h}^{e}$ is the residual vector due to discontinuity, computed as

$$\begin{aligned}
&\mathbf{f}^{acc,e} = \int_0^{L^e} \mathbf{N}_u^{s,\mathsf{T}} \ddot{\boldsymbol{\sigma}}\, dx; \\
&\mathbf{f}^{int,e} = \int_0^{L^e} \mathbf{B}_u^{s,\mathsf{T}} \boldsymbol{\sigma}\, dx = \mathbf{f}^{int,e}(\boldsymbol{\sigma}_{uT}) - \mathbf{f}^{int,e}(\boldsymbol{\sigma}_p); \\
&\mathbf{h}^{e} = \int_0^{L^e} \mathbf{G}^{\mathsf{T}} \boldsymbol{\sigma}_{uT}\, dx = \int_0^{L^e} \bar{\mathbf{G}}^{\mathsf{T}} \boldsymbol{\sigma}_{uT}\, dx + \mathbf{t}; \quad \bar{\mathbf{G}} = \begin{bmatrix} \bar{G} & 0 & 0 & 0 & 0 & 0 \\ 0 & \bar{G} & 0 & 0 & 0 & 0 \\ 0 & 0 & \bar{G} & 0 & 0 & 0 \\ 0 & 0 & 0 & 0 & 0 & 0 \\ 0 & 0 & 0 & 0 & 0 & 0 \\ 0 & 0 & 0 & 0 & 0 & 0 \end{bmatrix}; \\
&\mathbf{t}^{\mathsf{T}} = \left\{ t^u, t^v, t^w, 0, 0, 0 \right\}
\end{aligned} \tag{5.19}$$

By taking into account that the coupling between the mechanics with the pore fluid flow and heat flow occurs through the axial direction of the Timoshenko beam finite element, the vectors in (5.19) are computed as

$$\begin{aligned}
&\ddot{\boldsymbol{\sigma}}^{\mathsf{T}} = \left\{ \rho A^e \ddot{u}, \rho A^e \ddot{v}, \rho A^e \ddot{w}, \rho I^e_{pol} \ddot{\theta}_x, \rho I^e_{yy} \ddot{\theta}_y, \rho I^e_{zz} \ddot{\theta}_z \right\}; \\
&\boldsymbol{\sigma}^{\mathsf{T}} = \left\{ N, V_y, V_z, M_x, M_y, M_z \right\}; \\
&\boldsymbol{\sigma}^{\mathsf{T}} = \boldsymbol{\sigma}^{\mathsf{T}}_{uT} - \boldsymbol{\sigma}^{\mathsf{T}}_{p}; \\
&\boldsymbol{\sigma}^{T}_{uT} = \left\{ N'_{uT}, V'_{uT,y}, V'_{uT,z}, M'_{uT,x}, M'_{uT,y}, M'_{uT,z} \right\}; \quad \boldsymbol{\sigma}^{T}_{p} = \left\{ bp\backslash A^e, 0, 0, 0, 0, 0 \right\}; \\
&\boldsymbol{\sigma}^{\mathsf{T}}_{uT} = \boldsymbol{\sigma}^{\mathsf{T}}_{u} - \boldsymbol{\sigma}^{\mathsf{T}}_{T}; \\
&\boldsymbol{\sigma}^{\mathsf{T}}_{u} = \left\{ N', V'_y, V'_z, M'_x, M'_y, M'_z \right\}; \quad \boldsymbol{\sigma}^{\mathsf{T}}_{T} = \left\{ \beta^{uT}_T (T\backslash - T_0) A^e, 0, 0, 0, 0, 0 \right\}
\end{aligned} \tag{5.20}$$

where β_T^{uT} is the thermal stress for thermo-mechanical coupling in the axial direction. The stress resultant vector $\boldsymbol{\sigma}_u^{\top}$ results from displacements, and is computed in the same manner as described in Chapter 4, Section 4.3. The internal force vector **t** acting at the discontinuity is computed as

$$\mathbf{t} = \begin{bmatrix} 1\,0\,0\,0\,0\,0 \\ 0\,1\,0\,0\,0\,0 \\ 0\,0\,1\,0\,0\,0 \\ 0\,0\,0\,0\,0\,0 \\ 0\,0\,0\,0\,0\,0 \\ 0\,0\,0\,0\,0\,0 \end{bmatrix} \int_0^{L^e} \boldsymbol{\sigma}_{uT} dx \tag{5.21}$$

For linear elasticity, the thermal stress β_T^{uT} is a function of lattice Young's modulus E and thermal expansion coefficient of the solid phase $\bar{\beta}_s$, written as

$$\beta_T^{uT} = E k_{\beta_T^{uT}} \bar{\beta}_s \tag{5.22}$$

The coefficient $k_{\beta_T^{uT}}$ takes into account the difference between 1D thermo-mechanical coupling and the 3D thermo-mechanical coupling. Namely, in 3D thermo-mechanical coupling for isotropic case the thermal stress β_T can be expressed in terms of thermal expansion coefficient $\bar{\beta}_s$ and Lame's parameters for continuum model λ_L and μ_L, written as

$$\beta_T = (3\lambda_L + 2\mu_L)\bar{\beta}_s \tag{5.23}$$

The last expression can be rewritten in terms of oedometer modulus E_{oed} and Poisson's ratio ν for continuum model, as

$$\beta_T = \left(\frac{1+\nu}{1-\nu}\right) E_{oed} \bar{\beta}_s \tag{5.24}$$

Hence, the coefficient $k_{\beta_T^{uT}}$ can then be computed as

$$k_{\beta_T^{uT}} = \left(\frac{1+\nu}{1-\nu}\right) E_{oed}/E \tag{5.25}$$

5.3.3 Computational procedure

The system of equations governing the thermo-hydro-mechanical coupled problem for single Timoshenko beam finite element is written as

$$\mathbf{M}^e_{uu}\ddot{\bar{\mathbf{u}}} + \mathbf{f}^{int,e}(\boldsymbol{\sigma}_{uT}) - \mathbf{K}^e_{up}\bar{\mathbf{p}}^{\backslash} = \mathbf{f}^{ext,e} \tag{5.26}$$

$$\mathbf{K}^{e,\mathsf{T}}_{up}\dot{\bar{\mathbf{u}}} - \mathbf{K}^e_{pT}\dot{\bar{\mathbf{T}}}^{\backslash} + \mathbf{D}^e_{pp}\dot{\bar{\mathbf{p}}}^{\backslash} + \mathbf{K}^e_{pp}\bar{\mathbf{p}}^{\backslash} = \mathbf{q}^{ext,e} \tag{5.27}$$

$$\mathbf{D}^e_{TT}\dot{\bar{\mathbf{T}}}^{\backslash} + \mathbf{K}^e_{TT}\bar{\mathbf{T}}^{\backslash} = \mathbf{s}^{ext,e} \tag{5.28}$$

where $\mathbf{M}^e_{uu}$ is the mass matrix, $\mathbf{f}^{int,e}(\boldsymbol{\sigma}_{uT})$ is the internal load vector resulting from displacements and temperature changes, $\mathbf{K}^e_{up}$ and $\mathbf{K}^e_{pT}$ are the coupling matrices, $\mathbf{D}^e_{pp}$ is the compressibility matrix, $\mathbf{K}^e_{pp}$ is the permeability matrix, $\mathbf{D}^e_{TT}$ is the heat capacity matrix, $\mathbf{K}^e_{TT}$ is the conductivity matrix, and $\mathbf{f}^{e,ext}$, $\mathbf{q}^{e,ext}$, $\mathbf{s}^{e,ext}$ are the load vectors. The matrices $\mathbf{K}^e_{up}$, $\mathbf{K}^e_{pT}$, $\mathbf{D}^e_{pp}$, $\mathbf{K}^e_{pp}$, $\mathbf{D}^e_{TT}$ and $\mathbf{K}^e_{TT}$ are computed as

$$\begin{aligned}
\mathbf{K}^e_{up} &= \int_0^{L^e} \mathbf{B}^{s,\mathsf{T}}_{up}\, b\mathbf{N}^s_{up}\, dx; \qquad \mathbf{K}^e_{pT} = \int_{\Omega^e_{Tet4}} \mathbf{N}^{s,\mathsf{T}}_p\, \bar{\beta}_{sf}\mathbf{N}^s_T\, d\Omega \\
\mathbf{D}^e_{pp} &= \int_{\Omega^e_{Tet4}} \mathbf{N}^{s,\mathsf{T}}_p \frac{1}{M}\mathbf{N}^s_p\, d\Omega; \quad \mathbf{K}^e_{pp} = \int_{\Omega^e_{Tet4}} (\nabla\mathbf{N}^s_p)^{\mathsf{T}} \frac{k}{\gamma_f}\nabla\mathbf{N}^s_p\, d\Omega \\
\mathbf{D}^e_{TT} &= \int_{\Omega^e_{Tet4}} \mathbf{N}^{s,\mathsf{T}}_T \rho C_t \mathbf{N}^s_T\, d\Omega; \quad \mathbf{K}^e_{TT} = \int_{\Omega^e_{Tet4}} (\nabla\mathbf{N}^s_T)^{\mathsf{T}} k_T \nabla\mathbf{N}^s_T\, d\Omega
\end{aligned} \tag{5.29}$$

Here we note that in the global system of equations (Equations 5.27 and 5.28) we take the parts of the $\mathbf{D}^e_{pp}$, $\mathbf{K}^e_{pp}$, $\mathbf{K}^e_{pT}$, $\mathbf{D}^e_{TT}$ and $\mathbf{K}^e_{TT}$ matrices (Equation 5.29) that correspond to the nodes of Timoshenko beam finite element.

The solution in terms of unknown nodal displacements, pore pressures and temperatures is computed at discrete pseudo-time steps $t_1, t_2, ..., t_n$ using Newmark time-integration scheme. For a time step t_{n+1} and iteration i, the global system of equations to be solved is written as

$$\overset{n_{elem}}{\underset{e=1}{\mathbb{A}}}\left\{\begin{bmatrix} \frac{1}{\beta\Delta t^2}\mathbf{M}_{uu} + \bar{\mathbf{K}}_{uu} & -\mathbf{K}_{up} & -\bar{\mathbf{K}}_{uT} \\ \frac{\gamma}{\beta\Delta t}\mathbf{K}^{\mathsf{T}}_{up} & \frac{\gamma}{\beta\Delta t}\mathbf{D}_{pp} + \mathbf{K}_{pp} & \frac{\gamma}{\beta\Delta t}\mathbf{K}_{pT} \\ 0 & 0 & \frac{\gamma}{\beta\Delta t}\mathbf{D}_{TT} + \mathbf{K}_{TT} \end{bmatrix}^{e,(i)}_{n+1} \begin{Bmatrix} \Delta\bar{\mathbf{u}} \\ \Delta\bar{\mathbf{p}}^{\backslash} \\ \Delta\bar{\mathbf{T}}^{\backslash} \end{Bmatrix}^{e,(i)}_{n+1} = \begin{Bmatrix} \mathbf{r}_u \\ \mathbf{r}_p \\ \mathbf{r}_T \end{Bmatrix}^{e,(i)}_{n+1} \right\} \tag{5.30}$$

where $\bar{\mathbf{K}}^e_{uu}$ is the tangent stiffness matrix, $\bar{\mathbf{K}}^e_{uT}$ is the tangent coupling matrix , and $\mathbf{r}^{e,(i)}_{u,n+1}$, $\mathbf{r}^{e,(i)}_{p,n+1}$ and $\mathbf{r}^{e,(i)}_{T,n+1}$ are residuals pertaining to the solid, the pore fluid and the temperature part.

After solving the global system of equations, the new iterative values of unknown fields are updated as

$$\begin{aligned}
\bar{\mathbf{u}}^{(i+1)}_{n+1} &= \bar{\mathbf{u}}^{(i)}_{n+1} + \Delta\bar{\mathbf{u}}^{(i)}_{n+1} \\
\bar{\mathbf{p}}^{(i+1)}_{n+1} &= \bar{\mathbf{p}}^{(i)}_{n+1} + \Delta\bar{\mathbf{p}}^{(i)}_{n+1} \\
\bar{\mathbf{T}}^{(i+1)}_{n+1} &= \bar{\mathbf{T}}^{(i)}_{n+1} + \Delta\bar{\mathbf{T}}^{(i)}_{n+1}
\end{aligned} \tag{5.31}$$

The tangent stiffness matrix $\bar{\mathbf{K}}^e_{uu}$ and tangent coupling matrix $\bar{\mathbf{K}}^e_{uT}$ depend whether the element is in elasto-viscoplastic or softening part of the response. If the element is elasto-viscoplastic, the tangent stiffness matrix and tangent coupling matrix are defined as

$$\begin{aligned}
\bar{\mathbf{K}}^{e,(i)}_{uu,n+1} = \mathbf{K}^{e,(i)}_{uu,n+1} &= \left(\frac{\partial \mathbf{f}^{int}(\boldsymbol{\sigma}_{uT})}{\delta\bar{\mathbf{u}}}\right)^{e,(i)}_{n+1} = \int_0^{L^e} \mathbf{B}^{s,\mathsf{T}}_u \mathbf{C}^{ep,(i)}_{n+1} \mathbf{B}^s_u dx \\
\bar{\mathbf{K}}^{e,(i)}_{uT,n+1} = \mathbf{K}^{e,(i)}_{uT,n+1} &= \left(\frac{\partial \mathbf{f}^{int}(\boldsymbol{\sigma}_{uT})}{\delta\bar{\mathbf{T}}}\right)^{e,(i)}_{n+1} = \int_0^{L^e} \mathbf{B}^{s,\mathsf{T}}_{uT} C^{ep,u,(i)}_{n+1} k_{\beta^{uT}_T} \bar{\beta}_s A^e \mathbf{N}^s_{uT} dx; \\
\mathbf{B}^s_{uT} &= \begin{bmatrix} B_1 & 0 & 0 & 0 & 0 & B_2 & 0 & 0 & 0 & 0 \end{bmatrix}
\end{aligned} \tag{5.32}$$

Elasto-plastic tangent matrix is written as

$$\mathbf{C}^{ep,(i)}_{n+1} = \begin{bmatrix}
C^{ep,u}_{n+1} A^e & 0 & 0 & 0 & 0 & 0 \\
0 & C^{ep,v}_{n+1} A^e & 0 & 0 & 0 & 0 \\
0 & 0 & C^{ep,w}_{n+1} A^e & 0 & 0 & 0 \\
0 & 0 & 0 & GI^e_{pol} & 0 & 0 \\
0 & 0 & 0 & 0 & EI^e & 0 \\
0 & 0 & 0 & 0 & 0 & EI^e
\end{bmatrix} \tag{5.33}$$

where $C^{ep,u}_{n+1}$, $C^{ep,v}_{n+1}$ and $C^{ep,w}_{n+1}$ are elasto-plastic tangent moduli for axial and transverse directions. The local phase procedure for computing elasto-plastic tangent moduli is given in Section 2.4.4.1.

If the element is in the softening, the tangent stiffness matrix and tangent coupling matrix are obtained by performing static condensation procedure. The statically condensed tangent stiffness matrix is written as

$$\bar{\mathbf{K}}^{e,(i)}_{uu,n+1} = \hat{\mathbf{K}}^{e,(i)}_{uu,n+1} = \left[\mathbf{K}^{e,(i)}_{uu,n+1} - \mathbf{F}^{e,(i)}_{n+1}\left(\mathbf{H}^{e,(i)}_{n+1} + \mathbf{K}_\alpha\right)^{-1}\left(\mathbf{F}^{e,(i),\mathsf{T}}_{n+1} + \mathbf{K}_d\right)\right] \tag{5.34}$$

where

$$\begin{aligned}
\mathbf{K}^{e,(i)}_{uu,n+1} &= \left(\frac{\partial \mathbf{f}^{int}(\boldsymbol{\sigma}_{uT})}{\delta \bar{\mathbf{u}}}\right)^{e,(i)}_{n+1} = \int_0^{L^e} \mathbf{B}^{s,T}_u \mathbf{C}^{ep,(i)}_{n+1} \mathbf{B}^s_u dx \\
\mathbf{F}^{e,(i)}_{n+1} &= \left(\frac{\partial \mathbf{f}^{int}(\boldsymbol{\sigma}_{uT})}{\delta \boldsymbol{\alpha}}\right)^{e,(i)}_{n+1} = \int_0^{L^e} \mathbf{B}^{s,T}_u \mathbf{C}^{ep,(i)}_{n+1} \bar{\mathbf{G}} dx \\
\left(\mathbf{F}^{\mathsf{T}} + \mathbf{K}_d\right)^{e,(i)}_{n+1} &= \left(\frac{\partial \mathbf{h}}{\delta \bar{\mathbf{u}}}\right)^{e,(i)}_{n+1} = \int_0^{L^e} \bar{\mathbf{G}}^T \mathbf{C}^{ep,(i)}_{n+1} \mathbf{B}^s_u dx + \mathbf{K}_d \\
\left(\mathbf{H} + \mathbf{K}_\alpha\right)^{e,(i)}_{n+1} &= \left(\frac{\partial \mathbf{h}}{\delta \boldsymbol{\alpha}}\right)^{e,(i)}_{n+1} = \int_0^{L^e} \bar{\mathbf{G}}^T \mathbf{C}^{ep,(i)}_{n+1} \bar{\mathbf{G}} dx + \mathbf{K}_\alpha
\end{aligned} \tag{5.35}$$

The matrices $\mathbf{K}_d$ and $\mathbf{K}_\alpha$ depend on the current step in softening being elastic or plastic. If the current step in the softening is elastic, then

$$\mathbf{K}_d = \mathbf{C}^* \mathbf{B}^s_u; \quad \mathbf{K}_\alpha = \mathbf{0}; \quad \mathbf{C}^* = \begin{bmatrix} EA^e & 0 & 0 & 0 & 0 & 0 \\ 0 & k_c GA^e & 0 & 0 & 0 & 0 \\ 0 & 0 & k_c GA^e & 0 & 0 & 0 \\ 0 & 0 & 0 & 0 & 0 & 0 \\ 0 & 0 & 0 & 0 & 0 & 0 \\ 0 & 0 & 0 & 0 & 0 & 0 \end{bmatrix} \tag{5.36}$$

Else, if the current step in the softening is plastic, then

$$\mathbf{K}_d = \mathbf{0}; \quad \mathbf{K}_\alpha = \begin{bmatrix} K^u_\alpha A^e & 0 & 0 & 0 & 0 & 0 \\ 0 & K^v_\alpha A^e & 0 & 0 & 0 & 0 \\ 0 & 0 & K^w_\alpha A^e & 0 & 0 & 0 \\ 0 & 0 & 0 & 0 & 0 & 0 \\ 0 & 0 & 0 & 0 & 0 & 0 \\ 0 & 0 & 0 & 0 & 0 & 0 \end{bmatrix} \tag{5.37}$$

The local phase procedure for computing matrices K^u_α, K^v_α and K^w_α is given in Section 2.4.4.2.

By taking into account that the coupling of solid phase with fluid flow occurs through the axial direction of the Timoshenko beam finite element, the statically condensed tangent coupling matrix is written as

$$\bar{\mathbf{K}}^{e,(i)}_{uT,n+1} = \hat{\mathbf{K}}^{e,(i)}_{uT,n+1} = \left[\mathbf{K}^{e,(i)}_{uT,n+1} - \mathbf{Q}^{e,(i)}_{n+1}\left(\mathbf{Y}^{e,(i)}_{n+1} + \mathbf{K}_{\alpha T}\right)^{-1}\left(\mathbf{W}^{e,(i)}_{n+1} + \mathbf{K}_{T}\right)\right] \tag{5.38}$$

where

$$\begin{aligned}
\mathbf{K}^{e,(i)}_{uT,n+1} &= \left(\frac{\partial \mathbf{f}^{int}(\boldsymbol{\sigma}_{uT})}{\delta \bar{\mathbf{T}}}\right)^{e,(i)}_{n+1} = \int_0^{L^e} \mathbf{B}^{s,T}_{uT} C^{ep,u,(i)}_{n+1} k_{\beta^{uT}_T} \bar{\beta}_s A^e \mathbf{N}^s_{uT} dx \\
\mathbf{Q}^{e,(i)}_{n+1} &= \left(\frac{\partial \mathbf{f}^{int}(\boldsymbol{\sigma}_{uT})}{\delta \boldsymbol{\alpha}}\right)^{e,(i)}_{n+1} = \int_0^{L^e} \mathbf{B}^{s,T}_{uT} C^{ep,u,(i)}_{n+1} k_{\beta^{uT}_T} \bar{\beta}_s A^e \bar{G} dx \\
\left(\mathbf{W} + \mathbf{K}_T\right)^{e,(i)}_{n+1} &= \left(\frac{\partial \mathbf{h}}{\delta \mathbf{T}}\right)^{e,(i)}_{n+1} = \int_0^{L^e} \bar{G} C^{ep,u,(i)}_{n+1} k_{\beta^{uT}_T} \bar{\beta}_s A^e \mathbf{N}^s_{uT} dx + \mathbf{K}_T \\
\left(\mathbf{Y} + \mathbf{K}_{\alpha T}\right)^{e,(i)}_{n+1} &= \left(\frac{\partial \mathbf{h}}{\delta \boldsymbol{\alpha}}\right)^{e,(i)}_{n+1} = \int_0^{L^e} \bar{G} C^{ep,u,(i)}_{n+1} A^e \bar{G} dx + \mathbf{K}_{\alpha T}
\end{aligned} \tag{5.39}$$

The matrices $\mathbf{K}_T$ and $\mathbf{K}_{\alpha T}$ depend on the current step in softening being elastic or plastic. If the current step in the softening is elastic, then

$$\mathbf{K}_T = C^{ep,u,(i)}_{n+1} A^e \mathbf{N}^s_{uT}; \quad \mathbf{K}_{\alpha T} = 0 \tag{5.40}$$

Else, if the current step in the softening is plastic, then

$$\mathbf{K}_T = \mathbf{0}; \quad \mathbf{K}_{\alpha T} = K^u_\alpha A^e \tag{5.41}$$

5.4 Numerical results

In this section, we present the results of several numerical simulations, which serve to illustrate the proposed approach ability to deal with nonisothermal problems. All numerical implementations and computations are performed with the research version of the computer code FEAP, developed by R.L. Taylor [41]. In all numerical simulations, the finite element mesh is generated by using Delaunay tetrahedralization and GMSH software [91]. The cross-sectional properties of the Timoshenko beam finite elements are computed from Voronoi diagram by using MATLAB software [92], which uses Qhull code [154].

5.4.1 Nonisothermal saturated poro-elastic column

In this section, we perform a quasi-static thermo-elastic one-dimensional consolidation analysis of saturated column, with the aim to validate the coupled discrete beam lattice model of structure built of saturated nonisothermal porous medium. The problem of one-dimensional thermo-elastic consolidation was first solved by Aboustit *et al.* [33, 34], and is later used as a benchmark by Lewis *et al.* [36], Noorishad and Tsang [38], and Cui *et al.* [40] to test their finite element formulations in 2D framework. To test our model, we extend the problem analyzed in the literature for 2D case (Figure 5.2a) to the 3D case (Figure 5.2b) and we compare our results against reference solutions provided by Lewis *et al.* [36] and Cui *et al.* [40]. Because the problem analyzed is the problem of one-dimensional consolidation, the results computed for the 3D case should match those obtained for the 2D case. The problem analyzed is unit-less.

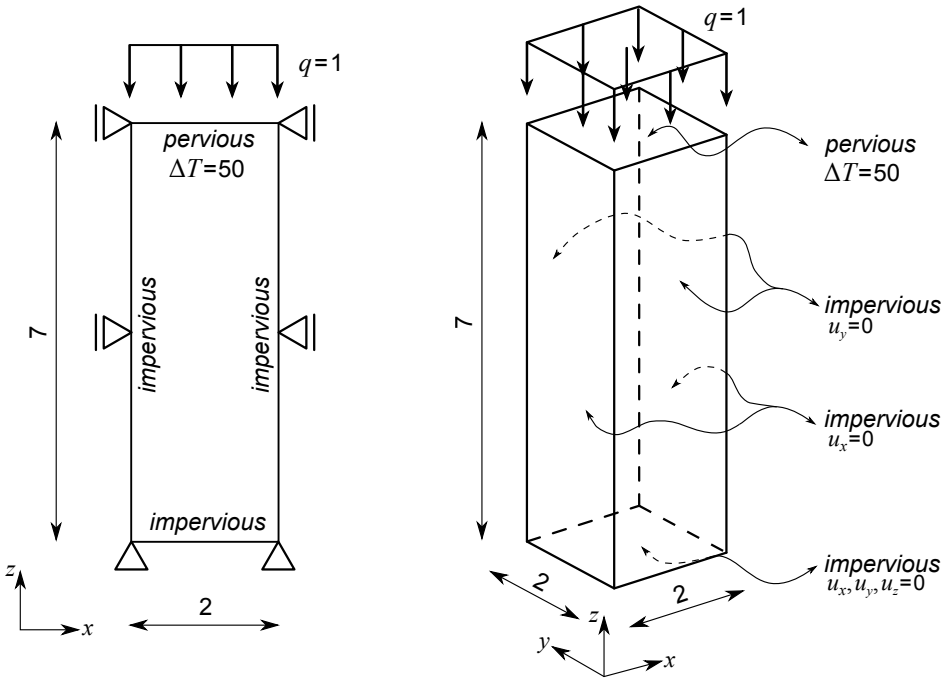

(a) 2D case, reference solution (b) 3D case, numerical model

Figure 5.2 Thermo-elastic consolidation of saturated column, problem statement

With the aim of inspecting the possible mesh dependency of the results, we perform a computation with a discrete model for two different mesh densities: coarse with 1437 Timoshenko beam finite elements (Figure 5.3a), and fine with 2875 Timoshenko beam finite elements (Figure 5.3b).

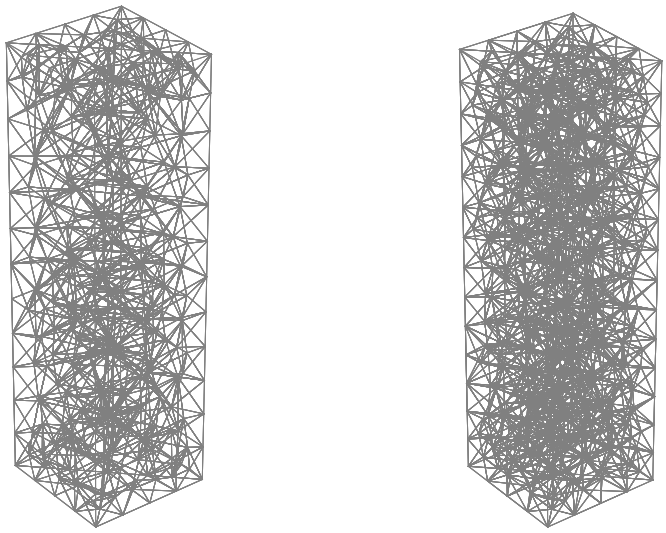

(a) Coarse mesh (b) Fine mesh

Figure 5.3 Finite element mesh densities

The linear elastic parameters of the continuum model are: Young's modulus $E = 6000$, and Poisson's ratio $\nu = 0.4$, which results with a value of oedometer modulus $E_{oed} = 12857$. The identified linear elastic parameters of the Timoshenko beam finite element are: Young's modulus $E = 16463$, and Poisson's ratio $\nu = 0$. The coefficient of permeability is $k/\gamma_f = 4 \cdot 10^{-6}$, Biot's constant is $b = 1$ and Biot's modulus is $1/M \to 0$. The coefficient of thermal conductivity is $k_T = 0.2$, the effective heat capacity is $\rho C_T = 40$, the thermal expansion coefficient of the solid phase is $\bar{\beta}_s = 0.3 \cdot 10^{-6}$ and the reference temperature is $T_0 = 0$, for both continuum and discrete model. The temperature term in the continuity equation is omitted, i.e. $\bar{\beta}_{sf}$ is set to 0. The coefficient $k_{\beta_T^{ut}}$ is identified as 1.82.

The saturated poro-elastic column (Figure 5.2b) is subjected to unit vertical surface pressure and a constant surface temperature $T = 50$. The time step values used in the numerical simulations are indicated in Table 5.1 [36, 40].

Table 5.1 Time stepping scheme

Time interval	Number of time steps
0.01	10
0.1	10
10	10
100	10
1000	20

We perform three types of computations. The first is the isothermal consolidation with the applied surface pressure only, the second is the thermal consolidation with the applied surface temperature only, and the third is the thermal consolidation with applied both the surface temperature and the surface pressure.

The computed results in terms of vertical displacements of column top for all three cases are shown in Figures 5.4a-5.4c. We can conclude that a good match between the computed results and reference values is obtained. The computed results are practically mesh independent. We note that the results for the thermal consolidation with the applied surface temperature only are not given for comparison in [40].

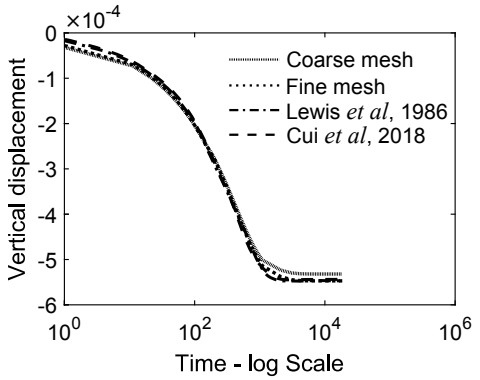

(a) Isothermal case

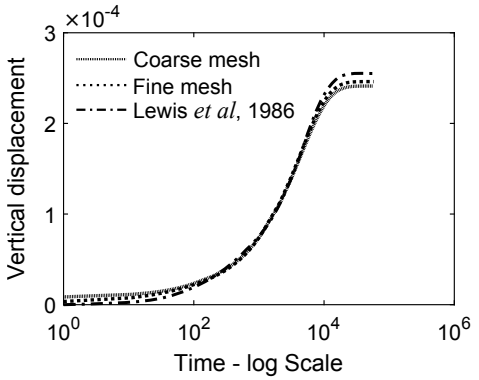

(b) Thermal case: surface temperature

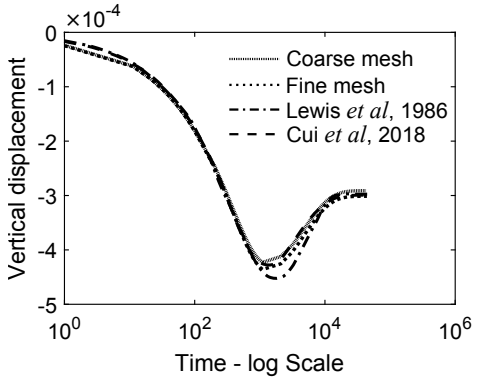

(c) Thermal case: surface temperature and pressure

Figure 5.4 Saturated poro-elastic column: vertical displacement of column top

The computed excess pore pressure and temperature at the $z = 6$ m measured from the bottom of the column for the third - thermal consolidation case are shown in Figures 5.5a and 5.5b. We observe a good match between the computed results and reference solutions, with results being practically mesh independent.

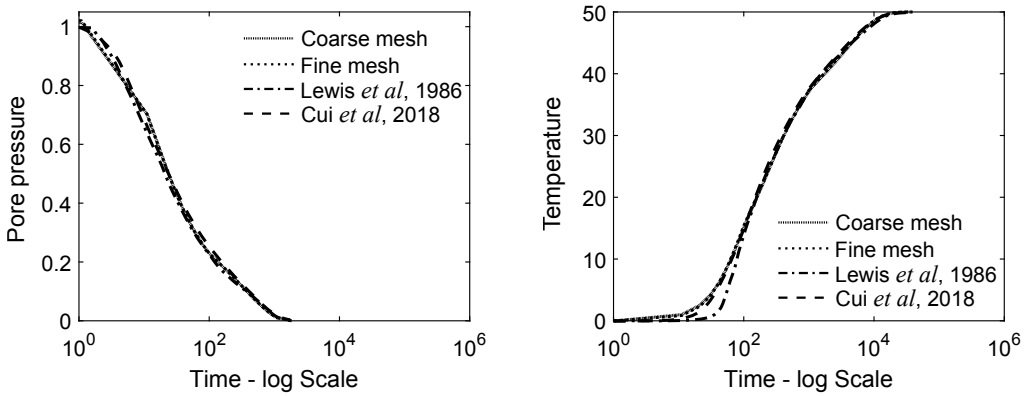

(a) Excess pore pressure at $z = 6$ m

(b) Temperature at $z = 6$ m

Figure 5.5 Thermal case, applied surface temperature and pressure: computed results

Next, we perform a thermo-mechanical computation (the pore pressure field is excluded from the computation) for the case of applied surface temperature only, and we compare the computed results with those obtained with the 3D numerical model of a column constructed in FEAP by using FEAP built-in solid elements [41]. The temperature evolution computed with discrete model is shown in Figures 5.7a-5.7c.

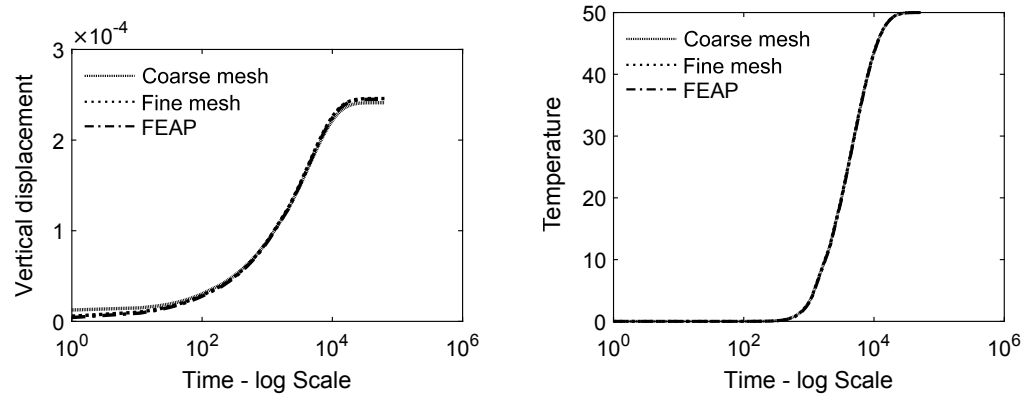

(a) Vertical displacements of column top

(b) Temperature at column bottom

Figure 5.6 Thermo-mechanical computation, applied surface temperature: comparison with 3D numerical model in FEAP

The results presented in this Section, suggest that the coefficient of thermal conductivity, the effective heat capacity and thermal expansion coefficient of the coupled discrete beam lattice model closely match those of an equivalent continuum model. Hence, they can be easily identified from standard experimental tests.

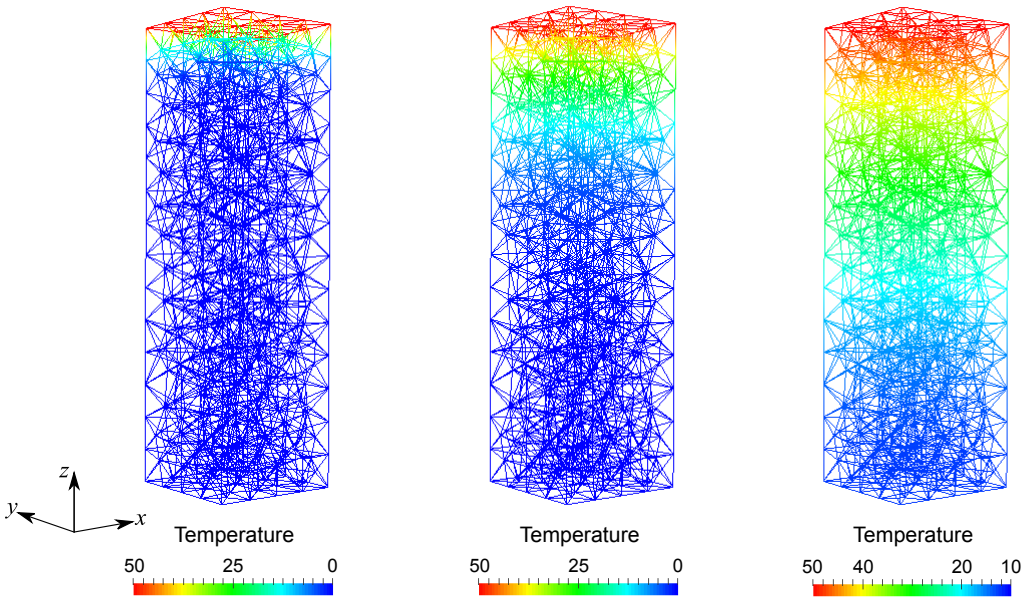

(a) Time step: 20 (b) Time step: 30 (c) Time step: 40

Figure 5.7 Temperature evolution, applied surface temperature

5.4.2 Thermal mechanical compression test

In this section, we perform a thermal mechanical compression test. We first subject the specimen to high temperatures, after which we impose vertical displacements on the top base of the specimen. We assume that the inertial effects are negligible. The geometry of the specimen and the boundary conditions are shown in Figure 5.8a. The finite element mesh is shown in Figure 5.8b.

The material parameters of the Timoshenko beam finite element are shown in Table 5.2. The linear hardening modulus is $H_{lh} = 2 \cdot 10^3$ kPa, the linear kinematic hardening modulus is $H_{lk} = 2 \cdot 10^3$ kPa, nonlinear hardening parameter is $H_{nlk} = 2 \cdot 10^2$, and the viscosity parameter is $\eta = 20$ kPa s. The coefficient of permeability is $k = 10^{-8}$ m/s, the specific weight of the water is $\gamma_w = 10$ kN/m^3, Biot's constant is $b = 1$ and Biot's modulus is $1/M \to 0$. The coefficient of thermal conductivity is $k_T = 2$ W/mK, the effective heat capacity is $\rho C_T = 1850$ kJ/Km^3, the thermal expansion coefficient of the solid phase is $\bar{\beta}_s = 0.00001\ (^\circ C)^{-1}$ and the reference temperature is $T_0 = 0^\circ$. The temperature term in the continuity equation is omitted, i.e. $\bar{\beta}_{sf}$ is set to 0. The coefficient $k_{\beta_T^{ut}}$ is selected as 1.0.

To investigate the temperature effects on the stiffness and load carrying capacity of the specimen, we assume that the material parameters: Young's modulus, yield limits, fracture limits and fracture energies of Timoshenko beam finite element are temperature dependent. We assume linear temperature dependence, written as

$$m = m\big(1-\omega_T(T-T_0)\big), \quad T > T_0 \tag{5.42}$$

where m is the material parameter, T and T_0 are the temperature and the reference temperature in the element and ω_T is the parameter controlling the temperature dependence.

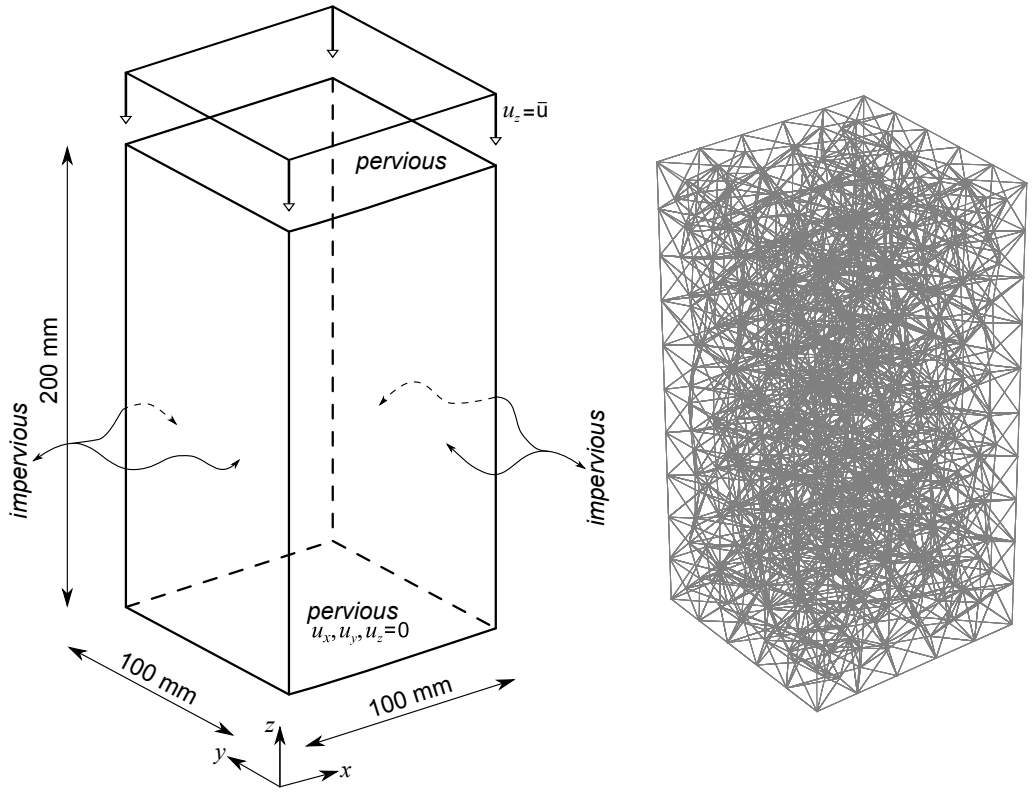

(a) Problem statement (b) Finite element mesh

Figure 5.8 Thermal mechanical compression test

Table 5.2 Thermal mechanical compression test: material parameters of the finite element

Young's modulus [kPa]	Poisson's ratio [/]	Yield limit [kPa]	Fracture limit [kPa]	Fracture energy [kN/m]
$E = 20000$	$\nu = 0.2$	$\sigma_{y,t} = 10$ $\sigma_{y,c} = 100$ $\sigma_{y,s} = 12$	$\sigma_{f,t} = 12$ $\sigma_{f,c} = 120$ $\sigma_{f,s} = 15$	$G_{f,t} = 20$ $G_{f,c} = 100$ $G_{f,s} = 10$

Next, we perform several numerical simulations of thermal compression test on dry (Biot's constant $b = 0 \rightarrow$ matrix $\mathbf{K}^e_{up}$ is a null matrix) and saturated specimen

(Biot's constant $b = 1$) for three values of parameter $\omega_T = -0.0001;\ 0;\ 0.0001$. We select the same value of ω_T for all material parameters, for which we assumed are temperature dependent. First, we subject the specimen to a temperature of 600°. After the temperature has reached a steady state throughout the specimen, we impose vertical displacements on the top base of the specimen with a constant rate of $v = 1 \cdot 10^{-5}$ m/s.

The computed results are shown in Figure 5.9. We can conclude that, depending on the value of ω_T, the stiffness and ultimate load level have decreased or increased when compared to the case of the temperature independent material parameters ($\omega_T = 0$). The broken cohesive links in increasing softening at the end of the loading program for saturated specimen and $\omega_T = -0.001$ are shown in Figures 5.10a-5.10c.

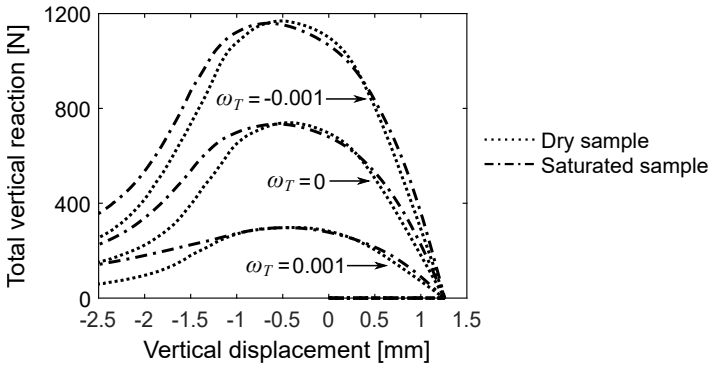

Figure 5.9 Thermal mechanical compression test: computed results

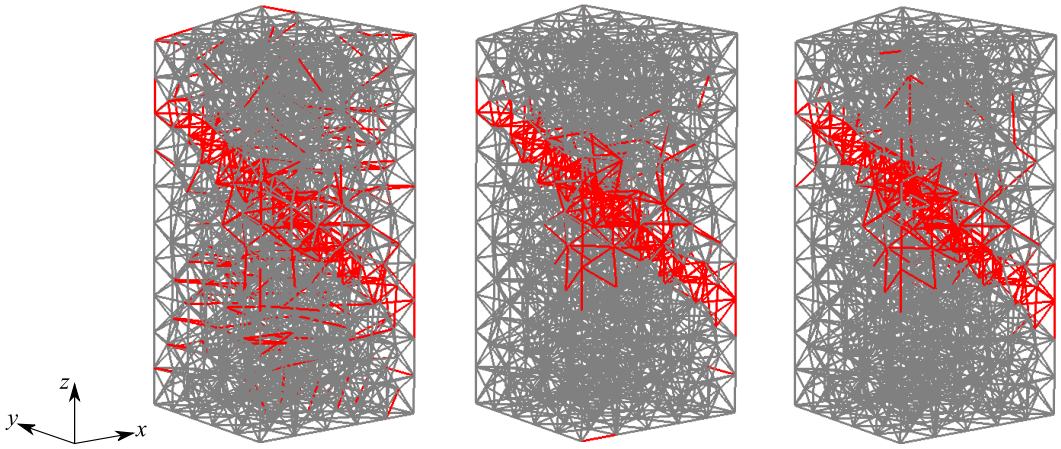

(a) Broken cohesive links: mode I

(b) Broken cohesive links: mode II

(c) Broken cohesive links: mode III

Figure 5.10 Failure mode for thermal mechancal compression test

The value of ω_T depends on the type of material and has to be identified through more elaborate parameter identification procedures. For example, the exposure of

the rock or concrete specimen to the elevated temperatures results in a decrease in the compressive strength, whereas for clay specimen the compressive strength increases.

5.4.3 Dam-reservoir system

In concrete dams, the temperature gradient near the exposed surface can cause surface cracks, which can affect structural durability. These surface cracks can also result in the long-term degradation of the load carrying capacity and stiffness of the dam, especially due to the large seasonal ambient temperature variations. Hence, the thermal effects in the structure have to be evaluated in order to set the initial conditions for the further failure analyses and to ensure the durability of the exposed surfaces and structure in general.

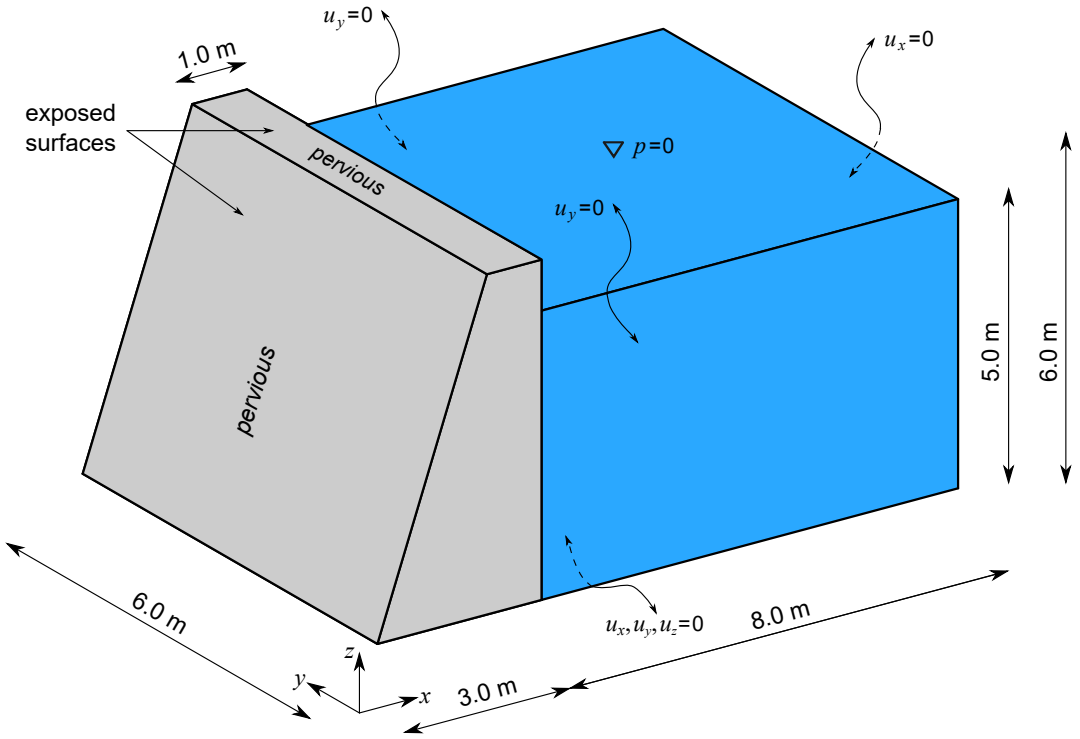

Figure 5.11 Geometry of dam-reservoir system

In this numerical example, we simulate a dam-reservoir system (Figure 5.11) subjected to combined mechanical and thermal loads. The mechanical loads are due to the self-weight and hydrostatic loading of the reservoir, and thermal loads are due to heating of the dam surfaces, which are exposed to the solar radiation (Figure 5.12a). We assume that the reference temperature in the dam is $T_0 = 20°C$, and we increase the temperature of the exposed surfaces up to $40°C$, after which is kept constant (Figure 5.12b). The temperature of the reservoir and dam foundation

is assumed to be constant and equal to $T = 20°C$. In order to be able to connect the structure and external fluid finite elements at the fluid-structure interface, an additional temperature degree of freedom has been added to the external fluid finite element. The temperature of the dam foundation is imposed as a boundary condition. The bottom base of the dam is kept fixed, and the movement of the dam in y direction is restrained.

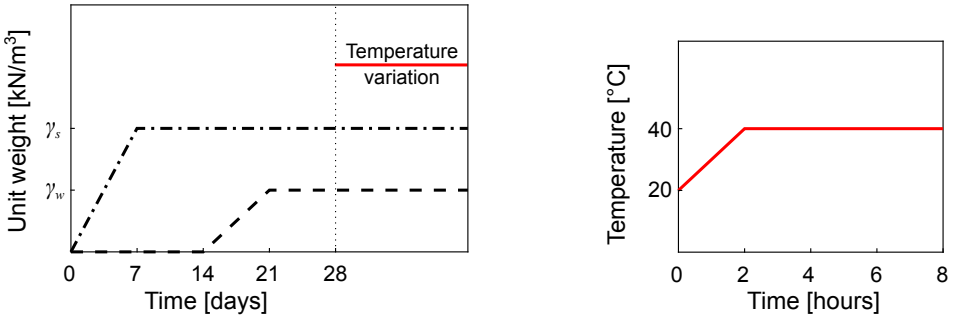

(a) Loading program (b) Temperature variation

Figure 5.12 Loading program combining mechanical and thermal loads

Young's modulus and Poisson's ratio of the Timoshenko beam finite element are $E = 10^4$ MPa and $\nu = 0$. The same values of yield shear stress, ultimate shear stress, and fracture energy are selected for both transverse directions (marked with subscript $_s$). The yield and fracture limits for the Timoshenko beam finite element in tension, compression and shear: $\sigma_{y,t} = 0.015$ MPa; $\sigma_{y,c} = 0.20$ MPa; $\sigma_{y,s} = 0.015$ MPa; $\sigma_{f,t} = 0.02$ MPa; $\sigma_{f,c} = 0.30$ MPa; $\sigma_{f,s} = 0.02$ MPa. The fracture energies in tension, compression and shear are: $G_{f,t} = 0.01$ GN/m; $G_{f,c} = 0.1$ GN/m; $G_{f,s} = 0.01$ GN/m. The linear hardening modulus is $H_{lh} = 10^3$ MPa. Young's modulus, yield limits, fracture limits and fracture energies are assumed to be temperature dependent, and the parameter controlling the temperature dependence ω_T is selected as 0.001.

The specific weight of the dam material is $\gamma_s = 20$ kN/m^3, and the specific weight of the water is $\gamma_w = 10$ kN/m^3. The coefficient of permeability is $k = 10^{-7}$ m/s, Biot's constant is $b = 1$ and Biot's modulus is $M = 10^6$ MPa. The coefficient of thermal conductivity is $k_T = 1$ W/mK, the effective heat capacity is $\rho C_T = 1500$ kJ/Km^3 and the thermal expansion coefficient of the solid phase is $\bar{\beta}_s = 0.00001$ $(°C)^{-1}$. The temperature term in the continuity equation is omitted, i.e. $\bar{\beta}_{sf}$ is set to 0. The coefficient $k_{\beta_T^{ut}}$ is selected as 1.0. The bulk modulus of the outside water is $\beta = 10^3$ MPa. The vorticity constraint is omitted throughout this numerical example.

We note that in this numerical example, we assumed the temperature dependence of the material parameters of dam material. However, this assumption can be omitted without significant influence on the computed results, because the temperature in the dam varies in a relatively narrow range.

The computed temperature distribution in the body of the dam is shown in Figure 5.13. We can conclude that the temperature variation (Figure 5.12b) affect the temperature less than 0.5 m into a cross-section, which is due to the high heat capacity and relatively low thermal conductivity of the dam material.

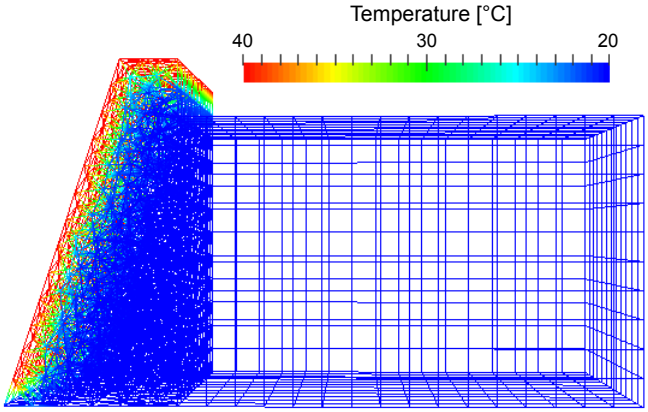

Figure 5.13 Temperature evolution in the dam

The broken cohesive links in increasing softening at the end of the loading program are shown in Figures 5.14a-5.14c. The broken cohesive links can be interpreted as cracks formed and still propagating in the dam. Thus, we can conclude that the temperature variation contributes to cracking near the exposed surfaces.

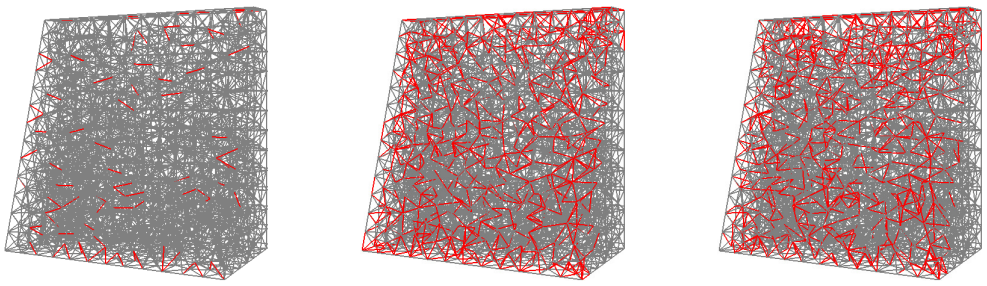

(a) Broken cohesive links: mode I

(b) Broken cohesive links: mode II

(c) Broken cohesive links: mode III

Figure 5.14 Broken cohesive links in increasing softening near exposed surfaces

The computed horizontal displacements (x direction) of the tip of the dam → point A(3, 3, 6)[m] for thermal loading phase are shown in Figure 5.15a. The distribution of horizontal displacements at the end of the loading program is shown in Figure 5.15b.

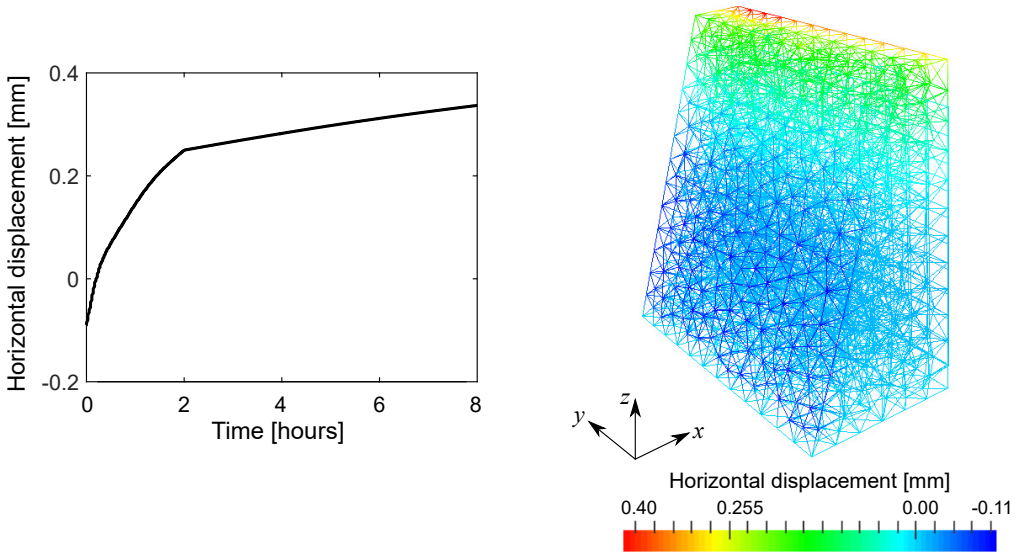

(a) Horizontal displacement at point A

(b) Horizontal displacements of dam structure

Figure 5.15 Horizontal displacements, x direction

The proposed numerical analysis can be further extended to account for the loading history throughout the dam operating period, which allows for a more precise investigation of the current state and remaining resistance of the existing dams. The safety analysis of this kind involves more complex loading program, which includes ambient temperature variations over the dam operating period. Namely, the large seasonal ambient temperature changes contribute to the long-term degradation in dam structure. Hence, aside from the self-weight and hydrostatic loading of the external reservoir, which are considered as the fundamental load cases, the effects of the large seasonal ambient temperature changes have to be computed in order to set the initial conditions for the computation of remaining resistance. The ambient temperatures over a period of months or years, depending on the dam operating period, are obtained from in-situ data measurements, and can include daily temperature variations, the weekly averages or can be approximated by sinusoidal function if the data follow sinusoidal pattern (Figure 5.16, for illustrative purposes not result of real data measurements). To more precisely model the effects of ambient temperature changes on the response of dam structure, convective heat transfer as a result of temperature differences between exposed surfaces and ambient temperature should be added in the numerical model, as well as radiation.

The self-weight, hydrostatic loading, and long-term temperature effects define initial conditions for further safety analysis, which can also include accidental loads such as earthquake or fire that can occur during a dam lifespan. From

the standpoint of engineering practice, it is essential to be able to quantify the remaining resistance of the structure, which previously experienced considerable damage from extreme loads of this kind.

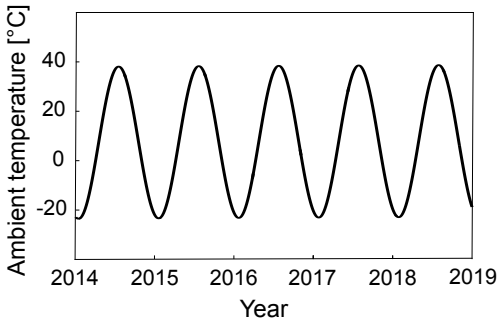

Figure 5.16 Sinusoidal ambient temperature change, illustrative example

To decrease computational cost, this kind of numerical analysis would require, operator split solution procedure with multi-scale analysis in time can be utilized [156, 157]. Namely, a large time step can be selected for the thermal part followed by a number of smaller time steps for the mechanical part, where the time step during mechanical computation can be controlled with the damage growth.

5.5 Concluding remarks

In this Chapter, we presented a coupled discrete beam lattice model of structure built of a nonisothermal saturated porous medium, which is an extension of the coupled discrete beam lattice model previously presented in Chapter 4, for the isothermal case.

We have confirmed through the results of validation computations in the linear elastic regime of structure response that the coefficient of thermal conductivity, the effective heat capacity and the thermal expansion coefficient of coupled discrete beam lattice model closely match those of an equivalent continuum model. Hence, they can be easily identified from standard experimental tests.

Next, we have illustrated the temperature effects on the stiffness and load carrying capacity of the structure by implementing the linear temperature dependence of the material parameters. The parameter controlling the temperature dependence has to be identified through more elaborate parameter identification procedures.

Finally, we have simulated the response and cracking of the dam structure subjected to combined mechanical and thermal loads. This type of numerical analysis can be further extended to failure analyses, that can also account for

the long-term effects of the large seasonal ambient temperature changes on the integrity and durability of the dam structure.

CHAPTER 6

CONCLUSIONS AND PERSPECTIVES

Conclusions

In this thesis, we studied the issue of the overall safety of structures built of saturated poro-plastic cohesive material in application to acoustic fluid-structure interaction problems, such as dam-reservoir interaction. We presented a novel approach to numerical modeling of dam-reservoir interaction, with the emphasis on the numerical representations of the structure and the external fluid.

The first feature of the proposed approach is the numerical representation of the structure in terms of a saturated porous medium. The macro-scale response and ultimate failure modes in the pore-saturated structure are captured with a coupled discrete beam lattice model based on Voronoi cell representation of the domain with cohesive links as inelastic Timoshenko beam finite elements enhanced with additional kinematics in terms of embedded strong discontinuities. The internal interaction of solid phase and pore fluid is handled with Biot's porous media theory and Darcy's law for pore fluid flow, resulting with an additional pressure-type degree of freedom placed at each node of a Timoshenko beam finite element.

The second feature of the proposed approach is the representation of the small motion of external fluid in confined conditions with the acoustic wave theory, Lagrangian formulation and mixed displacement/pressure finite element approximation, resulting with the displacement and pressure degrees of freedom. The finite element representations of the pore-saturated structure and the external fluid allows for the structure and the external fluid finite elements to share the displacement and pressure degrees of freedom. Thus, the issue of the fluid-structure interface is solved in an efficient and straightforward manner by directly connecting the structure and external fluid finite elements at common nodes.

The proposed numerical models of pore-saturated structure, external fluid and ultimately numerical model of acoustic fluid-structure interaction are first presented in 2D framework, and later extended to the 3D framework. The proposed numerical model of the pore-saturated structure in the 3D framework is further extended to the nonisothermal case.

We performed several numerical simulations with the aim to test the potential applications of the proposed approach. The successful application of discrete lattice models depends on the appropriate modeling of the micro-scale, which is in this case represented by enhanced Timoshenko beam finite elements. The results of numerical simulations of pore-saturated structure response demonstrate the proposed coupled discrete beam lattice capabilities to predict the complete macro-scale response and to capture true failure modes in the pore-saturated structure under extreme loads. The numerical simulations performed in linear elastic regime confirm that the coefficient of permeability, the coefficient of thermal conductivity, the effective heat capacity and the thermal expansion coefficient of coupled discrete beam lattice model closely match those of an equivalent continuum model, thus can be obtained directly as a result of standard experimental tests. The linear elastic parameters of Timoshenko beam finite element can be easily identified from standard experimental tests in combination with numerical tests, as shown in the numerical examples. Other parameters, such as yield and fracture limits, have to be identified through more elaborate parameter identification procedures such as the probability based ones.

The numerical simulations of acoustic fluid-structure interaction show that the proposed numerical model of interaction ensures the direct exchange of both the motion and the pressure at the fluid-structure interface. Thus, we are able to take into account the influence of the external fluid acting both as the source of pore saturation and the source of external loading on the structure. The results of numerical simulations in the linear elastic regime of structure response confirm that the proposed numerical model is able to predict the hydrostatic and hydrodynamic pressure distributions in close agreement with analytical solutions. Furthermore, the numerical simulations in the nonlinear regime of structure response illustrate the proposed numerical model ability to deal with the progressive localized failure of pore-saturated dam structure in interaction with the reservoir under extreme loads. Thus, we are able to quantify the remaining resistance and to provide an overall safety assessment of dam structure to potential overload with respect to fundamental load cases.

Perspectives

The proposed approach for acoustic fluid-structure interaction can have practical importance and can be used in various situations in engineering practice. The proposed numerical model of fluid-structure interaction can be used for predicting the safety and durability of existing dams in Bosnia and Herzegovina while taking into account existing defects or weak spots in the dam structure. It could also serve as a tool for numerical computations in the structural analysis and design of new dams and reservoirs.

Future works on the presented research include

- Testing the application of the 3D model of acoustic fluid-structure interaction in failure analyses of dam structures with complex geometries.
- Failure analyses of dam structure with complex loading programs involving large seasonal ambient temperature variations and extreme mechanical loads.
- Implementation of probability based identification procedures for determining the material parameters of Timoshenko beam finite element, such as yield limits, fracture limits and fracture energies, which would enable the comparison of numerical results with in-situ data measurements of real dam structures.
- Development of the coupled discrete beam lattice model of the structure built of a partially saturated porous medium.

REFERENCES

[1] K. Terzaghi. *Theoretical soil mechanics*. Chapman And Hali, Limited John Wiler And Sons, Inc; New York, 1944.

[2] M.A. Biot. General theory of three-dimensional consolidation. *Journal of applied physics*, 12(2):155–164, 1941.

[3] J.H. Prevost. Implicit-explicit schemes for nonlinear consolidation. *Computer Methods in Applied Mechanics and Engineering*, 39(2):225–239, 1983.

[4] O.C. Zienkiewicz and T. Shiomi. Dynamic behaviour of saturated porous media; the generalized biot formulation and its numerical solution. *International journal for numerical and analytical methods in geomechanics*, 8(1):71–96, 1984.

[5] R. W. Lewis and B. A. Schrefler. *The finite element method in the static and dynamic deformation and consolidation of porous media*. John Wiley, 1998.

[6] J. Réthoré, R. De Borst, and M.-A. Abellan. A two-scale model for fluid flow in an unsaturated porous medium with cohesive cracks. *Computational Mechanics*, 42(2):227–238, 2008.

[7] T. Mohammadnejad and A.R. Khoei. Hydro-mechanical modeling of cohesive crack propagation in multiphase porous media using the extended finite element method. *International Journal for Numerical and Analytical Methods in Geomechanics*, 37(10):1247–1279, 2013.

[8] T.D. Cao, E. Milanese, E.W. Remij, P. Rizzato, J.J.C Remmers, L. Simoni, J.M. Huyghe, F. Hussain, and B.A. Schrefler. Interaction between crack tip advancement and fluid flow in fracturing saturated porous media. *Mechanics Research Communications*, 80:24–37, 2017.

[9] E.W. Remij, J.J.C. Remmers, J.M. Huyghe, and D.M.J. Smeulders. An investigation of the step-wise propagation of a mode-ii fracture in a poroelastic medium. *Mechanics Research Communications*, 80:10–15, 2017.

[10] M. Vahab and N. Khalili. X-fem modeling of multizone hydraulic fracturing treatments within saturated porous media. *Rock Mechanics and Rock Engineering*, pages 1–21, 2018.

[11] R. De Borst, J. Réthoré, and M.-A. Abellan. A numerical approach for arbitrary cracks in a fluid-saturated medium. *Archive of Applied Mechanics*, 75(10-12):595–606, 2006.

[12] F. Kraaijeveld, J.M. Huyghe, J.J.C. Remmers, and R. De Borst. Two-dimensional mode i crack propagation in saturated ionized porous media using partition of unity finite elements. *Journal of Applied Mechanics*, 80(2):020907, 2013.

[13] F. Armero and C. Callari. An analysis of strong discontinuities in a saturated poro-plastic solid. *International journal for numerical methods in engineering*, 46(10):1673–1698, 1999.

[14] C. Callari and F. Armero. Finite element methods for the analysis of strong discontinuities in coupled poro-plastic media. *Computer Methods in Applied Mechanics and Engineering*, 191(39-40):4371–4400, 2002.

[15] C. Callari and F. Armero. Analysis and numerical simulation of strong discontinuities in finite strain poroplasticity. *Computer Methods in Applied Mechanics and Engineering*, 193(27-29):2941–2986, 2004.

[16] C. Callari, F. Armero, and A. Abati. Strong discontinuities in partially saturated poroplastic solids. *Computer Methods in Applied Mechanics and Engineering*, 199(23-24):1513–1535, 2010.

[17] V.P. Nguyen, H. Lian, T. Rabczuk, and S. Bordas. Modelling hydraulic fractures in porous media using flow cohesive interface elements. *Engineering Geology*, 225:68–82, 2017.

[18] B.A. Schrefler, S. Secchi, and L. Simoni. On adaptive refinement techniques in multi-field problems including cohesive fracture. *Computer methods in applied mechanics and engineering*, 195(4-6):444–461, 2006.

[19] S. Secchi, L. Simoni, and B.A. Schrefler. Mesh adaptation and transfer schemes for discrete fracture propagation in porous materials. *International journal for numerical and analytical methods in geomechanics*, 31(2):331–345, 2007.

[20] S. Secchi and B.A. Schrefler. A method for 3-d hydraulic fracturing simulation. *International journal of fracture*, 178(1-2):245–258, 2012.

[21] T.D. Cao, F. Hussain, and B.A. Schrefler. Porous media fracturing dynamics: stepwise crack advancement and fluid pressure oscillations. *Journal of the Mechanics and Physics of Solids*, 111:113–133, 2018.

[22] E. Milanese, O. Yılmaz, J.-F. Molinari, and B.A. Schrefler. Avalanches in dry and saturated disordered media at fracture. *Physical Review E*, 93(4):043002, 2016.

[23] E. Milanese, O. Yılmaz, and B.A. Molinari, J.-F.and Schrefler. Avalanches in dry and saturated disordered media at fracture in shear and mixed mode scenarios. *Mechanics Research Communications*, 80:58–68, 2017.

[24] M.F. Wheeler, T. Wick, and W. Wollner. An augmented-lagrangian method for the phase-field approach for pressurized fractures. *Computer Methods in Applied Mechanics and Engineering*, 271:69–85, 2014.

[25] A. Mikelic, M.F. Wheeler, and T. Wick. A phase-field method for propagating fluid-filled fractures coupled to a surrounding porous medium. *Multiscale Modeling & Simulation*, 13(1):367–398, 2015.

[26] A. Mikelić, M.F. Wheeler, and T. Wick. Phase-field modeling of a fluid-driven fracture in a poroelastic medium. *Computational Geosciences*, 19(6):1171–1195, 2015.

[27] S. Lee, M.F. Wheeler, and T. Wick. Pressure and fluid-driven fracture propagation in porous media using an adaptive finite element phase field model. *Computer Methods in Applied Mechanics and Engineering*, 305:111–132, 2016.

[28] J.E. Bolander Jr and S. Berton. Simulation of shrinkage induced cracking in cement composite overlays. *Cement and Concrete Composites*, 26(7):861–871, 2004.

[29] P. Grassl. A lattice approach to model flow in cracked concrete. *Cement and Concrete Composites*, 31(7):454–460, 2009.

[30] B. Šavija, J. Pacheco, and E. Schlangen. Lattice modeling of chloride diffusion in sound and cracked concrete. *Cement and Concrete Composites*, 42:30–40, 2013.

[31] B. Šavija, M. Luković, and E. Schlangen. Lattice modeling of rapid chloride migration in concrete. *Cement and Concrete Research*, 61:49–63, 2014.

[32] M. Nikolic, A. Ibrahimbegovic, and P. Miscevic. Discrete element model for the analysis of fluid-saturated fractured poro-plastic medium based on sharp crack representation with embedded strong discontinuities. *Computer Methods in Applied Mechanics and Engineering*, 298:407–427, 2016.

[33] B.L. Aboustit, S.H. Advani, and J.K. Lee. Variational principles and finite element simulations for thermo-elastic consolidation. *International journal for numerical and analytical methods in geomechanics*, 9(1):49–69, 1985.

[34] B.L. Aboustit. *Finite element invesitagtions of thermo-elastic and thermo-plastic consolidation*. PhD thesis, 1983. The Ohio State University.

[35] A.M. Britto, C. Savvidou, M.J. Gunn, and J.R. Booker. Finite element analysis of the coupled heat flow and consolidation around hot buried objects. *Soils and Foundations*, 32(1):13–25, 1992.

[36] R.W. Lewis, C.E. Majorana, and B.A. Schrefler. A coupled finite element model for the consolidation of nonisothermal elastoplastic porous media. *Transport in porous media*, 1(2):155–178, 1986.

[37] R.W. Lewis, P.J. Roberts, and B.A. Schrefler. Finite element modelling of two-phase heat and fluid flow in deforming porous media. *Transport in Porous Media*, 4(4):319–334, 1989.

[38] J. Noorishad and C.-F. Tsang. Coupled thermohydroelasticity phenomena in variably saturated fractured porous rocks–formulation and numerical solution. In *Developments in geotechnical engineering*, volume 79, pages 93–134. Elsevier, 1996.

[39] B. Gatmiri and P. Delage. A formulation of fully coupled thermal–hydraulic–mechanical behaviour of saturated porous media—numerical approach. *International journal for numerical and analytical methods in geomechanics*, 21(3):199–225, 1997.

[40] W. Cui, D.M. Potts, L. Zdravković, K.A. Gawecka, and D.M.G. Taborda. An alternative coupled thermo-hydro-mechanical finite element formulation for fully saturated soils. *Computers and Geotechnics*, 94:22–30, 2018.

[41] O.C. Zienkiewicz and R.L. Taylor. *The Finite Element Method, vols. I, II, II*. Elsevier, 2005.

[42] R. Ohayon and C. Soize. *Structural Acoustics and Vibration*. Academic Press, 1998.

[43] F. Fahy and P. Gardonio. *Sound and Structural Vibration: Radiation, Transmission and Response*. Academic Press, 2007.

[44] O.C. Zienkiewicz and P. Bettess. Fluid-structure dynamic interaction and wave forces. an introduction to numerical treatment. *International Journal for Numerical Methods in Engineering*, 13(1):1–16, 1978.

[45] H. Morand and R. Ohayon. Variational formulations for the elasto acoustic vibration problem-finite element results. pages 785–796, 1976.

[46] H. Morand and R. Ohayon. Substructure variational analysis of the vibrations of coupled fluid–structure systems. finite element results. *International Journal for Numerical Methods in Engineering*, 14(5):741–755, 1979.

[47] H. Morand and R. Ohayon. *Fluid–Structure Interaction: Applied Numerical Methods*. Wiley, 1995.

[48] G.C. Everstine. A symmetric potential formulation for fluid-structure interaction. *Journal of Sound Vibration*, 79:157–160, 1981.

[49] L.G. Olson and K.J. Bathe. Analysis of fluid-structure interactions. a direct symmetric coupled formulation based on the fluid velocity potential. *Computers & Structures*, 21(1-2):21–32, 1985.

[50] E. Kock and L. Olson. Fluid-structure interaction analysis by the finite element method–a variational approach. *International journal for numerical methods in engineering*, 31(3):463–491, 1991.

[51] P. Saini, S.S.and Bettess and O.C. Zienkiewicz. Coupled hydrodynamic response of concrete gravity dams using finite and infinite elements. *Earthquake Engineering & Structural Dynamics*, 6(4):363–374, 1978.

[52] M. Cervera, J. Oliver, and R. Faria. Seismic evaluation of concrete dams via continuum damage models. *Earthquake engineering & structural dynamics*, 24(9):1225–1245, 1995.

[53] Y. Calayir, A.A. Dumanoğlu, and A. Bayraktar. Earthquake analysis of gravity dam-reservoir systems using the eulerian and lagrangian approaches. *Computers & structures*, 59(5):877–890, 1996.

[54] G.C. Everstine. Finite element formulations of structural acoustics problems. *Computers & Structures*, 65(3):307–321, 1997.

[55] S. Küçükarslan, S.B. Coşkun, and B. Taşkın. Transient analysis of dam–reservoir interaction including the reservoir bottom effects. *Journal of Fluids and Structures*, 20(8):1073–1084, 2005.

[56] I. Gogoi and D. Maity. Influence of sediment layers on dynamic behavior of aged concrete dams. *Journal of engineering mechanics*, 133(4):400–413, 2007.

[57] X. Wang and L.B. Wang. Dynamic analysis of a water–soil–pore water coupling system. *Computers & structures*, 85(11-14):1020–1031, 2007.

[58] N. Bouaanani and F.Y. Lu. Assessment of potential-based fluid finite elements for seismic analysis of dam–reservoir systems. *Computers & Structures*, 87(3-4):206–224, 2009.

[59] S. Mitra and K.P. Sinhamahapatra. 2d simulation of fluid-structure interaction using finite element method. *Finite Elements in Analysis and Design*, 45(1):52–59, 2008.

[60] K.K. Mandal and D. Maity. 2d finite element analysis of rectangular water tank with separator wall using direct coupling. *Coupled systems mechanics*, 4(4):317–336, 2015.

[61] A.K. Chopra, E.L. Wilson, and I. Farhoomand. Earthquake analysis of reservoir-dam systems. In *Proceedings of the Fourth World Conference on Earthquake Engineering*, volume 2, pages 1–10, 1969.

[62] T.A. Shugar and M.G. Katona. Development of finite element head injury model. *Journal of the Engineering Mechanics Division*, 101(3):223–239, 1975.

[63] L. Kiefling and G.C. Feng. Fluid-structure finite element vibrational analysis. *AIAA Journal*, 14(2):199–203, 1976.

[64] D. Shantaram, D.R.J. Owen, and O.C. Zienkiewicz. Dynamic transient behaviour of two-and three-dimensional structures including plasticity, large deformation effects and fluid interaction. *Earthquake Engineering & Structural Dynamics*, 4(6):561–578, 1976.

[65] T.B. Belytschko and J.M. Kennedy. A fluid-structure finite element method for the analysis of reactor safety problems. *Nuclear Engineering and Design*, 38(1):71–81, 1976.

[66] T.B. Khalil and R.P. Hubbard. Parametric study of head response by finite element modeling. *Journal of Biomechanics*, 10(2):119–132, 1977.

[67] E.L. Wilson. Finite elements for foundations, joints and fluids. *Finite elements in geomechanics*, pages 319–350, 1977.

[68] K.J. Bathe and W.F. Hahn. On transient analysis of fluid-structure systems. *Computers & Structures*, 10(1-2):383–391, 1979.

[69] M.A. Hamdi, Y. Ousset, and G. Verchery. A displacement method for the analysis of vibrations of coupled fluid-structure systems. *International Journal for Numerical Methods in Engineering*, 13(1):139–150, 1978.

[70] N. Akkas, H.U. Akay, and C. Yilmaz. Applicability of general-purpose finite element programs in solid-fluid interaction problems. *Computers & Structures*, 10(5):773–783, 1979.

[71] L.G. Olson and K.J. Bathe. A study of displacement-based fluid finite elements for calculating frequencies of fluid and fluid-structure systems. *Nuclear Engineering and Design*, 76(2):137–151, 1983.

[72] H.C. Chen and R.L. Taylor. Vibration analysis of fluid–solid systems using a finite element displacement formulation. *International Journal for Numerical Methods in Engineering*, 29(4):683–698, 1990.

[73] E.L. Wilson and M. Khalvati. Finite elements for the dynamic analysis of fluid-solid systems. *International Journal for Numerical Methods in Engineering*, 19(11):1657–1668, 1983.

[74] K.J. Bathe, C. Nitikitpaiboon, and X. Wang. A mixed displacement-based finite element formulation for acoustic fluid-structure interaction. *Computers & Structures*, 56(2-3):225–237, 1995.

[75] X. Wang and K.J. Bathe. Displacement/pressure based mixed finite element formulations for acoustic fluid-structure interaction problems. *International journal for numerical methods in engineering*, 40(11):2001–2017, 1997.

[76] X. Wang and K.J. Bathe. On mixed elements for acoustic fluid-structure interactions. *Mathematical Models and Methods in Applied Sciences*, 7(03):329–343, 1997.

[77] Y. Calayir and A.A. Dumanoğlu. Static and dynamic analysis of fluid and fluid-structure systems by the lagrangian method. *Computers & structures*, 49(4):625–632, 1993.

[78] Y. Calayir and M. Karaton. A continuum damage concrete model for earthquake analysis of concrete gravity dam–reservoir systems. *Soil Dynamics and Earthquake Engineering*, 25(11):857–869, 2005.

[79] Y. Calayir and M. Karaton. Seismic fracture analysis of concrete gravity dams including dam–reservoir interaction. *Computers & structures*, 83(19-20):1595–1606, 2005.

[80] M. Akköse, S. Adanur, A. Bayraktar, and A. A. Dumanoğlu. Elasto-plastic earthquake response of arch dams including fluid–structure interaction by the lagrangian approach. *Applied Mathematical Modelling*, 32(11):2396–2412, 2008.

[81] A. Bilici, Y.and Bayraktar, K. Soyluk, K. Haciefendioğlu, Ş. Ateş, and S. Adanur. Stochastic dynamic response of dam–reservoir–foundation systems to spatially varying earthquake ground motions. *Soil Dynamics and Earthquake Engineering*, 29(3):444–458, 2009.

[82] L. Pelecanos, S. Kontoe, and L. Zdravković. Numerical modelling of hydrodynamic pressures on dams. *Computers and Geotechnics*, 53:68–82, 2013.

[83] M.E. Kartal and A. Bayraktar. Non-linear earthquake response of cfr dam–reservoir–foundation systems. *Mathematical and Computer Modelling of Dynamical Systems*, 19(4):353–374, 2013.

[84] L. Pelecanos, S. Kontoe, and L. Zdravković. The effects of dam–reservoir interaction on the nonlinear seismic response of earth dams. *Journal of Earthquake Engineering*, pages 1–23, 2018.

[85] H.M. Westergaard. Water pressures on dams during earthquakes. *Trans. ASCE*, 98:418–432, 1933.

[86] J.S.-H. Kuo. *Fluid-structure interactions: Added mass computations for incompressible fluid*. University of California, College of Engineering, Earthquake Engineering Research Center, 1982.

[87] S.S. Bhattacharjee and P. Leger. Seismic cracking and energy dissipation in concrete gravity dams. *Earthquake Engineering & Structural Dynamics*, 22(11):991–1007, 1993.

[88] F. Ghrib and R. Tinawi. An application of damage mechanics for seismic analysis of concrete gravity dams. *Earthquake Engineering & Structural Dynamics*, 24(2):157–173, 1995.

[89] J. Lee and G.L. Fenves. A plastic-damage concrete model for earthquake analysis of dams. *Earthquake engineering & structural dynamics*, 27(9):937–956, 1998.

[90] M. Ghaemian and A. Ghobarah. Nonlinear seismic response of concrete gravity dams with dam–reservoir interaction. *Engineering Structures*, 21(4):306–315, 1999.

[91] C. Geuzaine and Remacle J.-F. Gmsh: A 3-d finite element mesh generator with built-in pre-and post-processing facilities. *International Journal for Numerical Methods in Engineering*, 79(11):1309–1331, 2009.

[92] MATLAB. *version 8.5.0.197613 (R2015a)*. The MathWorks Inc., Natick, Massachusetts, 2015.

[93] F. Armero and K. Garikipati. An analysis of strong discontinuities in multiplicative finite strain plasticity and their relation with the numerical simulation of strain localization in solids. *International Journal of Solids and Structures*, 33(20-22):2863–2885, 1996.

[94] J. Oliver. Modelling strong discontinuities in solid mechanics via strain softening constitutive equations. part 2: Numerical simulation. *International journal for numerical methods in engineering*, 39(21):3601–3623, 1996.

[95] A. Ibrahimbegovic and D. Brancherie. Combined hardening and softening constitutive model of plasticity: precursor to shear slip line failure. *Computational Mechanics*, 31(1):88–100, 2003.

[96] C. Linder and F. Armero. Finite elements with embedded strong discontinuities for the modeling of failure in solids. *International Journal for Numerical Methods in Engineering*, 72(12):1391–1433, 2007.

[97] D. Brancherie and A. Ibrahimbegovic. Novel anisotropic continuum-discrete damage model capable of representing localized failure of massive structures: Part i: theoretical formulation and numerical implementation. *Engineering Computations*, 26(1/2):100–127, 2009.

[98] M. Hautefeuille, S. Melnyk, J.-B. Colliat, and A. Ibrahimbegovic. Failure model for heterogeneous structures using structured meshes and accounting for probability aspects. *Engineering Computations*, 26(1/2):166–184, 2009.

[99] J. Dujc, B. Brank, and A. Ibrahimbegovic. Quadrilateral finite element with embedded strong discontinuity for failure analysis of solids. *Computer Modeling in Engineering and Sciences*, 69(3):223, 2010.

[100] J. Dujc, B. Brank, and A. Ibrahimbegovic. Stress-hybrid quadrilateral finite element with embedded strong discontinuity for failure analysis of plane stress solids. *International journal for numerical methods in engineering*, 94(12):1075–1098, 2013.

[101] T. Saksala and A. Ibrahimbegovic. Anisotropic viscodamage–viscoplastic consistency constitutive model with a parabolic cap for rocks with brittle and ductile behaviour. *International Journal of Rock Mechanics and Mining Sciences*, 70:460–473, 2014.

[102] T. Saksala, D. Brancherie, I. Harari, and A. Ibrahimbegovic. Combined continuum damage-embedded discontinuity model for explicit dynamic fracture analyses of quasi-brittle materials. *International Journal for Numerical Methods in Engineering*, 101(3):230–250, 2015.

[103] X.N. Do, A. Ibrahimbegovic, and D. Brancherie. Dynamics framework for 2d anisotropic continuum-discrete damage model for progressive localized failure of massive structures. *Computers & Structures*, 183:14–26, 2017.

[104] L. Benedetti, M. Cervera, and M. Chiumenti. 3d numerical modelling of twisting cracks under bending and torsion of skew notched beams. *Engineering Fracture Mechanics*, 176:235–256, 2017.

[105] M. Nikolić, E. Karavelić, A. Ibrahimbegovic, and P. Miščević. Lattice element models and their peculiarities. *Archives of Computational Methods in Engineering*, 25(3):753–784, 2018.

[106] E. Schlangen and E.J. Garboczi. Fracture simulations of concrete using lattice models: computational aspects. *Engineering fracture mechanics*, 57(2-3):319–332, 1997.

[107] M. Ostoja-Starzewski. Lattice models in micromechanics. *Applied Mechanics Reviews*, 55(1):35–60, 2002.

[108] B.L. Karihaloo, P.F. Shao, and Q.Z. Xiao. Lattice modelling of the failure of particle composites. *Engineering Fracture Mechanics*, 70(17):2385–2406, 2003.

[109] J.E. Bolander and N. Sukumar. Irregular lattice model for quasistatic crack propagation. *Physical Review B*, 71(9):094106, 2005.

[110] S. Berton and J.E. Bolander. Crack band model of fracture in irregular lattices. *Computer Methods in Applied Mechanics and Engineering*, 195(52):7172–7181, 2006.

[111] A. Ibrahimbegovic and A. Delaplace. Microscale and mesoscale discrete models for dynamic fracture of structures built of brittle material. *Computers & structures*, 81(12):1255–1265, 2003.

[112] A. Ibrahimbegovic and S. Melnyk. Embedded discontinuity finite element method for modeling of localized failure in heterogeneous materials with structured mesh: an alternative to extended finite element method. *Computational Mechanics*, 40(1):149–155, 2007.

[113] N. Benkemoun, M. Hautefeuille, J.-B. Colliat, and A. Ibrahimbegovic. Failure of heterogeneous materials: 3d meso-scale fe models with embedded discontinuities. *International Journal for Numerical Methods in Engineering*, 82(13):1671–1688, 2010.

[114] N. Benkemoun, A. Ibrahimbegovic, and J.-B. Colliat. Anisotropic constitutive model of plasticity capable of accounting for details of meso-structure of two-phase composite material. *Computers & Structures*, 90:153–162, 2012.

[115] M. Nikolic, A. Ibrahimbegovic, and P. Miscevic. Brittle and ductile failure of rocks: embedded discontinuity approach for representing mode i and mode ii failure mechanisms. *International Journal for Numerical Methods in Engineering*, 102(8):1507–1526, 2015.

[116] N. Cvitanovic, M. Nikolic, and A. Ibrahimbegovic. Influence of specimen shape deviations on uniaxial compressive strength of limestone and similar rocks. *International Journal of Rock Mechanics and Mining Sciences*, 80:357–372, 2015.

[117] M. Nikolic and A. Ibrahimbegovic. Rock mechanics model capable of representing initial heterogeneities and full set of 3d failure mechanisms. *Computer Methods in Applied Mechanics and Engineering*, 290:209–227, 2015.

[118] M. Nikolic. *Rock mechanics, failure phenomena with pre-existing cracks and internal fluid flow through cracks*. PhD thesis, 2015. Thèse de doctorat dirigée par Ibrahimbegovic, Adnan Mécanique, génie mécanique, génie civil Cachan, Ecole normale supérieure 2015.

[119] P.C. Hammer, O.J. Marlowe, and A.H. Stroud. Numerical integration over simplexes and cones. *Mathematical Tables and Other Aids to Computation*, 10(55):130–137, 1956.

[120] A. Hrennikoff. Solution of problems of elasticity by the framework method. *J. appl. Mech.*, no. 8. ser. A:169–175, 1941.

[121] E. Hadzalic, A. Ibrahimbegovic, and S. Dolarevic. Failure mechanisms in coupled soil-foundation systems. *Coupled Systems Mechanics*, 7(1):27–42, 2018.

[122] E. Hadzalic, A. Ibrahimbegovic, and M. Nikolic. Failure mechanisms in coupled poro-plastic medium. *Coupled Systems Mechanics*, 7(1):43–59, 2018.

[123] E. Hadzalic, A. Ibrahimbegovic, S. Dolarevic, and M. Nikolic. Macroscale response of dry and saturated soil subjected to footing load. In *Proceedings of ECCOMAS MSF 2017 Thematic conference, Ljubljana, Slovenia*, pages 41–50, 20-22 September 2017.

[124] A. Ibrahimbegovic. *Nonlinear solid mechanics: theoretical formulations and finite element solution methods*, volume 160. Springer Science & Business Media, 2009.

[125] M. Jukić, B. Brank, and A. Ibrahimbegović. Embedded discontinuity finite element formulation for failure analysis of planar reinforced concrete beams and frames. *Engineering Structures*, 50:115–125, 2013.

[126] M. Jukić, B. Brank, and A. Ibrahimbegovic. Failure analysis of reinforced concrete frames by beam finite element that combines damage, plasticity and embedded discontinuity. *Engineering structures*, 75:507–527, 2014.

[127] P.J. Armstrong and C.O. Frederick. A mathematical representation of the multiaxial bauschinger effect. *CEBG Report RD/B/N, 731*, 1966.

[128] M. Pastor, T. Li, X. Liu, and O.C. Zienkiewicz. Stabilized low-order finite elements for failure and localization problems in undrained soils and foundations. *Computer Methods in Applied Mechanics and Engineering*, 174(1-2):219–234, 1999.

[129] I. Babuška. The finite element method with lagrangian multipliers. *Numerische Mathematik*, 20(3):179–192, 1973.

[130] F. Brezzi. On the existence, uniqueness and approximation of saddle-point problems arising from lagrangian multipliers. *Revue française d'automatique, informatique, recherche opérationnelle. Analyse numérique*, 8(R2):129–151, 1974.

[131] O.C. Zienkiewicz, S. Qu, R.L. Taylor, and S. Nakazawa. The patch test for mixed formulations. *International Journal for Numerical Methods in Engineering*, 23(10):1873–1883, 1986.

[132] L. Sanavia, B.A. Schrefler, and P. Steinmann. A formulation for an unsaturated porous medium undergoing large inelastic strains. *Computational Mechanics*, 28(2):137–151, 2002.

[133] O.C. Zienkiewicz, A.H.C. Chan, M. Pastor, D.K. Paul, and T. Shiomi. Static and dynamic behaviour of soils: a rational approach to quantitative solutions. i. fully saturated problems. *Proc. R. Soc. Lond. A*, 429(1877):285–309, 1990.

[134] H. Matthies and G. Strang. The solution of nonlinear finite element equations. *International journal for numerical methods in engineering*, 14(11):1613–1626, 1979.

[135] W.M. Swolfs R.B.J. Brinkgreve, S. Kumarswamy and F. Foria. *PLAXIS 2D Manuals*. 2018.

[136] R. de Boer, W. Ehlers, and Z. Liu. One-dimensional transient wave propagation in fluid-saturated incompressible porous media. *Archive of applied mechanics*, 63(1):59–72, 1993.

[137] A. Kucerova, D. Brancherie, A. Ibrahimbegovic, J. Zeman, and Z. Bittnar. Novel anisotropic continuum-discrete damage model capable of representing localized failure of massive structures: Part ii: identification from tests under heterogeneous stress field. *Engineering Computations*, 26(1/2):128–144, 2009.

[138] B.V. Rosić, A. Kučerová, J. Sỳkora, O. Pajonk, A. Litvinenko, and H.G. Matthies. Parameter identification in a probabilistic setting. *Engineering Structures*, 50:179–196, 2013.

[139] S.M. Sarfaraz, B. V. Rosić, H.G. Matthies, and A. Ibrahimbegovic. Stochastic upscaling via linear bayesian updating. In *Multiscale Modeling of Heterogeneous Structures*, pages 163–181. Springer, 2018.

[140] H.J. Siriwardane and C.S. Desai. Two numerical schemes for nonlinear consolidation. *International Journal for Numerical Methods in Engineering*, 17(3):405–426, 1981.

[141] E. Hadzalic, A. Ibrahimbegovic, and S. Dolarevic. Fluid-structure interaction system predicting both internal pore pressure and outside hydrodynamic pressure. *Coupled Systems Mechanics*, 7(6):649–668, 2018.

[142] E. Hadzalic, A. Ibrahimbegovic, and S. Dolarevic. Theoretical formulation and seamless discrete approximation for localized failure of saturated poroplastic structure interacting with reservoir. *Computers & Structures*, 214:73–93, 2019.

[143] E. Hadzalic, A. Ibrahimbegovic, and S. Dolarevic. Novel method for acoustic fluid-structure interaction in application to overall safety of structures in quasi-static setting. In *Proceedings of CILAMCE Congress, Paris/Compiègne, France*, pages 171–174, 11-14 November 2018.

[144] F. Brezzi and M. Fortin. *Mixed and hybrid finite element methods*, volume 15. Springer Science & Business Media, 2012.

[145] K.J. Bathe. *Finite Element Procedures*. Prentice-Hall, Englewood Cliffs, NJ, 1996.

[146] D. Chapelle and K.J. Bathe. The inf-sup test. *Computers & Structures*, 47(4-5):537–545, 1993.

[147] K.J. Bathe. The inf–sup condition and its evaluation for mixed finite element methods. *Computers & structures*, 79(2):243–252, 2001.

[148] T. Von Kármán. Discussion of water pressures on dams during earthquakes. *Trans. ASCE*, 98:434–436, 1933.

[149] A.T. Chwang and G.W. Housner. Hydrodynamic pressures on sloping dams during earthquakes. part 1. momentum method. *Journal of Fluid Mechanics*, 87(2):335–341, 1978.

[150] A.T. Chwang. Hydrodynamic pressures on sloping dams during earthquakes. part 2. exact theory. *Journal of Fluid Mechanics*, 87(2):343–348, 1978.

[151] P.L.-F. Liu. Hydrodynamic pressures on rigid dams during earthquakes. *Journal of fluid mechanics*, 165:131–145, 1986.

[152] A.K. Chopra. *Dynamics of Structures: Theory and Applications to Earthquake Engineering*. Civil Engineering and Engineering Mechanics Series. Prentice Hall, 2012.

[153] M. Gellert and R. Harbord. Moderate degree cubature formulas for 3-d tetrahedral finite-element approximations. *Communications in applied numerical methods*, 7(6):487–495, 1991.

[154] C.B. Barber, D.P. Dobkin, and H. Huhdanpaa. The quickhull algorithm for convex hulls. *ACM Transactions on Mathematical Software (TOMS)*, 22(4):469–483, 1996.

[155] J.R. Booker and C. Savvidou. Consolidation around a point heat source. *International Journal for Numerical and Analytical Methods in Geomechanics*, 9(2):173–184, 1985.

[156] A. Ibrahimbegovic, J.B. Colliat, and L. Davenne. Thermomechanical coupling in folded plates and non-smooth shells. *Computer methods in applied mechanics and engineering*, 194(21-24):2686–2707, 2005.

[157] R. Niekamp, A. Ibrahimbegovic, and H.G. Matthies. Formulation, solution and ctl software for coupled thermomechanics systems. *Coupled systems mechanics*, 3(1):1–25, 2014.

LIST OF FIGURES

LIST OF TABLES